



ATLAS Note

GROUP-2017-XX



23rd April 2021

Draft version 0.1

1

2 **A Deep Learning Approach to Differential**
3 **Measurements of Higgs - Top Interactions in**
4 **Multilepton Final States**

5

The ATLAS Collaboration

6 Several theories Beyond the Standard Model modify the momentum spectrum of the Higgs
7 Boson, without significantly altering the overall rate of Higgs produced from top quark pairs.
8 A differential measurement of the Higgs transverse momentum provides a way to search for
9 these effects at the LHC. Because of the challenges inherent to reconstructing the Higgs in
10 multilepton final states, a deep learning approach is used to predict the momentum spectrum
11 of the Higgs for events where the Higgs Boson is produced from top quark pairs and decays
12 to final states that include multiple leptons. The regressed Higgs p_T is fit to data for events
13 with two or three leptons in the final state, and estimates of the sensitivity to variations in the
14 Higgs p_T spectrum are given.

© 2021 CERN for the benefit of the ATLAS Collaboration.

15 Reproduction of this article or parts of it is allowed as specified in the CC-BY-4.0 license.

16 **Contents**

| | | |
|----|--|----|
| 17 | I Introduction | 7 |
| 18 | 1 Introduction | 7 |
| 19 | II Theoretical Motivation | 10 |
| 20 | 2 The Standard Model and the Higgs Boson | 10 |
| 21 | 2.1 The Forces and Particles of the Standard Model | 10 |
| 22 | 2.2 The Higgs Mechanism | 13 |
| 23 | 2.2.1 The Higgs Field | 13 |
| 24 | 2.2.2 Electroweak Symmetry Breaking | 15 |
| 25 | 2.3 $t\bar{t}H$ Production | 18 |
| 26 | 2.4 WZ + Heavy Flavor Production | 20 |
| 27 | 2.5 Extensions to the Standard Model | 21 |
| 28 | III The LHC and the ATLAS Detector | 24 |
| 29 | 3 The LHC | 24 |
| 30 | 4 The ATLAS Detector | 27 |
| 31 | 4.1 Inner Detector | 29 |
| 32 | 4.2 Calorimeters | 30 |
| 33 | 4.3 Muon Spectrometer | 31 |
| 34 | 4.4 Trigger System | 32 |
| 35 | IV Measurement of WZ + Heavy Flavor | 33 |
| 36 | 5 Introduction | 33 |
| 37 | 6 Data and Monte Carlo Samples | 35 |
| 38 | 6.1 Data Samples | 35 |
| 39 | 6.2 Monte Carlo Samples | 35 |
| 40 | 7 Object Reconstruction | 36 |
| 41 | 7.1 Trigger | 37 |
| 42 | 7.2 Light leptons | 37 |
| 43 | 7.3 Jets | 38 |
| 44 | 7.4 B-tagged Jets | 39 |
| 45 | 7.5 Missing transverse energy | 41 |

| | | |
|----|--|------------|
| 46 | 7.6 Overlap removal | 41 |
| 47 | 8 Event Selection and Signal Region Definitions | 42 |
| 48 | 8.1 Event Preselection | 42 |
| 49 | 8.2 Fit Regions | 47 |
| 50 | 8.3 Non-Prompt Lepton Estimation | 64 |
| 51 | 8.3.1 $t\bar{t}$ Validation | 64 |
| 52 | 8.3.2 Z+jets Validation | 70 |
| 53 | 9 tZ Interference Studies and Separation Multivariate Analysis | 75 |
| 54 | 9.1 Top Mass Reconstruction | 75 |
| 55 | 9.2 tZ BDT | 77 |
| 56 | 10 Data and Monte Carlo Samples | 82 |
| 57 | 10.1 Data Samples | 82 |
| 58 | 10.2 Monte Carlo Samples | 82 |
| 59 | 11 Object Reconstruction | 83 |
| 60 | 11.1 Trigger | 84 |
| 61 | 11.2 Light leptons | 84 |
| 62 | 11.3 Jets | 85 |
| 63 | 11.4 B-tagged Jets | 86 |
| 64 | 11.5 Missing transverse energy | 88 |
| 65 | 11.6 Overlap removal | 88 |
| 66 | 12 Event Selection and Signal Region Definitions | 89 |
| 67 | 12.1 Event Preselection | 89 |
| 68 | 12.2 Fit Regions | 94 |
| 69 | 12.3 Non-Prompt Lepton Estimation | 111 |
| 70 | 12.3.1 $t\bar{t}$ Validation | 111 |
| 71 | 12.3.2 Z+jets Validation | 117 |
| 72 | 13 tZ Interference Studies and Separation Multivariate Analysis | 122 |
| 73 | 13.1 Top Mass Reconstruction | 122 |
| 74 | 13.2 tZ BDT | 124 |
| 75 | 14 Systematic Uncertainties | 128 |
| 76 | 15 Results | 137 |
| 77 | 15.1 1-jet Fit Results | 138 |
| 78 | 15.2 2-jet Fit Results | 147 |

| | |
|--|------------|
| 79 V Differential Studies of $t\bar{t}H$ Multilepton | 156 |
| 80 16 Data and Monte Carlo Samples | 156 |
| 81 16.1 Data Samples | 157 |
| 82 16.2 Monte Carlo Samples | 157 |
| 83 17 Object Reconstruction | 159 |
| 84 17.1 Trigger Requirements | 160 |
| 85 17.2 Light Leptons | 160 |
| 86 17.3 Jets | 161 |
| 87 17.4 Missing Transverse Energy | 162 |
| 88 17.5 Overlap removal | 162 |
| 89 18 Higgs Momentum Reconstruction | 163 |
| 90 18.1 Decay Candidate Reconstruction | 164 |
| 91 18.2 b-jet Identification | 165 |
| 92 18.2.1 2lSS Channel | 166 |
| 93 18.2.2 3l Channel | 171 |
| 94 18.3 Higgs Reconstruction | 174 |
| 95 18.3.1 2lSS Channel | 175 |
| 96 18.3.2 3l Semi-leptonic Channel | 179 |
| 97 18.3.3 3l Fully-leptonic Channel | 183 |
| 98 18.4 p_T Prediction | 187 |
| 99 18.4.1 2lSS Channel | 188 |
| 100 18.4.2 3l Semi-leptonic Channel | 191 |
| 101 18.4.3 3l Fully-leptonic Channel | 195 |
| 102 18.5 3l Decay Mode | 198 |
| 103 19 Signal Region Definitions | 200 |
| 104 19.1 Pre-MVA Event Selection | 201 |
| 105 19.2 Event MVA | 206 |
| 106 19.3 Signal Region Definitions | 214 |
| 107 20 Background Rejection MVA | 217 |
| 108 20.1 Pre-MVA Event Selection | 218 |
| 109 20.2 Event MVA | 220 |
| 110 20.3 Signal Region Definitions | 229 |
| 111 20.3.1 2lSS | 230 |
| 112 20.3.2 3l – Semi – leptonic | 230 |
| 113 20.3.3 3l – Fully – leptonic | 230 |
| 114 21 Systematic Uncertainties | 230 |
| 115 22 Results | 235 |
| 116 22.1 Results - 80 fb^{-1} | 236 |

| | | |
|-----|---|-----|
| 117 | 22.2 Projected Results - 140 fb ⁻¹ | 240 |
|-----|---|-----|

| | | |
|-----|----------------------|------------|
| 118 | VI Conclusion | 244 |
|-----|----------------------|------------|

| | | |
|-----|---|------------|
| 119 | Appendices | 251 |
| 120 | .1 Non-prompt lepton MVA | 251 |
| 121 | .2 Non-prompt CR Modelling | 256 |
| 122 | .3 tZ Interference Studies | 261 |
| 123 | .4 Alternate tZ Inclusive Fit | 265 |
| 124 | .4.1 tZ Inclusive Fit | 266 |
| 125 | .4.2 Floating tZ | 267 |
| 126 | .5 DSID list | 268 |
| 127 | A Machine Learning Models | 291 |
| 128 | A.1 Higgs Reconstruction Models | 291 |
| 129 | A.1.1 b-jet Identification Features - 2lSS | 291 |
| 130 | A.1.2 b-jet Identification Features - 3l | 295 |
| 131 | A.1.3 Higgs Reconstruction Features - 2lSS | 300 |
| 132 | A.1.4 Higgs Reconstruction Features - 3lS | 305 |
| 133 | A.1.5 Higgs Reconstruction Features - 3lF | 310 |
| 134 | A.2 Background Rejection MVAs | 314 |
| 135 | A.2.1 Background Rejection MVA Features - 2lSS | 314 |
| 136 | A.2.2 Background Rejection MVA Features - 3l | 318 |
| 137 | A.3 Alternate b-jet Identification Algorithm | 323 |
| 138 | A.4 Binary Classification of the Higgs p _T | 324 |
| 139 | A.5 Impact of Alternative Jet Selection | 325 |

140 Part I

141 Introduction

142 1 Introduction

143 Particle physics is an attempt to describe the fundamental building blocks of the universe and
144 their interactions. The Standard Model (SM) - our best current theory of fundamental particle
145 physics - does a remarkable job of that. All known fundamental particles and (almost) all of the
146 forces underlying their interactions can be explained by the SM, and the predictions from this
147 theory agree with experiment to an incredibly precise degree. This is especially true since the
148 Higgs Boson, the last piece of the SM predicted decades before, was finally discovered at the
149 Large Hadron Collider (LHC) in 2012.

150 Despite the success of the SM, there remains significant work to be done. For one, the
151 SM is incomplete: it fails to provide a description of gravity, to give an explanation for the
152 observation of Dark Matter, or to provide a mechanism for neutrinos to gain mass. Further, a
153 Higgs Boson with a mass of around 125 GeV, as observed at the LHC, gives rise to what is
154 known a hierarchy problem - such a low mass Higgs requires a seemingly unnatural level of “fine
155 tuning” that is unexplained by the SM.

156 A promising avenue for addressing these problems is to study the properties of the Higgs
157 Boson and the way it interacts with other particles, in part simply because these interactions

158 have not been measured before. Its interactions with the Top Quark are a particularly promising
159 place to look. Because the Higgs Field is responsible for allowing particle to acquire mass, the
160 strength of a particle's interaction with the Higgs Boson is proportional to its mass. As the most
161 massive of the fundamental particles, the Top Quark has the strongest coupling to the Higgs
162 Boson, meaning any new physics in the Higgs sector is likely to present itself most prominently
163 in its interaction with the Top Quark.

164 These interactions can be measured by directly by studying the production of a Higgs
165 Boson in association with a pair of Top Quarks ($t\bar{t}H$). While studies have been done measuring
166 the overall rate of $t\bar{t}H$ production, there are several theories of physics Beyond the Standard
167 Model (BSM) that would affect the kinematics of $t\bar{t}H$ production without altering its overall
168 rate. This dissertation attempts to make a differential measurement of the kinematics of the
169 Higgs Boson in $t\bar{t}H$ events in order to search for these BSM effects.

170 The proton-proton collision data collected by the ATLAS detector at the LHC from 2015-
171 2018 provides the opportunity to make this measurement for the first time. The unprecedented
172 energy achieved by the LHC during this period greatly increase the rate at which $t\bar{t}H$ events are
173 produced, and the large amount of data collected provides the necessary statistics for a differential
174 measurement to be performed.

175 A study of $t\bar{t}H$ events with multiple leptons in the final state is performed, using 139 fb^{-1}
176 of data from proton-proton collisions at an energy $\sqrt{s} = 13 \text{ TeV}$ collected by the ATLAS detector
177 from 2015-2018. Events are separated into channels based on the number of light leptons in the

178 final state - either two same-sign leptons, or three leptons. A deep neural network is used to
179 reconstruct the momentum of the Higgs Boson in each event. This momentum spectrum is fit to
180 data for each analysis channel, the result of which is used to place limits on BSM effects.

181 An additional study of WZ produced in association with a heavy flavor jet (including both
182 b-jets and charm jets) is also included. This process mimics the final state of $t\bar{t}H$ multilpjeton
183 events, making it an important background for that analysis. However, this process is poorly
184 understood, and difficult to simulate accurately, introducing large systematic uncertainties for
185 analyses that include it as a background. Therefore, a measurement of WZ + heavy flavor in the
186 fully leptonic decay mode is performed.

187 This dissertation begins with a brief explanation of the SM, its limitations, and the theor-
188 etical motivation behind this work in Part II. This is followed by a description of the LHC and
189 the ATLAS detector in Part III. Part IV details a measurement of WZ + heavy flavor. Studies
190 of differential measurements of $t\bar{t}H$ are then described in Part V, and preliminary results are
191 presented. Finally, the results of these studies are summarized in the conclusion, Part VI.

192 Part II**193 Theoretical Motivation****194 2 The Standard Model and the Higgs Boson**

195 The Standard Model of particle physics (SM) is a Quantum Field Theory (QFT) describing the
196 known fundamental particles and their interactions. It accounts for three of the four known
197 fundamental force - electromagnetism, the weak nuclear force, and the strong nuclear force, but
198 not gravity. Further, the SM describes a mechanism for combining the weak and electromagnetic
199 forces into a singular interaction, known as the electroweak force. It is a non-Abelian gauge
200 theory, invariant under the Lie Group $SU(3)_C \otimes SU(2)_L \otimes U(1)_Y$, where C refers to color
201 charge, L, the helicity of the particle, and Y, the hypercharge.

202 2.1 The Forces and Particles of the Standard Model

203 The SM particles, summarized in Figure 2.1, can be classified into two general categories based
204 on their spin: fermions, and bosons.

Standard Model of Elementary Particles

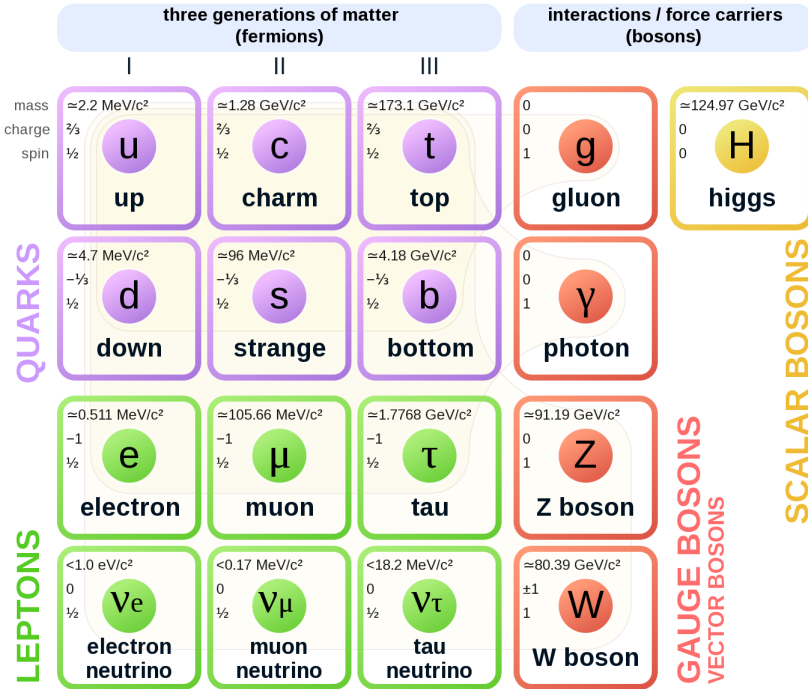


Figure 2.1: A summary of the particles of the Standard Model, including their mass, charge and spin, with the fermions listed on the left, and the bosons on the right. [1]

205 Fermions are particles with $\frac{1}{2}$ -integer spin, which according to the spin-statistics theorem,
 206 causes them to comply with the Pauli-exclusion principle. They can be separated into two groups,
 207 leptons and quarks, each of which consist of three generations of particles with increasing mass.

208 Leptons are fermions interact via the electroweak force, but not the strong force. The three
 209 generation of leptons consist of the electron and electron neutrino, the muon and muon neutrino,
 210 the tau and tau neutrino. The quarks, which do interact via the strong force - which is to say they
 211 have color charge - in addition to the electroweak force. The three generations include the up
 212 and down quarks, the strange and charm quarks, and the top and bottom quarks. Each of these

213 generations form left-handed doublets invariant under SU(2) transformations. For the leptons

214 these doublets are:

$$\begin{pmatrix} e^- \\ \nu_e \end{pmatrix}_L, \begin{pmatrix} \mu^- \\ \nu_\mu \end{pmatrix}_L, \begin{pmatrix} \tau^- \\ \nu_\tau \end{pmatrix}_L \quad (2.1)$$

215 And for the quarks:

$$\begin{pmatrix} u \\ d \end{pmatrix}_L, \begin{pmatrix} s \\ c \end{pmatrix}_L, \begin{pmatrix} t \\ b \end{pmatrix}_L \quad (2.2)$$

216 For both leptons and quarks, the heavier generations can decay into the lighter generation

217 of particles, while the first generation does not decay. Hence, ordinary matter generally consists

218 of this first generation of fermions - electrons, up quarks, and down quarks. Each of these

219 fermions has a corresponding anti-particle, which has an equal mass as its partner but opposite

220 charge. The fermions acquire their mass via the Higgs Mechanism, except for the neutrinos,

221 whose mass has been experimentally confirmed but is not accounted for in the SM.

222 Bosons, by contrast, have integer spin, and are therefore unconstrained by the Pauli-

223 exclusion principle. The SM includes two kinds of bosons: Gauge bosons, which are spin-1

224 particles that mediate the interactions between the fermions, and a single scalar, i.e. spin-0,

225 particle - the Higgs Boson. Of the gauge bosons, the W^+ , W^- and Z bosons - which are the

²²⁶ mass eigenstates of the electroweak bosons - mediate the weak interaction, while the photon
²²⁷ mediates the electric force, and the gluon mediates the strong force.

²²⁸ **2.2 The Higgs Mechanism**

²²⁹ A key feature of the SM is the gauge invariance of its Lagrangian. However, any terms added to
²³⁰ the Lagrangian giving mass to the the gauge bosons would violate the underlying symmetry of
²³¹ the theory. This presents a clear problem with the theory: The experimental observation that the
²³² W and Z bosons have mass seems to contradict the basic structure of the SM.

²³³ Rather than abandoning gauge invariance, an alternative way for particles to acquire mass
²³⁴ beyond adding a simple mass term to the Lagrangian was theorized by Higgs, Englert and Brout
²³⁵ in 1964 [2]. This procedure for introducing masses for the gauge bosons while preserving local
²³⁶ gauge invariance, known as the Higgs mechanism, was incorporated into the electroweak theory
²³⁷ by Weinberg in 1967 [3].

²³⁸ **2.2.1 The Higgs Field**

²³⁹ The Higgs mechanism introduces a complex scalar SU(2) doublet, Φ , with the form:

$$\Phi = \begin{pmatrix} \phi^+ \\ \phi^0 \end{pmatrix}_L \quad (2.3)$$

240 This field introduces a scalar potential to the Lagrangian of the form:

$$V(\Phi) = \mu^2 |\Phi^\dagger \Phi| + \lambda (|\Phi^\dagger \Phi|)^2 \quad (2.4)$$

241 Where μ and λ are free parameters of the new field. This represents the most general
 242 potential allowed while preserving $SU(2)_L$ invariance and renormalizability. In the case that
 243 $\mu^2 < 0$, this potential takes the form shown in Figure 2.2.

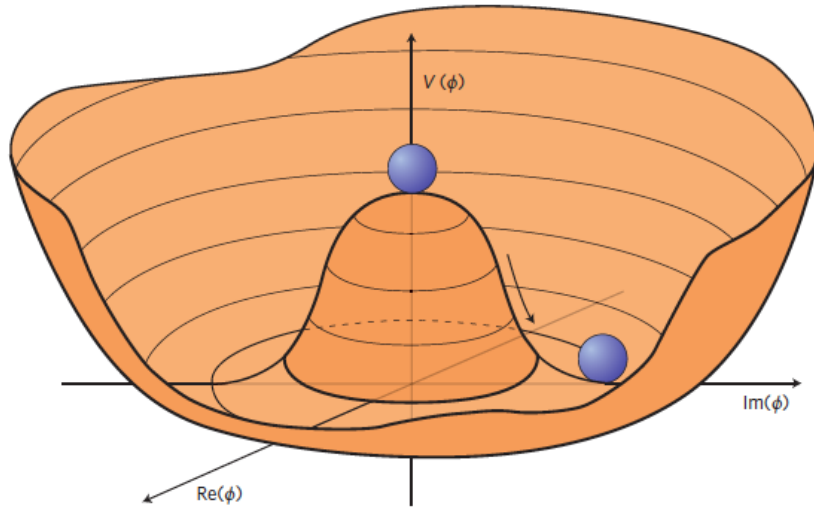


Figure 2.2: The value of the Higgs potential, $V(\Phi)$ as a function of Φ , for the case that $\mu^2 < 0$ [4].

244 The significant feature of this potential is that its minimum does not occur for a value of
 245 $\Phi = 0$. Instead, it is minimized when $|\Phi^\dagger \Phi| = -\mu^2/\lambda$. This means that in its ground state, the
 246 Higgs field takes on a non-zero value - referred to as a vacuum expectation value (VEV). So while
 247 the Higgs potential is globally symmetric, about the minimum this symmetry is broken. Since

²⁴⁸ the minimum is determined only by $\Phi^\dagger \Phi$, there is some ambiguity in the particular definition of

²⁴⁹ the VEV, but it is generally represented as

$$\langle \Phi \rangle = \frac{1}{\sqrt{2}} \begin{pmatrix} 0 \\ v \end{pmatrix} \quad (2.5)$$

²⁵⁰ The full value of Φ can be written as

$$\langle \Phi \rangle = \frac{1}{\sqrt{2}} \begin{pmatrix} 0 \\ v + H/\sqrt{2} \end{pmatrix} \quad (2.6)$$

²⁵¹ with v being the value of the VEV, and H being the real value of the scalar field.

²⁵² 2.2.2 Electroweak Symmetry Breaking

²⁵³ The Electroweak (EWK) interaction is described in the SM by a $SU(2)_L \otimes U(1)_Y$ gauge theory.

²⁵⁴ This theory predicts three $SU(2)_L$ gauge boson, $W_\mu^1, W_\mu^2, W_\mu^3$, and a single $U(1)_Y$ gauge boson,

²⁵⁵ B_μ . The couplings of these bosons to the Higgs field show up in the kinetic terms of the scalar

²⁵⁶ field Φ in the Lagrangian:

$$(D_\mu \Phi)^\dagger (D^\mu \Phi) = |(\partial_\mu - \frac{i g}{2} W_\mu^a \sigma^a - \frac{i g'}{2} B_\mu Y) \phi|^2 \quad (2.7)$$

257 Here D_μ represents the covariant derivative required to preserve gauge invariance, g and
 258 g' represent coupling constant of the gauge bosons, σ^a denotes the Pauli matrices of $SU(2)$,
 259 and Y represents the hypercharge of $U(1)$. The terms in this interaction which contribute to the
 260 masses of the gauge bosons can be written as:

$$\frac{1}{2}(0, v) \left(\frac{g}{2} W_\mu^a \sigma^a - \frac{g'}{2} B_\mu \right)^2 \begin{pmatrix} 0 \\ v \end{pmatrix} \quad (2.8)$$

261 Expanding these terms into the mass eigenstates of the electroweak interaction yields four
 262 physical gauge bosons, two charged and two neutral, which are linear combinations of the fields
 263 W_μ^1 , W_μ^2 , W_μ^3 , and B_μ :

$$\begin{aligned} W_\mu^\pm &= \frac{1}{\sqrt{2}} (W_\mu^1 \pm i W_\mu^2) \\ Z^\mu &= \frac{1}{\sqrt{(g^2 + g'^2)}} (-g' B_\mu + g W_\mu^3) \\ A^\mu &= \frac{1}{\sqrt{(g^2 + g'^2)}} (g B_\mu + g' W_\mu^3) \end{aligned} \quad (2.9)$$

264 And the masses of these fields are given by:

$$\begin{aligned} M_W^2 &= \frac{1}{4} g^2 v^2 \\ M_Z^2 &= \frac{1}{4} (g^2 + g'^2) v^2 \\ M_A^2 &= 0 \end{aligned} \quad (2.10)$$

265 This produces exactly the particles we observe - three massive gauge bosons and a single
 266 massless photon. The massless photon represents the portion of the gauge symmetry, a single
 267 $U(1)$ of the electromagnetic force, that remains unbroken by the VEV.

268 Interactions with the Higgs field also lead to the generation of the fermion masses, which
 269 in the Lagrangian take the form:

$$-\lambda_\psi(\bar{\psi}_L \phi \psi_R + \bar{\psi}_R \phi^\dagger \psi_L) \quad (2.11)$$

270 After symmetry breaking has occurred and ϕ has taken on the value of the VEV as written
 271 in equation 2.5, the mass terms of the fermions become $\lambda_\psi v$. Written this way, the fermion
 272 masses are proportional to their Yukawa coupling to the VEV, λ_ψ .

273 Based on the equation 2.6, an additional mass term, $\mu^2 H^2$ arises from the potential $V(\Phi)$.
 274 This term can be understood as an excitation of the Higgs field, a scalar boson with mass $M_H = \mu$.
 275 This is the Higgs boson, which comes about as a natural prediction of electroweak symmetry
 276 breaking.

277 The fermion's Yukawa coupling to the VEV take the same form as the fermion's coupling
 278 to the Higgs boson - λ_ψ . Therefore, the strength of a fermion's interaction with the Higgs is
 279 directly proportional to its mass. We now have a model that predicts a Higgs boson with mass
 280 $M_H = \mu$, which interacts with the fermions with coupling strength λ_ψ . Because μ and λ_ψ are

²⁸¹ free parameters of the theory, the mass of the Higgs boson and its interactions with the fermions

²⁸² must be measured experimentally.

²⁸³ **2.3 $t\bar{t}H$ Production**

²⁸⁴ The strength of a particles interaction with the Higgs, given by its Yukawa coupling, is propor-
²⁸⁵ tionate to its mass. The top quark - as the heaviest known particle - has the strongest interaction,
²⁸⁶ making this interaction particularly interesting to study. While several processes involve interac-
²⁸⁷ tions between the Higgs and the top, some Higgs production modes include the top interaction
²⁸⁸ only as a part of a loop diagram, such as the gluon-gluon fusion diagram shown in Figure 2.3.
²⁸⁹ This process therefore only allows for an indirect probe of the Higgs-top Yukawa coupling, as
²⁹⁰ the flavor of the quark in this diagram is not unique.

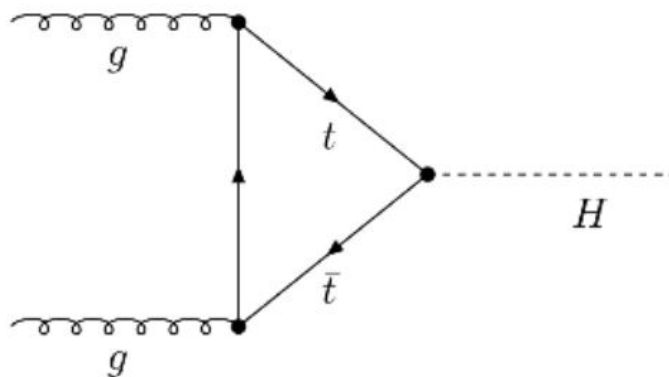


Figure 2.3: Diagram of a Higgs boson produced via gluon-gluon fusion.

²⁹¹ Studying the Higgs produced in association with top quark pairs, $t\bar{t}H$, allows this interac-
²⁹² tion to be measured directly. This process, as shown in Figure 2.4, involves a unique coupling

²⁹³ between the Higgs and the top, which can be identified by the top quark pair in the final state.

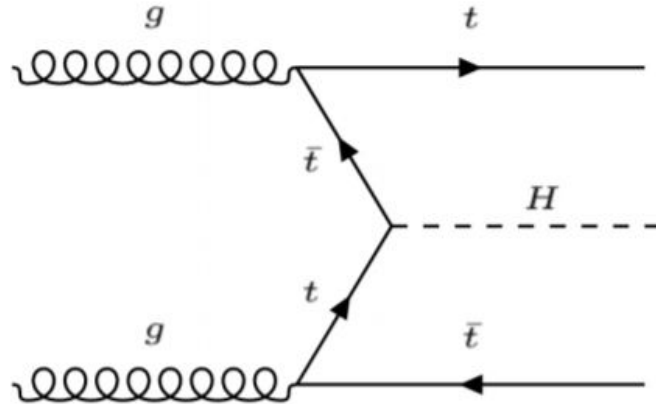


Figure 2.4: Diagram of a Higgs boson produced in association with a pair of top quarks.

²⁹⁴ The Higgs boson, as well as the top quarks, have very short lifetimes - on the order of
²⁹⁵ 10^{-22} s and 10^{-25} s respectively - meaning they can only be observed via their decay products.
²⁹⁶ This thesis focuses on $t\bar{t}H$ events with multiple leptons in the final state, $t\bar{t}H - ML$. This
²⁹⁷ includes $H \rightarrow W^+W^-$ events, where at least one of the W bosons decays leptonically.

²⁹⁸ While the branching ratio of $H \rightarrow W^+W^-$ is smaller than $H \rightarrow b\bar{b}$, it produces a clearer
²⁹⁹ signal. On the other hand, $H \rightarrow \gamma\gamma$ produces the most easily identifiable signal, but has a much
³⁰⁰ smaller branching ratio than $H \rightarrow W^+W^-$. Therefore, compared with other final state, the
³⁰¹ $t\bar{t}H - ML$ channel is an attractive candidate for study, as it involves a good balance between
³⁰² statistical power and identifiability.

303 2.4 WZ + Heavy Flavor Production

304 Part IV is dedicated to a measurement of WZ produced in association with a heavy flavor jet
 305 - namely, a charm or b-jet - in the fully leptonic channel. In the instance that both the W
 306 and Z bosons decay leptonically, this process produces a final state similar to $t\bar{t}H$, making it
 307 an irreducible background for $t\bar{t}H$ – ML specifically, and any analysis that includes multiple
 308 leptons and b-tagged jets in the final state.

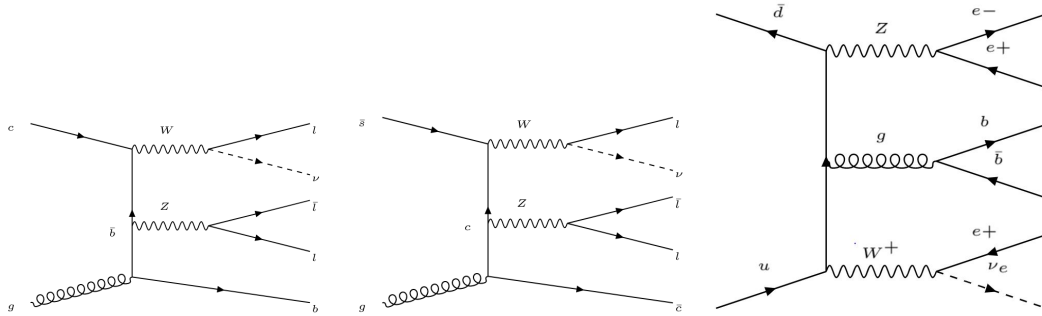


Figure 2.5: Example Feynman diagrams of WZ + heavy flavor production

309 The b-jets produced in this process can be thought of in two different ways: either as
 310 originating from the quark “sea” of the initial state hadrons, or as the result of gluons from
 311 the colliding protons splitting into $b\bar{b}$ pairs. However, the heavy flavor contribution to the
 312 parton distribution function (PDF) of the proton is uncertain, and simulations of this process
 313 disagree depending on which of these two approaches one considers. This makes WZ + heavy
 314 flavor difficult to accurately simulate, and introduces a large uncertainty for any analysis which
 315 includes it as a background, motivating a measurement of this process.

316 **2.5 Extensions to the Standard Model**

317 While the SM has been tested to great precision, particularly at the LHC, it is generally accepted
318 that it is only valid up to a certain energy scale. It is assumed that above a certain energy, at the
319 scale where something like a Grand Unified Theory (GUT) or quantum gravity become relevant,
320 the SM will not be applicable. Further, there are several experimental observations that the SM
321 fails to explain. For example, the SM predicts neutrinos to be massless, despite experimental
322 observation to the contrary, and fails to explain the observation of dark matter and dark energy.

323 Another example, relevant to the Higgs sector, is known as the hierarchy problem: large
324 quantum corrections to the Higgs mass from loop diagrams, such as those shown in Figure 2.6,
325 are many orders of magnitude larger than the Higgs mass itself. The observed value of the Higgs
326 mass therefore requires extremely precise cancellation between these corrections and the bare
327 mass of the Higgs, a cancellation which seems unnatural and suggests something missing in our
328 theoretical picture.

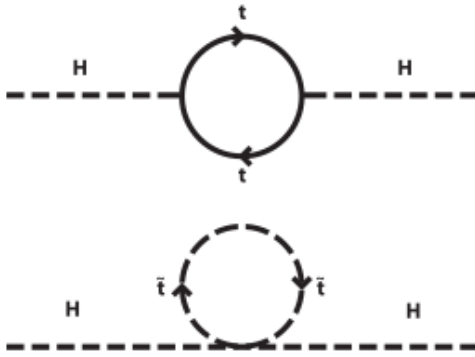


Figure 2.6: Above diagram is the leading order correction to the Higgs mass via a top quark loop, and below is the stop squark loop, coming from a supersymmetric extension of the SM, that provides a potential cancellation of the top diagram.

Because so many of the properties of the Higgs boson have not yet been studied, its interactions are a promising place to search for new physics that could resolve some of the limitations of the SM. As explained above, the interactions of the Higgs with the top quark, as in $t\bar{t}H$ production, are particularly interesting: As the most massive particle in the Standard Model, the top quark is the most strongly interacting with the Higgs. Therefore, any new physics effects are likely to be seen most prominently in this interaction.

These interactions can be measured directly by studying the production of a Higgs Boson in association with a pair of Top Quarks ($t\bar{t}H$). While this process has been observed by both the ATLAS [5] and CMS [6] collaborations, these analyses have focused on measuring the overall rate of $t\bar{t}H$ production. There are several theories of physics Beyond the Standard Model (BSM), however, that would affect the kinematics of $t\bar{t}H$ production without altering its overall rate [7].

341 An Effective Field Theory approach can be used to model the low energy effects of new,
 342 high energy physics, by parameterizing BSM effects as higher dimensional operators. These
 343 additional operators can then be added to the SM Lagrangian to write an effective Lagrangian
 344 that accounts for the effects of these higher energy physics. The lowest order of these that could
 345 contribute to Higgs-top couplings are dimension-six, as represented in Equation 2.12.

$$\mathcal{L}_{\text{eff}} = \mathcal{L}_{\text{SM}} + \frac{f}{\Lambda} O^6 \quad (2.12)$$

346 Here Λ represents the energy scale of the new physics, and f is a Wilson coefficient which
 347 represents the strength of the effective coupling. An experimental observation of any non-zero
 348 value of f would be a sign of BSM physics.

349 The addition of these operators can be shown to modify the transverse momentum (p_T)
 350 spectrum of the Higgs Boson in Higg-top interactions, without effecting the overall rate of $t\bar{t}H$
 351 production [8]. The effect of these higher order effects on the as shown in Figure 2.7.

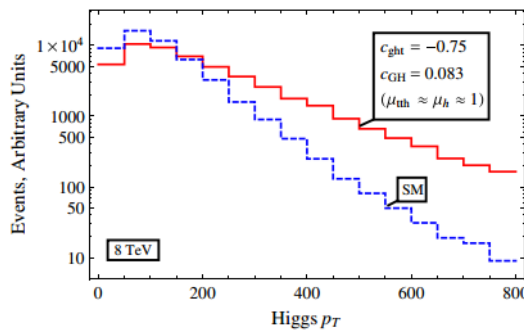


Figure 2.7: The momentum spectrum of the Higgs boson produced via top-quarks with (red) and without (blue) the presence of dimension-six operators.

352 This provides a clear, physics observable that could be used to search for BSM effect.

353 Therefore, reconstructing the momentum spectrum of the Higgs in $t\bar{t}H$ events provides a means

354 to observe new physics in the Higgs sector.

355 **Part III**

356 **The LHC and the ATLAS Detector**

357 **3 The LHC**

358 The Large Hadron Collider (LHC) is a particle accelerator consisting of a 27 km ring, designed

359 to collide protons at high energy. Located outside of Geneva, Switzerland and buried about 100

360 m underground, it consists of a ring of superconducting magnets which are used to accelerate

361 opposing beams of protons - or lead ions - which collide at the center of one of the various

362 detectors located around the LHC ring which record the result of these collisions. These

363 detectors include two general purpose detectors, ATLAS and CMS, which are designed to make

364 precision measurements of a broad range of physics phenomenon, and two more specialized

365 experiments, LHCb and ALICE, which are optimized to study b-quarks and heavy-ion physics,

366 respectively.

367 The LHC first began running in 2009 at a proton-proton center of mass energy of $\sqrt{s} = 8$

368 TeV. It operated at this energy from 2009 to 2012, known as Run 1, and data collected during

369 this period was used in discovering the Higgs Boson. The LHC began running again in 2015,
370 and collected data at an increased energy of $\sqrt{s} = 13$ TeV until 2018, a period referred to as Run
371 2.

372 The LHC consists of a chain of accelerators, which accelerate the protons to higher and
373 higher energies until they are injected into the main ring. This process is summarized in figure
374 3.1. Protons extracted from a tank of ionized hydrogen are fed into a linear accelerator, LINAC2,
375 where they reach an energy of 50 MeV. From there, they enter a series of three separate circular
376 accelerators, before being injected into the main accelerator ring at an energy of 450 GeV. Within
377 the main ring protons are separated into two separate beams moving in opposite directions,
378 and their energy is increased to their full collision energy. Radiofrequency cavities are used to
379 accelerate these particles and sort them into bunches. From 2015-2018, these bunches consisted
380 of around 100 billion protons each with an energy of 6.5 TeV per proton, which collided at a rate
381 of 40 MHz, or every 25 ns.

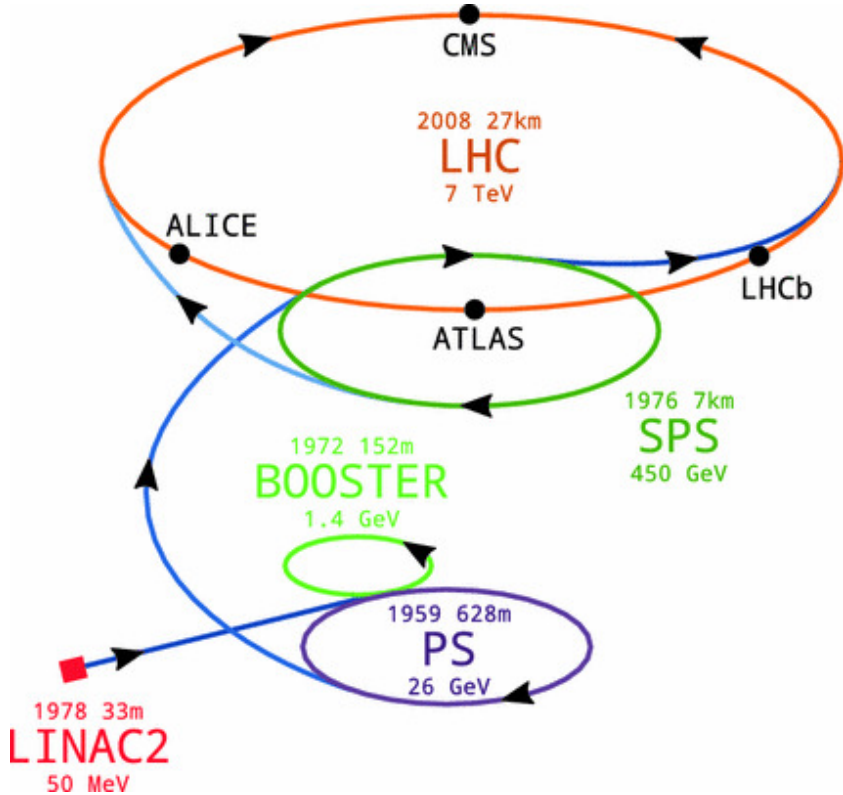


Figure 3.1: A summary of the accelerator chain used to feed protons into the LHC [].

382 Because these proton bunches consist of a large number of particles, each bunch crossing
 383 consists of not just one, but several direct proton-proton collisions. The number of interactions
 384 that occur per bunch crossing, μ , is known as pileup. During Run 2, the average pileup for bunch
 385 crossings was around $\langle \mu \rangle = 35$, with values typically ranging between 10 and 70.

386 The amount of data collected by the LHC is measured in terms of luminosity, which is the

387 ratio of the number of events detected per unit time, $\frac{dN}{dt}$, and the interaction cross-section, σ .

$$\mathcal{L} = \frac{1}{\sigma} \frac{dN}{dt} \quad (3.1)$$

388 The design luminosity of the LHC is $10^{34} \text{ cm}^{-2}\text{s}^{-1}$, however the LHC has achieved a
 389 luminosity of over $2 \times 10^{34} \text{ cm}^{-2}\text{s}^{-1}$. The total luminosity is then this instantaneous luminosity
 390 integrated over time.

$$\mathcal{L}_{\text{int}} = \int \mathcal{L} dt \quad (3.2)$$

391 The integrated luminosity collected by the ATLAS detector as of the end of 2018 is around
 392 140 fb^{-1} , exceeding the expected integrated luminosity of 100 fb^{-1} .

393 4 The ATLAS Detector

394 ATLAS (a not terribly natural acronym for “A Toroidal LHC Apparatus”) is a general purpose
 395 detector designed to maximize the detection efficiency of all physics objects, including leptons,
 396 jets, and photons. This means it is capable of measuring all SM particles, with the exception of
 397 neutrinos, the presence of which can be inferred based on missing transverse momentum. The
 398 detector measures 44 m long, and 25 m tall.

399 The ATLAS detector consists of multiple layers, each of which serves a different purpose
 400 in reconstructing collisions. At the very center of the detector is the interaction point where the
 401 proton beams of the LHC collide.

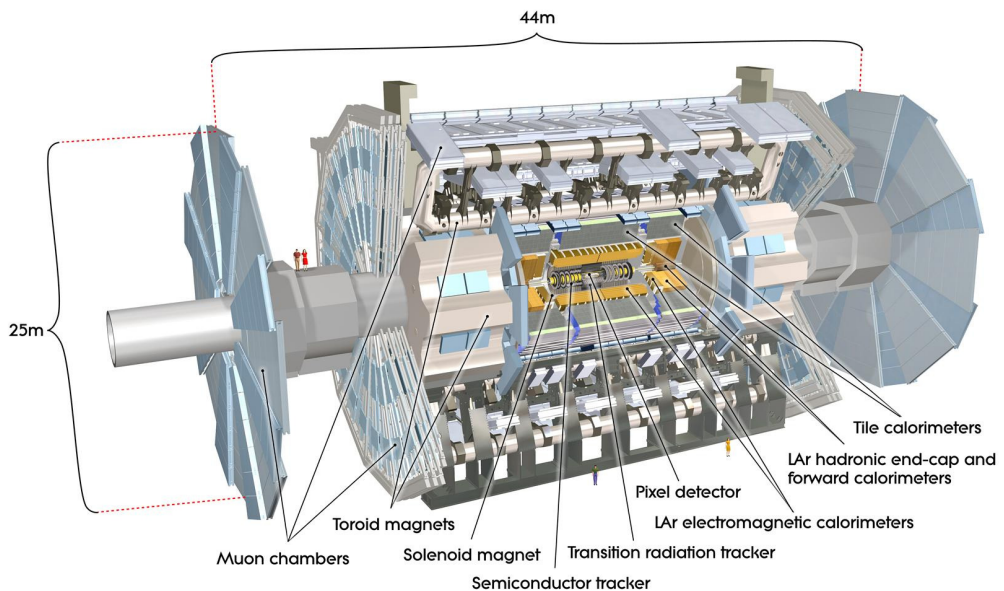


Figure 4.1: Cutaway view of the ATLAS detector, with labels of its major components [].

402 **4.1 Inner Detector**

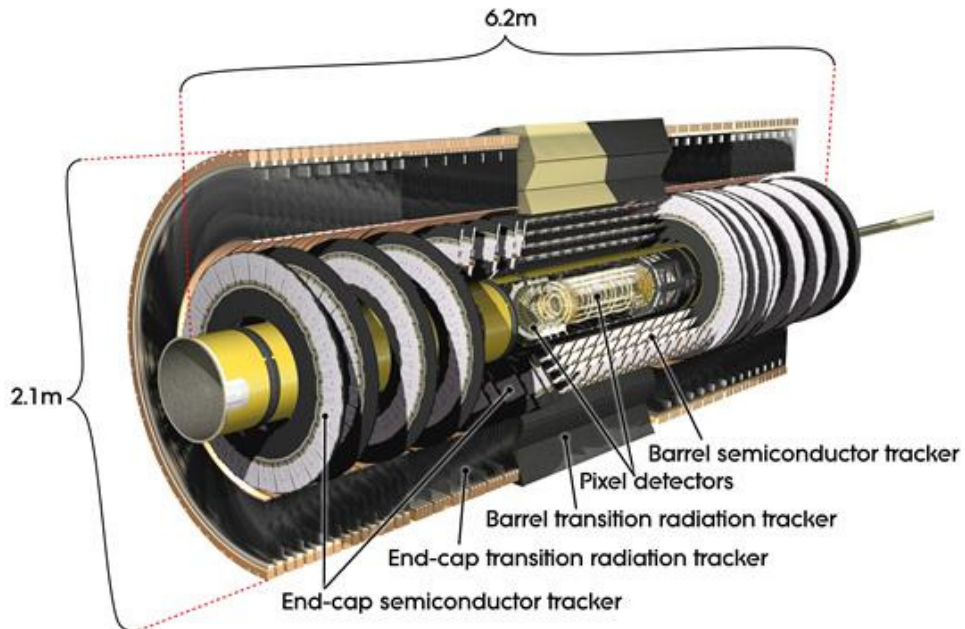


Figure 4.2: Cutaway view of the Inner Detector [].

403 Just surrounding the interaction point is the Inner Detector, designed to track the path of charged
 404 particles moving through the detector. An inner solenoid surrounding the Innder Detector is
 405 used to produces a magnetic field of 2 T. This large magnetic field causes the path of charged
 406 particles moving through the Inner Detector to bend. Because this magnetic field is uniform and
 407 well known, it can be used in conjunction with the curvature of a particles path to measure its
 408 charge and momentum.

409 The Inner Detector consists of three components - the Pixel Detector, the Semi-Conductor
 410 Tracker (SCT), and the Transition Radiation Tracker (TRT). The Pixel Detector is the innermost

⁴¹¹ of these, beginning just 33.25 mm away from the beam line. It consists of three silicon layers
⁴¹² along the barrel, as well as three endcap layers, covering a range of $|\eta| < 2.5$.

⁴¹³ The Semiconductor Tracker (SCT) is similar to the Pixel detector, but uses long strips
⁴¹⁴ rather than small pixel to cover a larger spatial area.

⁴¹⁵ 4.2 Calorimeters

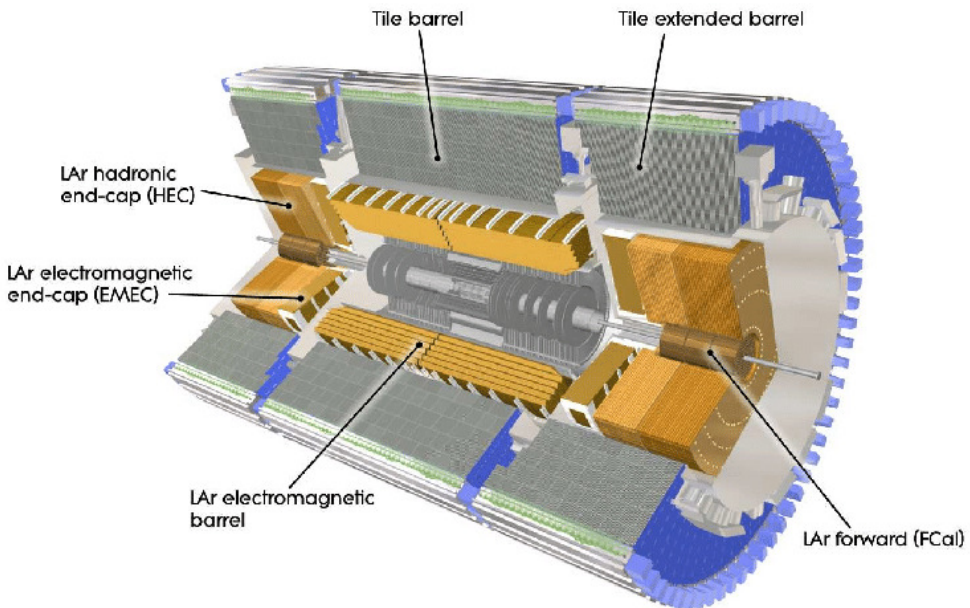


Figure 4.3: Cutaway view of the calorimeter system of the ATLAS detector [].

⁴¹⁶ Situated outside the Inner Detector are two concentric calorimeters. The inner calorimeter uses
⁴¹⁷ liquid argon (LAr) to measure energy of particles that interact electromagnetically, which includes
⁴¹⁸ photons and any charged particle. The LAr calorimeter is made of heavy metals, primarily lead
⁴¹⁹ and copper, which causes electromagnetically interacting particles to shower, depositing their

420 energy in the detector. The showering of the high energy particles that pass through calorimeter
421 cause the liquid argon to ionize, and the ionized electrons are detected by electronic readouts.
422 The LAr calorimeter consists of around 180,000 readout channels.

423 The outer calorimeter measures the energy from particles that pass through the EM calor-
424 imeter, and measures the energy of particles that interact via the strong force. This is primarily
425 hadrons. It is composed of steel plates to cause hadronic showering and scintillating tiles as the
426 active material. The signals from the hadronic calorimeter are read out by photomultiplier tubes
427 (PMTs).

428 **4.3 Muon Spectrometer**

429 Because muons are heavier than electrons and photons, and do not interact via the strong force,
430 they generally pass through the detector without being stopped by the calorimeters. The outermost
431 components of the detector are designed specifically to measure the energy and momentum of
432 muons produced in the LHC. The muon spectrometer consists of tracking and triggering system.
433 It extends from the outside of the calormeter system, about a 4.25 m radius from the beam line,
434 to a radius of 11 m. This large detector system is necessary to accurately measure the momentum
435 of muons, which is essential not only for measurements involving the muons themselves, but also
436 to accurately estimate the missing energy in each event.

437 Two large toroidal magnets within the muon system generate a large magnetic field which
438 covers an area 26 m long with a radius of 10 m. Because the area covered by this magnet system

439 is so large, a uniform magnetic field like the one produced in the Inner Detector is impractical.
440 Instead, the magnetic field that exists in the muon spectrometer ranges between 2 T and 8 T, and
441 is much less uniform. The path of the muons passing through the spectrometer is bent by this
442 field, allowing their charge to be determined.

443 1200 tracking chambers are placed in the muon system in order to precisely measure the
444 tracks of muons with high spatial resolution.

445 **4.4 Trigger System**

446 Because of the high collision rate and large amount of data collected by the various subdetectors,
447 ATLAS produces far more data than can actually be stored. Each event produces around 25 Mb
448 of raw data, which multiplied by the bunch crossing rate of 40 MHz, comes out to around a
449 petabyte of data every second. The information from every event cannot practically be stored,
450 therefore a sophisticated trigger system is employed in real time to determine whether events are
451 sufficiently interesting to be worth storing.

452 The trigger system in ATLAS involves multiple levels, each of which select out which
453 events move on to the next level of scrutiny. The level-1 trigger uses hardware information from
454 the calorimeters and muon spectrometer to select events that contain candidates for particles
455 commonly used in analysis, such as energetic leptons and jets. The level-1 trigger reduces the
456 rate of events from 40 MHz to around 100 kHz.

457 Events that pass the level-1 trigger move to the High-Level Trigger (HLT). The HLT takes
458 place outside of the detector in software, and looks for properties such as a large amount of
459 missing transverse energy, well defined leptons, and multiple high energy jets. Events that pass
460 the HLT are stored and used for analysis. Because the specifics of the HLT are determined by
461 software rather than hardware, the thresholds can be changed throughout the run of the detector
462 in response to run conditions such as changes to pileup and luminosity. After the HLT is applied,
463 the event rate is reduced to around 1000 per second, which are recorded for analysis.

464 **Part IV**

465 **Measurement of WZ + Heavy Flavor**

466 **5 Introduction**

467 The production of WZ in association with a heavy flavor jet represents an important background
468 for many major analyses. This includes any process with leptons and b-jets in the final state,
469 such as $t\bar{t}H$, $t\bar{t}W$, and $t\bar{t}Z$. While precise measurements have been made of WZ production
470 [9], WZ + heavy flavor remains poorly understood. This is largely because the QCD processes
471 involved in the production of the b-jet make it difficult to simulate accurately. This introduces a
472 large uncertainty for analyses that include this process as a background.

473 Motivated by its relevance to the $t\bar{t}H$ multilepton analysis, we perform a study of the fully

474 leptonic decay mode of this channel; that is, events where both the W and Z decay leptonically.
 475 Because WZ has no associated jets at leading order, while the major backgrounds for this channel
 476 tend to have high jet multiplicity, events with more than two jets are rejected. This gives a final
 477 state signature of three leptons and one or two jets.

478 Events that meet this selection criteria are sorted into pseudo-continuous b-tagging regions
 479 based on the DL1r b-tag score of their associated jets. This is done to separate WZ + b-jet events
 480 from WZ + charm and WZ + light jets. These regions are fit to data in order make a more
 481 accurate estimate of the contribution of WZ + heavy-flavor, where heavy-flavor jets include
 482 b-jets and charm jets. The full Run-2 dataset collected by the ATLAS detector, representing 139
 483 fb^{-1} of data from pp collisions at $\sqrt{s} = 13 \text{ TeV}$, is used for this study.

484 Section 10 details the data and Monte Carlo (MC) samples used in the analysis. The
 485 reconstruction of various physics objects is described in Section 11. Section 12 describes the
 486 event selection applied to these samples, along the definitions of the various regions used in
 487 the fit. The multivariate analysis techniques used to separate the tZ background from WZ +
 488 heavy flavor are described in Section 13. Section 21 describes the various sources of systematic
 489 uncertainties considered in the fit. Finally, the results of the analysis are summarized in Section
 490 22, followed by a brief conclusion in Section ??.

491 **The current state of the analysis shows blinded results for the full 2018 dataset.**
 492 **Regions containing >5% WZ+b events are blinded, and results are from Asimov, MC only**
 493 **fits.**

494 **6 Data and Monte Carlo Samples**

495 **6.1 Data Samples**

496 The study uses a sample of proton-proton collision data collected by the ATLAS detector from
497 2015 through 2018 at an energy of $\sqrt{s} = 13$ TeV, which represents an integrated luminosity of
498 139 fb^{-1} . This data set was collected with a bunch crossing rate of 25 ns. All data used in this
499 analysis was verified by data quality checks.

500 **6.2 Monte Carlo Samples**

501 Several different generators were used to produce Monte Carlo simulations of the signal and
502 background processes. For all samples, the response of the ATLAS detector is simulated using
503 Geant4. The WZ signal samples are simulated using Sherpa 2.2.2 [10]. Specific information
504 about the Monte Carlo samples being used can be found in Table 26.

Table 1: The configurations used for event generation of signal and background processes, including the event generator, matrix element (ME) order, parton shower algorithm, and parton distribution function (PDF).

| Process | Event generator | ME order | Parton Shower | PDF |
|---------------------------------|---------------------------|----------------------|------------------------|-----------------------------------|
| WZ, VV | SHERPA 2.2.2 | MEPS NLO | SHERPA | CT10 |
| tZ | MG5_AMC | NLO | PYTHIA 8 | CTEQ6L1 |
| t̄tW | MG5_AMC (SHERPA 2.1.1) | NLO (LO multileg) | PYTHIA 8 (SHERPA) | NNPDF 3.0 NLO (NNPDF 3.0 NLO) |
| t̄t(Z/γ* → ll) | MG5_AMC | NLO | PYTHIA 8 | NNPDF 3.0 NLO |
| t̄tH | MG5_AMC (MG5_AMC) | NLO (NLO) | PYTHIA 8 (HERWIG++) | NNPDF 3.0 NLO [11] (CT10 [12]) |
| tHqb | MG5_AMC | LO | PYTHIA 8 | CT10 |
| tHW | MG5_AMC (SHERPA 2.1.1) | NLO (LO multileg) | HERWIG++ (SHERPA) | CT10 (NNPDF 3.0 NLO) |
| tWZ | MG5_AMC | NLO | PYTHIA 8 | NNPDF 2.3 LO |
| t̄t̄t, t̄t̄t̄t̄ | MG5_AMC | LO | PYTHIA 8 | NNPDF 2.3 LO |
| t̄tW+W- | MG5_AMC | LO | PYTHIA 8 | NNPDF 2.3 LO |
| t̄t | POWHEG-BOX v2 [13] | NLO | PYTHIA 8 | NNPDF 3.0 NLO |
| t̄t̄γ | MG5_AMC | LO | PYTHIA 8 | NNPDF 2.3 LO |
| s-, t-channel, Wt single top | POWHEG-BOX v1 [14] | NLO | PYTHIA 6 | CT10 |
| qqVV, VVV | | | | |
| Z → l+l- | SHERPA 2.2.1 | MEPS NLO | SHERPA | NNPDF 3.0 NLO |

7 Object Reconstruction

- 506 All regions defined in this analysis share a common lepton, jet, and overall event preselection.
507 The selection applied to each physics object is detailed here; the event preselection, and the
508 selection used to define the various fit regions, is described in Section 12.

509 **7.1 Trigger**

510 Events are required to be selected by dilepton triggers, as summarized in Table 28.

| Dilepton triggers (2015) | |
|-------------------------------|----------------------------|
| $\mu\mu$ (asymm.) | HLT_mu18_mu8noL1 |
| ee (symm.) | HLT_2e12_lhloose_L12EM10VH |
| $e\mu, \mu e$ (\sim symm.) | HLT_e17_lhloose_mu14 |
| Dilepton triggers (2016) | |
| $\mu\mu$ (asymm.) | HLT_mu22_mu8noL1 |
| ee (symm.) | HLT_2e17_lhvloose_nod0 |
| $e\mu, \mu e$ (\sim symm.) | HLT_e17_lhloose_nod0_mu14 |
| Dilepton triggers (2017) | |
| $\mu\mu$ (asymm.) | HLT_mu22_mu8noL1 |
| ee (symm.) | HLT_2e24_lhvloose_nod0 |
| $e\mu, \mu e$ (\sim symm.) | HLT_e17_lhloose_nod0_mu14 |
| Dilepton triggers (2018) | |
| $\mu\mu$ (asymm.) | HLT_mu22_mu8noL1 |
| ee (symm.) | HLT_2e24_lhvloose_nod0 |
| $e\mu, \mu e$ (\sim symm.) | HLT_e17_lhloose_nod0_mu14 |

Table 2: List of lowest p_T -threshold, un-prescaled dilepton triggers used for 2015-2018 data taking.

511 **7.2 Light leptons**

512 Electron candidates are reconstructed from energy clusters in the electromagnetic calorimeter
 513 that are associated with charged particle tracks reconstructed in the inner detector [15]. Electron
 514 candidates are required to have $p_T > 10$ GeV and $|\eta_{\text{cluster}}| < 2.47$. Muon candidates are
 515 reconstructed by combining inner detector tracks with track segments or full tracks in the muon
 516 spectrometer [16]. Muon candidates are required to have $p_T > 10$ GeV and $|\eta| < 2.5$. Candidates

517 in the transition region between different electromagnetic calorimeter components, $1.37 < | $\eta_{\text{cluster}}| < 1.52$$, are rejected. A multivariate likelihood discriminant combining shower shape
 518 and track information is used to distinguish real electrons from hadronic showers (fake electrons).
 519
 520 To further reduce the non-prompt electron contribution, the track is required to be consistent
 521 with originating from the primary vertex; requirements are imposed on the transverse impact
 522 parameter significance ($|d_0|/\sigma_{d_0} < 5$) and the longitudinal impact parameter ($|\Delta z_0 \sin \theta_\ell| < 0.5$
 523 mm). Electron candidates are required to pass TightLH identification.

524 Muon candidates are reconstructed by combining inner detector tracks with track segments
 525 or full tracks in the muon spectrometer [16]. Muon candidates are required to have $p_T > 10$ GeV
 526 and $|\eta| < 2.5$. The longitudinal impact parameter is the same for both electrons and muons, while
 527 muons are required to pass a slightly tighter transverse impact parameter, $|d_0|/\sigma_{d_0} < 3$. Muons
 528 are also required to pass Medium ID requirements.

529 Leptons are additionally required to pass a non-prompt BDT selection developed by the
 530 $t\bar{t}H$ multilepton/ $t\bar{t}W$ analysis group. This BDT and the WPs used are summarized in Appendix
 531 .1, and described in detail in [17]. Optimized working points and scale factors for this BDT are
 532 taken from that analysis.

533 7.3 Jets

534 Jets are reconstructed from calibrated topological clusters built from energy deposits in the
 535 calorimeters [18], using the anti- k_t algorithm with a radius parameter $R = 0.4$. Particle Flow, or

536 PFlow, jets are used in the analysis, which are hadronic objects reconstructed using information
537 from both the tracker and the calorimeter. Jets with energy contributions likely arising from noise
538 or detector effects are removed from consideration [19], and only jets satisfying $p_T > 25$ GeV
539 and $|\eta| < 2.5$ are used in this analysis. For jets with $p_T < 60$ GeV and $|\eta| < 2.4$, a jet-track
540 association algorithm is used to confirm that the jet originates from the selected primary vertex,
541 in order to reject jets arising from pileup collisions [20].

542 **7.4 B-tagged Jets**

543 In order to make a measurement of $WZ +$ heavy flavor it is necessary to distinguish these events
544 from $WZ +$ light jets. For this purpose, the DL1r b-tagging algorithm is used to distinguish
545 heavy flavor jets from lighter ones. The DL1r algorithm uses jet kinematics, particularly jet
546 vertex information, as input for a neural network which assigns each jet a score designed to
547 reflect how likely that jet is to have originated from a b-quark.

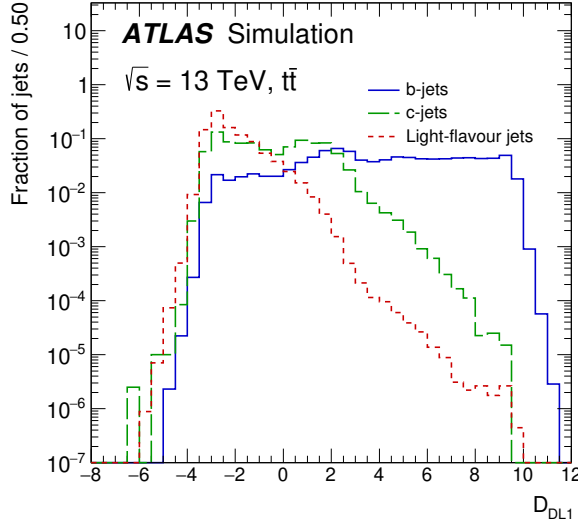


Figure 7.1: Output distribution of the DL1r algorithm for b-jets, charm jets, and light jets

548 From the output of the BDT, calibrated working points (WPs) are developed based on the
 549 efficiency of truth b-jets at particular values of the DL1r algorithm. The working points used in
 550 this analysis are summarized in Table 10.

| WP | none | loose | medium | tight | tightest |
|--------|------|-------|--------|-------|----------|
| b eff. | - | 85% | 77% | 70% | 60% |

Table 3: B-tagging Working Points by tightness and b-jet efficiency

551 A tighter WP will accept fewer b-jets, but reject a higher fraction of charm and light jets.
 552 Generally, analyses that include b-jets will use a fixed working point, for example, requiring that
 553 a jet pass the 70% threshold. By instead treating these working point as bins, e.g. events with
 554 jets that fall between the 85% and 77% WPs fall into one bin, while events with jets passing the
 555 60% WP fall into another, and looking at the full psuedo-continuous DL1r spectrum of the jets,

556 additional information can be gained. The psuedo-continuous b-tag spectrum is used in this case
557 to separate out WZ + b, WZ + charm, and WZ + light.

558 **7.5 Missing transverse energy**

559 Missing transverse momentum (E_T^{miss}) is used as part of the event selection. The missing
560 transverse momentum vector is defined as the inverse of the sum of the transverse momenta of
561 all reconstructed physics objects as well as remaining unclustered energy, the latter of which is
562 estimated from low- p_T tracks associated with the primary vertex but not assigned to a hard object,
563 with object definitions taken from [21]. Light leptons considered in the E_T^{miss} reconstruction are
564 required to have $p_T > 10 \text{ GeV}$, while jets are required to have $p_T > 20 \text{ GeV}$.

565 **7.6 Overlap removal**

566 To avoid double counting objects and remove leptons originating from decays of hadrons, overlap
567 removal is performed in the following order: any electron candidate within $\Delta R = 0.1$ of another
568 electron candidate with higher p_T is removed; any electron candidate within $\Delta R = 0.1$ of a muon
569 candidate is removed; any jet within $\Delta R = 0.3$ of an electron candidate is removed; if a muon
570 candidate and a jet lie within $\Delta R = \min(0.4, 0.04 + 10[\text{GeV}] / p_T(\text{muon}))$ of each other, the jet
571 is kept and the muon is removed.

572 This algorithm is applied to the preselected objects. The overlap removal procedure is
573 summarized in Table 29.

| Keep | Remove | Cone size (ΔR) |
|-------------|-----------------------|---|
| electron | electron (low p_T) | 0.1 |
| muon | electron | 0.1 |
| electron | jet | 0.3 |
| jet | muon | $\min(0.4, 0.04 + 10[\text{GeV}]/p_T(\text{muon}))$ |
| electron | tau | 0.2 |

Table 4: Summary of the overlap removal procedure between electrons, muons, and jets.

574 8 Event Selection and Signal Region Definitions

575 Event are required to pass a preselection described in Section 12.1 and summarized in Table 12.
 576 Those that pass this preselection are divided into various fit regions described in Section 12.2,
 577 based on the number of jets in the event, and the b-tag score of those jets.

578 8.1 Event Preselection

579 Events are required to include exactly three reconstructed light leptons passing the requirement
 580 described in 11.2, which have a total charge of ± 1 .

581 The leptons are ordered in the analysis code as 0, 1, and 2. Lepton 0 is the lepton whose
 582 charge is opposite the other two. Lepton 1 is the lepton closest to the opposite charge lepton, i.e.
 583 the smallest ΔR , leaving lepton 2 as the lepton further from the opposite charge lepton. Lepton
 584 0 is required to have $p_T > 10 \text{ GeV}$, while the same sign leptons, 1 and 2, are required to have
 585 $p_T > 20 \text{ GeV}$ to reduce the contribution of non-prompt leptons.

586 The invariant mass of at least one pair of opposite sign, same flavor leptons is required
 587 to fall within 10 GeV of the mass of the Z boson, 91.2 GeV. Events where one of the opposite
 588 sign pairs have an invariant mass less than 12 GeV are rejected in order to suppress low mass
 589 resonances.

590 An additional requirement is placed on the missing transverse energy, $E_T^{\text{miss}} > 20 \text{ GeV}$,
 591 and the transverse mass of the W candidate, $m(E_T^{\text{miss}} + l_{\text{other}}) > 30 \text{ GeV}$, where E_T^{miss} is the
 592 missing transverse energy, and l_{other} is the lepton not included in the Z-candidate.

593 Events are required to have one or two reconstructed jets passing the selection described
 594 in Section 11.3. Events with more than two jets are rejected in order to reduce the contribution
 595 of backgrounds such as $t\bar{t}Z$ and $t\bar{t}W$, which tend to have higher jet multiplicity.

Event Selection

Exactly three leptons with charge ± 1
 Two same-charge leptons with $p_T > 20 \text{ GeV}$
 One opposite charge lepton with $p_T > 10 \text{ GeV}$
 $m(l^+l^-)$ within 10 GeV of 91.2 GeV
 Transverse mass of W-candidate, $m_T(E_T^{\text{miss}} + l_{\text{ep other}}) > 30 \text{ GeV}$
 Missing transverse energy, $E_T^{\text{miss}} > 20 \text{ GeV}$
 One or two jets with $p_T > 25 \text{ GeV}$

Table 5: Summary of the selection applied to events for inclusion in the fit

596 The event yields in the preselection region for both data and Monte Carlo are summarized
 597 in Table 12.1, which shows good agreement between data and Monte Carlo, and demonstrates
 598 that this region consists primarily of WZ events. The WZ events are split into WZ + b, WZ
 599 + c, and WZ + 1 based on the truth flavor of the associated jet in the event. Specifically, this

600 determination is made based on the HadronConeExclTruthLabelID of the jet, as recommended
 601 by the b-tagging working group [22]. In this ordering b-jet supersedes charm, which supersedes
 602 light. That is, WZ + 1 events contain no charm and no b jets at truth level, WZ + c contain at
 603 least one truth charm and no b-jets, and WZ + b contains at least one truth b-jet.

| Process | Events |
|------------|-----------------|
| WZ + b | 167.6 ± 6.5 |
| WZ + c | 1080 ± 40 |
| WZ + l | 7220 ± 310 |
| Other VV | 850 ± 140 |
| t̄tW | 16.8 ± 2.3 |
| t̄tZ | 115 ± 17 |
| rare Top | 2.2 ± 0.1 |
| Single top | 0.10 ± 0.45 |
| Three top | 0.01 ± 0.01 |
| Four top | 0.02 ± 0.01 |
| t̄tWW | 0.23 ± 0.05 |
| Z + jets | 600 ± 260 |
| V + γ | 37 ± 54 |
| tZ | 190 ± 70 |
| tW | 5.5 ± 1.2 |
| WtZ | 25.8 ± 1.1 |
| VVV | 26.2 ± 0.9 |
| VH | 94 ± 7 |
| t̄t | 108.68 ± 8 |
| t̄tH | 4.3 ± 0.5 |
| Total | 10600 ± 530 |
| Data | 10574 |

Table 6: Event yields in the preselection region at 139.0 fb^{-1}

604 Here Other VV represents diboson processes other than WZ, and consists predominantly
 605 of $ZZ \rightarrow ll\bar{l}\bar{l}$ events where one of the leptons is not reconstructed.

606 Simulations are further validated by comparing the kinematic distributions of the Monte

607 Carlo with data, which are shown in Figure 12.1. Here, bins with 5% or more WZ+b are
608 blinded.

WZ Fit Region - Inclusive

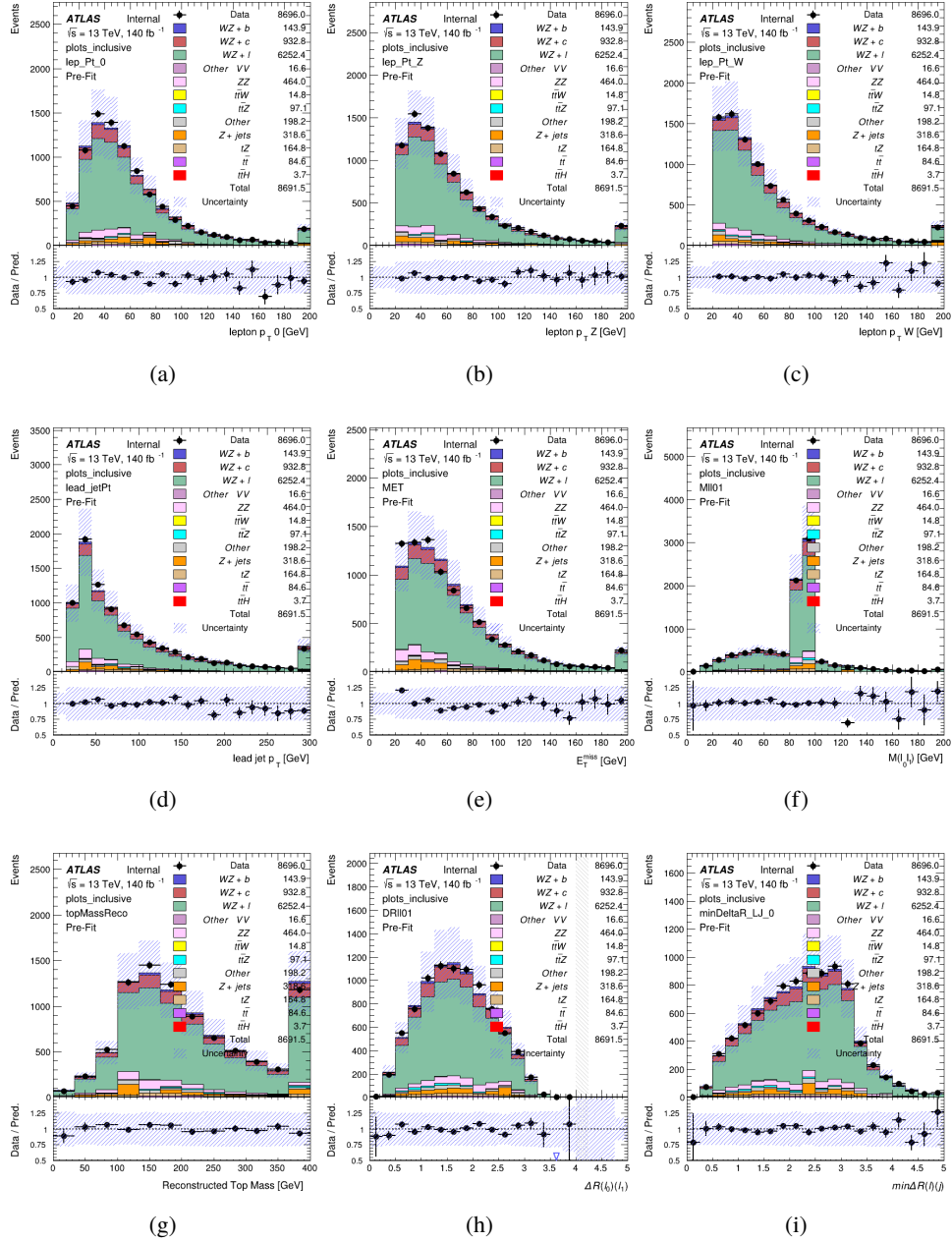


Figure 8.1: Comparisons between the data and MC distributions in the preselection region for (a) the p_T of the opposite sign lepton, (b) the p_T of the other lepton from the Z candidate, (c) the p_T of the lepton from the W candidate, (d) the leading jet p_T , (e) the E_T^{miss} , and (f) the invariant mass of leptons 0 and 1, (g) the reconstructed top mass, (h) $\Delta(R)$ between lepton 0 and 1, (i) the $\Delta(R)$ between the closest lepton and jet.

609 **8.2 Fit Regions**

610 Once preselection has been applied, the remaining events are categorized into one of twelve
 611 orthogonal regions. The regions used in the fit are summarized in Table 14.

Table 7: A list of the regions used in the fit and the selection used for each.

| Region | Selection |
|-------------|--|
| 1j, <85% | $N_{\text{jets}} = 1, n\text{Jets_DL1r_85} = 0$ |
| 1j, 85%-77% | $N_{\text{jets}} = 1, n\text{Jets_DL1r_85} = 1, n\text{Jets_DL1r_77} = 0$ |
| 1j, 77%-70% | $N_{\text{jets}} = 1, n\text{Jets_DL1r_77} = 1, n\text{Jets_DL1r_70} = 0$ |
| 1j, 70%-60% | $N_{\text{jets}} = 1, n\text{Jets_DL1r_70} = 1, n\text{Jets_DL1r_60} = 0$ |
| 1j, >60% | $N_{\text{jets}} = 1, n\text{Jets_DL1r_60} = 1, tZ \text{ BDT} > 0.725$ |
| 1j tZ CR | $N_{\text{jets}} = 1, n\text{Jets_DL1r_60} = 1, tZ \text{ BDT} < 0.725$ |
| 2j, <85% | $N_{\text{jets}} = 2, n\text{Jets_DL1r_85} = 0$ |
| 2j, 85%-77% | $N_{\text{jets}} = 2, n\text{Jets_DL1r_85} \geq 1, n\text{Jets_DL1r_77} = 0$ |
| 2j, 77%-70% | $N_{\text{jets}} = 2, n\text{Jets_DL1r_77} \geq 1, n\text{Jets_DL1r_70} = 0$ |
| 2j, 70%-60% | $N_{\text{jets}} = 2, n\text{Jets_DL1r_70} \geq 1, n\text{Jets_DL1r_60} = 0$ |
| 2j, >60% | $N_{\text{jets}} = 2, n\text{Jets_DL1r_60} \geq 1, tZ \text{ BDT} > 0.725$ |
| 2j tZ CR | $N_{\text{jets}} = 2, n\text{Jets_DL1r_60} \geq 1, tZ \text{ BDT} < 0.725$ |

612 The working points discussed in Section 11.4 are used to separate events into fit regions
 613 based on the highest working point reached by a jet in each event. Because the background
 614 composition differs significantly based on the number of b-jets, events are further subdivided
 615 into 1-jet and 2-jet regions in order to minimize the impact of background uncertainties.

616 An unfolding procedure is performed to account for differences in the number of recon-
 617 structed jets compared to the number of truth jets in each event. The `AntiKt4TruthDressedWZJets`
 618 truth jet collection is used to make this determination. In order to account for migration of WZ+1-
 619 jet and WZ+2-jet events between the 1-jet and 2-jet bins at reco level, the signal samples are
 620 separated based on the number of truth jets. Events with 0 jets or more than 3 jets at truth level,

yet fall within one of the categories listed in Table 14, are categorized as WZ + other, and treated as a background. The migration matrix in the number of jets at truth level versus reco level is shown in Figure 12.2. The composition of the number of truth jets in each reco jet bin is taken from MC, with uncertainties in these estimates described in detail in Section 21.

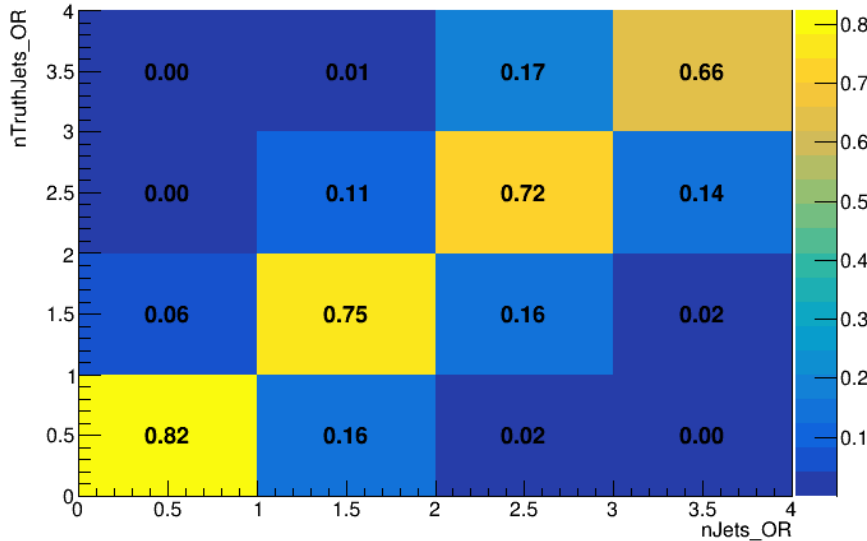


Figure 8.2: Number of truth jets compared to the number of reconstructed jets in each WZ event falling in the preselection region. Each row is normalized to unity.

An additional tZ control region is created based on the BDT described in Section 13. The region with 1-jet passing the 60% working point is split in two - a signal enriched region of events with a BDT score greater than 0.03, and a tZ control region including events with less than 0.03. This cutoff is arrived at by performing an Asimov fit with a variety of cutoffs, and selecting the value that produces the highest significance for the measurement of WZ + b.

The modeling in each region is validated by comparing data and MC predictions for

631 various kinematic distributions. These plot are shown in Figures [12.3-12.16](#).

WZ Fit Region - 1j Inclusive

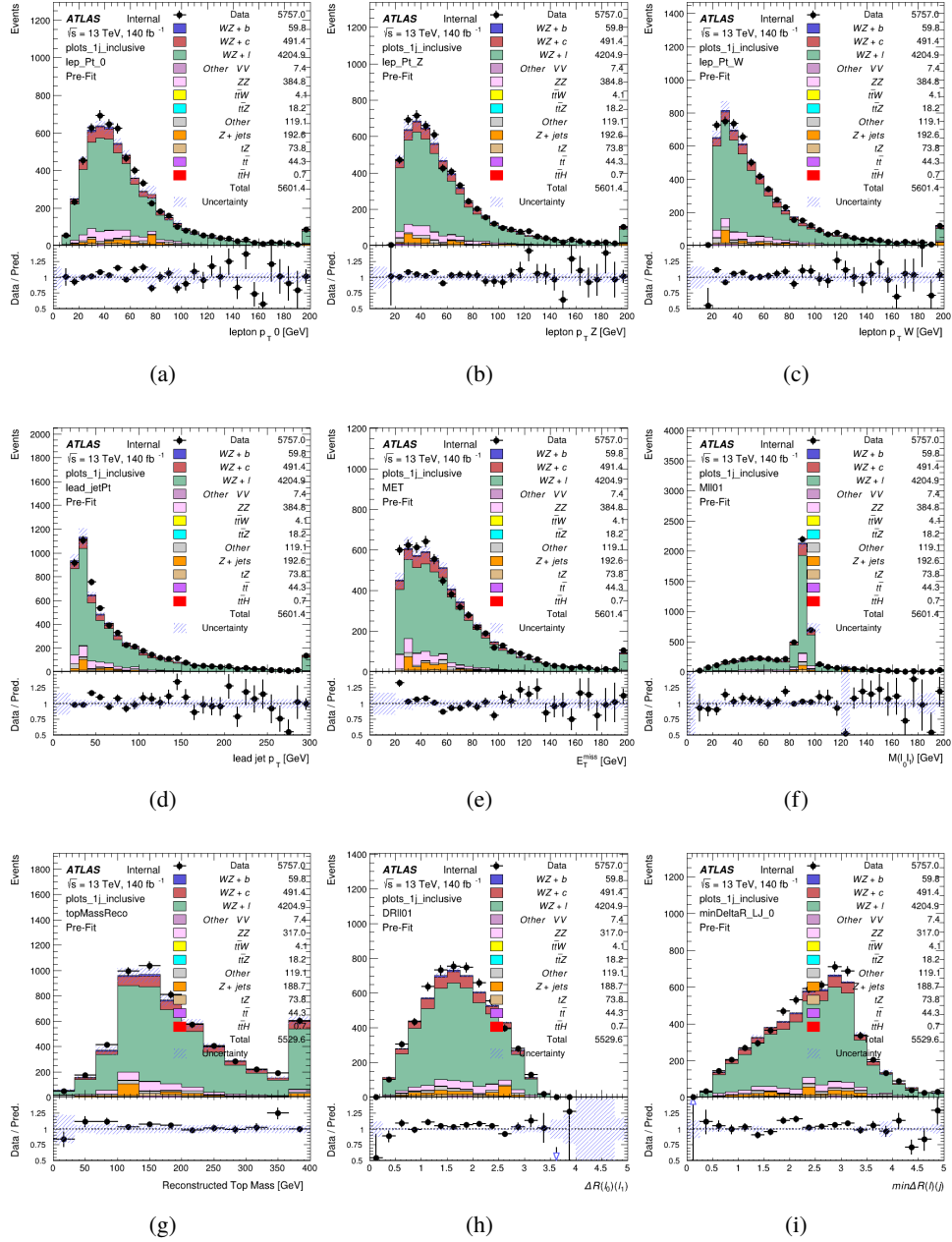


Figure 8.3: Comparisons between the data and MC distributions in the preselection region for (a) the p_T of the opposite sign lepton, (b) the p_T of the other lepton from the Z candidate, (c) the p_T of the lepton from the W candidate, (d) the leading jet p_T , (e) the E_T^{miss} , and (f) the invariant mass of leptons 0 and 1, (g) the reconstructed top mass, (h) $\Delta(R)$ between lepton 0 and 1, (i) the $\Delta(R)$ between the closest lepton and jet.

WZ Fit Region - 1j < 85% WP

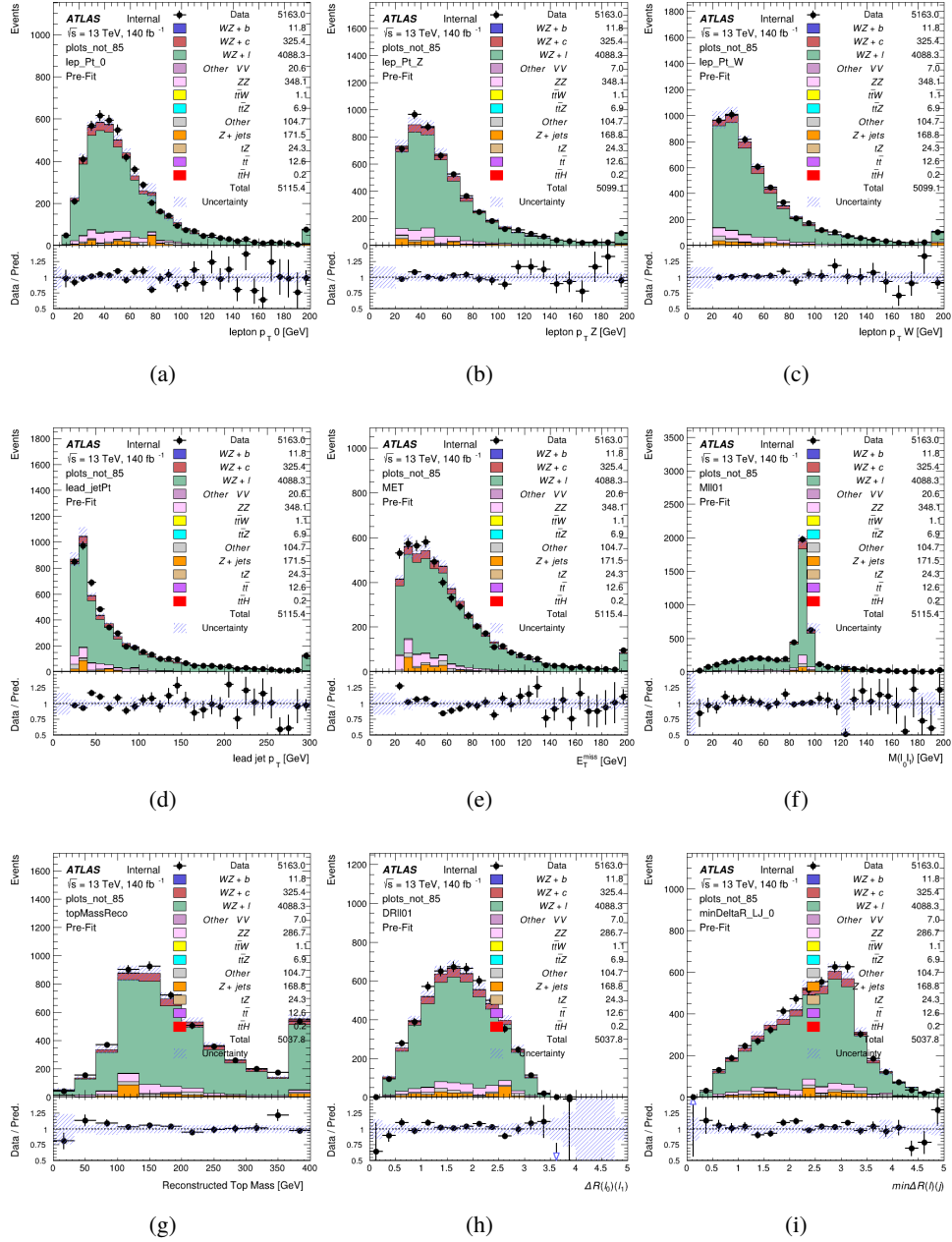


Figure 8.4: Comparisons between the data and MC distributions in the preselection region for (a) the p_T of the opposite sign lepton, (b) the p_T of the other lepton from the Z candidate, (c) the p_T of the lepton from the W candidate, (d) the leading jet p_T , (e) the E_T^{miss} , and (f) the invariant mass of leptons 0 and 1, (g) the reconstructed top mass, (h) $\Delta(R)$ between lepton 0 and 1, (i) the $\Delta(R)$ between the closest lepton and jet.

WZ Fit Region - 1j 77-85% WP

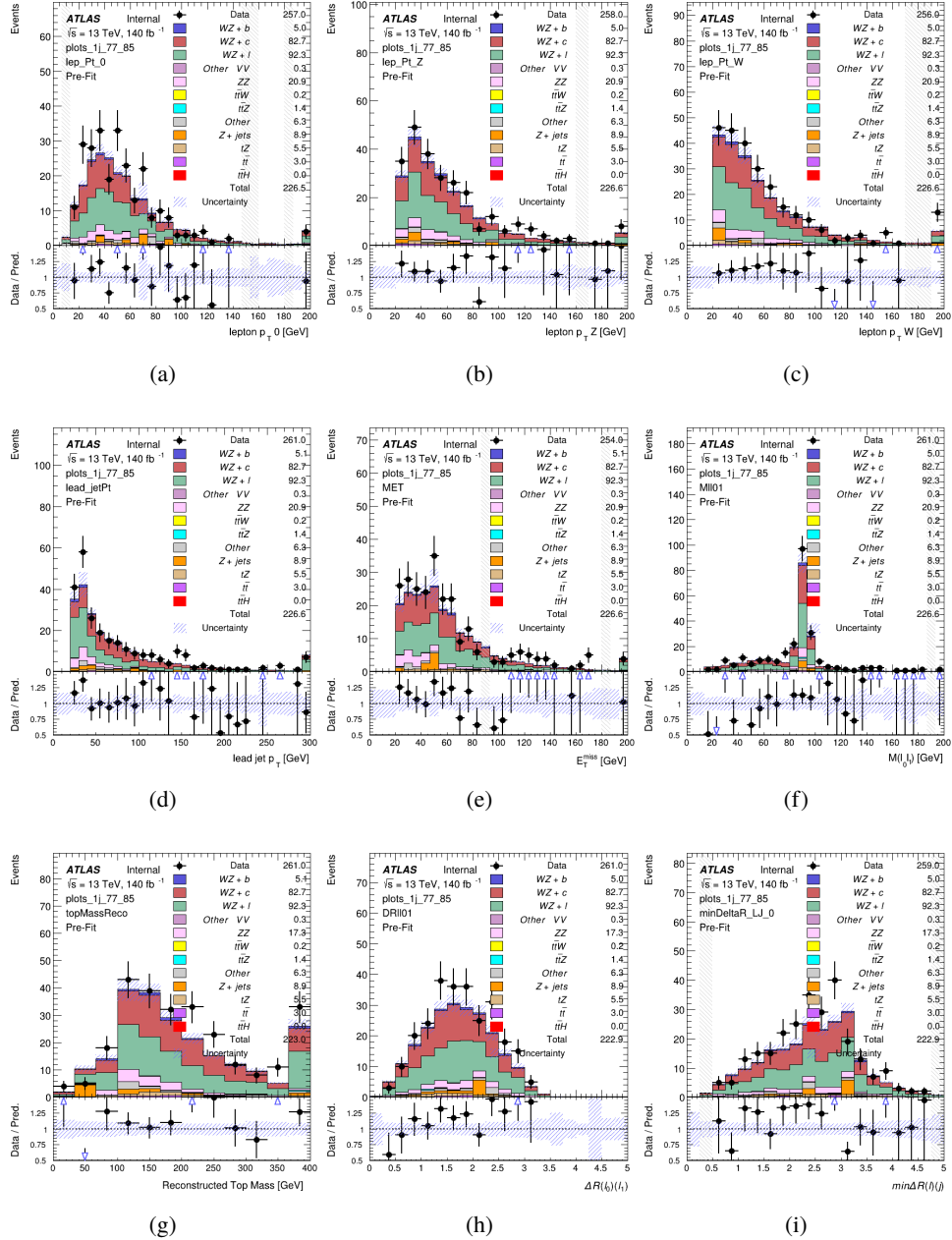


Figure 8.5: Comparisons between the data and MC distributions in the preselection region for (a) the p_T of the opposite sign lepton, (b) the p_T of the other lepton from the Z candidate, (c) the p_T of the lepton from the W candidate, (d) the leading jet p_T , (e) the E_T^{miss} , and (f) the invariant mass of leptons 0 and 1, (g) the reconstructed top mass, (h) $\Delta(R)$ between lepton 0 and 1, (i) the $\Delta(R)$ between the closest lepton and jet.

WZ Fit Region - 1j 70-77% WP

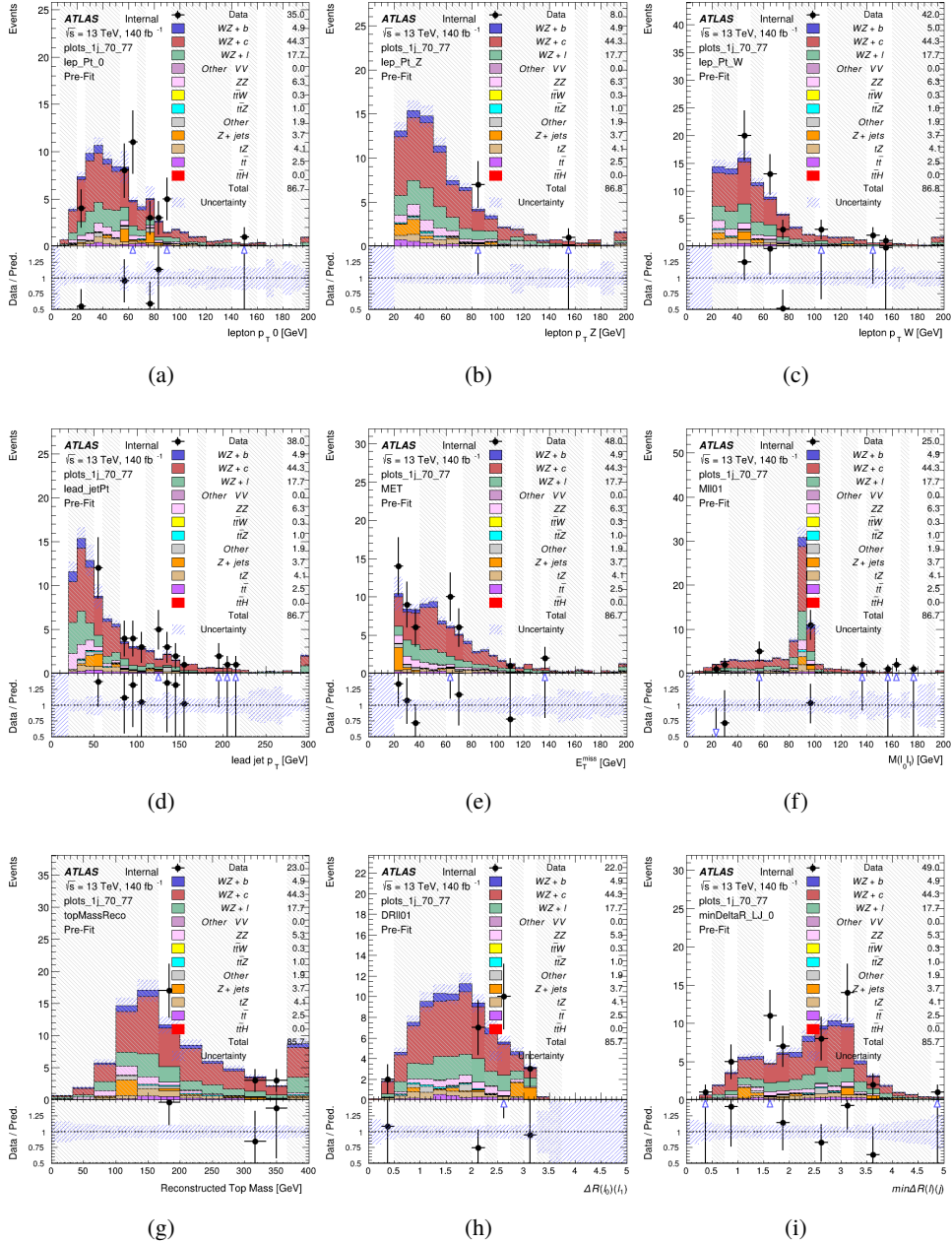


Figure 8.6: Comparisons between the data and MC distributions in the preselection region for (a) the p_T of the opposite sign lepton, (b) the p_T of the other lepton from the Z candidate, (c) the p_T of the lepton from the W candidate, (d) the leading jet p_T , (e) the E_T^{miss} , and (f) the invariant mass of leptons 0 and 1, (g) the reconstructed top mass, (h) $\Delta(R)$ between lepton 0 and 1, (i) the $\Delta(R)$ between the closest lepton and jet.

WZ Fit Region - 1j 60-70% WP

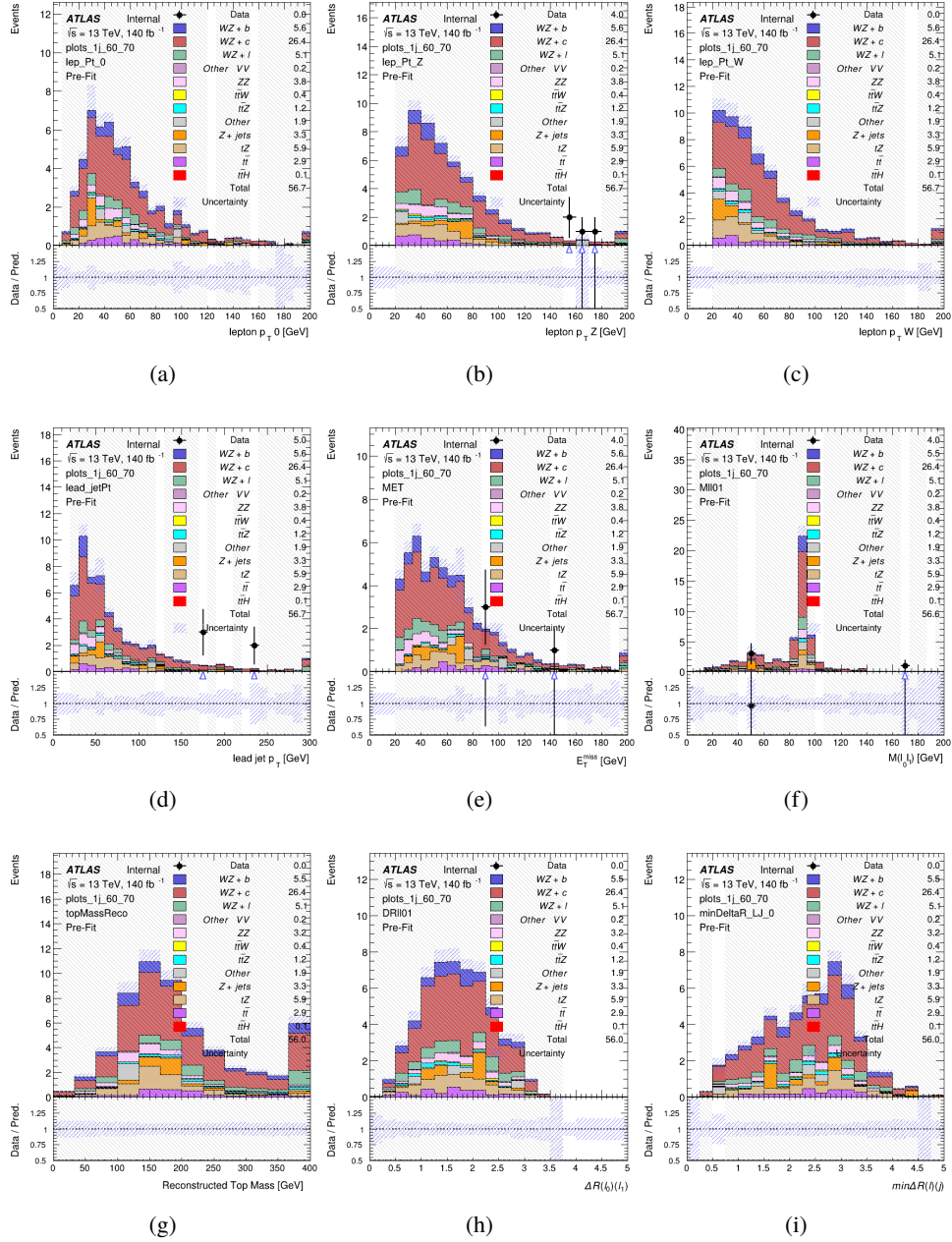


Figure 8.7: Comparisons between the data and MC distributions in the preselection region for (a) the p_T of the opposite sign lepton, (b) the p_T of the other lepton from the Z candidate, (c) the p_T of the lepton from the W candidate, (d) the leading jet p_T , (e) the E_T^{miss} , and (f) the invariant mass of leptons 0 and 1, (g) the reconstructed top mass, (h) $\Delta(R)$ between lepton 0 and 1, (i) the $\Delta(R)$ between the closest lepton and jet.

WZ Fit Region - 1j 60% WP

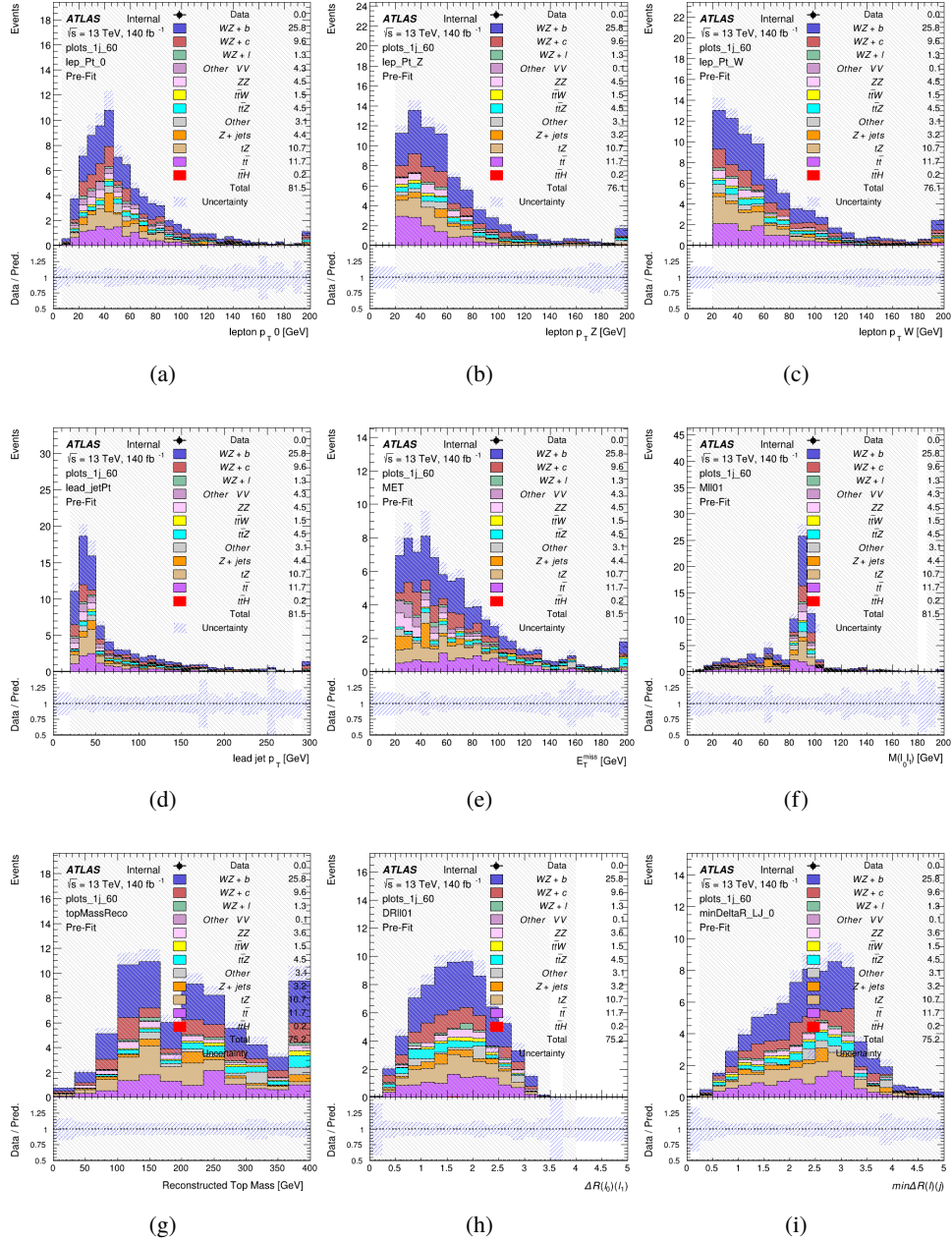


Figure 8.8: Comparisons between the data and MC distributions in the preselection region for (a) the p_T of the opposite sign lepton, (b) the p_T of the other lepton from the Z candidate, (c) the p_T of the lepton from the W candidate, (d) the leading jet p_T , (e) the E_T^{miss} , and (f) the invariant mass of leptons 0 and 1, (g) the reconstructed top mass, (h) $\Delta(R)$ between lepton 0 and 1, (i) the $\Delta(R)$ between the closest lepton and jet.

WZ Fit Region - tZ-CR

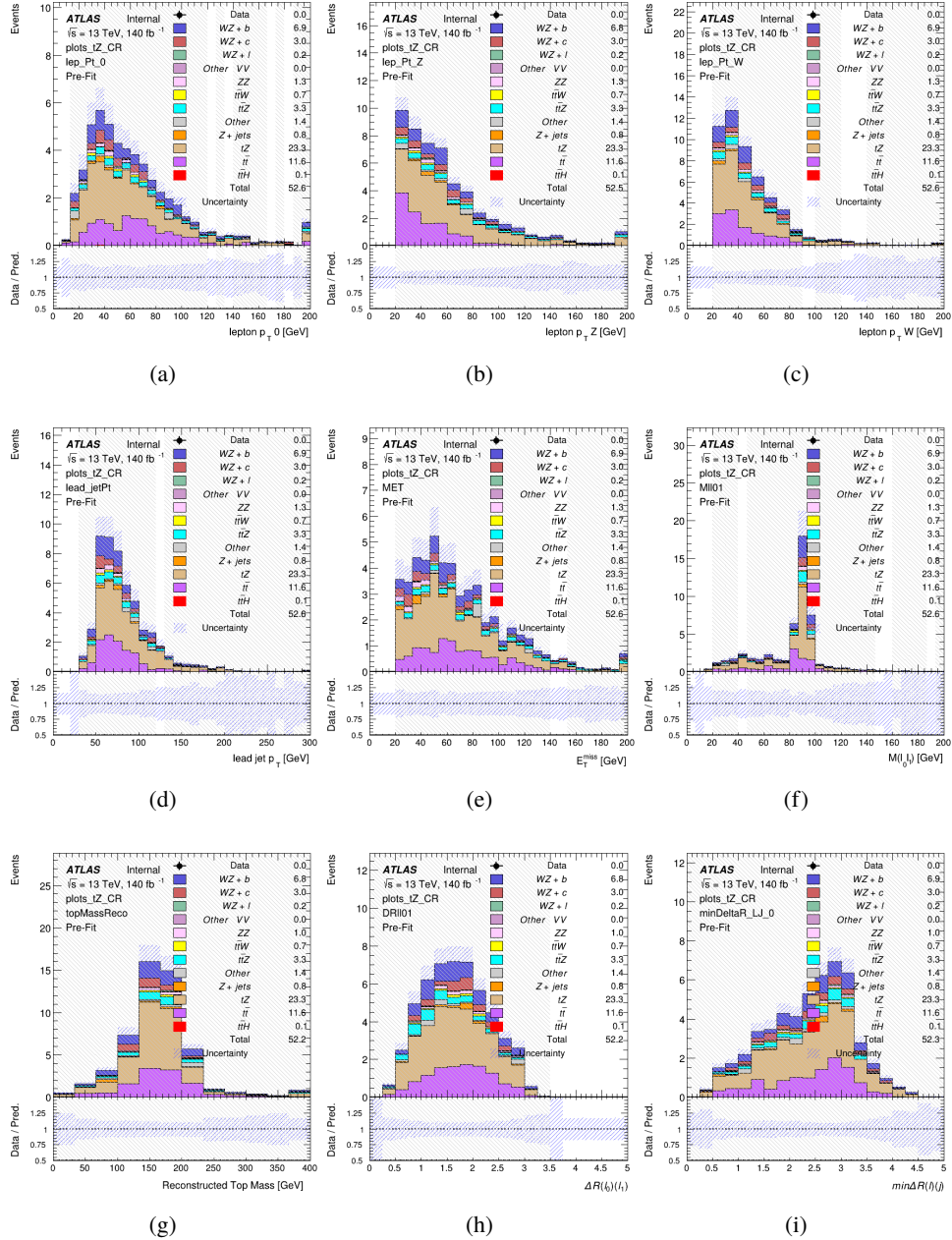


Figure 8.9: Comparisons between the data and MC distributions in the preselection region for (a) the p_T of the opposite sign lepton, (b) the p_T of the other lepton from the Z candidate, (c) the p_T of the lepton from the W candidate, (d) the leading jet p_T , (e) the E_T^{miss} , and (f) the invariant mass of leptons 0 and 1, (g) the reconstructed top mass, (h) $\Delta(R)$ between lepton 0 and 1, (i) the $\Delta(R)$ between the closest lepton and jet.

WZ Fit Region - 2j Inclusive

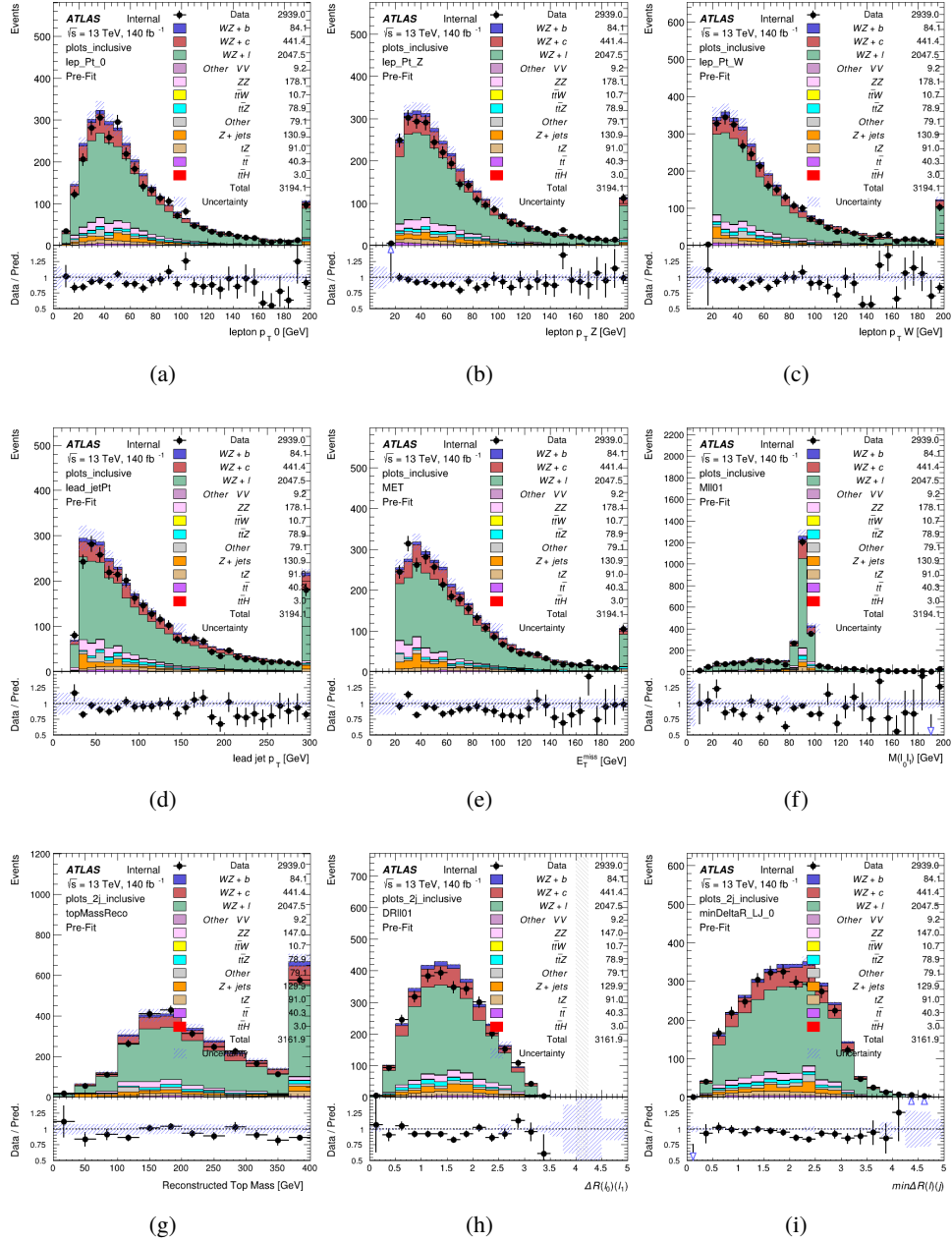


Figure 8.10: Comparisons between the data and MC distributions in the preselection region for (a) the p_T of the opposite sign lepton, (b) the p_T of the other lepton from the Z candidate, (c) the p_T of the lepton from the W candidate, (d) the leading jet p_T , (e) the E_T^{miss} , and (f) the invariant mass of leptons 0 and 1, (g) the reconstructed top mass, (h) $\Delta(R)$ between lepton 0 and 1, (i) the $\Delta(R)$ between the closest lepton and jet.

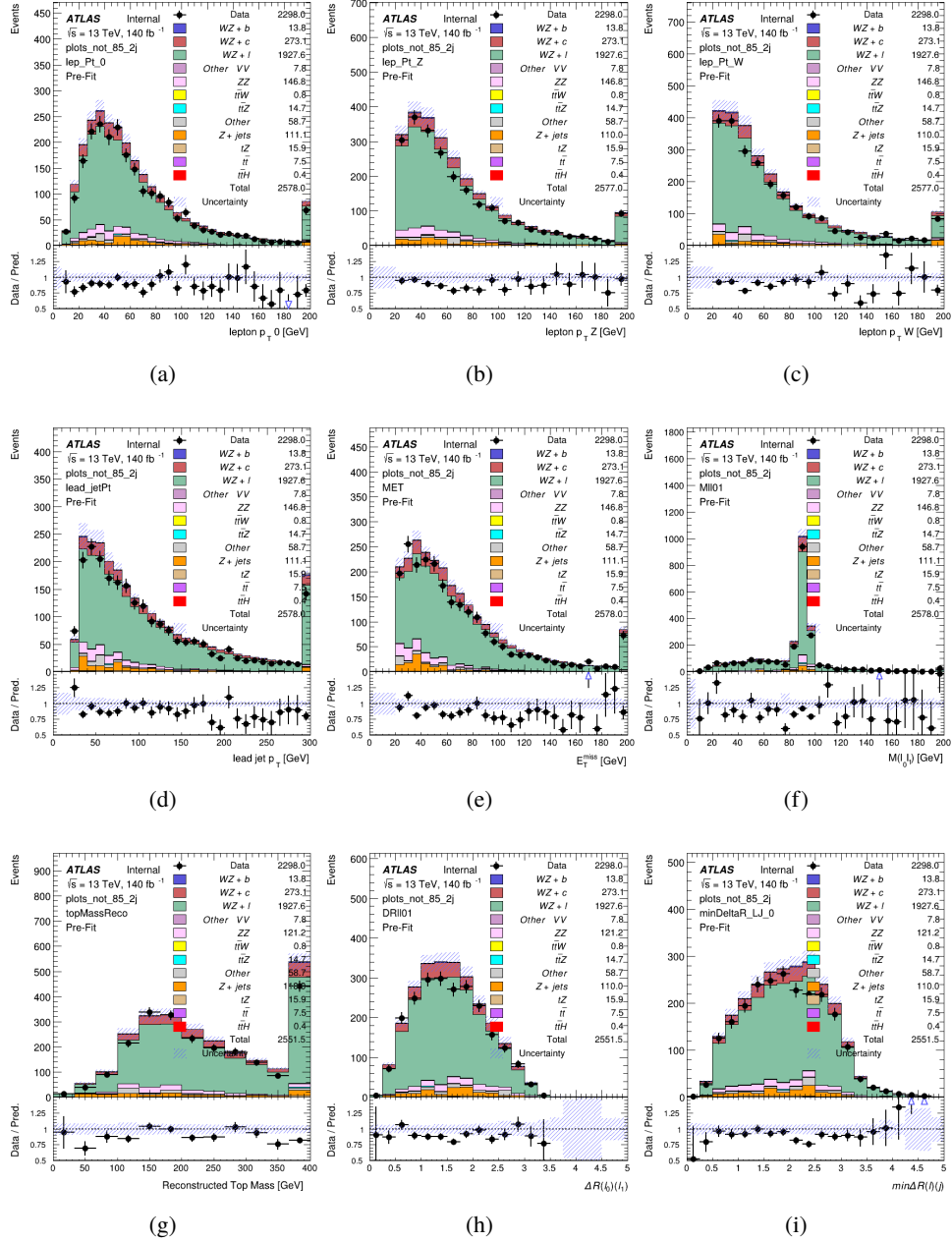
WZ Fit Region - $2j < 85\%$ WP

Figure 8.11: Comparisons between the data and MC distributions in the preselection region for (a) the p_T of the opposite sign lepton, (b) the p_T of the other lepton from the Z candidate, (c) the p_T of the lepton from the W candidate, (d) the leading jet p_T , (e) the E_T^{miss} , and (f) the invariant mass of leptons 0 and 1, (g) the reconstructed top mass, (h) $\Delta(R)$ between lepton 0 and 1, (i) the $\Delta(R)$ between the closest lepton and jet.

WZ Fit Region - 2j 77-85% WP

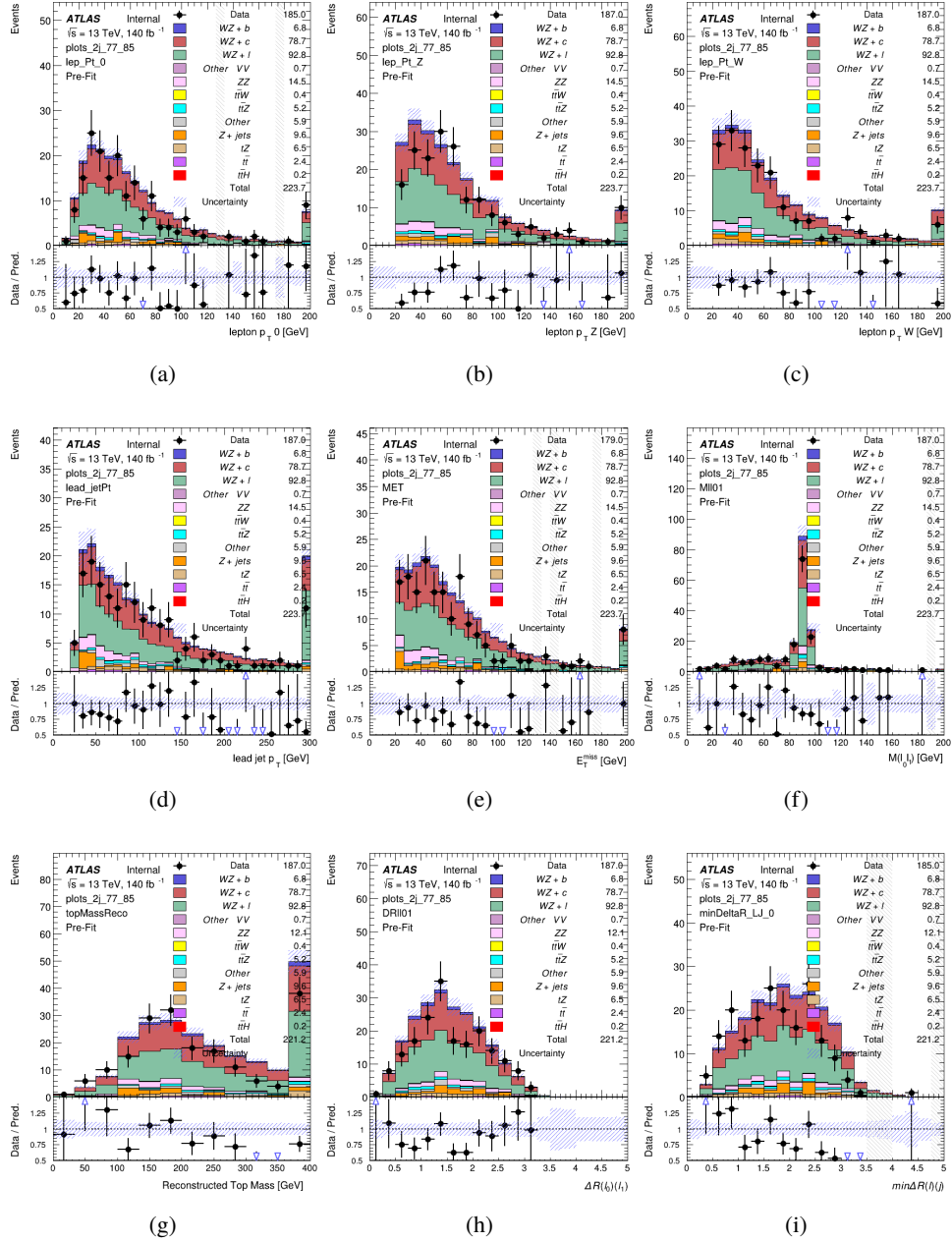


Figure 8.12: Comparisons between the data and MC distributions in the preselection region for (a) the p_T of the opposite sign lepton, (b) the p_T of the other lepton from the Z candidate, (c) the p_T of the lepton from the W candidate, (d) the leading jet p_T , (e) the E_T^{miss} , and (f) the invariant mass of leptons 0 and 1, (g) the reconstructed top mass, (h) $\Delta(R)$ between lepton 0 and 1, (i) the $\Delta(R)$ between the closest lepton and jet.

WZ Fit Region - 2j 70-77% WP

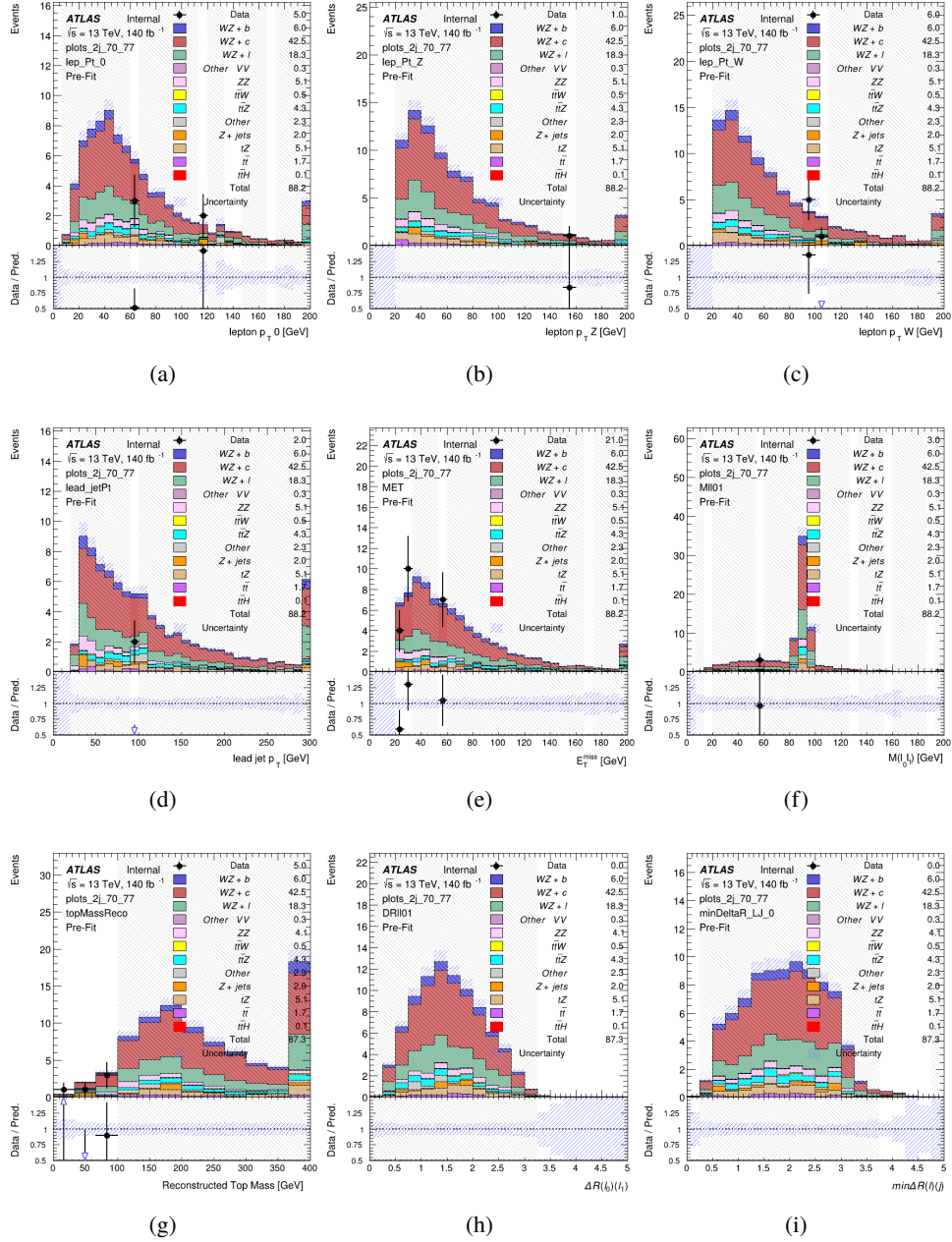


Figure 8.13: Comparisons between the data and MC distributions in the preselection region for (a) the p_T of the opposite sign lepton, (b) the p_T of the other lepton from the Z candidate, (c) the p_T of the lepton from the W candidate, (d) the leading jet p_T , (e) the E_T^{miss} , and (f) the invariant mass of leptons 0 and 1, (g) the reconstructed top mass, (h) $\Delta(R)$ between lepton 0 and 1, (i) the $\Delta(R)$ between the closest lepton and jet.

WZ Fit Region - 2j 60-70% WP

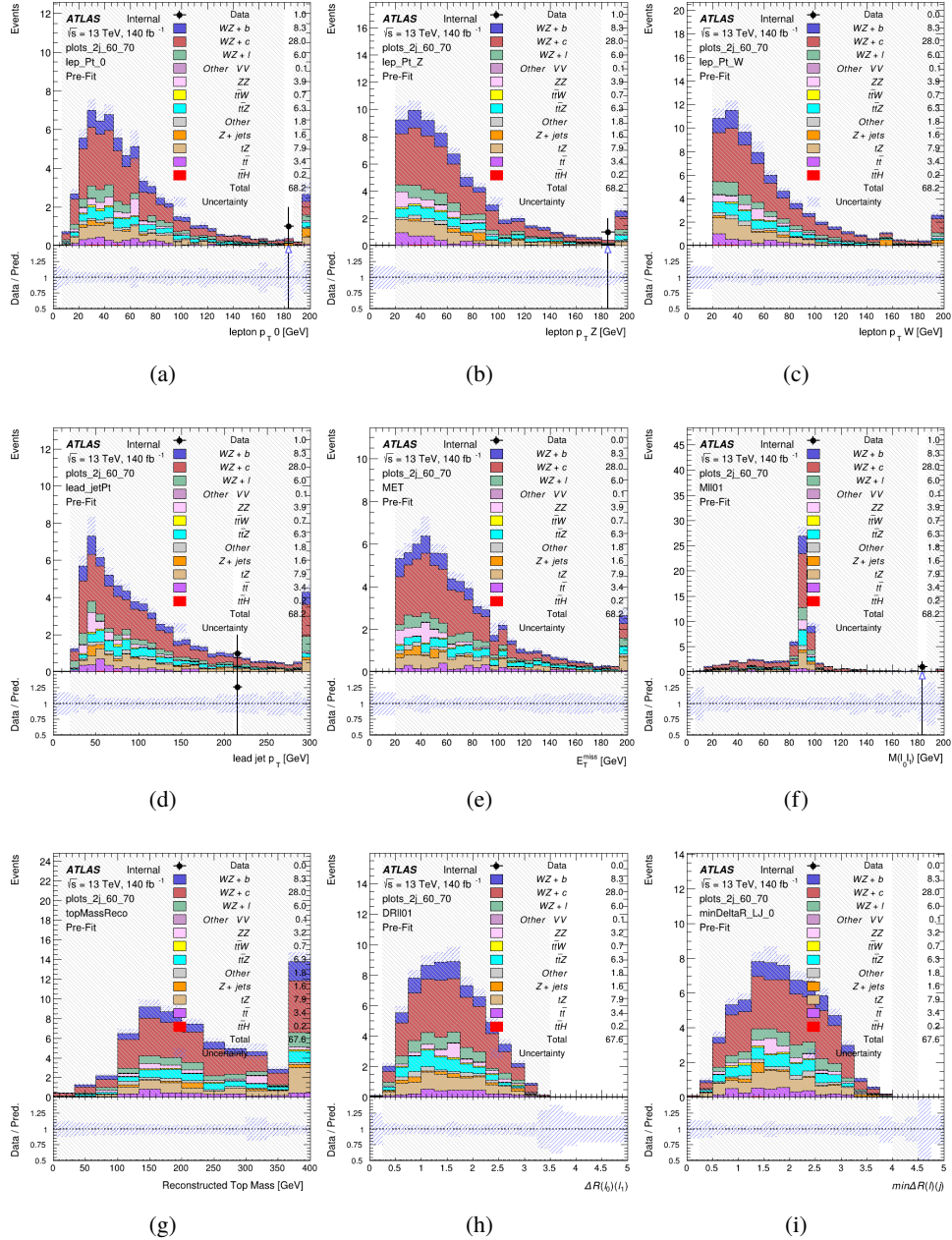


Figure 8.14: Comparisons between the data and MC distributions in the preselection region for (a) the p_T of the opposite sign lepton, (b) the p_T of the other lepton from the Z candidate, (c) the p_T of the lepton from the W candidate, (d) the leading jet p_T , (e) the E_T^{miss} , and (f) the invariant mass of leptons 0 and 1, (g) the reconstructed top mass, (h) $\Delta(R)$ between lepton 0 and 1, (i) the $\Delta(R)$ between the closest lepton and jet.

WZ Fit Region - 2j 60% WP

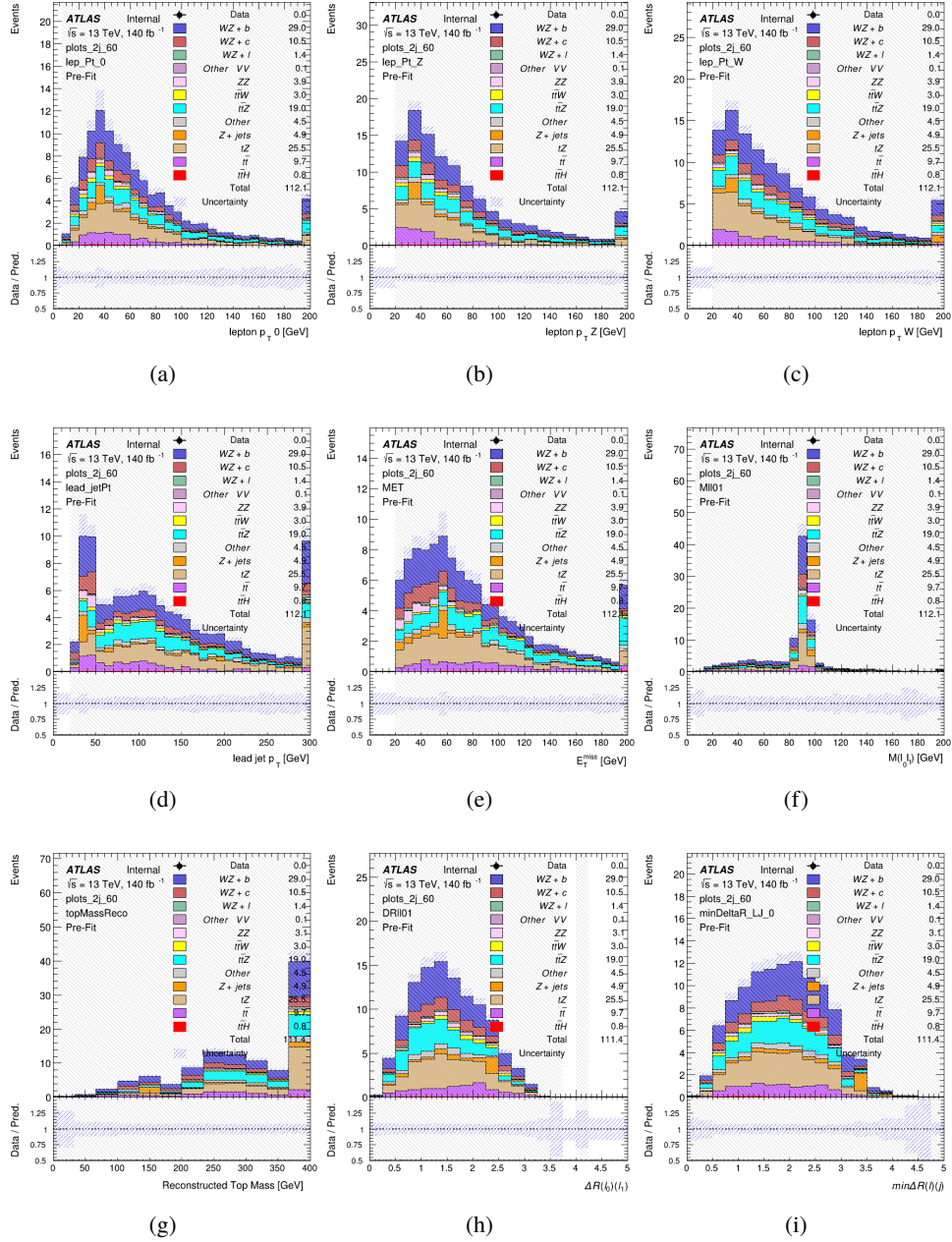


Figure 8.15: Comparisons between the data and MC distributions in the preselection region for (a) the p_T of the opposite sign lepton, (b) the p_T of the other lepton from the Z candidate, (c) the p_T of the lepton from the W candidate, (d) the leading jet p_T , (e) the E_T^{miss} , and (f) the invariant mass of leptons 0 and 1, (g) the reconstructed top mass, (h) $\Delta(R)$ between lepton 0 and 1, (i) the $\Delta(R)$ between the closest lepton and jet.

WZ Fit Region - tZ-CR-2j

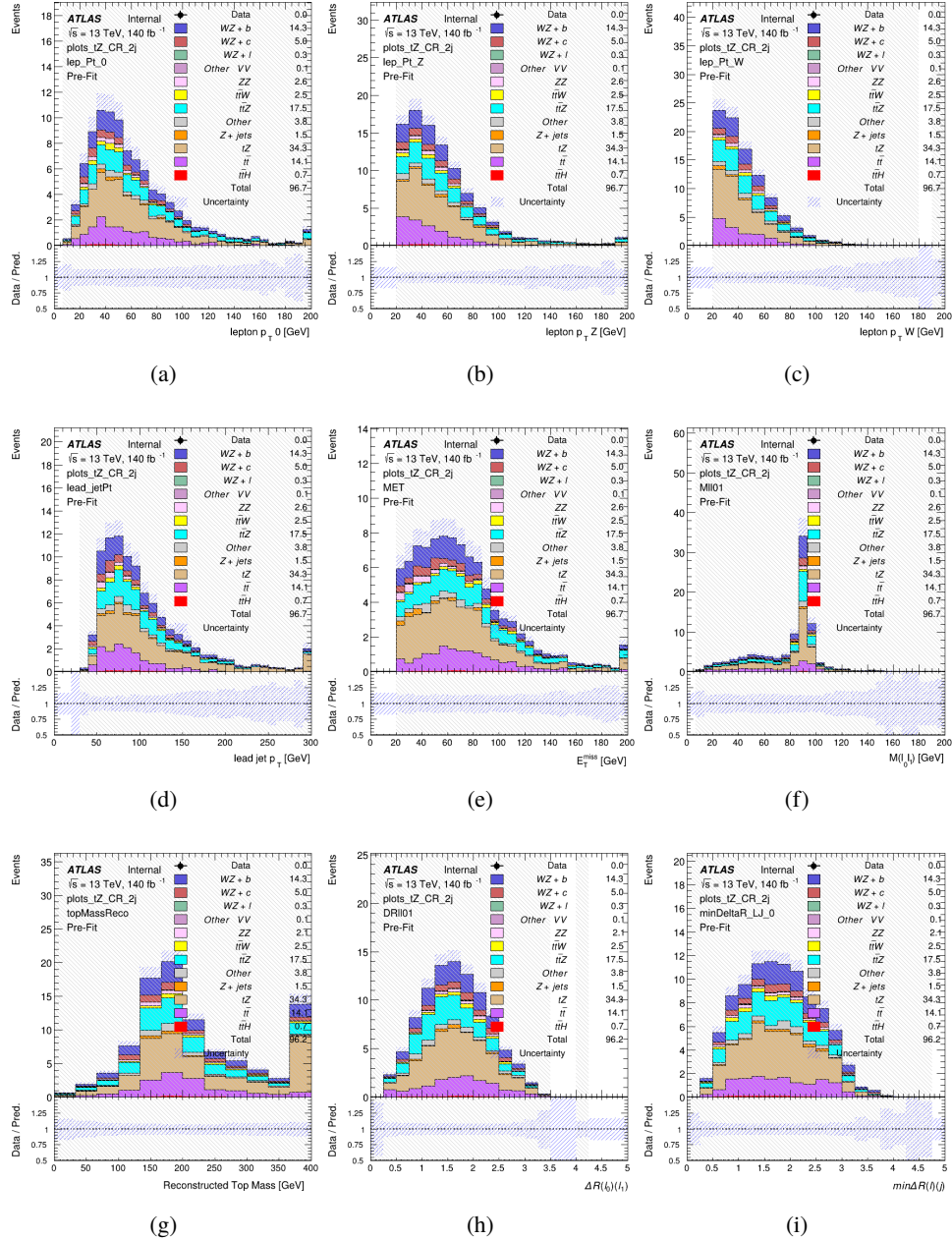


Figure 8.16: Comparisons between the data and MC distributions in the preselection region for (a) the p_T of the opposite sign lepton, (b) the p_T of the other lepton from the Z candidate, (c) the p_T of the lepton from the W candidate, (d) the leading jet p_T , (e) the E_T^{miss} , and (f) the invariant mass of leptons 0 and 1, (g) the reconstructed top mass, (h) $\Delta(R)$ between lepton 0 and 1, (i) the $\Delta(R)$ between the closest lepton and jet.

632 **8.3 Non-Prompt Lepton Estimation**

633 Two processes act as sources of non-prompt leptons appear in the analysis: $t\bar{t}$ and Z+jet
 634 production both produce two prompt leptons, and each contribute to the 3l region when an
 635 additional non-prompt lepton appears in the event. The contribution of these processes is
 636 estimated with Monte Carlo simulations, which are validated using enriched control regions.

637 The modelling in the Z+jets and $t\bar{t}$ CRs is further validated for each of the pseudo-
 638 continuous b-tag regions used in the analysis. The relevant lepton p_T spectrum in each b-tag
 639 region is shown in Appendix .2 for these CRs after the correction factors derived below have
 640 been applied.

641 **8.3.1 $t\bar{t}$ Validation**

642 $t\bar{t}$ events can produce two prompt leptons from the decay of each of the tops. These top decays
 643 produce two b-quarks, the decay of which can produce additional non-prompt leptons, which
 644 occasionally pass the event preselection. In order to validate that the Monte Carlo accurately
 645 simulates this process accurately, the MC prediction in a non-prompt $t\bar{t}$ enriched control region
 646 is compared to data.

647 The $t\bar{t}$ control region is similar to the preselection region - three leptons meeting the
 648 criteria described in Section 12 are required, and the requirements on E_T^{miss} remain the same.
 649 However, the selection requiring a lepton pair form a Z-candidate are reversed. Events where the

650 invariant mass of any two opposite sign, same flavor leptons falls within 10 GeV of 91.2 GeV are
651 rejected. This ensures the $t\bar{t}$ control region is orthogonal to the preselection region.

652 Further, because the jet multiplicity of $t\bar{t}$ events tends to be higher than WZ, the number
653 of jets in each event is required to be greater than 1. As b-jets are almost invariably produced
654 from top decays, at least one b-tagged jet passing the 70% DL1r WP in each event is required.

655 Various kinematic plots of this region are shown in Figure 12.17.

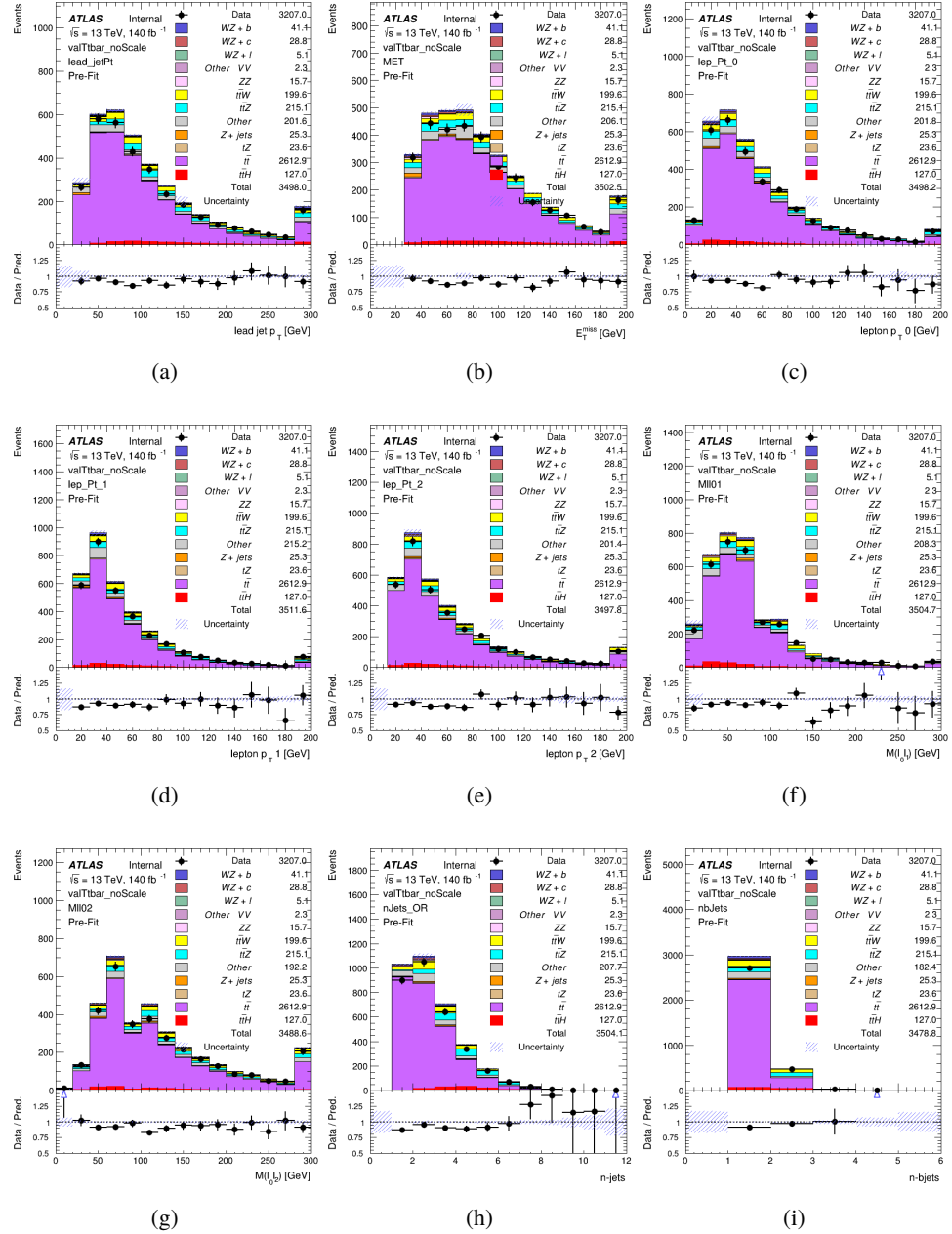


Figure 8.17: Comparisons between the data and MC distributions in the $t\bar{t}$ control region for (a) the p_T of the leading jet, (b) the missing transverse energy, (c) the p_T of lepton 0, (d) p_T of lepton 1, (e) p_T of lepton 2, (f) the invariant mass of leptons 0 and 1, (g) the invariant mass of leptons 0 and 2, (h) the number of jets, (i) the number of b-tagged jets.

656 The shape of each distribution agrees quite well between data and MC, with a constant
657 offset between the two. This is accounted for by applying a constant correction factor of 0.883
658 to the $t\bar{t}$ MC prediction. Plots showing the kinematics of the $t\bar{t}$ VR after this correction factor
659 has been applied are shown in Figure 12.18.

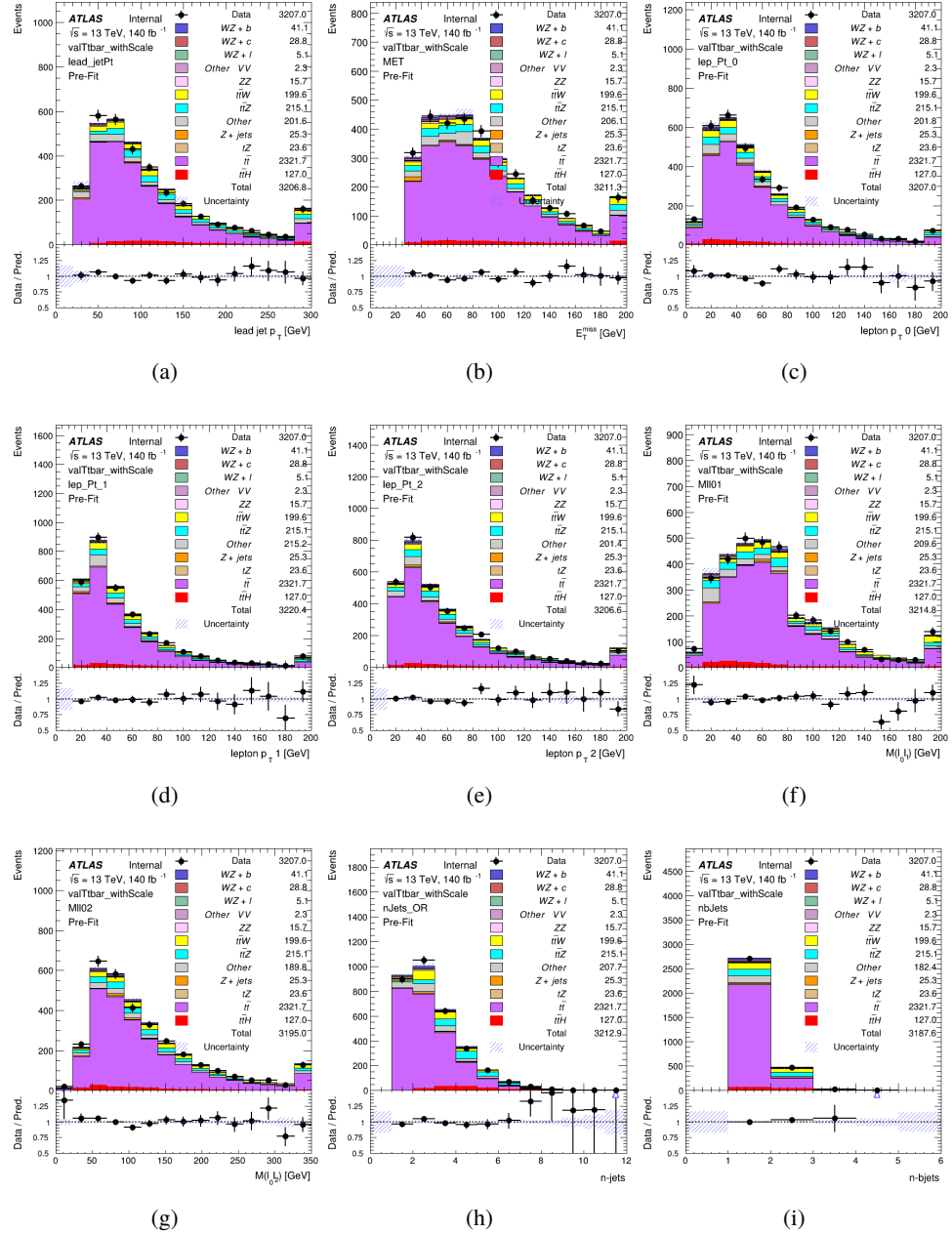


Figure 8.18: Comparisons between the data and MC distributions in the $t\bar{t}$ control region after the correction factor has been applied for (a) the p_T of the leading jet, (b) the missing transverse energy, (c) the p_T of lepton 0, (d) p_T of lepton 1, (e) p_T of lepton 2, (f) the invariant mass of leptons 0 and 1, (g) the invariant mass of leptons 0 and 2, (h) the number of jets, (i) the number of b-tagged jets.

660 The modeling is further validated by looking at the yield in the $t\bar{t}$ VR for each DL1r WP,
 661 giving a clearer correspondence to the signal regions used in the fit. Each region shown in Figure
 662 12.19 requires one or more jets pass the listed WP, with no jets passing the next highest WP.

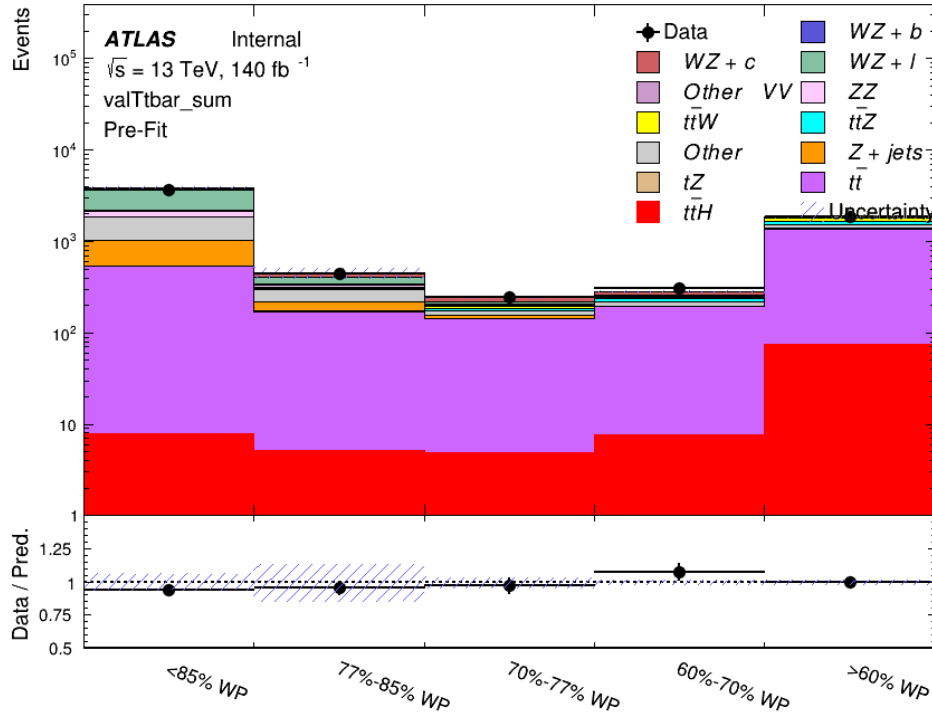


Figure 8.19: Data and MC comparisons for each DL1r WP for both 1-jet and 2-jet regions, after the $t\bar{t}$ VR selection and correction factor have been applied

663 As data and MC are found to agree within 20% for each of these working points, a 20%
 664 systematic uncertainty on the $t\bar{t}$ prediction is included for the analysis.

665 8.3.2 Z+jets Validation

666 Similar to $t\bar{t}$, a non-prompt Z +jets control region is produced in order to validate the MC
667 predictions. The lepton requirements remain the same as the preselection region. Because no
668 neutrinos are present for this process, the E_T^{miss} cut is reversed, requiring $E_T^{\text{miss}} < 30 \text{ GeV}$. This
669 also ensures this control region is orthogonal to the preselection region. Further, the number of
670 jets in each event is required to be greater than or equal to one. Various kinematic plots of this
671 region are shown below. The general agreement between data and MC in each of these suggests
672 that the non-prompt contribution of Z +jets is well modeled by Monte Carlo.

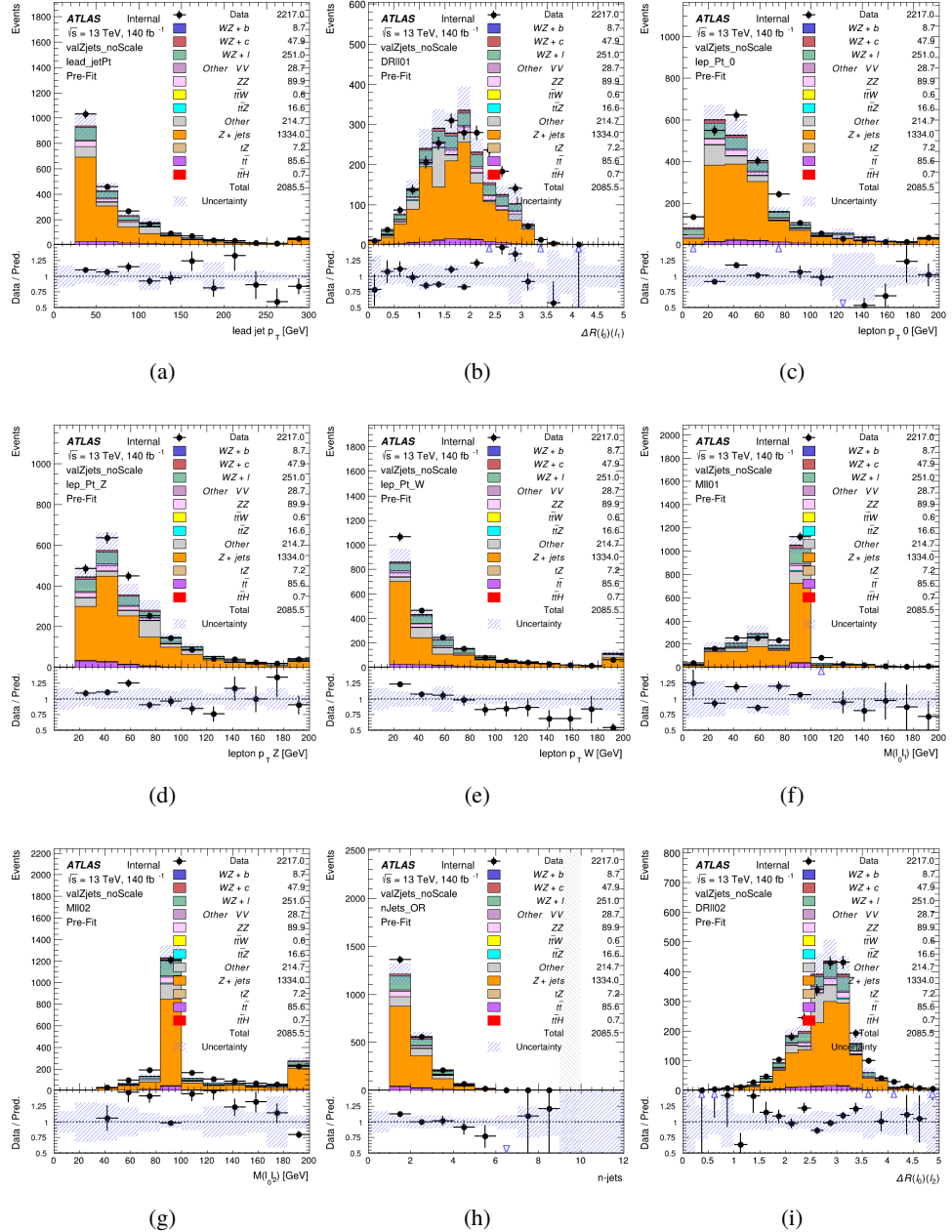


Figure 8.20: Comparisons between the data and MC distributions in the Z+jets control region for (a) the p_T of the leading jet, (b) ΔR between leptons 0 and 1, (c) the p_T of lepton 0, (d) p_T of SS lepton from the Z candidate, (e) p_T of the SS lepton from the W candidate, (f) the invariant mass of leptons 0 and 1, (g) the invariant mass of leptons 0 and 2, (h) the number of jets, (i) ΔR between leptons 0 and 2. Includes only statistical uncertainties

673 While there is general agreement between data and MC within statistical uncertainty, the
674 shape of the p_T spectrum of the lepton from the W is found to differ. To account for this
675 discrepancy, a variable correction factor is applied to Z+jets. χ^2 minimization of the lepton 2 p_T
676 spectrum is performed to derive a correction factor of $1.53 - 6.6 * 10^{-6}(\text{lep}_\text{Pt}_W)$. Kinematic
677 plots of the Z + jets control region after this correction factor has been aplied are shown in Figure
678 [12.21](#).

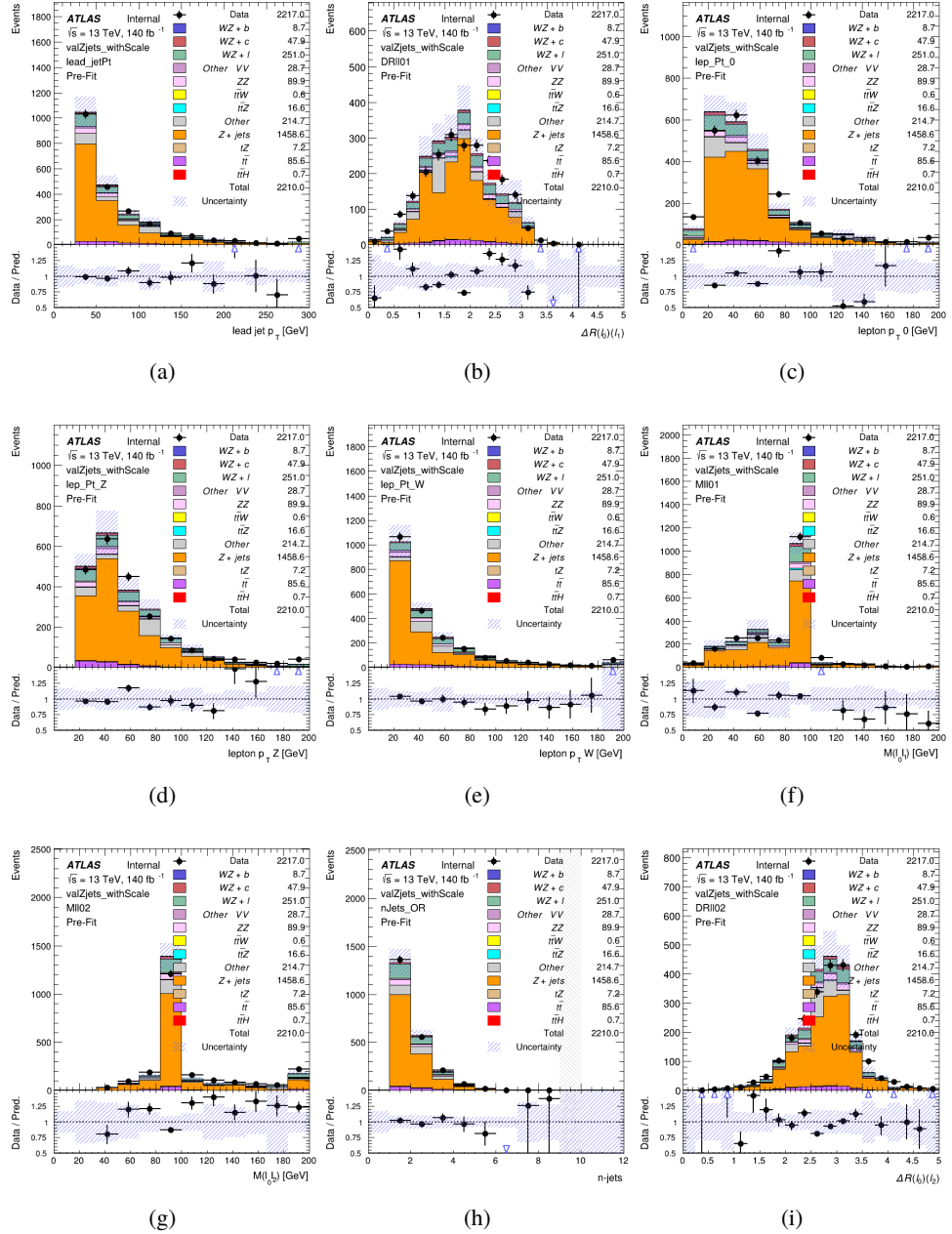


Figure 8.21: Comparisons between the data and MC distributions in the $Z + \text{jets}$ control region after the correction factor has been applied for (a) the p_T of the leading jet, (b) ΔR between leptons 0 and 1, (c) the p_T of lepton 0, (d) p_T of SS lepton from the Z candidate, (e) p_T of the SS lepton from the W candidate, (f) the invariant mass of leptons 0 and 1, (g) the invariant mass of leptons 0 and 2, (h) the number of jets, (i) ΔR between leptons 0 and 2

679 The modeling is further validated by looking at the yield in the Z+jets VR for each DL1r
 680 WP, giving a clearer correspondence to the signal regions used in the fit. Each region shown in
 681 Figure 12.22 requires one or more jets pass the listed WP, with no jets passing the next highest
 682 WP.

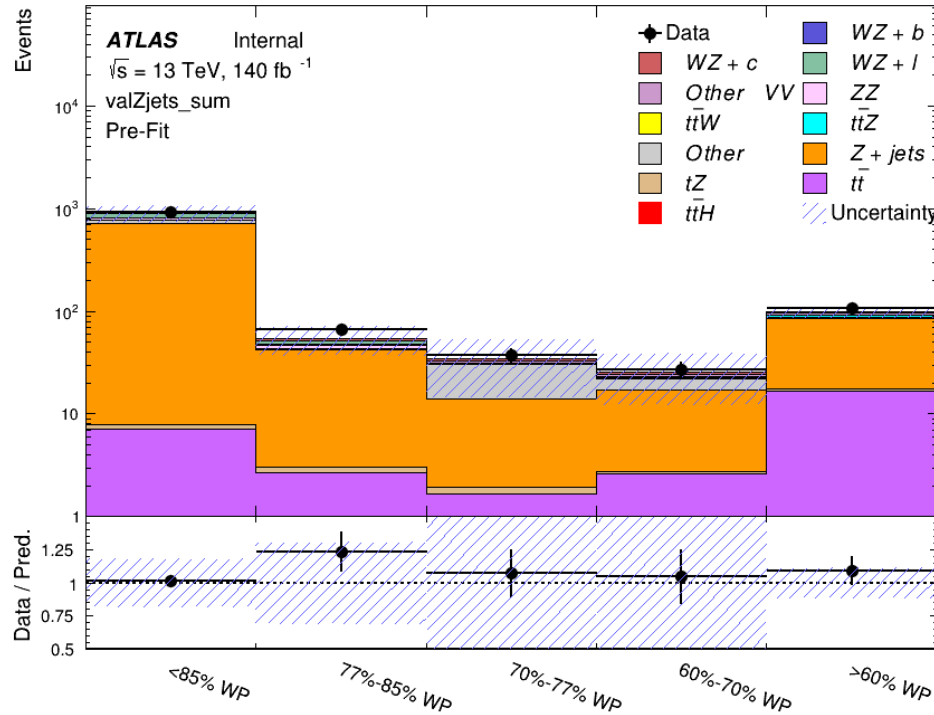


Figure 8.22: Data and MC comparisons for each DL1r WP for both 1-jet and 2-jet regions, after the Z+jets VR selection and correction factor have been applied

683 For each of the b-tagging working points considered, the data falls within 25% of the MC
 684 prediction once this correction factor has been applied. Therefore, a 25% systematic uncertainty
 685 is applied to Z + jets in the analysis.

686 9 tZ Interference Studies and Separation Multivariate Analysis

687 Because tZ produces a final state identical to signal, it represents a predominant background in
688 the most signal enriched regions. That is, the region with one jet passing the 60% DL1r WP.
689 Therefore, a boosted decision tree (BDT) algorithm is trained using TMVA [23] to separate WZ
690 + heavy flavor from tZ.

691 Separation between tZ and WZ + heavy flavor is achieved in part by reconstructing the
692 invariant mass of the top candidate, which clusters more closely to the top mass for tZ than WZ
693 + heavy flavor.

694 The result of this BDT is used to create a tZ enriched region in the fit, reducing its impact
695 on the measurement of WZ + heavy flavor.

696 9.1 Top Mass Reconstruction

697 The reconstruction of the top mass follows the procedure described in detail in section 6.1 of
698 [24]. The mass of the top quark candidate is reconstructed from the jet, the lepton not included
699 in the Z-candidate, and a reconstructed neutrino. In the case that there is one jet in the event,
700 there is only possible b-jet candidate. For events with two jets, the jet with the highest DL1r
701 score is used.

702 The neutrino from the W decay is expected to be the only source of E_T^{miss} . Therefore, the
 703 E_T and ϕ of the neutrino are taken from the E_T^{miss} measurement. This leaves the z-component
 704 of the neutrino momentum, $p_{\nu z}$ as the only unknown.

705 This unknown is solved for by taking the combined invariant mass of the lepton and
 706 neutrino to give the invariant mass of the W boson:

$$707 \quad (p_l + p_\nu)^2 = m_W^2$$

708 Expanding this out into components, this equation gives:

$$709 \quad \sqrt{p_{T\nu}^2 + p_{z\nu}^2} E_l = \frac{m_W^2 - m_l^2}{2} + p_{T\nu}(p_{lx}\cos\phi_\nu + p_{ly}\sin\phi_\nu) + p_{lz}p_{\nu z}$$

710 This equation gives two solutions for $p_{\nu z}$. For cases where only one of these solutions is
 711 real, that is taken as the value of $p_{\nu z}$. For instances with two real solutions, the one which is
 712 shown to be correct in the largest fraction of simulations is taken. For cases when no real solution
 713 is found, often because of detector effects, the value of E_T^{miss} is varied in decreasing increments
 714 of 100 MeV until a real solution is found.

715 The reconstructed top mass distribution for tZ and WZ + b can be seen in figure 13.1.

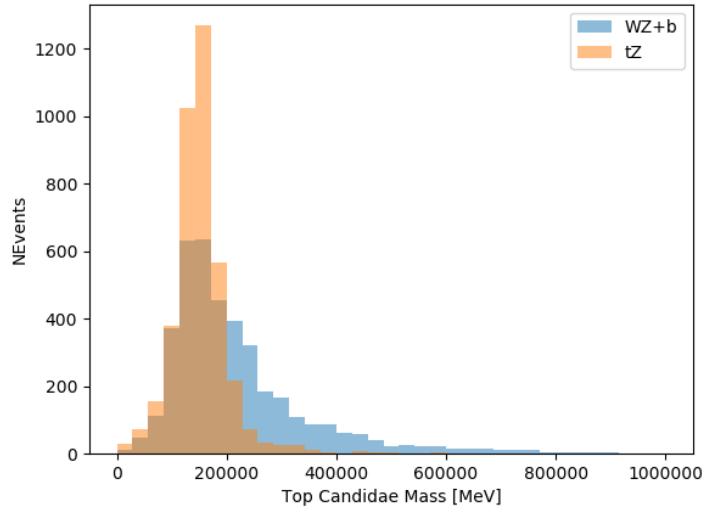


Figure 9.1: Reconstructed top mass distributions for tZ and WZ + b, measured in MeV.

716 9.2 tZ BDT

717 A Boosted Decision Tree (BDT), specifically XGBoost [25], is used to provide separation between
 718 tZ and WZ+b. The following kinematic variables are used as inputs:

719 • The invariant mass of the reconstructed top candidate

720 • p_T of each of the leptons, jet

721 • The invariant mass of each combination of lepton pairs, $M(l\bar{l})$

722 • E_T^{miss}

723 • Distance between each combination of leptons, $\Delta R(l\bar{l})$

- 724 • Distance between each lepton and the jet, $\Delta R(lj)$

725 The training samples included only events meeting the requirements of the 1-jet, >60%
726 region, i.e. passing all the selection described in section 12 and having exactly one jet which
727 passes the tightest (60%) DL1r working point.

728 The distributions of a few of these features for both signal and background is shown in
729 figure 13.2.

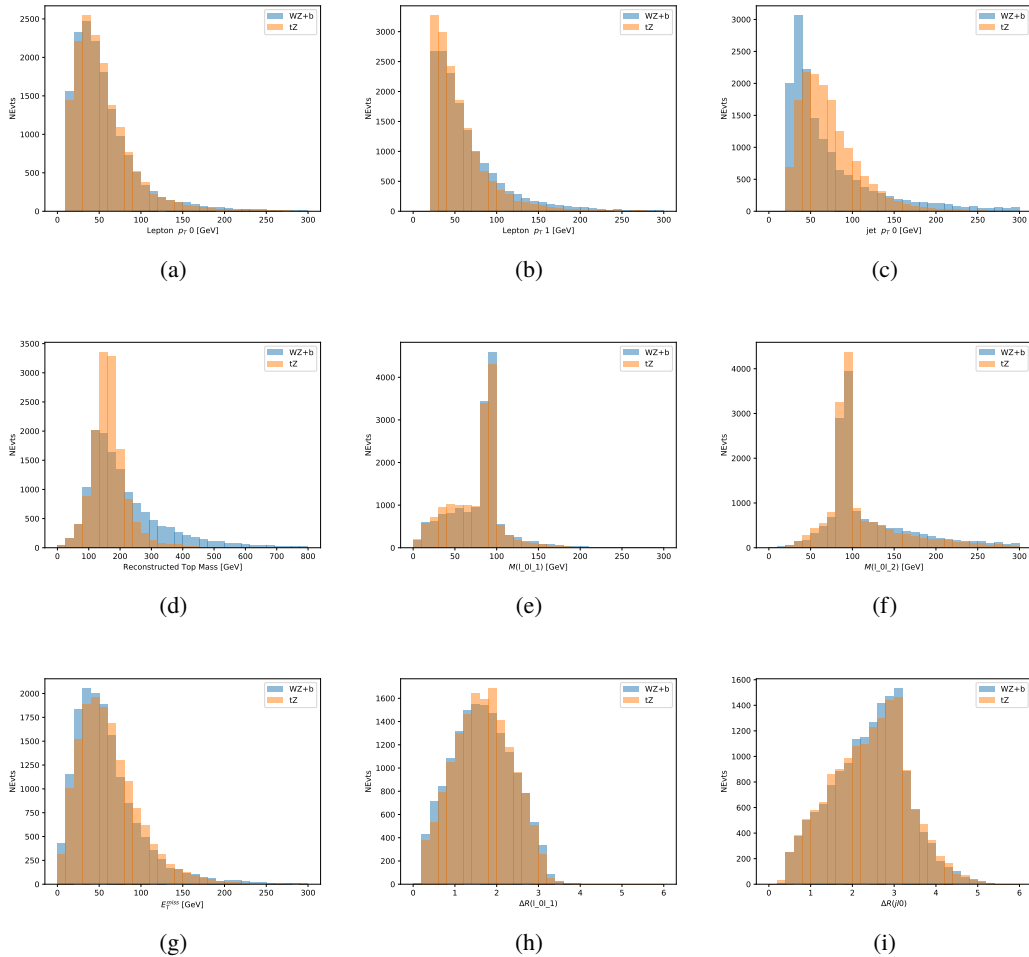


Figure 9.2: Distribution of input features of the BDT for signal (WZ) and background (tZ). Both are scaled to an equal number of events. (a), (b) and (c) show the p_T of lepton 0, lepton 1, and the jet, (d) show the reconstructed top mass, (e) and (f) show the invariant mass of leptons 0 and 1, leptons 0 and 2. (g) shows the E_T^{miss} of each event. (h) and (i) show the ΔR between lepton 0 and lepton 1, and the jet.

730 A sample of 20,000 background (tZ) and signal (WZ+b) Monte Carlo events are used to
 731 train the BDT. And additional 5,000 events are reserved for testing the model, in order to prevent
 732 over-fitting. A total of 750 decision trees with a maximum depth of 6 branches are used to build
 733 the model. These parameters are chosen empirically, by training several models with different

734 parameters and selecting the one that gave the best separation for the test sample.

735 The results of the BDT training are shown in figure 13.3. The output scores for both signal
 736 and background events is shown on the left. The right shows the receiving operating characteristic
 737 (ROC) curve that results from the MVA. The ROC curve represents the background rejection
 738 as a function of signal efficiency, where each point on the curve represents a different response
 739 score. The ROC curve of the BDT is compared to the performance of using an optimal set of flat
 740 selections on the same set of input variables.

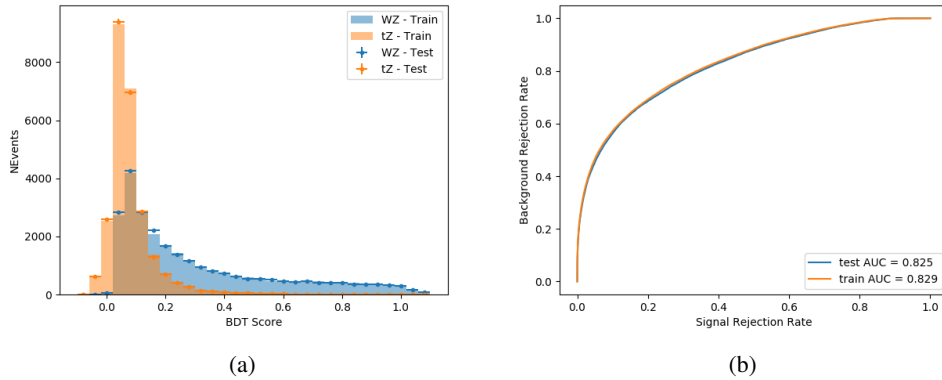


Figure 9.3: Distribution of the BDT response for signal and background events on the left, the ROC curve for the BDT on the right.

741 The relative important of each input feature in the model, measured by how often they
 742 appeared in the decision trees, is shown in figure 13.4.

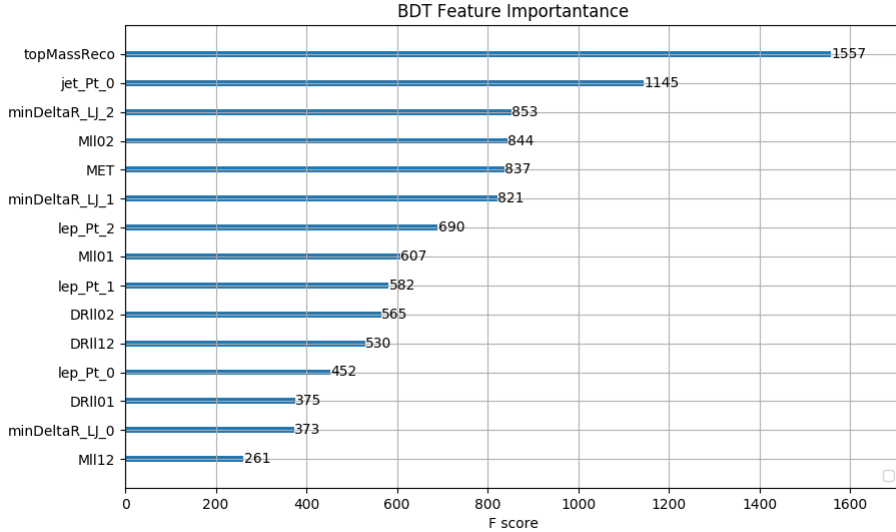


Figure 9.4: Relative importance of each input feature in the model.

743 These results suggest that some amount of separation can be achieved between these two
 744 processes, with a high BDT score selecting a set of events that is pure in $WZ + b$. A BDT score
 745 of 0.725 is selected as a cutoff, where events with scores higher than this form a signal enriched
 746 region, and events with scores lower than this form a $t\bar{Z}$ control region. This cutoff is selected by
 747 varying the value of this cutoff in stat-only Asimov fits, and selecting the value that minimizes
 748 the statistical uncertainty on $WZ + b$.

749 **10 Data and Monte Carlo Samples**

750 **10.1 Data Samples**

751 The study uses a sample of proton-proton collision data collected by the ATLAS detector from
752 2015 through 2018 at an energy of $\sqrt{s} = 13$ TeV, which represents an integrated luminosity of
753 139 fb^{-1} . This data set was collected with a bunch crossing rate of 25 ns. All data used in this
754 analysis was verified by data quality checks.

755 **10.2 Monte Carlo Samples**

756 Several different generators were used to produce Monte Carlo simulations of the signal and
757 background processes. For all samples, the response of the ATLAS detector is simulated using
758 Geant4. The WZ signal samples are simulated using Sherpa 2.2.2 [10]. Specific information
759 about the Monte Carlo samples being used can be found in Table 26.

Table 8: The configurations used for event generation of signal and background processes, including the event generator, matrix element (ME) order, parton shower algorithm, and parton distribution function (PDF).

| Process | Event generator | ME order | Parton Shower | PDF |
|---------------------------------|---------------------------|----------------------|------------------------|-----------------------------------|
| WZ, VV | SHERPA 2.2.2 | MEPS NLO | SHERPA | CT10 |
| tZ | MG5_AMC | NLO | PYTHIA 8 | CTEQ6L1 |
| t̄tW | MG5_AMC (SHERPA 2.1.1) | NLO (LO multileg) | PYTHIA 8 (SHERPA) | NNPDF 3.0 NLO (NNPDF 3.0 NLO) |
| t̄t(Z/γ* → ll) | MG5_AMC | NLO | PYTHIA 8 | NNPDF 3.0 NLO |
| t̄tH | MG5_AMC (MG5_AMC) | NLO (NLO) | PYTHIA 8 (HERWIG++) | NNPDF 3.0 NLO [11] (CT10 [12]) |
| tHqb | MG5_AMC | LO | PYTHIA 8 | CT10 |
| tHW | MG5_AMC (SHERPA 2.1.1) | NLO (LO multileg) | HERWIG++ (SHERPA) | CT10 (NNPDF 3.0 NLO) |
| tWZ | MG5_AMC | NLO | PYTHIA 8 | NNPDF 2.3 LO |
| t̄t̄t, t̄t̄t̄t̄ | MG5_AMC | LO | PYTHIA 8 | NNPDF 2.3 LO |
| t̄tW+W- | MG5_AMC | LO | PYTHIA 8 | NNPDF 2.3 LO |
| t̄t | POWHEG-BOX v2 [13] | NLO | PYTHIA 8 | NNPDF 3.0 NLO |
| t̄t̄γ | MG5_AMC | LO | PYTHIA 8 | NNPDF 2.3 LO |
| s-, t-channel, Wt single top | POWHEG-BOX v1 [14] | NLO | PYTHIA 6 | CT10 |
| qqVV, VVV | | | | |
| Z → l+l- | SHERPA 2.2.1 | MEPS NLO | SHERPA | NNPDF 3.0 NLO |

11 Object Reconstruction

- 761 All regions defined in this analysis share a common lepton, jet, and overall event preselection.
762 The selection applied to each physics object is detailed here; the event preselection, and the
763 selection used to define the various fit regions, is described in Section 12.

764 **11.1 Trigger**

765 Events are required to be selected by dilepton triggers, as summarized in Table 28.

| Dilepton triggers (2015) | |
|-------------------------------|----------------------------|
| $\mu\mu$ (asymm.) | HLT_mu18_mu8noL1 |
| ee (symm.) | HLT_2e12_lhloose_L12EM10VH |
| $e\mu, \mu e$ (\sim symm.) | HLT_e17_lhloose_mu14 |
| Dilepton triggers (2016) | |
| $\mu\mu$ (asymm.) | HLT_mu22_mu8noL1 |
| ee (symm.) | HLT_2e17_lhvloose_nod0 |
| $e\mu, \mu e$ (\sim symm.) | HLT_e17_lhloose_nod0_mu14 |
| Dilepton triggers (2017) | |
| $\mu\mu$ (asymm.) | HLT_mu22_mu8noL1 |
| ee (symm.) | HLT_2e24_lhvloose_nod0 |
| $e\mu, \mu e$ (\sim symm.) | HLT_e17_lhloose_nod0_mu14 |
| Dilepton triggers (2018) | |
| $\mu\mu$ (asymm.) | HLT_mu22_mu8noL1 |
| ee (symm.) | HLT_2e24_lhvloose_nod0 |
| $e\mu, \mu e$ (\sim symm.) | HLT_e17_lhloose_nod0_mu14 |

Table 9: List of lowest p_T -threshold, un-prescaled dilepton triggers used for 2015-2018 data taking.

766 **11.2 Light leptons**

767 Electron candidates are reconstructed from energy clusters in the electromagnetic calorimeter
 768 that are associated with charged particle tracks reconstructed in the inner detector [15]. Electron
 769 candidates are required to have $p_T > 10$ GeV and $|\eta_{\text{cluster}}| < 2.47$. Muon candidates are
 770 reconstructed by combining inner detector tracks with track segments or full tracks in the muon
 771 spectrometer [16]. Muon candidates are required to have $p_T > 10$ GeV and $|\eta| < 2.5$. Candidates

772 in the transition region between different electromagnetic calorimeter components, $1.37 <$
 773 $|\eta_{\text{cluster}}| < 1.52$, are rejected. A multivariate likelihood discriminant combining shower shape
 774 and track information is used to distinguish real electrons from hadronic showers (fake electrons).
 775 To further reduce the non-prompt electron contribution, the track is required to be consistent
 776 with originating from the primary vertex; requirements are imposed on the transverse impact
 777 parameter significance ($|d_0|/\sigma_{d_0} < 5$) and the longitudinal impact parameter ($|\Delta z_0 \sin \theta_\ell| < 0.5$
 778 mm). Electron candidates are required to pass TightLH identification.

779 Muon candidates are reconstructed by combining inner detector tracks with track segments
 780 or full tracks in the muon spectrometer [16]. Muon candidates are required to have $p_T > 10$ GeV
 781 and $|\eta| < 2.5$. The longitudinal impact parameter is the same for both electrons and muons, while
 782 muons are required to pass a slightly tighter transverse impact parameter, $|d_0|/\sigma_{d_0} < 3$. Muons
 783 are also required to pass Medium ID requirements.

784 Leptons are additionally required to pass a non-prompt BDT selection developed by the
 785 $t\bar{t}H$ multilepton/ $t\bar{t}W$ analysis group. This BDT and the WPs used are summarized in Appendix
 786 .1, and described in detail in [17]. Optimized working points and scale factors for this BDT are
 787 taken from that analysis.

788 11.3 Jets

789 Jets are reconstructed from calibrated topological clusters built from energy deposits in the
 790 calorimeters [18], using the anti- k_t algorithm with a radius parameter $R = 0.4$. Particle Flow, or

791 PFlow, jets are used in the analysis, which are hadronic objects reconstructed using information
792 from both the tracker and the calorimeter. Jets with energy contributions likely arising from noise
793 or detector effects are removed from consideration [19], and only jets satisfying $p_T > 25$ GeV
794 and $|\eta| < 2.5$ are used in this analysis. For jets with $p_T < 60$ GeV and $|\eta| < 2.4$, a jet-track
795 association algorithm is used to confirm that the jet originates from the selected primary vertex,
796 in order to reject jets arising from pileup collisions [20].

797 **11.4 B-tagged Jets**

798 In order to make a measurement of $WZ +$ heavy flavor it is necessary to distinguish these events
799 from $WZ +$ light jets. For this purpose, the DL1r b-tagging algorithm is used to distinguish
800 heavy flavor jets from lighter ones. The DL1r algorithm uses jet kinematics, particularly jet
801 vertex information, as input for a neural network which assigns each jet a score designed to
802 reflect how likely that jet is to have originated from a b-quark.

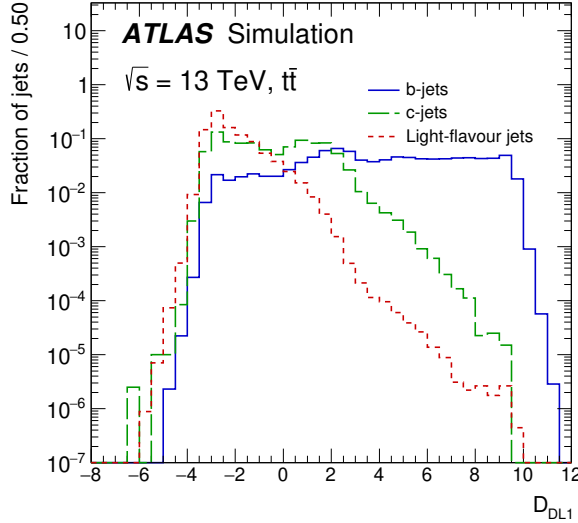


Figure 11.1: Output distribution of the DL1r algorithm for b-jets, charm jets, and light jets

803 From the output of the BDT, calibrated working points (WPs) are developed based on the
 804 efficiency of truth b-jets at particular values of the DL1r algorithm. The working points used in
 805 this analysis are summarized in Table 10.

| WP | none | loose | medium | tight | tightest |
|--------|------|-------|--------|-------|----------|
| b eff. | - | 85% | 77% | 70% | 60% |

Table 10: B-tagging Working Points by tightness and b-jet efficiency

806 A tighter WP will accept fewer b-jets, but reject a higher fraction of charm and light jets.
 807 Generally, analyses that include b-jets will use a fixed working point, for example, requiring that
 808 a jet pass the 70% threshold. By instead treating these working point as bins, e.g. events with
 809 jets that fall between the 85% and 77% WPs fall into one bin, while events with jets passing the
 810 60% WP fall into another, and looking at the full psuedo-continuous DL1r spectrum of the jets,

811 additional information can be gained. The psuedo-continuous b-tag spectrum is used in this case
812 to separate out WZ + b, WZ + charm, and WZ + light.

813 **11.5 Missing transverse energy**

814 Missing transverse momentum (E_T^{miss}) is used as part of the event selection. The missing
815 transverse momentum vector is defined as the inverse of the sum of the transverse momenta of
816 all reconstructed physics objects as well as remaining unclustered energy, the latter of which is
817 estimated from low- p_T tracks associated with the primary vertex but not assigned to a hard object,
818 with object definitions taken from [21]. Light leptons considered in the E_T^{miss} reconstruction are
819 required to have $p_T > 10 \text{ GeV}$, while jets are required to have $p_T > 20 \text{ GeV}$.

820 **11.6 Overlap removal**

821 To avoid double counting objects and remove leptons originating from decays of hadrons, overlap
822 removal is performed in the following order: any electron candidate within $\Delta R = 0.1$ of another
823 electron candidate with higher p_T is removed; any electron candidate within $\Delta R = 0.1$ of a muon
824 candidate is removed; any jet within $\Delta R = 0.3$ of an electron candidate is removed; if a muon
825 candidate and a jet lie within $\Delta R = \min(0.4, 0.04 + 10[\text{GeV}] / p_T(\text{muon}))$ of each other, the jet
826 is kept and the muon is removed.

827 This algorithm is applied to the preselected objects. The overlap removal procedure is
828 summarized in Table 29.

| Keep | Remove | Cone size (ΔR) |
|-------------|-----------------------|---|
| electron | electron (low p_T) | 0.1 |
| muon | electron | 0.1 |
| electron | jet | 0.3 |
| jet | muon | $\min(0.4, 0.04 + 10[\text{GeV}]/p_T(\text{muon}))$ |
| electron | tau | 0.2 |

Table 11: Summary of the overlap removal procedure between electrons, muons, and jets.

829 12 Event Selection and Signal Region Definitions

830 Event are required to pass a preselection described in Section 12.1 and summarized in Table 12.
 831 Those that pass this preselection are divided into various fit regions described in Section 12.2,
 832 based on the number of jets in the event, and the b-tag score of those jets.

833 12.1 Event Preselection

834 Events are required to include exactly three reconstructed light leptons passing the requirement
 835 described in 11.2, which have a total charge of ± 1 .

836 The leptons are ordered in the analysis code as 0, 1, and 2. Lepton 0 is the lepton whose
 837 charge is opposite the other two. Lepton 1 is the lepton closest to the opposite charge lepton, i.e.
 838 the smallest ΔR , leaving lepton 2 as the lepton further from the opposite charge lepton. Lepton
 839 0 is required to have $p_T > 10 \text{ GeV}$, while the same sign leptons, 1 and 2, are required to have
 840 $p_T > 20 \text{ GeV}$ to reduce the contribution of non-prompt leptons.

841 The invariant mass of at least one pair of opposite sign, same flavor leptons is required
 842 to fall within 10 GeV of the mass of the Z boson, 91.2 GeV. Events where one of the opposite
 843 sign pairs have an invariant mass less than 12 GeV are rejected in order to suppress low mass
 844 resonances.

845 An additional requirement is placed on the missing transverse energy, $E_T^{\text{miss}} > 20 \text{ GeV}$,
 846 and the transverse mass of the W candidate, $m(E_T^{\text{miss}} + l_{\text{other}}) > 30 \text{ GeV}$, where E_T^{miss} is the
 847 missing transverse energy, and l_{other} is the lepton not included in the Z-candidate.

848 Events are required to have one or two reconstructed jets passing the selection described
 849 in Section 11.3. Events with more than two jets are rejected in order to reduce the contribution
 850 of backgrounds such as $t\bar{t}Z$ and $t\bar{t}W$, which tend to have higher jet multiplicity.

Event Selection

Exactly three leptons with charge ± 1
 Two same-charge leptons with $p_T > 20 \text{ GeV}$
 One opposite charge lepton with $p_T > 10 \text{ GeV}$
 $m(l^+l^-)$ within 10 GeV of 91.2 GeV
 Transverse mass of W-candidate, $m_T(E_T^{\text{miss}} + l_{\text{ep other}}) > 30 \text{ GeV}$
 Missing transverse energy, $E_T^{\text{miss}} > 20 \text{ GeV}$
 One or two jets with $p_T > 25 \text{ GeV}$

Table 12: Summary of the selection applied to events for inclusion in the fit

851 The event yields in the preselection region for both data and Monte Carlo are summarized
 852 in Table 12.1, which shows good agreement between data and Monte Carlo, and demonstrates
 853 that this region consists primarily of WZ events. The WZ events are split into WZ + b, WZ
 854 + c, and WZ + 1 based on the truth flavor of the associated jet in the event. Specifically, this

855 determination is made based on the `HadronConeExclTruthLabelID` of the jet, as recommended
 856 by the b-tagging working group [22]. In this ordering b-jet supersedes charm, which supersedes
 857 light. That is, $WZ + l$ events contain no charm and no b jets at truth level, $WZ + c$ contain at
 858 least one truth charm and no b-jets, and $WZ + b$ contains at least one truth b-jet.

| Process | Events |
|-------------------|-----------------|
| $WZ + b$ | 167.6 ± 6.5 |
| $WZ + c$ | 1080 ± 40 |
| $WZ + l$ | 7220 ± 310 |
| Other VV | 850 ± 140 |
| $t\bar{t}W$ | 16.8 ± 2.3 |
| $t\bar{t}Z$ | 115 ± 17 |
| rare Top | 2.2 ± 0.1 |
| Single top | 0.10 ± 0.45 |
| Three top | 0.01 ± 0.01 |
| Four top | 0.02 ± 0.01 |
| $t\bar{t}WW$ | 0.23 ± 0.05 |
| $Z + \text{jets}$ | 600 ± 260 |
| $V + \gamma$ | 37 ± 54 |
| tZ | 190 ± 70 |
| tW | 5.5 ± 1.2 |
| WtZ | 25.8 ± 1.1 |
| VVV | 26.2 ± 0.9 |
| VH | 94 ± 7 |
| $t\bar{t}$ | 108.68 ± 8 |
| $t\bar{t}H$ | 4.3 ± 0.5 |
| Total | 10600 ± 530 |
| Data | 10574 |

Table 13: Event yields in the preselection region at 139.0 fb^{-1}

859 Here Other VV represents diboson processes other than WZ , and consists predominantly
 860 of $ZZ \rightarrow ll\bar{l}\bar{l}$ events where one of the leptons is not reconstructed.

861 Simulations are further validated by comparing the kinematic distributions of the Monte

862 Carlo with data, which are shown in Figure 12.1. Here, bins with 5% or more WZ+b are

863 blinded.

WZ Fit Region - Inclusive

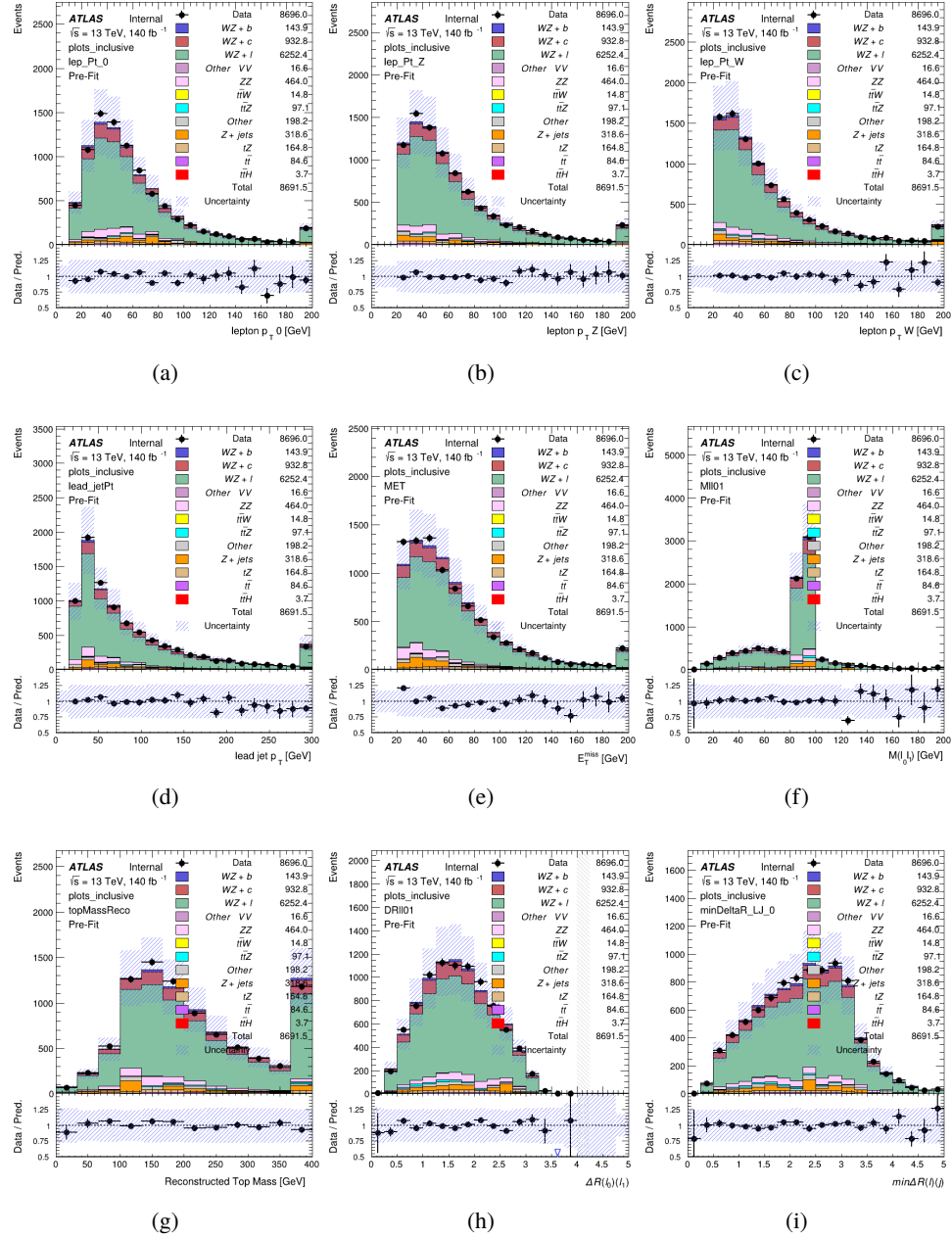


Figure 12.1: Comparisons between the data and MC distributions in the preselection region for (a) the p_T of the opposite sign lepton, (b) the p_T of the other lepton from the Z candidate, (c) the p_T of the lepton from the W candidate, (d) the leading jet p_T , (e) the E_T^{miss} , and (f) the invariant mass of leptons 0 and 1, (g) the reconstructed top mass, (h) $\Delta(R)$ between lepton 0 and 1, (i) the $\Delta(R)$ between the closest lepton and jet.

864 **12.2 Fit Regions**

865 Once preselection has been applied, the remaining events are categorized into one of twelve
 866 orthogonal regions. The regions used in the fit are summarized in Table 14.

Table 14: A list of the regions used in the fit and the selection used for each.

| Region | Selection |
|-------------|--|
| 1j, <85% | $N_{\text{jets}} = 1, n\text{Jets_DL1r_85} = 0$ |
| 1j, 85%-77% | $N_{\text{jets}} = 1, n\text{Jets_DL1r_85} = 1, n\text{Jets_DL1r_77} = 0$ |
| 1j, 77%-70% | $N_{\text{jets}} = 1, n\text{Jets_DL1r_77} = 1, n\text{Jets_DL1r_70} = 0$ |
| 1j, 70%-60% | $N_{\text{jets}} = 1, n\text{Jets_DL1r_70} = 1, n\text{Jets_DL1r_60} = 0$ |
| 1j, >60% | $N_{\text{jets}} = 1, n\text{Jets_DL1r_60} = 1, tZ \text{ BDT} > 0.725$ |
| 1j tZ CR | $N_{\text{jets}} = 1, n\text{Jets_DL1r_60} = 1, tZ \text{ BDT} < 0.725$ |
| 2j, <85% | $N_{\text{jets}} = 2, n\text{Jets_DL1r_85} = 0$ |
| 2j, 85%-77% | $N_{\text{jets}} = 2, n\text{Jets_DL1r_85} \geq 1, n\text{Jets_DL1r_77} = 0$ |
| 2j, 77%-70% | $N_{\text{jets}} = 2, n\text{Jets_DL1r_77} \geq 1, n\text{Jets_DL1r_70} = 0$ |
| 2j, 70%-60% | $N_{\text{jets}} = 2, n\text{Jets_DL1r_70} \geq 1, n\text{Jets_DL1r_60} = 0$ |
| 2j, >60% | $N_{\text{jets}} = 2, n\text{Jets_DL1r_60} \geq 1, tZ \text{ BDT} > 0.725$ |
| 2j tZ CR | $N_{\text{jets}} = 2, n\text{Jets_DL1r_60} \geq 1, tZ \text{ BDT} < 0.725$ |

867 The working points discussed in Section 11.4 are used to separate events into fit regions
 868 based on the highest working point reached by a jet in each event. Because the background
 869 composition differs significantly based on the number of b-jets, events are further subdivided
 870 into 1-jet and 2-jet regions in order to minimize the impact of background uncertainties.

871 An unfolding procedure is performed to account for differences in the number of recon-
 872 structed jets compared to the number of truth jets in each event. The `AntiKt4TruthDressedWZJets`
 873 truth jet collection is used to make this determination. In order to account for migration of WZ+1-
 874 jet and WZ+2-jet events between the 1-jet and 2-jet bins at reco level, the signal samples are
 875 separated based on the number of truth jets. Events with 0 jets or more than 3 jets at truth level,

yet fall within one of the categories listed in Table 14, are categorized as WZ + other, and treated as a background. The migration matrix in the number of jets at truth level versus reco level is shown in Figure 12.2. The composition of the number of truth jets in each reco jet bin is taken from MC, with uncertainties in these estimates described in detail in Section 21.

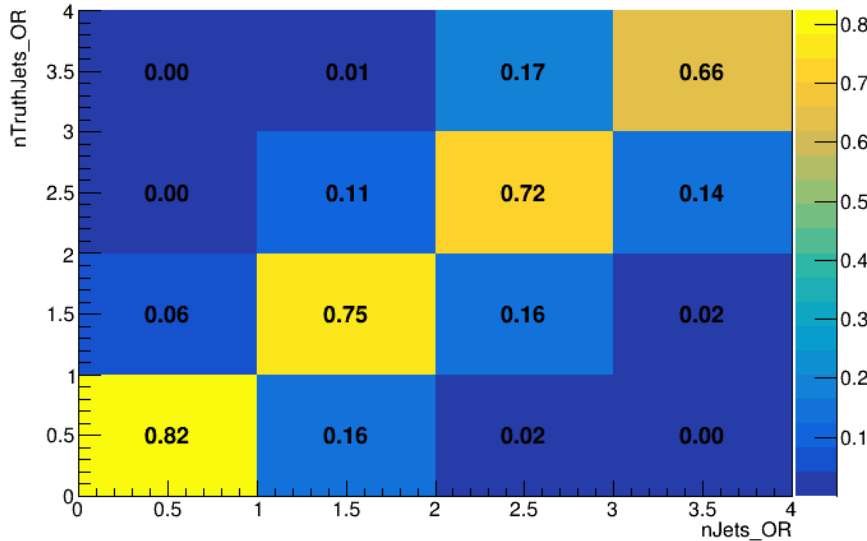


Figure 12.2: Number of truth jets compared to the number of reconstructed jets in each WZ event falling in the preselection region. Each row is normalized to unity.

An additional tZ control region is created based on the BDT described in Section 13. The region with 1-jet passing the 60% working point is split in two - a signal enriched region of events with a BDT score greater than 0.03, and a tZ control region including events with less than 0.03. This cutoff is arrived at by performing an Asimov fit with a variety of cutoffs, and selecting the value that produces the highest significance for the measurement of WZ + b.

The modeling in each region is validated by comparing data and MC predictions for

886 various kinematic distributions. These plot are shown in Figures 12.3-12.16.

WZ Fit Region - 1j Inclusive

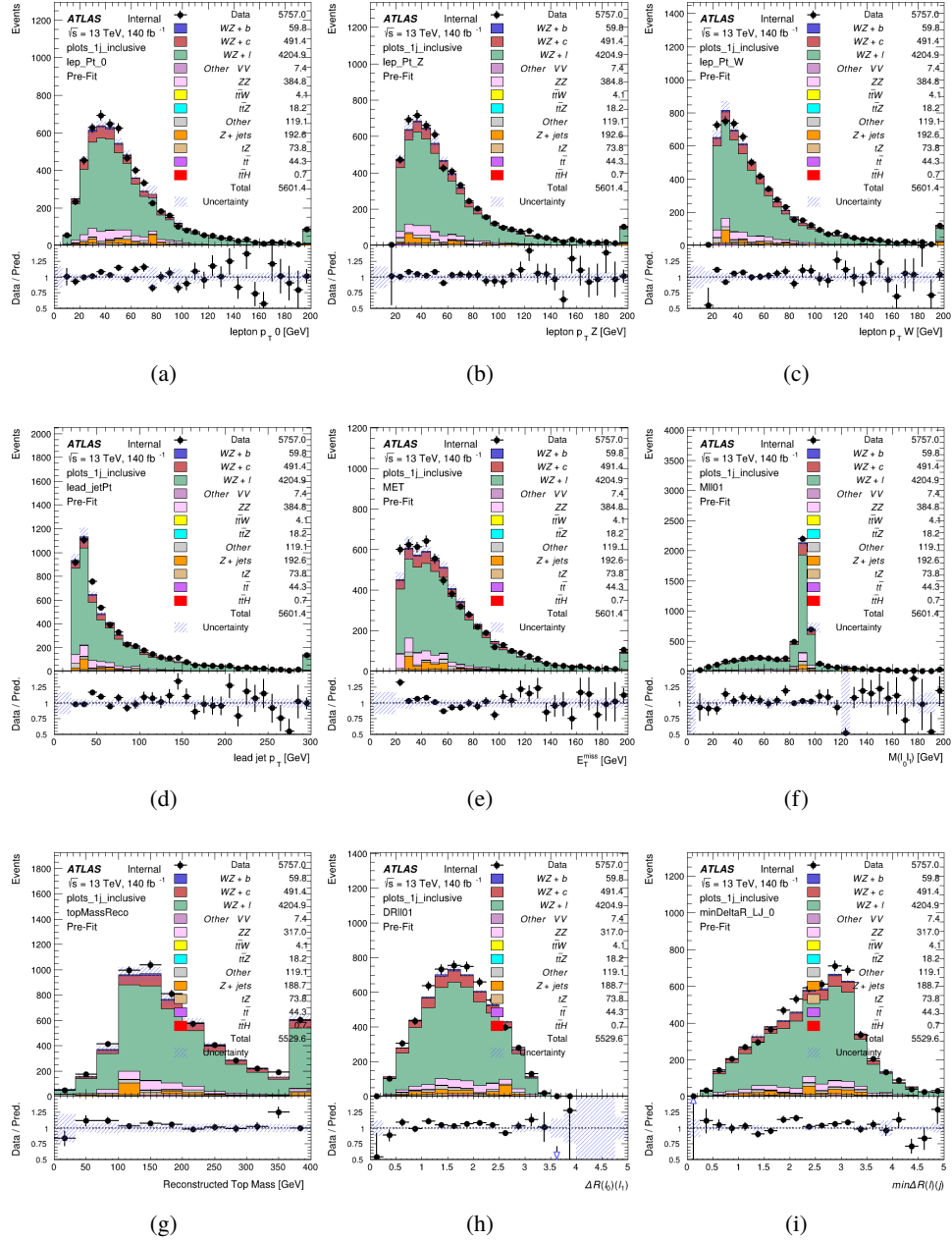


Figure 12.3: Comparisons between the data and MC distributions in the preselection region for (a) the p_T of the opposite sign lepton, (b) the p_T of the other lepton from the Z candidate, (c) the p_T of the lepton from the W candidate, (d) the leading jet p_T , (e) the E_T^{miss} , and (f) the invariant mass of leptons 0 and 1, (g) the reconstructed top mass, (h) $\Delta(R)$ between lepton 0 and 1, (i) the $\Delta(R)$ between the closest lepton and jet.

WZ Fit Region - 1j < 85% WP

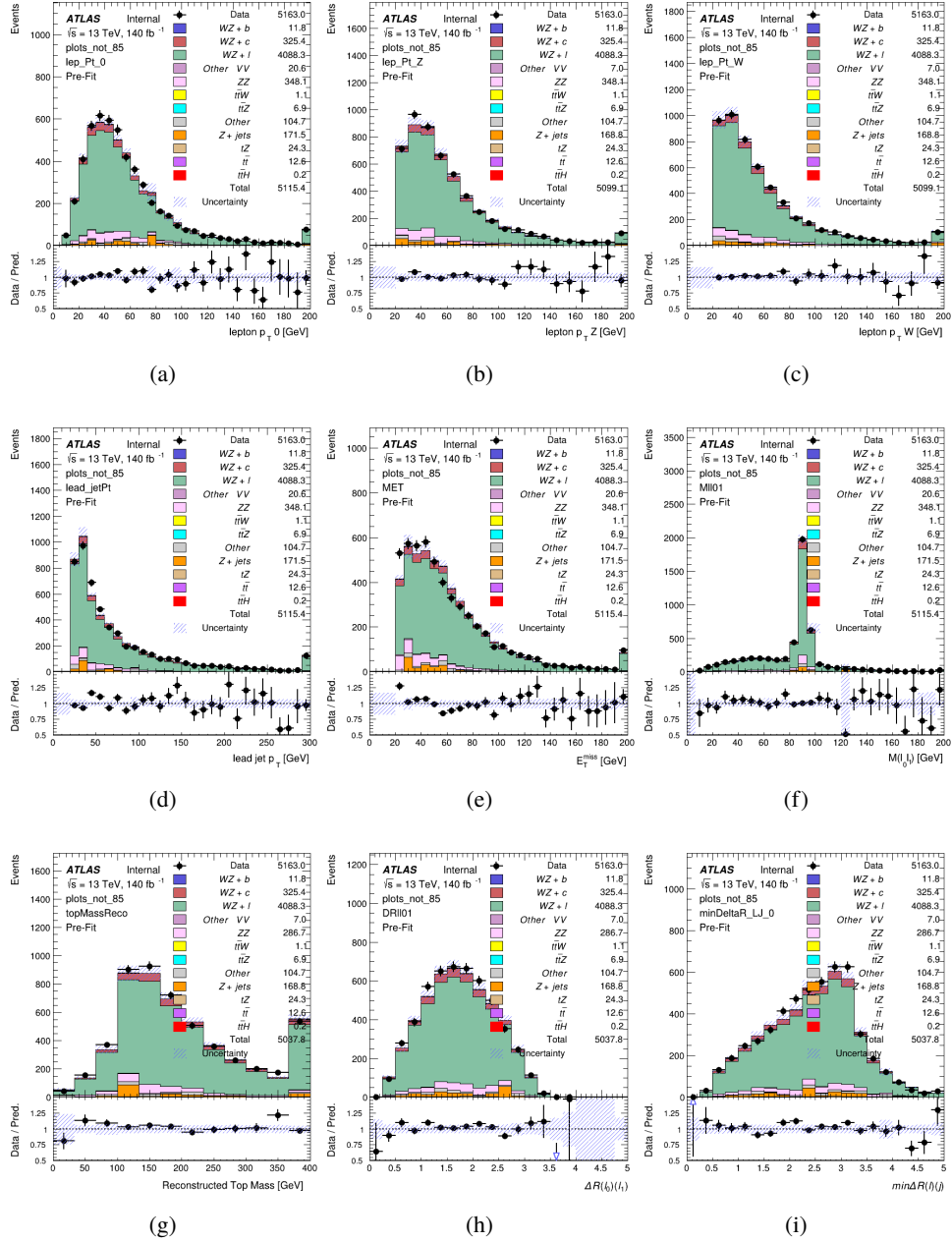


Figure 12.4: Comparisons between the data and MC distributions in the preselection region for (a) the p_T of the opposite sign lepton, (b) the p_T of the other lepton from the Z candidate, (c) the p_T of the lepton from the W candidate, (d) the leading jet p_T , (e) the E_T^{miss} , and (f) the invariant mass of leptons 0 and 1, (g) the reconstructed top mass, (h) $\Delta(R)$ between lepton 0 and 1, (i) the $\Delta(R)$ between the closest lepton and jet.

WZ Fit Region - 1j 77-85% WP

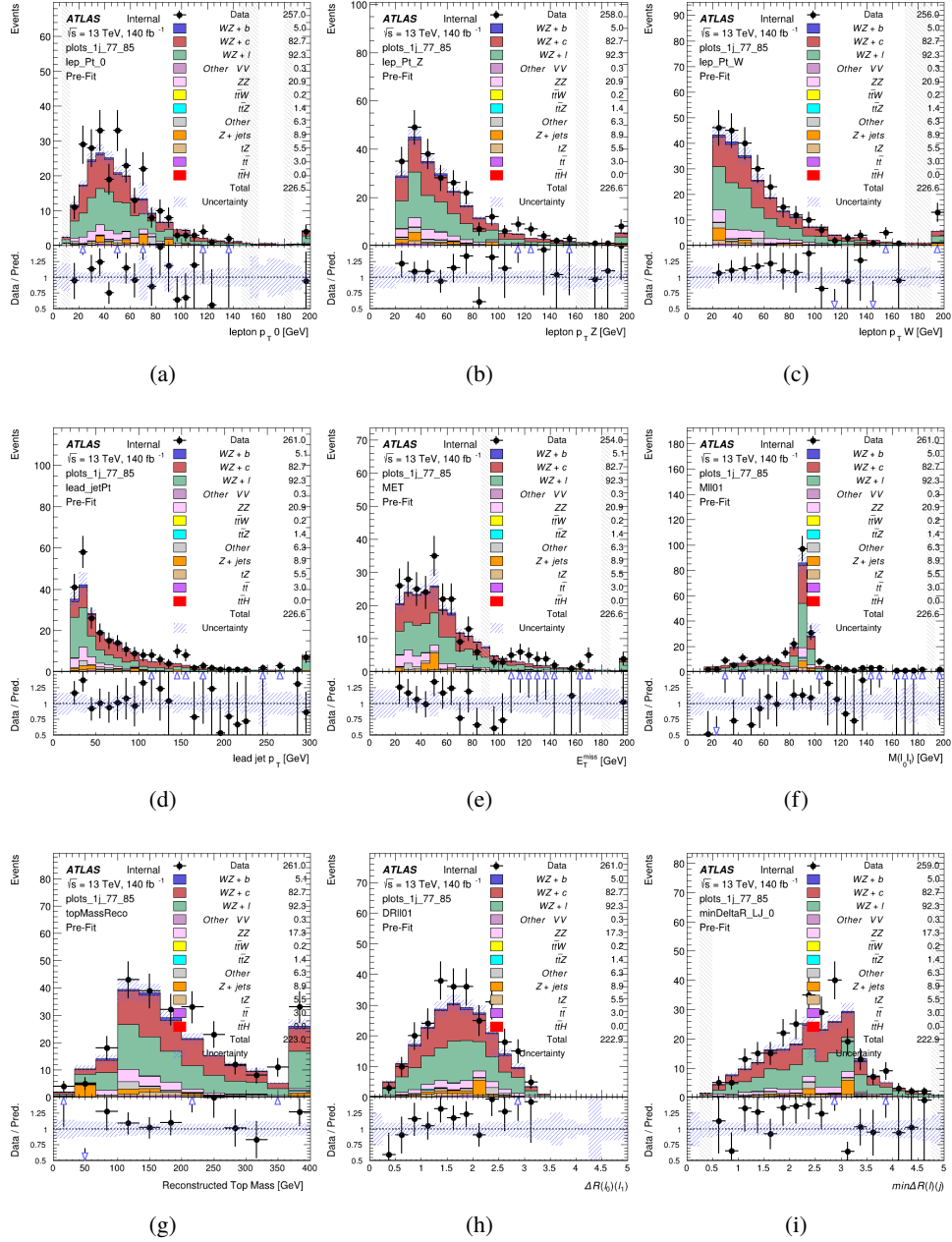


Figure 12.5: Comparisons between the data and MC distributions in the preselection region for (a) the p_T of the opposite sign lepton, (b) the p_T of the other lepton from the Z candidate, (c) the p_T of the lepton from the W candidate, (d) the leading jet p_T , (e) the E_T^{miss} , and (f) the invariant mass of leptons 0 and 1, (g) the reconstructed top mass, (h) $\Delta(R)$ between lepton 0 and 1, (i) the $\Delta(R)$ between the closest lepton and jet.

WZ Fit Region - 1j 70-77% WP

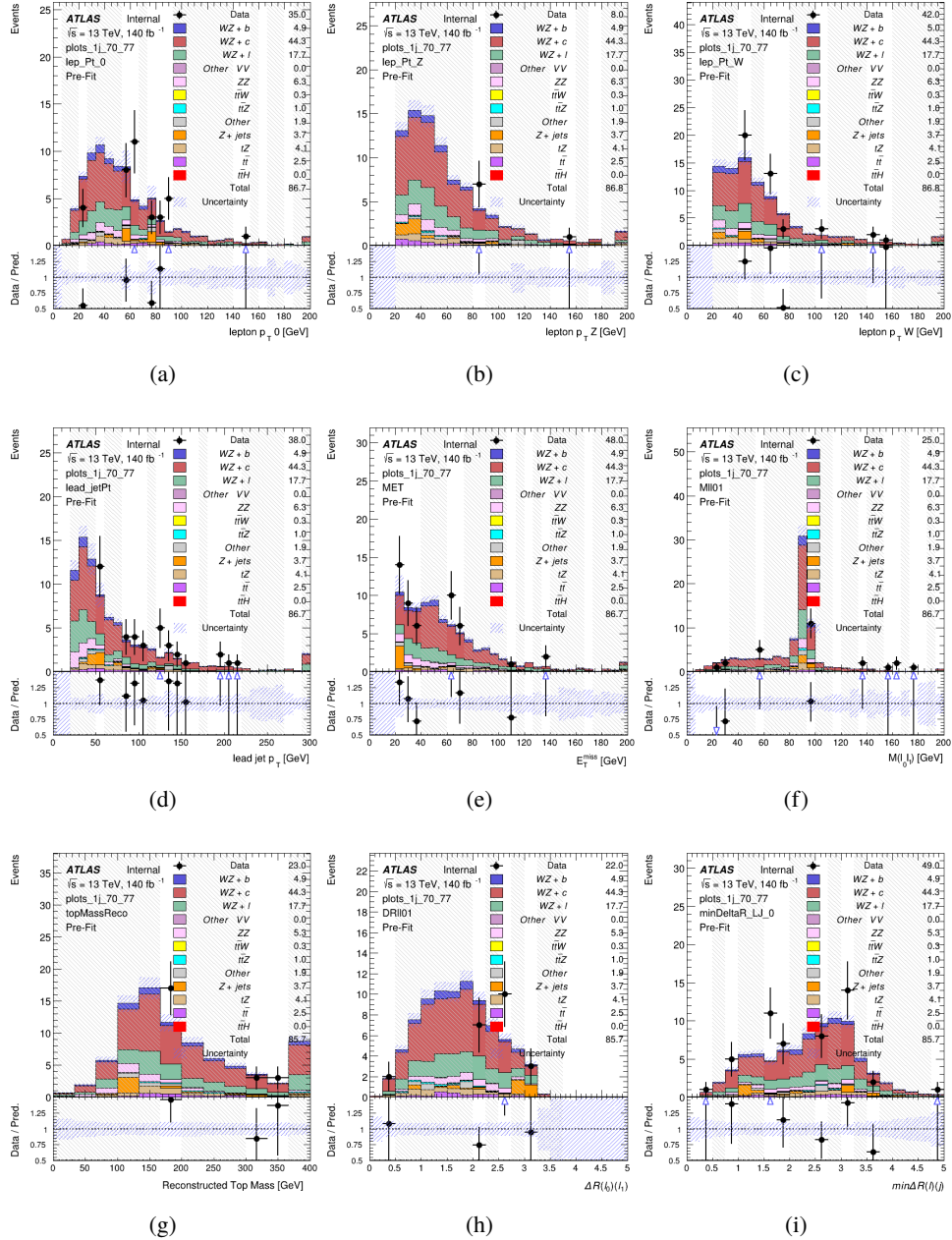


Figure 12.6: Comparisons between the data and MC distributions in the preselection region for (a) the p_T of the opposite sign lepton, (b) the p_T of the other lepton from the Z candidate, (c) the p_T of the lepton from the W candidate, (d) the leading jet p_T , (e) the E_T^{miss} , and (f) the invariant mass of leptons 0 and 1, (g) the reconstructed top mass, (h) $\Delta(R)$ between lepton 0 and 1, (i) the $\Delta(R)$ between the closest lepton and jet.

WZ Fit Region - 1j 60-70% WP

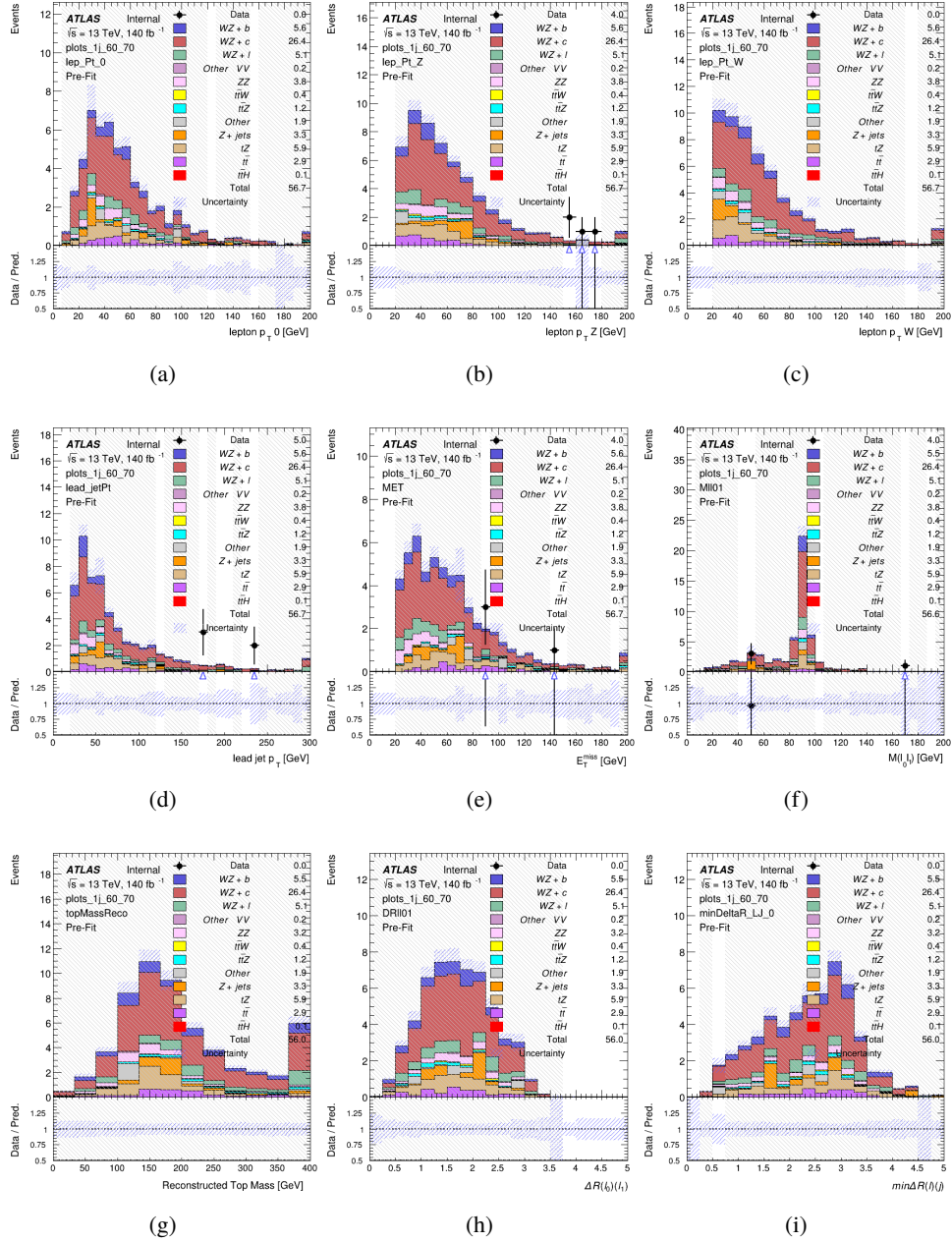


Figure 12.7: Comparisons between the data and MC distributions in the preselection region for (a) the p_T of the opposite sign lepton, (b) the p_T of the other lepton from the Z candidate, (c) the p_T of the lepton from the W candidate, (d) the leading jet p_T , (e) the E_T^{miss} , and (f) the invariant mass of leptons 0 and 1, (g) the reconstructed top mass, (h) $\Delta(R)$ between lepton 0 and 1, (i) the $\Delta(R)$ between the closest lepton and jet.

WZ Fit Region - 1j 60% WP

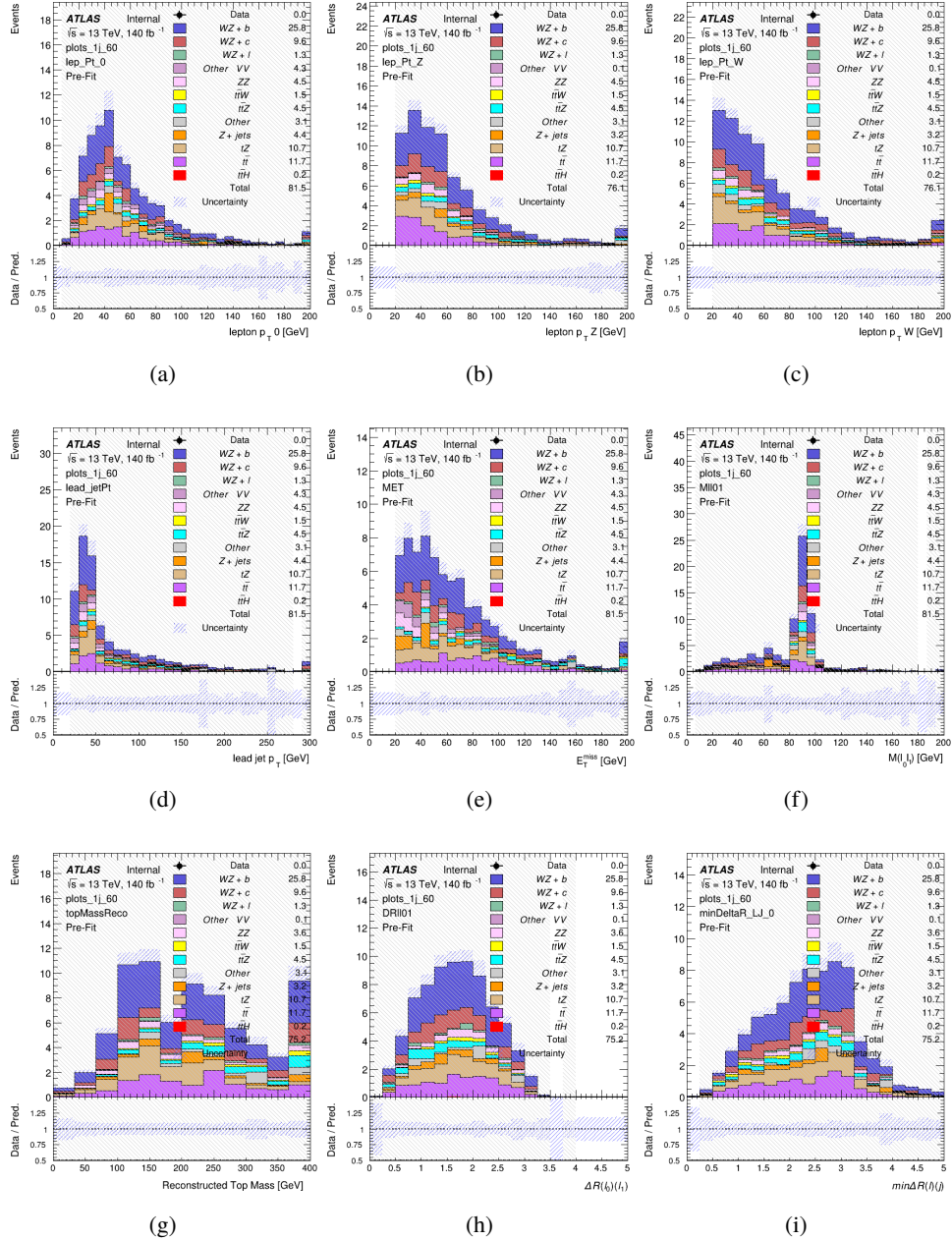


Figure 12.8: Comparisons between the data and MC distributions in the preselection region for (a) the p_T of the opposite sign lepton, (b) the p_T of the other lepton from the Z candidate, (c) the p_T of the lepton from the W candidate, (d) the leading jet p_T , (e) the E_T^{miss} , and (f) the invariant mass of leptons 0 and 1, (g) the reconstructed top mass, (h) $\Delta(R)$ between lepton 0 and 1, (i) the $\Delta(R)$ between the closest lepton and jet.

WZ Fit Region - tZ-CR

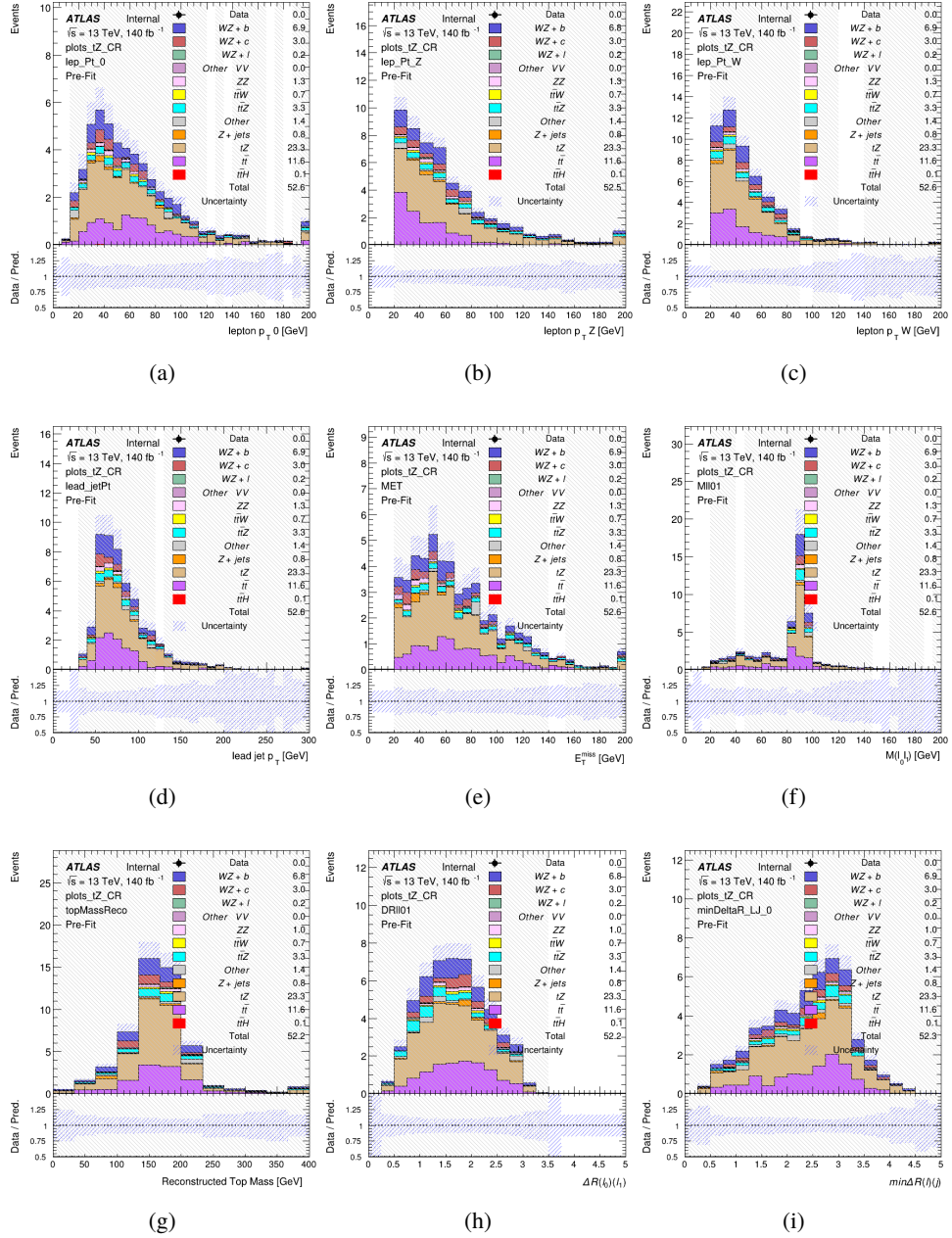


Figure 12.9: Comparisons between the data and MC distributions in the preselection region for (a) the p_T of the opposite sign lepton, (b) the p_T of the other lepton from the Z candidate, (c) the p_T of the lepton from the W candidate, (d) the leading jet p_T , (e) the E_T^{miss} , and (f) the invariant mass of leptons 0 and 1, (g) the reconstructed top mass, (h) $\Delta(R)$ between lepton 0 and 1, (i) the $\Delta(R)$ between the closest lepton and jet.

WZ Fit Region - 2j Inclusive

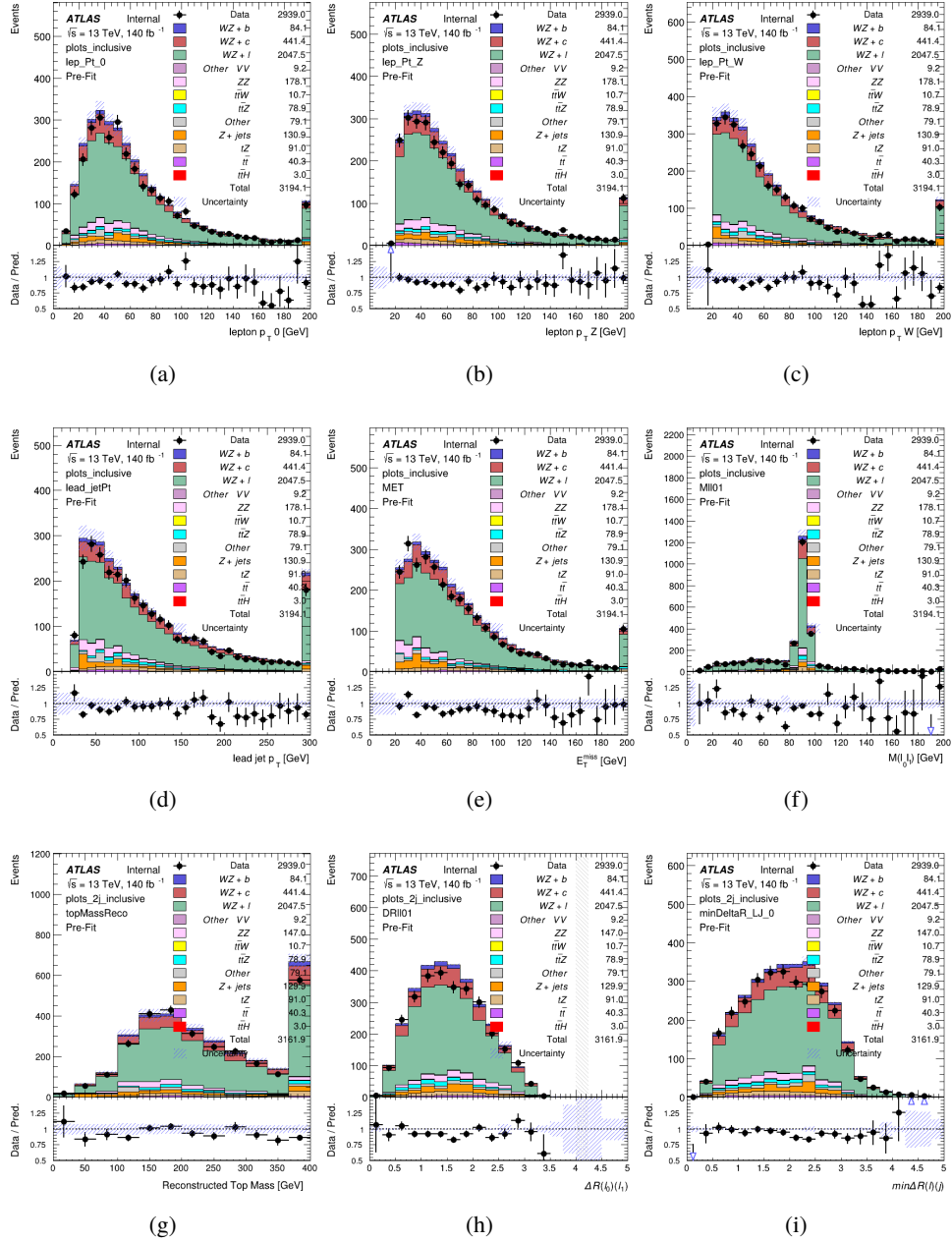


Figure 12.10: Comparisons between the data and MC distributions in the preselection region for (a) the p_T of the opposite sign lepton, (b) the p_T of the other lepton from the Z candidate, (c) the p_T of the lepton from the W candidate, (d) the leading jet p_T , (e) the E_T^{miss} , and (f) the invariant mass of leptons 0 and 1, (g) the reconstructed top mass, (h) $\Delta(R)$ between lepton 0 and 1, (i) the $\Delta(R)$ between the closest lepton and jet.

WZ Fit Region - 2j < 85% WP

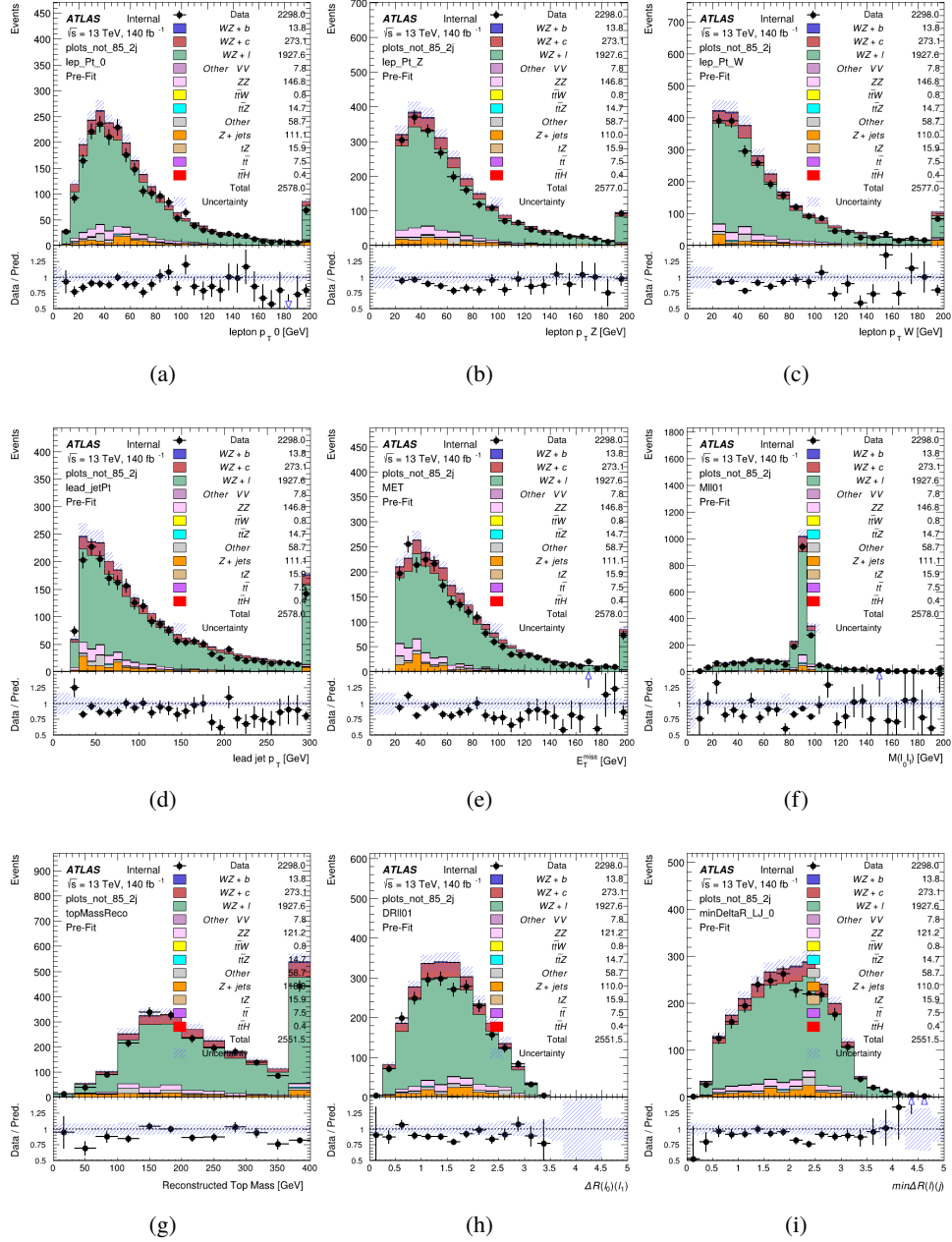


Figure 12.11: Comparisons between the data and MC distributions in the preselection region for (a) the p_T of the opposite sign lepton, (b) the p_T of the other lepton from the Z candidate, (c) the p_T of the lepton from the W candidate, (d) the leading jet p_T , (e) the E_T^{miss} , and (f) the invariant mass of leptons 0 and 1, (g) the reconstructed top mass, (h) $\Delta(R)$ between lepton 0 and 1, (i) the $\Delta(R)$ between the closest lepton and jet.

WZ Fit Region - 2j 77-85% WP

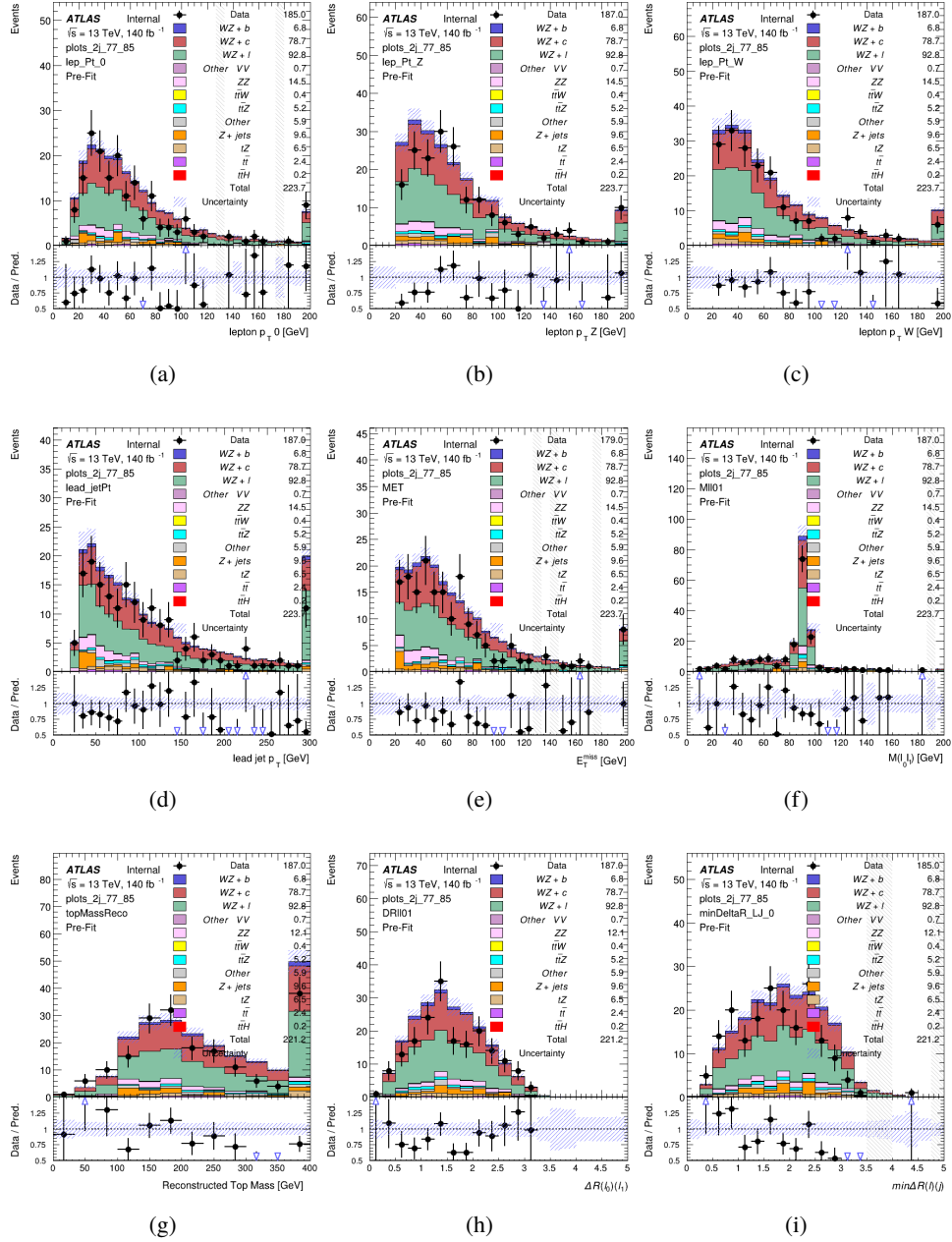


Figure 12.12: Comparisons between the data and MC distributions in the preselection region for (a) the p_T of the opposite sign lepton, (b) the p_T of the other lepton from the Z candidate, (c) the p_T of the lepton from the W candidate, (d) the leading jet p_T , (e) the E_T^{miss} , and (f) the invariant mass of leptons 0 and 1, (g) the reconstructed top mass, (h) $\Delta(R)$ between lepton 0 and 1, (i) the $\Delta(R)$ between the closest lepton and jet.

WZ Fit Region - 2j 70-77% WP

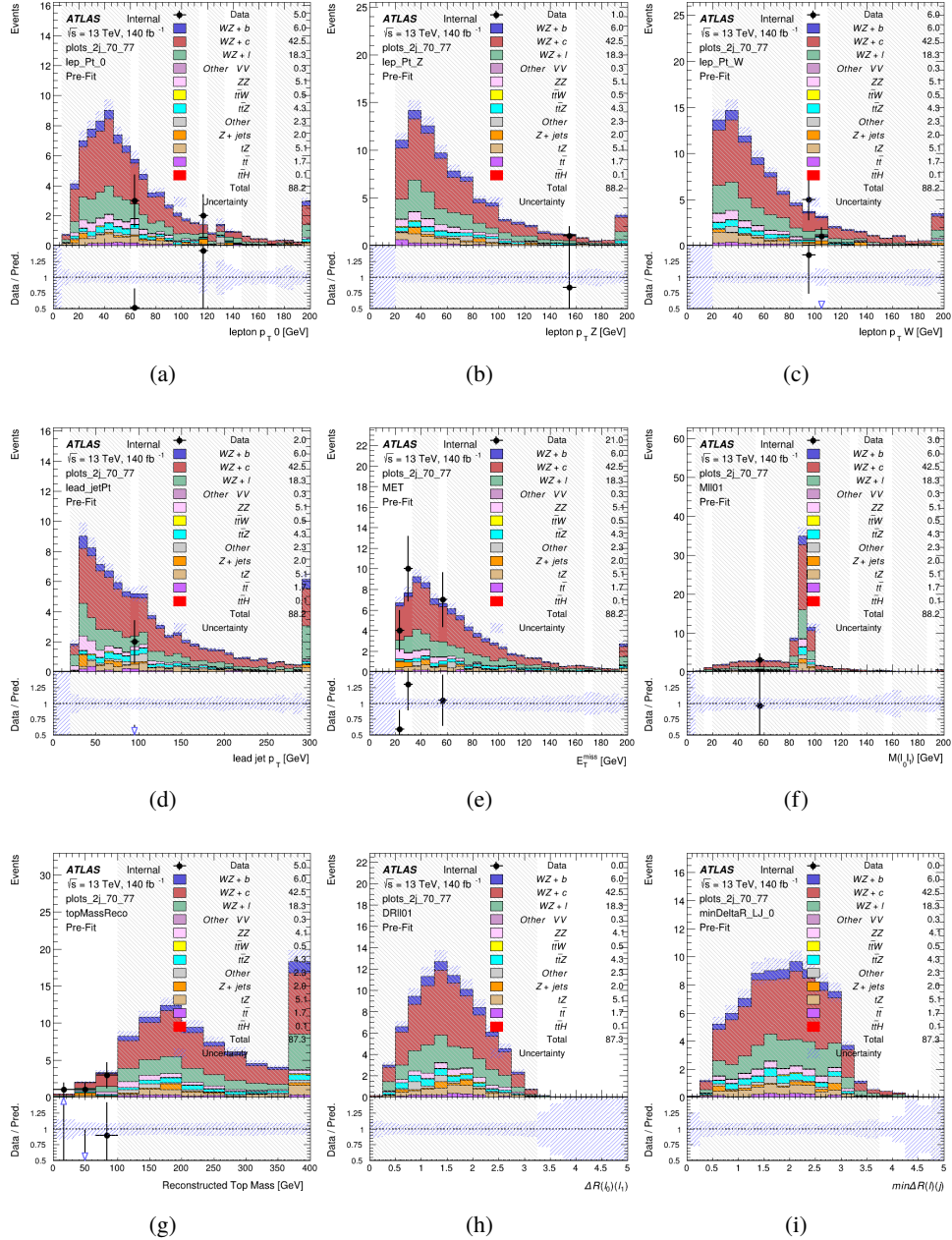


Figure 12.13: Comparisons between the data and MC distributions in the preselection region for (a) the p_T of the opposite sign lepton, (b) the p_T of the other lepton from the Z candidate, (c) the p_T of the lepton from the W candidate, (d) the leading jet p_T , (e) the E_T^{miss} , and (f) the invariant mass of leptons 0 and 1, (g) the reconstructed top mass, (h) $\Delta(R)$ between lepton 0 and 1, (i) the $\Delta(R)$ between the closest lepton and jet.

WZ Fit Region - 2j 60-70% WP

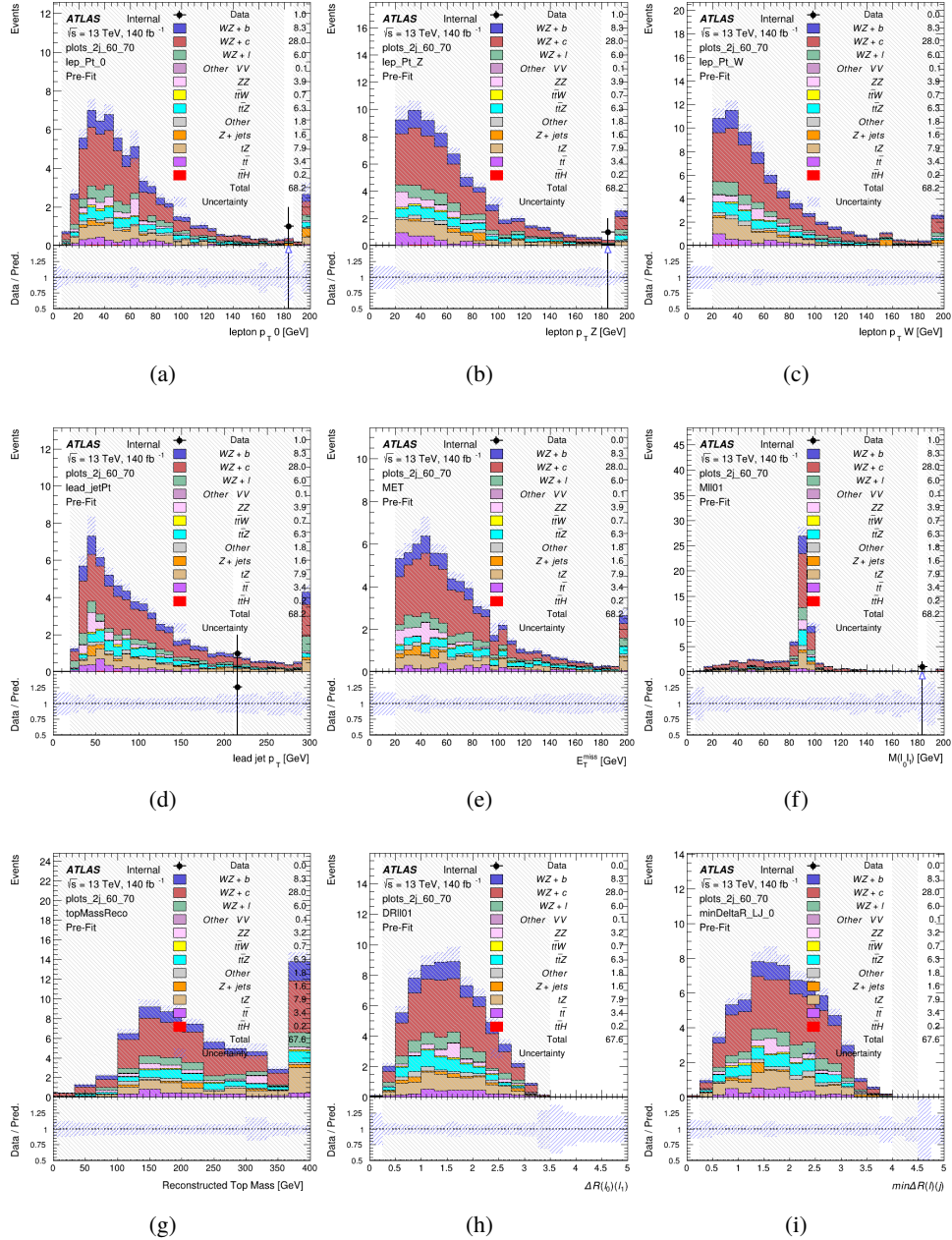


Figure 12.14: Comparisons between the data and MC distributions in the preselection region for (a) the p_T of the opposite sign lepton, (b) the p_T of the other lepton from the Z candidate, (c) the p_T of the lepton from the W candidate, (d) the leading jet p_T , (e) the E_T^{miss} , and (f) the invariant mass of leptons 0 and 1, (g) the reconstructed top mass, (h) $\Delta(R)$ between lepton 0 and 1, (i) the $\Delta(R)$ between the closest lepton and jet.

WZ Fit Region - 2j 60% WP

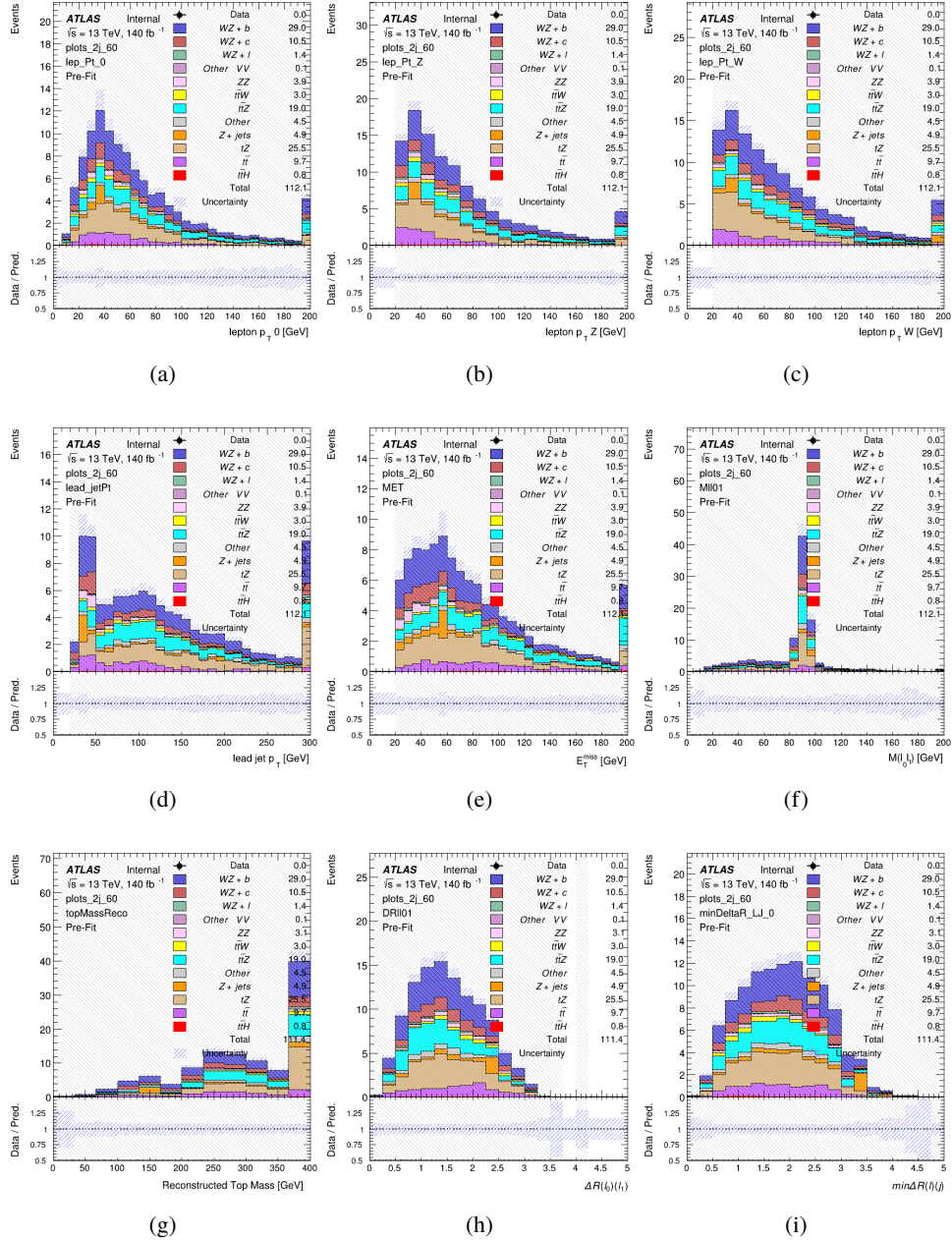


Figure 12.15: Comparisons between the data and MC distributions in the preselection region for (a) the p_T of the opposite sign lepton, (b) the p_T of the other lepton from the Z candidate, (c) the p_T of the lepton from the W candidate, (d) the leading jet p_T , (e) the E_T^{miss} , and (f) the invariant mass of leptons 0 and 1, (g) the reconstructed top mass, (h) $\Delta(R)$ between lepton 0 and 1, (i) the $\Delta(R)$ between the closest lepton and jet.

WZ Fit Region - tZ-CR-2j

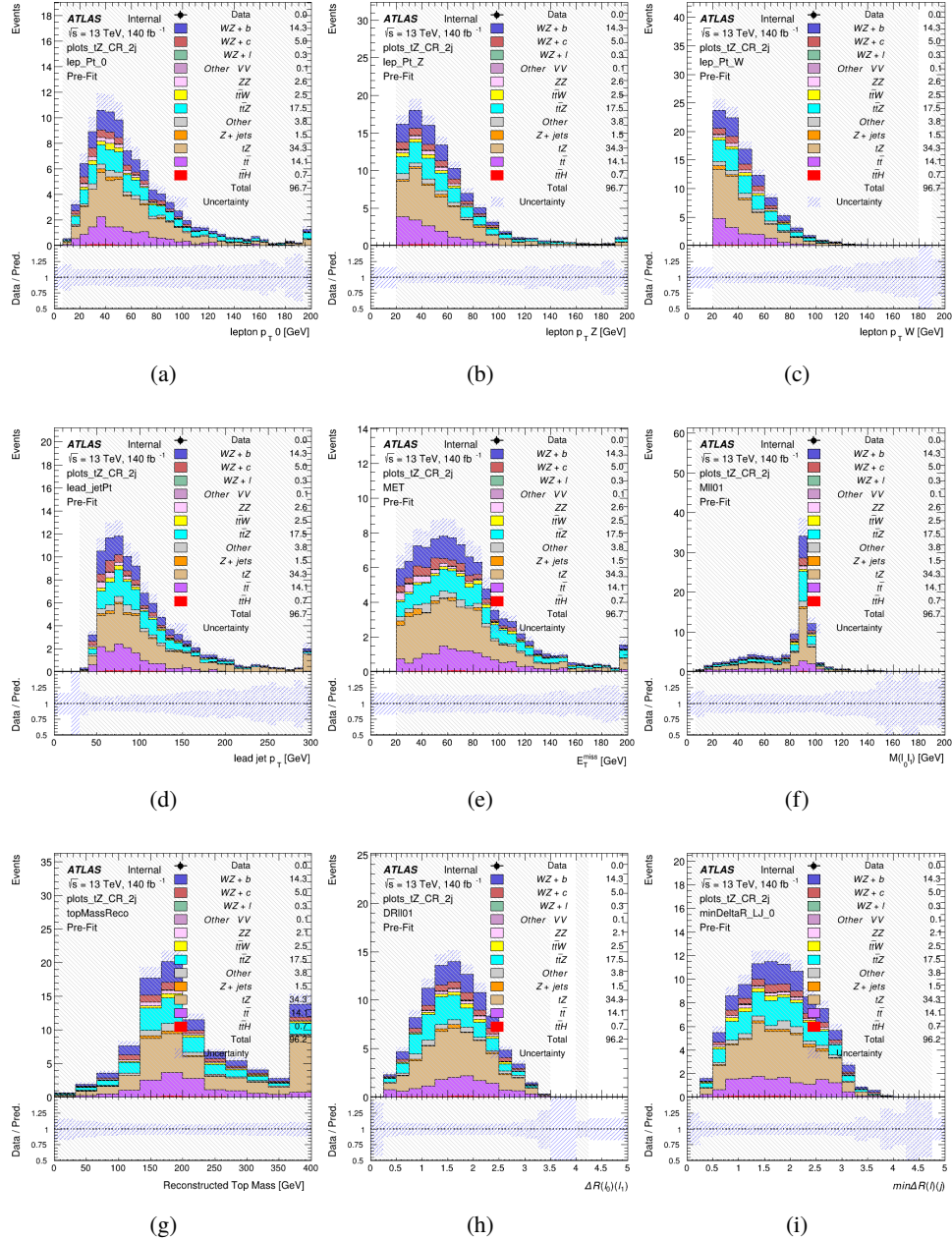


Figure 12.16: Comparisons between the data and MC distributions in the preselection region for (a) the p_T of the opposite sign lepton, (b) the p_T of the other lepton from the Z candidate, (c) the p_T of the lepton from the W candidate, (d) the leading jet p_T , (e) the E_T^{miss} , and (f) the invariant mass of leptons 0 and 1, (g) the reconstructed top mass, (h) $\Delta(R)$ between lepton 0 and 1, (i) the $\Delta(R)$ between the closest lepton and jet.

887 12.3 Non-Prompt Lepton Estimation

888 Two processes act as sources of non-prompt leptons appear in the analysis: $t\bar{t}$ and $Z+jet$
 889 production both produce two prompt leptons, and each contribute to the 31 region when an
 890 additional non-prompt lepton appears in the event. The contribution of these processes is
 891 estimated with Monte Carlo simulations, which are validated using enriched control regions.

892 The modelling in the $Z+jets$ and $t\bar{t}$ CRs is further validated for each of the pseudo-
 893 continuous b-tag regions used in the analysis. The relevant lepton p_T spectrum in each b-tag
 894 region is shown in Appendix .2 for these CRs after the correction factors derived below have
 895 been applied.

896 12.3.1 $t\bar{t}$ Validation

897 $t\bar{t}$ events can produce two prompt leptons from the decay of each of the tops. These top decays
 898 produce two b-quarks, the decay of which can produce additional non-prompt leptons, which
 899 occasionally pass the event preselection. In order to validate that the Monte Carlo accurately
 900 simulates this process accurately, the MC prediction in a non-prompt $t\bar{t}$ enriched control region
 901 is compared to data.

902 The $t\bar{t}$ control region is similar to the preselection region - three leptons meeting the
 903 criteria described in Section 12 are required, and the requirements on E_T^{miss} remain the same.
 904 However, the selection requiring a lepton pair form a Z-candidate are reversed. Events where the

905 invariant mass of any two opposite sign, same flavor leptons falls within 10 GeV of 91.2 GeV are
906 rejected. This ensures the $t\bar{t}$ control region is orthogonal to the preselection region.

907 Further, because the jet multiplicity of $t\bar{t}$ events tends to be higher than WZ, the number
908 of jets in each event is required to be greater than 1. As b-jets are almost invariably produced
909 from top decays, at least one b-tagged jet passing the 70% DL1r WP in each event is required.

910 Various kinematic plots of this region are shown in Figure 12.17.

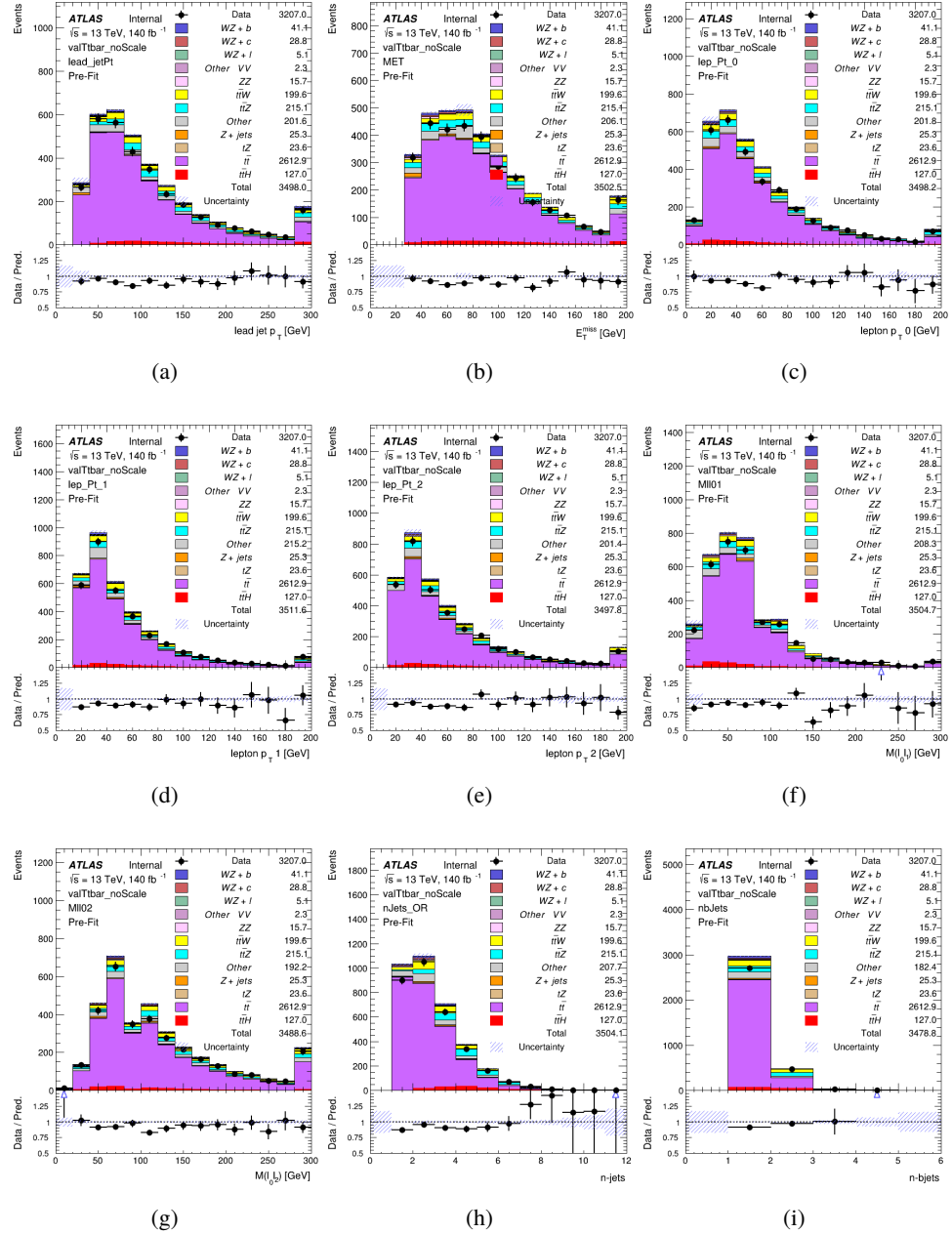


Figure 12.17: Comparisons between the data and MC distributions in the $t\bar{t}$ control region for (a) the p_T of the leading jet, (b) the missing transverse energy, (c) the p_T of lepton 0, (d) p_T of lepton 1, (e) p_T of lepton 2, (f) the invariant mass of leptons 0 and 1, (g) the invariant mass of leptons 0 and 2, (h) the number of jets, (i) the number of b-tagged jets.

911 The shape of each distribution agrees quite well between data and MC, with a constant
912 offset between the two. This is accounted for by applying a constant correction factor of 0.883
913 to the $t\bar{t}$ MC prediction. Plots showing the kinematics of the $t\bar{t}$ VR after this correction factor
914 has been applied are shown in Figure 12.18.

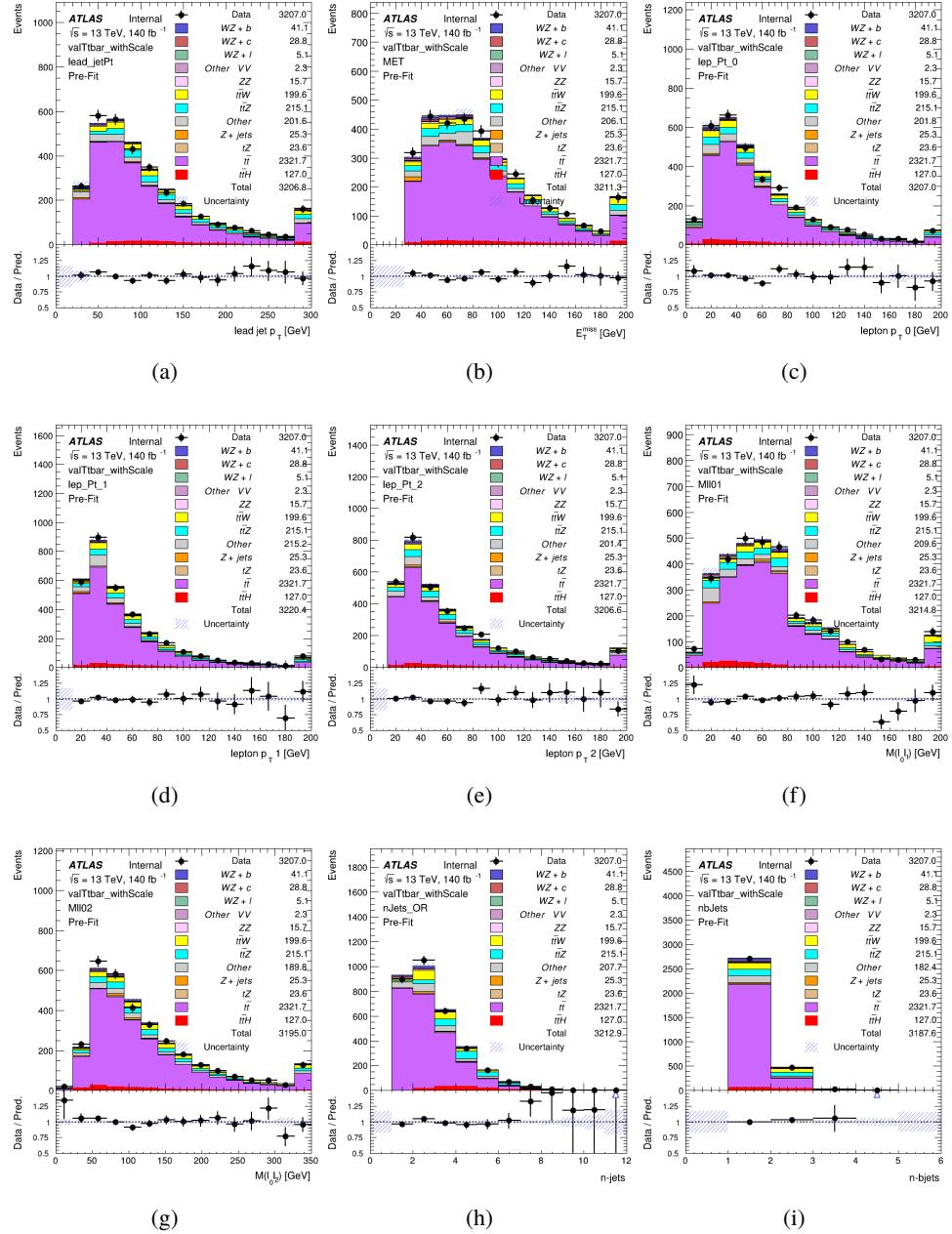


Figure 12.18: Comparisons between the data and MC distributions in the $t\bar{t}$ control region after the correction factor has been applied for (a) the p_T of the leading jet, (b) the missing transverse energy, (c) the p_T of lepton 0, (d) p_T of lepton 1, (e) p_T of lepton 2, (f) the invariant mass of leptons 0 and 1, (g) the invariant mass of leptons 0 and 2, (h) the number of jets, (i) the number of b-tagged jets.

915 The modeling is further validated by looking at the yield in the $t\bar{t}$ VR for each DL1r WP,
 916 giving a clearer correspondence to the signal regions used in the fit. Each region shown in Figure
 917 12.19 requires one or more jets pass the listed WP, with no jets passing the next highest WP.

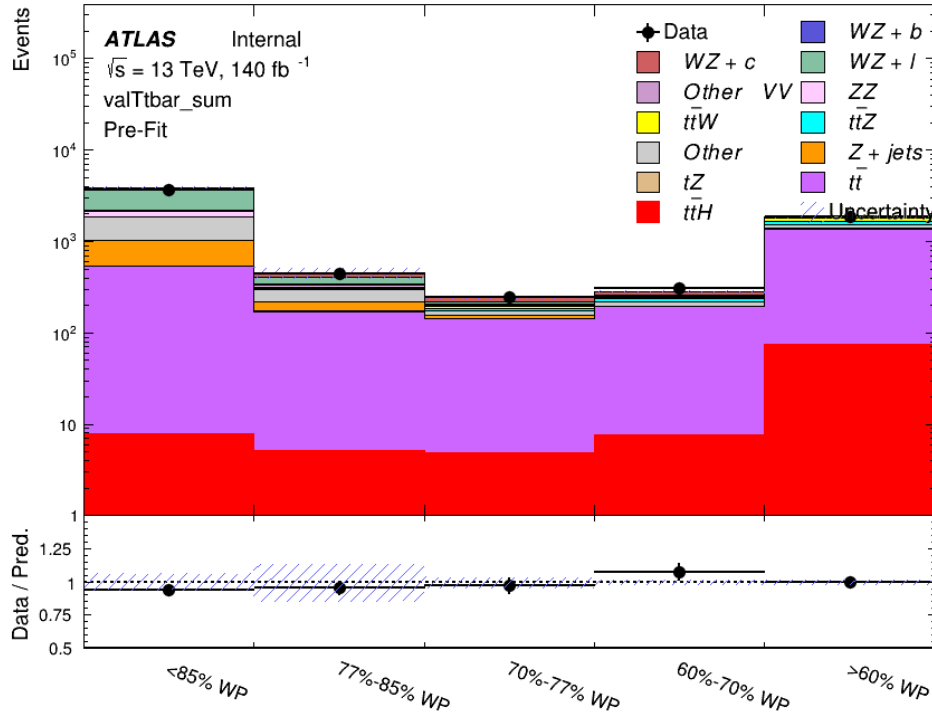


Figure 12.19: Data and MC comparisons for each DL1r WP for both 1-jet and 2-jet regions, after the $t\bar{t}$ VR selection and correction factor have been applied

918 As data and MC are found to agree within 20% for each of these working points, a 20%
 919 systematic uncertainty on the $t\bar{t}$ prediction is included for the analysis.

920 12.3.2 Z+jets Validation

921 Similar to $t\bar{t}$, a non-prompt Z +jets control region is produced in order to validate the MC
922 predictions. The lepton requirements remain the same as the preselection region. Because no
923 neutrinos are present for this process, the E_T^{miss} cut is reversed, requiring $E_T^{\text{miss}} < 30 \text{ GeV}$. This
924 also ensures this control region is orthogonal to the preselection region. Further, the number of
925 jets in each event is required to be greater than or equal to one. Various kinematic plots of this
926 region are shown below. The general agreement between data and MC in each of these suggests
927 that the non-prompt contribution of Z +jets is well modeled by Monte Carlo.

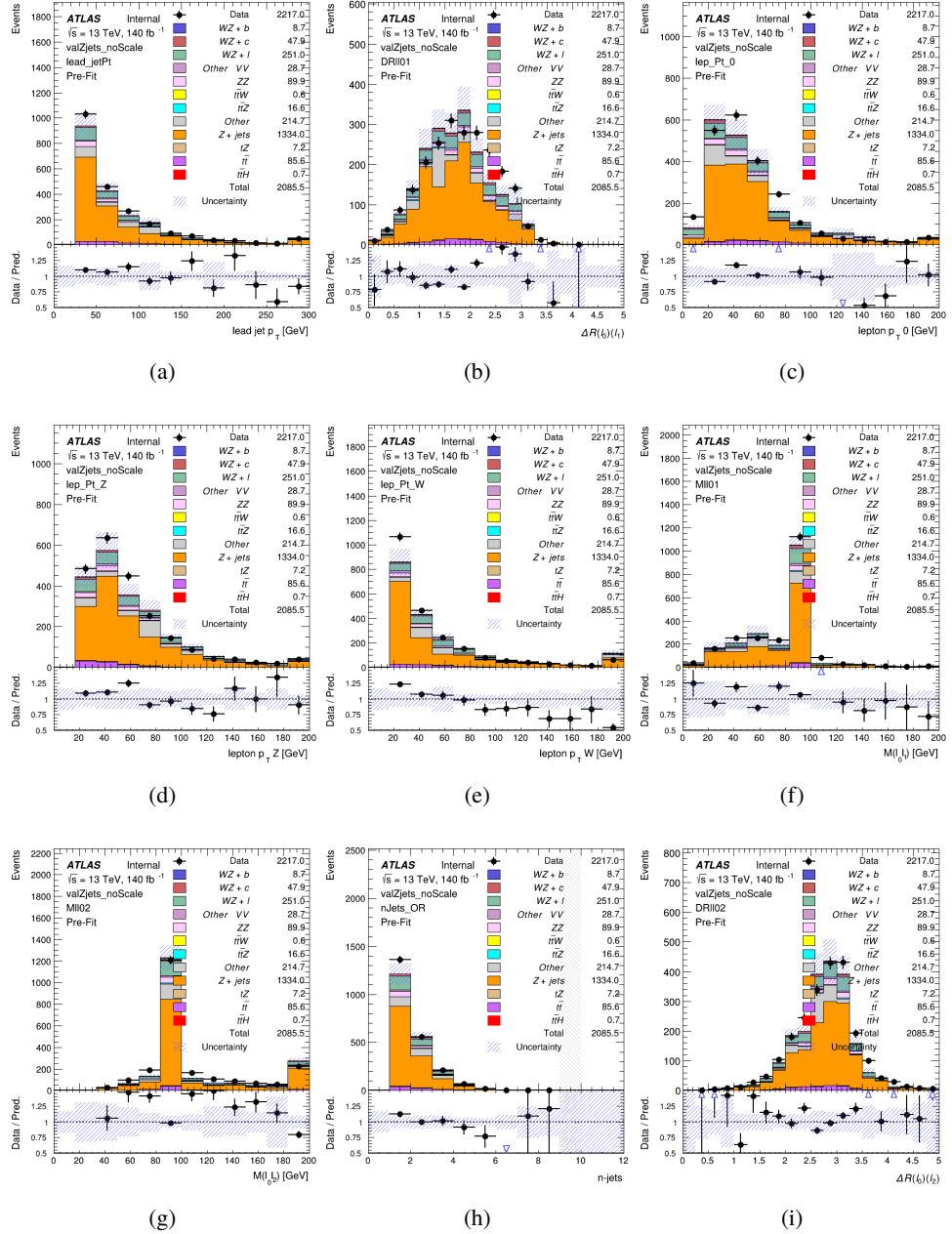


Figure 12.20: Comparisons between the data and MC distributions in the $Z+jets$ control region for (a) the p_T of the leading jet, (b) ΔR between leptons 0 and 1, (c) the p_T of lepton 0, (d) p_T of SS lepton from the Z candidate, (e) p_T of the SS lepton from the W candidate, (f) the invariant mass of leptons 0 and 1, (g) the invariant mass of leptons 0 and 2, (h) the number of jets, (i) ΔR between leptons 0 and 2. Includes only statistical uncertainties

928 While there is general agreement between data and MC within statistical uncertainty, the
929 shape of the p_T spectrum of the lepton from the W is found to differ. To account for this
930 discrepancy, a variable correction factor is applied to Z+jets. χ^2 minimization of the lepton 2 p_T
931 spectrum is performed to derive a correction factor of $1.53 - 6.6 * 10^{-6}(\text{lep_Pt_W})$. Kinematic
932 plots of the Z + jets control region after this correction factor has been aplied are shown in Figure
933 [12.21](#).

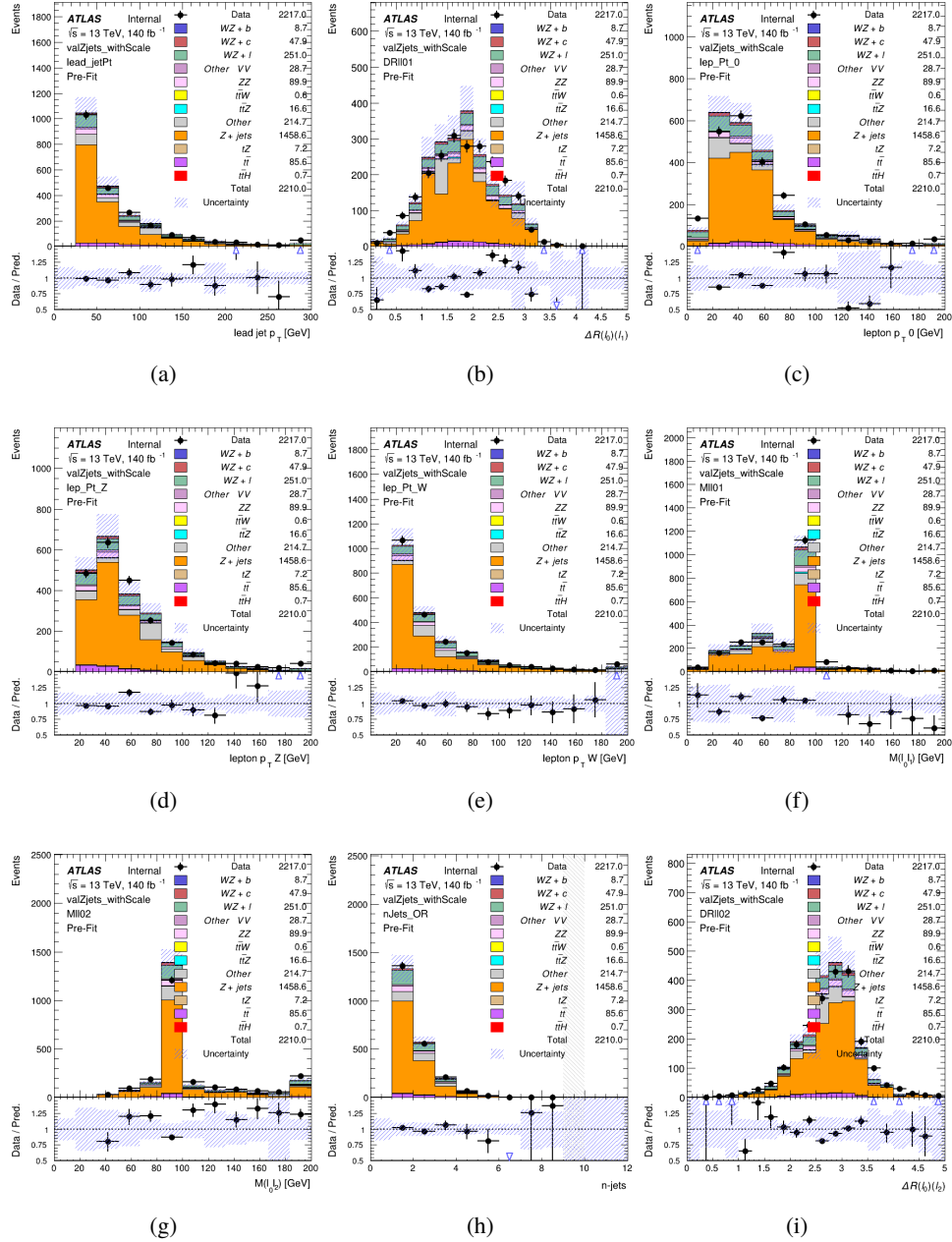


Figure 12.21: Comparisons between the data and MC distributions in the $Z + \text{jets}$ control region after the correction factor has been applied for (a) the p_T of the leading jet, (b) ΔR between leptons 0 and 1, (c) the p_T of lepton 0, (d) p_T of SS lepton from the Z candidate, (e) p_T of the SS lepton from the W candidate, (f) the invariant mass of leptons 0 and 1, (g) the invariant mass of leptons 0 and 2, (h) the number of jets, (i) ΔR between leptons 0 and 2

934 The modeling is further validated by looking at the yield in the Z+jets VR for each DL1r
 935 WP, giving a clearer correspondence to the signal regions used in the fit. Each region shown in
 936 Figure 12.22 requires one or more jets pass the listed WP, with no jets passing the next highest
 937 WP.

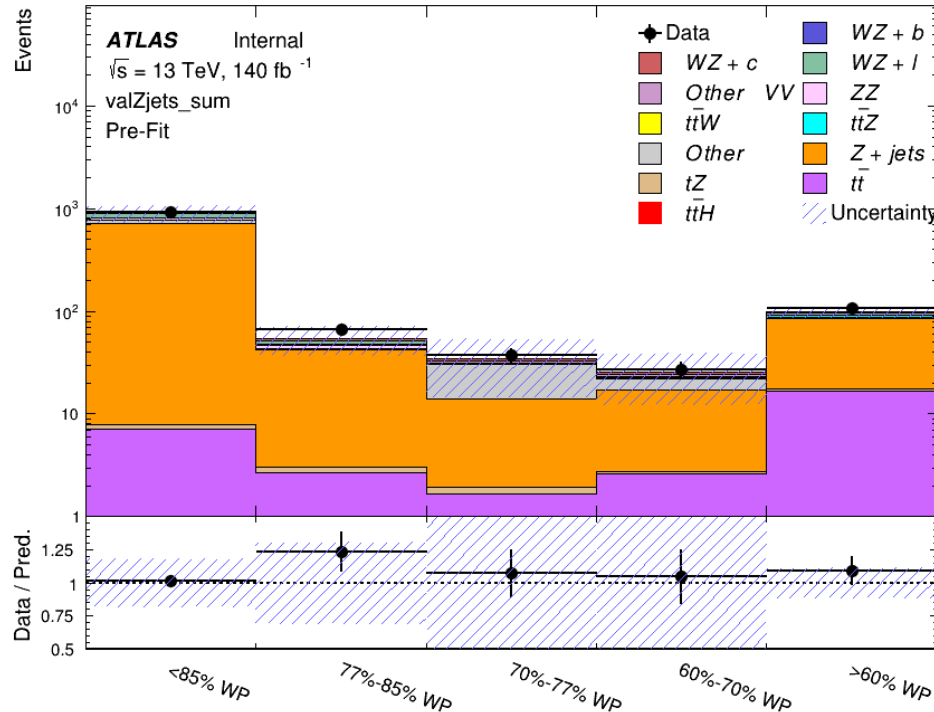


Figure 12.22: Data and MC comparisons for each DL1r WP for both 1-jet and 2-jet regions, after the Z+jets VR selection and correction factor have been applied

938 For each of the b-tagging working points considered, the data falls within 25% of the MC
 939 prediction once this correction factor has been applied. Therefore, a 25% systematic uncertainty
 940 is applied to Z + jets in the analysis.

941 13 tZ Interference Studies and Separation Multivariate Analysis

942 Because tZ produces a final state identical to signal, it represents a predominant background in
943 the most signal enriched regions. That is, the region with one jet passing the 60% DL1r WP.
944 Therefore, a boosted decision tree (BDT) algorithm is trained using TMVA [23] to separate WZ
945 + heavy flavor from tZ.

946 Separation between tZ and WZ + heavy flavor is achieved in part by reconstructing the
947 invariant mass of the top candidate, which clusters more closely to the top mass for tZ than WZ
948 + heavy flavor.

949 The result of this BDT is used to create a tZ enriched region in the fit, reducing its impact
950 on the measurement of WZ + heavy flavor.

951 13.1 Top Mass Reconstruction

952 The reconstruction of the top mass follows the procedure described in detail in section 6.1 of
953 [24]. The mass of the top quark candidate is reconstructed from the jet, the lepton not included
954 in the Z-candidate, and a reconstructed neutrino. In the case that there is one jet in the event,
955 there is only possible b-jet candidate. For events with two jets, the jet with the highest DL1r
956 score is used.

The neutrino from the W decay is expected to be the only source of E_T^{miss} . Therefore, the E_T and ϕ of the neutrino are taken from the E_T^{miss} measurement. This leaves the z-component of the neutrino momentum, p_{vz} as the only unknown.

This unknown is solved for by taking the combined invariant mass of the lepton and neutrino to give the invariant mass of the W boson:

$$(p_l + p_\nu)^2 = m_W^2$$

Expanding this out into components, this equation gives:

$$\sqrt{p_{T\gamma^2} + p_{z\gamma^2}} E_l = \frac{m_w^2 - m_l^2}{2} + p_{T\gamma}(p_{lx}\cos\phi_\gamma + p_{ly}\sin\phi_\gamma) + p_{lz}p_{vz}$$

This equation gives two solutions for p_{vz} . For cases where only one of these solutions is real, that is taken as the value of p_{vz} . For instances with two real solutions, the one which is shown to be correct in the largest fraction of simulations is taken. For cases when no real solution is found, often because of detector effects, the value of E_T^{miss} is varied in decreasing increments of 100 MeV until a real solution is found.

The reconstructed top mass distribution for tZ and WZ + b can be seen in figure 13.1.

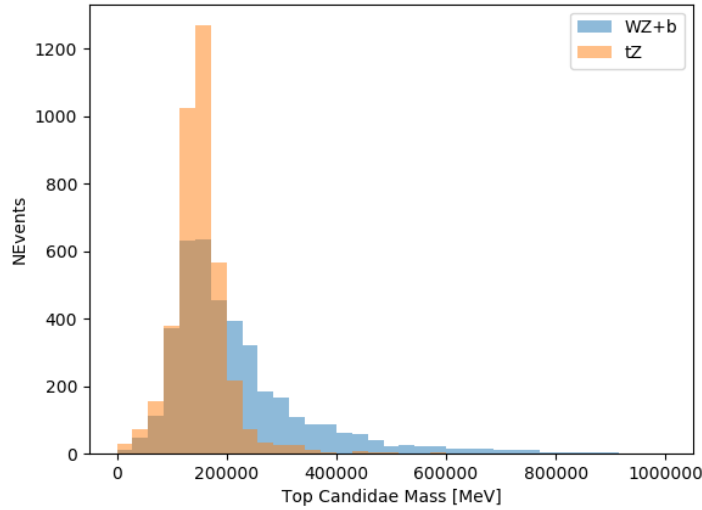


Figure 13.1: Reconstructed top mass distributions for tZ and WZ + b, measured in MeV.

971 13.2 tZ BDT

972 A Boosted Decision Tree (BDT), specifically XGBoost [25], is used to provide separation between
 973 tZ and WZ+b. The following kinematic variables are used as inputs:

974 • The invariant mass of the reconstructed top candidate

975 • p_T of each of the leptons, jet

976 • The invariant mass of each combination of lepton pairs, $M(l\bar{l})$

977 • E_T^{miss}

978 • Distance between each combination of leptons, $\Delta R(l\bar{l})$

- 979 • Distance between each lepton and the jet, $\Delta R(lj)$

980 The training samples included only events meeting the requirements of the 1-jet, $>60\%$
981 region, i.e. passing all the selection described in section 12 and having exactly one jet which
982 passes the tightest (60%) DL1r working point.

983 The distributions of a few of these features for both signal and background is shown in
984 figure 13.2.

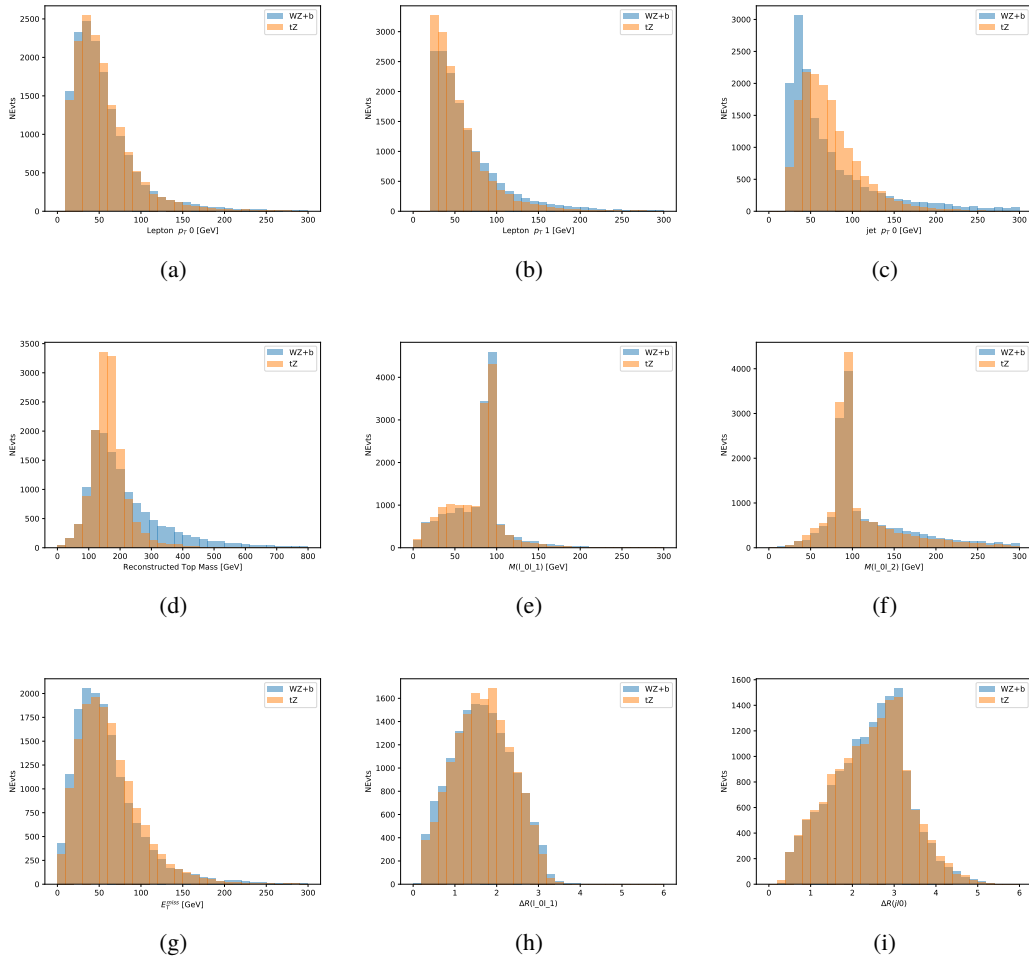


Figure 13.2: Distribution of input features of the BDT for signal (WZ) and background (tZ). Both are scaled to an equal number of events. (a), (b) and (c) show the p_T of lepton 0, lepton 1, and the jet, (d) show the reconstructed top mass, (e) and (f) show the invariant mass of leptons 0 and 1, leptons 0 and 2. (g) shows the E_T^{miss} of each event. (h) and (i) show the ΔR between lepton 0 and lepton 1, and the jet.

985 A sample of 20,000 background (tZ) and signal (WZ+b) Monte Carlo events are used to
 986 train the BDT. And additional 5,000 events are reserved for testing the model, in order to prevent
 987 over-fitting. A total of 750 decision trees with a maximum depth of 6 branches are used to build
 988 the model. These parameters are chosen empirically, by training several models with different

989 parameters and selecting the one that gave the best separation for the test sample.

990 The results of the BDT training are shown in figure 13.3. The output scores for both signal
 991 and background events is shown on the left. The right shows the receiving operating characteristic
 992 (ROC) curve that results from the MVA. The ROC curve represents the background rejection
 993 as a function of signal efficiency, where each point on the curve represents a different response
 994 score. The ROC curve of the BDT is compared to the performance of using an optimal set of flat
 995 selections on the same set of input variables.

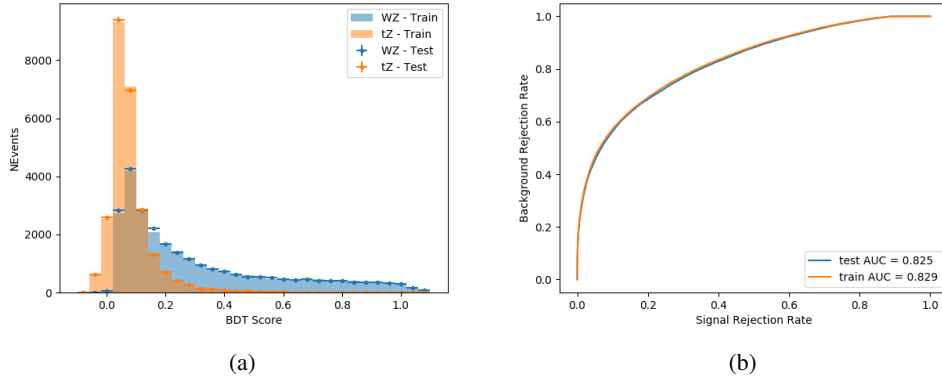


Figure 13.3: Distribution of the BDT response for signal and background events on the left, the ROC curve for the BDT on the right.

996 The relative important of each input feature in the model, measured by how often they
 997 appeared in the decision trees, is shown in figure 13.4.

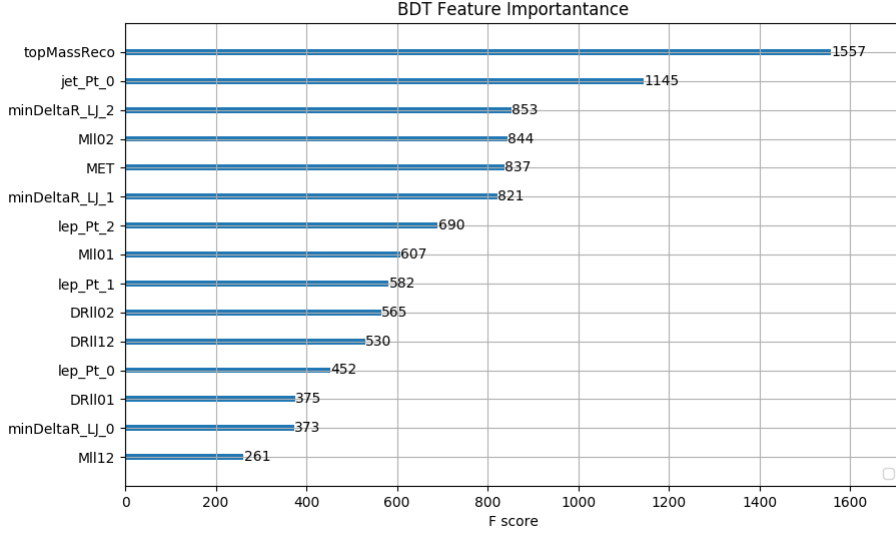


Figure 13.4: Relative importance of each input feature in the model.

998 These results suggest that some amount of separation can be achieved between these two
 999 processes, with a high BDT score selecting a set of events that is pure in $WZ + b$. A BDT score
 1000 of 0.725 is selected as a cutoff, where events with scores higher than this form a signal enriched
 1001 region, and events with scores lower than this form a tZ control region. This cutoff is selected by
 1002 varying the value of this cutoff in stat-only Asimov fits, and selecting the value that minimizes
 1003 the statistical uncertainty on $WZ + b$.

1004 14 Systematic Uncertainties

1005 The systematic uncertainties that are considered are summarized in Table 49. These are imple-
 1006 mented in the fit either as a normalization factors or as a shape variation or both in the signal

¹⁰⁰⁷ and background estimations. The numerical impact of each of these uncertainties is outlined in
¹⁰⁰⁸ Section 22.

Table 15: Sources of systematic uncertainty considered in the analysis.

| Systematic uncertainty | Components |
|--|------------|
| Luminosity | 1 |
| Pileup reweighting | 1 |
| Physics Objects | |
| Electron | 6 |
| Muon | 15 |
| Jet energy scale | 28 |
| Jet energy resolution | 8 |
| Jet vertex fraction | 1 |
| Jet flavor tagging | 131 |
| E_T^{miss} | 3 |
| Total (Experimental) | 194 |
| Signal Modeling | |
| Shape modelling | 3 |
| Renormalization and factorization scales | 5 |
| nJet Migration | 5 |
| Background Modeling | |
| Cross section | 15 |
| Renormalization and factorization scales | 12 |
| Total (Signal and background modeling) | 35 |
| Total (Overall) | 230 |

¹⁰⁰⁹ The uncertainty in the combined integrated luminosity is derived from a calibration of the
¹⁰¹⁰ luminosity scale performed for 13 TeV proton-proton collisions [26], [27].

¹⁰¹¹ The experimental uncertainties are related to the reconstruction and identification of light
¹⁰¹² leptons and b-tagging of jets, and to the reconstruction of E_T^{miss} . The TOTAL electron ID
¹⁰¹³ correlation model is used, corresponding to 1 electron ID systematic. Electron ID is found to be

1014 a subleading systematic that is unconstrained by the fit, making it an appropriate choice for this
1015 analysis.

1016 The sources which contribute to the uncertainty in the jet energy scale (JES) [28] are decom-
1017 posed into uncorrelated components and treated as independent sources in the analysis. The
1018 CategoryReduction model is used to account for JES uncertainties, which decomposes the uncer-
1019 tainties into 30 nuisance parameters included in the fit. The SimpleJER model is used to account
1020 for jet energy resolution (JER) uncertainties, and 8 JER uncertainty components included as
1021 NPs in the fit.

1022 The uncertainties in the b-tagging efficiencies measured in dedicated calibration analyses
1023 [29] are also decomposed into uncorrelated components. The large number of components for
1024 b-tagging is due to the calibration of the distribution of the MVA discriminant.

1025 The full list of systematic uncertainties considered in the analysis is summarized in Tables
1026 50, 51 and 52.

1027

| Experimental Systematics on Leptons and E_T^{miss} | | | |
|---|-------------------------------------|---|-------------------|
| Type | Description | Systematics Name | Application |
| Trigger | | | |
| Scale Factors | Trigger Efficiency | lepSFTrigTight_MU(EL)_SF_Trigger_STAT(SYST) | Event Weight |
| Muons | | | |
| Efficiencies | Reconstruction and Identification | lepSFObjTight_MU_SF_ID_STAT(SYST) | Event Weight |
| | Isolation | lepSFObjTight_MU_SF_Isol_STAT(SYST) | Event Weight |
| | Track To Vertex Association | lepSFObjTight_MU_SF_TTVA_STAT(SYST) | Event Weight |
| p_T Scale | p_T Scale | MUONS_SCALE | p_T Correction |
| Resolution | Inner Detector Energy Resolution | MUONS_ID | p_T Correction |
| | Muon Spectrometer Energy Resolution | MUONS_MS | p_T Correction |
| Electrons | | | |
| Efficiencies | Reconstruction | lepSFObjTight_EL_SF_ID | Event Weight |
| | Identification | lepSFObjTight_EL_SF_Reco | Event Weight |
| | Isolation | lepSFObjTight_EL_SF_Isol | Event Weight |
| Scale Factor | Energy Scale | EG_SCALE_ALL | Energy Correction |
| Resolution | Energy Resolution | EG_RESOLUTION_ALL | Energy Correction |
| E_T^{miss} | | | |
| Soft Tracks Terms | Resolution | MET_SoftTrk_ResoPerp | p_T Correction |
| | Resolution | MET_SoftTrk_ResoPara | p_T Correction |
| | Scale | MET_SoftTrk_ScaleUp | p_T Correction |
| | Scale | MET_SoftTrk_ScaleDown | p_T Correction |

Table 16: Summary of experimental systematics considered for leptons and E_T^{miss} . Includes type, description, name of systematic as used in the fit, and mode of application. The mode of application indicates the systematic evaluation, e.g. as an overall event re-weighting (Event Weight) or rescaling (p_T Correction).

| Experimental Systematics on Jets | | | |
|----------------------------------|--------------------------|--|--|
| Type | Origin | Systematics Name | Application |
| Jet Vertex Tagger | | JVT | Event Weight |
| Energy Scale | Calibration Method | JET_21NP_ JET_EffectiveNP_1-19 | p _T Correction p _T Correction |
| | η inter-calibration | JET_EtaIntercalibration_Modelling JET_EtaIntercalibration_NonClosure JET_EtaIntercalibration_TotalStat | p _T Correction p _T Correction p _T Correction |
| | High p _T jets | JET_SingleParticle_HighPt | p _T Correction |
| | Pile-Up | JET_Pileup_OffsetNPV JET_Pileup_OffsetMu JET_Pileup_PtTerm JET_Pileup_RhoTopology | p _T Correction p _T Correction p _T Correction p _T Correction |
| | Non Closure | JET_PunchThrough_MC15 | p _T Correction |
| | Flavour | JET_Flavor_Response JET_BJES_Response JET_Flavor_Composition | p _T Correction p _T Correction p _T Correction |
| Resolution | | JET_JER_SINGLE_NP | Event Weight |

Table 17: Jet systematics take into account effects of jets calibration method, η inter-calibration, high p_T jets, pile-up, and flavor response. They are all diagonalised into effective parameters.

| Experimental Systematics on b-tagging | | |
|---------------------------------------|---|---|
| Type | Origin | Systematic Name |
| Scale Factors | DL1r b-tagger efficiency on b originated jets in bins of η | DL1r_Continuous_EventWeight_B0-29 |
| | DL1r b-tagger efficiency on c originated jets in bins of η | DL1r_Continuous_EventWeight_C0-19 |
| | DL1r b-tagger efficiency on light flavoured originated jets in bins of η and p_T | DL1r_Continuous_EventWeight_Light0-79 |
| | DL1r b-tagger extrapolation efficiency | DL1r_Continuous_EventWeight_extrapolation DL1r_Continuous_EventWeight_extrapolation_from_charm |

Table 18: Summary of experimental systematics to be included for b-tagging of jets in the analysis, using the continuous DL1r tagging algorithm. All of the b-tagging related systematics are applied as event weights. From left: type, description, and the name of systematic used in the fit.

1028 Theoretical uncertainties applied to MC predictions, including cross section, PDF, and scale
 1029 uncertainties are taken from theory calculations, with the exception of non-prompt and diboson
 1030 backgrounds. The cross-section uncertainty on tZ is taken from [30]. Derivation of the non-
 1031 prompt background uncertainties, Z+jets and t \bar{t} , are explained in detail in Section 12.3. These
 1032 normalization uncertainties are chosen so as to account for the complete uncertainty in the
 1033 non-prompt contribution, and therefore no additional modelling uncertainties are considered for
 1034 Z+jets and t \bar{t} .

1035 The other VV + heavy flavor processes (namely VV+b and VV+charm, which primarily
 1036 consist of ZZ events) are also poorly understood, because these processes involve the same
 1037 physics as WZ + heavy flavor, and have also not been measured. Therefore, a conservative 50%

1038 uncertainty is applied to those samples. While this uncertainty is large, it is found to have little
 1039 impact on the significance of the final result.

1040 The theory uncertainties applied to the predominate background estimates are summarized
 1041 in Table 53.

| Process | X-section [%] |
|--------------------------------|---|
| tZ | X-sec: ± 15.2 QCD Scale: $^{+5.2}_{-1.3}$ PDF($+\alpha_S$): ± 1.2 |
| t̄ H (aMC@NLO+Pythia8) | QCD Scale: $^{+5.8}_{-9.2}$ PDF($+\alpha_S$): ± 3.6 |
| t̄ Z (aMC@NLO+Pythia8) | QCD Scale: $^{+9.6}_{-11.3}$ PDF($+\alpha_S$): ± 4 |
| t̄ W (aMC@NLO+Pythia8) | QCD Scale: $^{+12.9}_{-11.5}$ PDF($+\alpha_S$): ± 3.4 |
| VV + b/charm (Sherpa 2.2.1) | ± 50 |
| VV + light (Sherpa 2.2.1) | ± 6 |
| t̄ t | ± 20 |
| Z + jets | ± 25 |
| Others | ± 50 |

Table 19: Summary of theoretical uncertainties for MC predictions in the analysis.

1042 Additional signal uncertainties are estimated by comparing estimates from the nominal Sherpa
 1043 WZ samples with alternate WZ samples generated with Powheg+PYTHIA8 (DSID 361601).
 1044 MC/MC scale factors are applied to make these comparisons. The shape of the templates used
 1045 in the fit are compared between these two samples for WZ + b, WZ + charm and WZ + light, as
 1046 shown in Figures 14.1 and 14.2. Each of these plots are normalized to unity in order to capture
 1047 differences in shape.

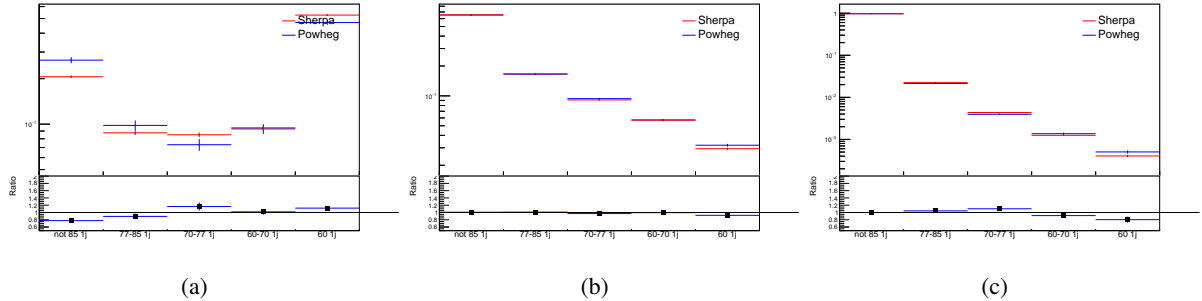


Figure 14.1: Comparison between Sherpa and Powheg predictions of the distribution of (a) $\text{WZ} + \text{b}$, (b) $\text{WZ} + \text{charm}$, and (c) $\text{WZ} + \text{light}$ among the various b-tag WPs used in the 1-jet fit.

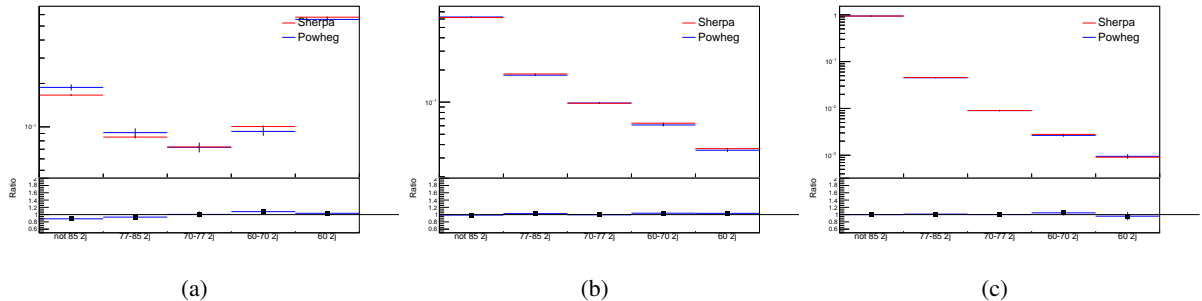


Figure 14.2: Comparison between Sherpa and Powheg predictions of the distribution of (a) $\text{WZ} + \text{b}$, (b) $\text{WZ} + \text{charm}$, and (c) $\text{WZ} + \text{light}$ among the various b-tag WPs used in the 2-jet fit.

1048 Separate systematics are included in the fit for $\text{WZ} + \text{b}$, $\text{WZ} + \text{charm}$ and $\text{WZ} + \text{light}$,
 1049 where the distribution among each of the fit regions is varied based on the prediction of the
 1050 Powheg sample.

1051 A similar approach is taken to account for uncertainties in migrations between the number of
 1052 reco and truth jets. The fraction of events with 1 truth jet which fall into the 1 jet bin versus the
 1053 2 jet bin at reco level is compared for Sherpa and Powheg. The same is done for events with 2
 1054 truth jets. This comparison is shown in figure 14.3.

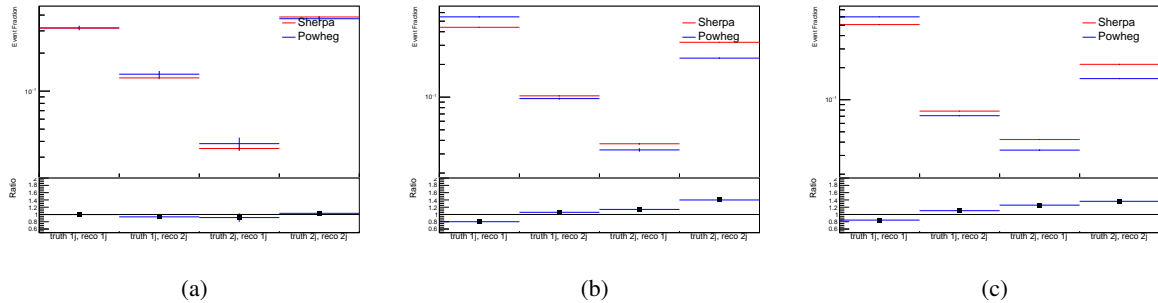


Figure 14.3: Comparison between Sherpa and Powheg predictions for truth jet migrations between the 1 and 2 jet reco bins for (a) WZ + b, (b) WZ + charm, and (c) WZ + light

1055 A systematic is included where events are shifted between the 1-jet and 2-jet regions based
1056 on the differences between these two shapes. This is done independently for each of the WZ +
1057 b, WZ + charm, and WZ + light templates.

Additional systematics are included to account for the uncertainty in the contamination of 0 jet and 3 or more jet events (at truth level) in the 1 and 2 reco jet bins. Because these events fall outside the scope of this measurement, these events are included as a background. As such, a normalization, rather than a shape, uncertainty is applied for this background.

1062 The number of WZ events with 0-jets and $>=3$ -jets in the reconstructed 1-jet and 2-jet
 1063 regions are compared for Sherpa and Powheg, as seen in figure 14.4. These differences are taken
 1064 as separate normalization systematics on the yield of WZ+0-jet and WZ+ $>=3$ -jet events.

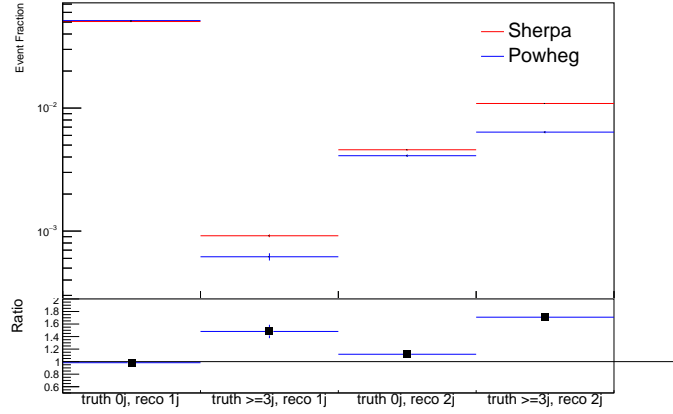


Figure 14.4: Comparison between Sherpa and Powheg predictions for 0 and ≥ 3 truth jet contributions in the 1 and 2 jet reco bins

15 Results

1065 A separate maximum-likelihood fit is performed over the 1-jet and 2-jet fit regions in order to
 1066 extract the best-fit value of the $WZ + b$ -jet and $WZ + c$ charm jet contributions. The $WZ + b$,
 1067 $WZ + c$ and $WZ + \text{light}$ contributions are allowed to float, with the remaining background
 1068 contributions are held fixed. **The current fit strategy treats the $WZ + b$ -jet contribution as**
 1069 **the parameter of interest, with the normalization of the $WZ + c$ and the $WZ + \text{light}$**
 1070 **contributions taken as systematic uncertainties. This could however be adjusted, depending**
 1071 **on whether it is decided the goal of the analysis should be to measure $WZ+b$ specifically or**
 1072 **$WZ + \text{heavy flavor overall}$.** The result of the fit is used to extract the cross-section of $WZ +$
 1073 heavy-flavor production.

1075 A maximum likelihood fit to data is performed simultaneously in the regions described

1076 in Section 12. The parameters μ_{WZ+b} , $\mu_{WZ+charm}$, $\mu_{WZ+light}$, where $\mu = \sigma_{\text{observed}}/\sigma_{\text{SM}}$, are
 1077 extracted from the fit.

1078 The Asimov fit for 1-jet events gives an expected μ value of $1.00^{+0.37}_{-0.35}(\text{stat})^{+0.24}_{-0.22}(\text{sys})$ for
 1079 $WZ + b$. The fitted cross-section modifiers for $WZ + \text{charm}$ and $WZ + \text{light}$ are $1.00 \pm 0.17 \pm 0.15$
 1080 and $1.00 \pm 0.04 \pm 0.07$, respectively.

1081 The expected cross-section of $WZ+b$ with 1 associated jet obtained from the fit is
 1082 $1.74^{+0.65}_{-0.61}(\text{stat})^{+0.42}_{-0.37}(\text{sys}) \text{ fb}$ with an expected significance of 2.2σ . The expected cross-section
 1083 of $WZ + \text{charm}$ is measured to be $14.6 \pm 2.5(\text{stat}) \pm 2.1(\text{sys}) \text{ fb}$, with a correlation of -0.23.

1084 For 2-jet events, the fit gives an expected μ value of $1.00^{+0.34}_{-0.33}(\text{stat})^{+0.29}_{-0.28}(\text{sys})$ for $WZ +$
 1085 b . The fitted cross-section modifiers for $WZ + \text{charm}$ and $WZ + \text{light}$ are $1.00 \pm 0.17 \pm 0.15$ and
 1086 $1.00 \pm 0.04 \pm 0.08$, respectively.

1087 The expected $WZ + b$ cross-section in the 2-jet region is $2.46^{+0.83}_{-0.81}(\text{stat})^{+0.073}_{-0.68}(\text{sys}) \text{ fb}$
 1088 with an expected significance of 2.6σ . The 2-jet expected cross-section of $WZ + \text{charm}$ is
 1089 $12.7 \pm 2.2(\text{stat}) \pm 2.0(\text{sys}) \text{ fb}$, and the correlation between $WZ + \text{charm}$ and $WZ + b$ is -0.26.

1090 15.1 1-jet Fit Results

1091 **The results of the fit are currently blinded.**

1092 The pre-fit yields in each of the regions used in the fit are shown in Table 15.1, and

1093 summarized in Figure 15.1.

1094

| Sample | 1j, <85% WP | 1j, 77%-85% WP | 1j, 70%-77% WP | 1j, 60%-70% WP | 1j, >60% WP | tZ CR |
|--------------|-----------------|-----------------|-----------------|-----------------|-----------------|-----------------|
| WZ + b - 1j | 8.1 ± 1.6 | 4.7 ± 0.5 | 4.6 ± 0.4 | 5.1 ± 0.4 | 18.2 ± 2.4 | 4.8 ± 0.6 |
| WZ + c - 1j | 260 ± 22 | 81 ± 6 | 43.1 ± 3.6 | 25.8 ± 2.6 | 9.4 ± 1.8 | 2.9 ± 0.6 |
| WZ + l - 1j | 3090 ± 250 | 91 ± 13 | 17 ± 3 | 4.9 ± 1.6 | 1.3 ± 0.4 | 0.2 ± 0.1 |
| WZ + b - 2j | 1.10 ± 0.37 | 0.44 ± 0.11 | 0.39 ± 0.06 | 0.62 ± 0.14 | 2.1 ± 0.5 | 0.59 ± 0.14 |
| WZ + c - 2j | 21 ± 5 | 5.6 ± 1.2 | 3.0 ± 0.7 | 2.0 ± 0.5 | 0.70 ± 0.20 | 0.30 ± 0.08 |
| WZ + l - 2j | 250 ± 60 | 5.7 ± 1.6 | 0.73 ± 0.53 | 0.31 ± 0.15 | 0.07 ± 0.06 | 0.01 ± 0.01 |
| WZ - Other | 13 ± 5 | 1.4 ± 0.4 | 0.42 ± 0.08 | 0.2 ± 0.01 | 0.30 ± 0.05 | 0.67 ± 0.15 |
| Other VV | 6.2 ± 0.6 | 0.2 ± 0.4 | 0.2 ± 0.04 | 0.07 ± 0.1 | 0.1 ± 0.1 | 0.1 ± 0.2 |
| ZZ | 336 ± 26 | 17.8 ± 2.1 | 4.3 ± 0.6 | 1.7 ± 0.5 | 0.36 ± 0.08 | 0.10 ± 0.03 |
| t̄tW | 1.1 ± 0.2 | 0.2 ± 0.1 | 0.3 ± 0.1 | 0.4 ± 0.1 | 1.5 ± 0.3 | 0.7 ± 0.2 |
| t̄tZ | 6.8 ± 1.2 | 1.4 ± 0.3 | 1.0 ± 0.2 | 1.2 ± 0.2 | 4.4 ± 0.8 | 3.2 ± 0.6 |
| Z + jets | 169 ± 38 | 8.9 ± 1.9 | 3.7 ± 0.8 | 3.3 ± 0.7 | 3.2 ± 0.7 | 0.8 ± 0.17 |
| V + γ | 45 ± 28 | 1.9 ± 2.4 | 0.1 ± 0.1 | 0.02 ± 0.01 | 1.0 ± 0.9 | 0.02 ± 0.03 |
| tZ | 24.3 ± 4.3 | 5.5 ± 1.1 | 4.1 ± 0.8 | 5.9 ± 1.1 | 10.7 ± 2.0 | 23 ± 4 |
| tW | 1.4 ± 0.8 | 0.2 ± 0.5 | 0.0 ± 0.2 | 0.7 ± 0.6 | 0.26 ± 0.42 | 0.39 ± 0.41 |
| WtZ | 2.3 ± 1.2 | 0.6 ± 0.3 | 0.3 ± 0.21 | 0.27 ± 0.2 | 1.1 ± 0.7 | 0.6 ± 0.5 |
| VVV | 12.4 ± 0.5 | 0.93 ± 0.06 | 0.35 ± 0.03 | 0.13 ± 0.02 | 0.14 ± 0.03 | 0.02 ± 0.01 |
| VH | 40 ± 6 | 2.6 ± 1.4 | 0.9 ± 0.8 | 0.7 ± 0.8 | 0.5 ± 0.6 | 0.0 ± 0.0 |
| t̄t | 12.1 ± 1.6 | 2.9 ± 0.6 | 2.5 ± 0.5 | 2.8 ± 0.5 | 11.2 ± 1.4 | 10.9 ± 1.5 |
| t̄tH | 0.24 ± 0.03 | 0.05 ± 0.01 | 0.04 ± 0.01 | 0.06 ± 0.01 | 0.20 ± 0.03 | 0.13 ± 0.02 |
| Total | 5010 ± 260 | 227 ± 24 | 88 ± 12 | 57 ± 8 | 76 ± 16 | 53 ± 8 |

Table 20: Pre-fit yields in each of the 1-jet fit regions.

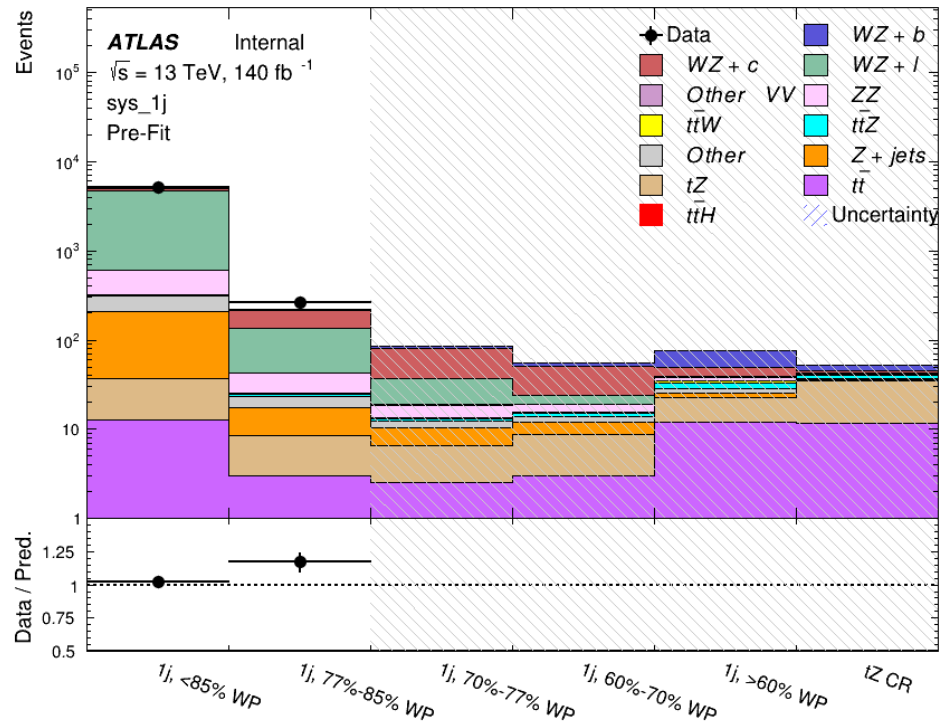


Figure 15.1: Pre-fit summary of the 1-jet fit regions.

1095

The post-fit yields in each region are summarized in Figure 15.1.

1096

| | 1j, <85% WP | 1j, 77%-85% WP | 1j, 70%-77% WP | 1j, 60%-70% WP | 1j, >60% WP | tZ CR |
|-------------|-----------------|-----------------|-----------------|-----------------|-----------------|----------------|
| WZ + b | 8.1 ± 4.9 | 4.7 ± 2.0 | 4.6 ± 2.0 | 5.1 ± 2.1 | 18 ± 10 | 5.0 ± 2.5 |
| WZ + c | 260 ± 60 | 80 ± 14 | 43 ± 7 | 26 ± 5 | 9.4 ± 2.3 | 2.9 ± 0.7 |
| WZ + l | 3090 ± 130 | 90 ± 11 | 17.3 ± 2.8 | 4.9 ± 1.6 | 1.3 ± 0.4 | 0.23 ± 0.1 |
| WZ + b - 2j | 1.10 ± 0.37 | 0.44 ± 0.11 | 0.39 ± 0.06 | 0.62 ± 0.14 | 2.1 ± 0.5 | 0.59 ± 0.1 |
| WZ + c - 2j | 21 ± 5 | 5.6 ± 1.2 | 3.0 ± 0.7 | 2.0 ± 0.5 | 0.70 ± 0.20 | 0.30 ± 0.0 |
| WZ + l - 2j | 250 ± 60 | 5.7 ± 1.6 | 0.73 ± 0.53 | 0.31 ± 0.15 | 0.07 ± 0.06 | 0.01 ± 0.0 |
| WZ - Other | 13 ± 5 | 1.4 ± 0.4 | 0.42 ± 0.08 | 0.2 ± 0.01 | 0.30 ± 0.05 | 0.67 ± 0.1 |
| Other VV | 6.2 ± 0.6 | 0.92 ± 0.07 | 0.02 ± 0.01 | 0.01 ± 0.01 | 0.01 ± 0.01 | 0.01 ± 0.0 |
| ZZ | 346 ± 57 | 19 ± 5 | 4.3 ± 0.8 | 2.7 ± 0.5 | 2.4 ± 0.1 | 2.1 ± 0.6 |
| t̄tW | 1.09 ± 0.21 | 0.2 ± 0.1 | 0.1 ± 0.1 | 0.4 ± 0.1 | 1.5 ± 0.3 | 0.1 ± 0.2 |
| t̄tZ | 6.8 ± 1.2 | 1.4 ± 0.3 | 1.0 ± 0.2 | 1.2 ± 0.2 | 4.4 ± 0.7 | 3.2 ± 0.5 |
| rare Top | 0.14 ± 0.04 | 0.04 ± 0.02 | 0.04 ± 0.0 | 0.1 ± 0.03 | 0.14 ± 0.04 | 0.15 ± 0.0 |
| t̄tWW | 0.04 ± 0.03 | 0.01 ± 0.02 | 0.01 ± 0.01 | 0.01 ± 0.01 | 0.01 ± 0.02 | 0.01 ± 0.0 |
| Z + jets | 169 ± 37 | 8.9 ± 1.9 | 3.7 ± 0.8 | 3.3 ± 0.7 | 3.2 ± 0.7 | 0.8 ± 0.2 |
| W + jets | 0.01 ± 0.01 | 0.01 ± 0.0 |
| V + γ | 46 ± 28 | 1.9 ± 2.4 | 0.1 ± 0.1 | 0.0 ± 0.2 | 1.0 ± 0.9 | 0.0 ± 0.0 |
| tZ | 24 ± 4 | 5.5 ± 1.0 | 4.1 ± 0.8 | 5.9 ± 1.1 | 10.7 ± 1.8 | 23.3 ± 3.7 |
| tW | 1.37 ± 0.82 | 0.18 ± 0.26 | 0.01 ± 0.12 | 0.67 ± 0.64 | 0.26 ± 0.42 | 0.39 ± 0.4 |
| WtZ | 2.3 ± 1.2 | 0.6 ± 0.3 | 0.3 ± 0.2 | 0.3 ± 0.2 | 1.1 ± 0.6 | 0.6 ± 0.3 |
| VVV | 12.4 ± 0.4 | 0.9 ± 0.1 | 0.4 ± 0.1 | 0.13 ± 0.02 | 0.14 ± 0.03 | 0.02 ± 0.0 |
| VH | 40 ± 6 | 2.6 ± 1.4 | 0.9 ± 0.8 | 0.7 ± 0.8 | 0.4 ± 0.6 | 0.01 ± 0.0 |
| t̄t | 12.1 ± 1.6 | 2.9 ± 0.6 | 2.5 ± 0.5 | 2.8 ± 0.5 | 11.2 ± 1.5 | 10.9 ± 1.4 |
| t̄tH | 0.24 ± 0.03 | 0.05 ± 0.01 | 0.04 ± 0.01 | 0.06 ± 0.01 | 0.20 ± 0.03 | 0.13 ± 0.0 |
| Total | 5100 ± 110 | 227 ± 12 | 87 ± 6 | 56.7 ± 4.4 | 76 ± 9 | 52.5 ± 4.2 |

Table 21: Post-fit yields in each of the 1-jet fit regions.

1097

A post-fit summary plot of the 1-jet fitted regions is shown in Figure 15.2:

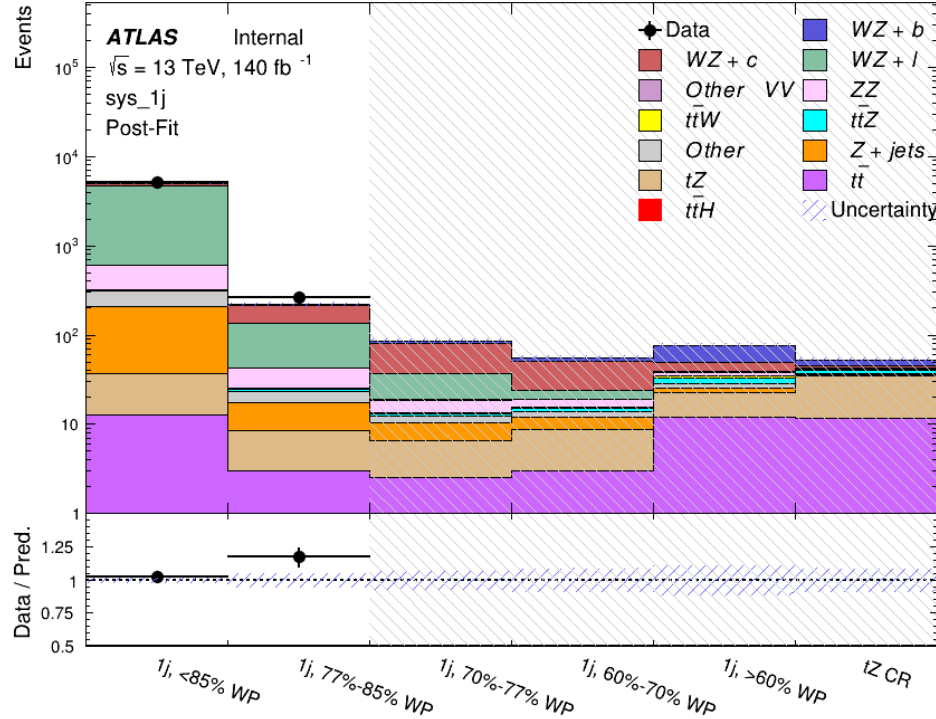


Figure 15.2: Post-fit summary of the 1-jet fit regions.

1098 As described in Section 21, there are 226 systematic uncertainties that are considered
 1099 as NPs in the fit. These NPs are constrained by Gaussian or log-normal probability density
 1100 functions. The latter are used for normalisation factors to ensure that they are always positive.
 1101 The expected number of signal and background events are functions of the likelihood. The prior
 1102 for each NP is added as a penalty term, decreasing the likelihood as it is shifted away from its
 1103 nominal value.

1104 The impact of each NP is calculated by performing the fit with the parameter of interest held
 1105 fixed, varied from its fitted value by its uncertainty, and calculating $\Delta\mu$ relative to the baseline

¹¹⁰⁶ fit. The impact of the most significant sources of systematic uncertainties is summarized in Table

¹¹⁰⁷ [22.](#)

| Uncertainty Source | $\Delta\mu$ | |
|---------------------------------|-------------|-------|
| WZ + light cross-section | 0.13 | -0.12 |
| WZ + charm cross-section | -0.10 | 0.12 |
| Jet Energy Scale | 0.08 | 0.13 |
| tZ cross-section | -0.10 | 0.10 |
| Jet Energy Resolution | -0.10 | 0.10 |
| Luminosity | -0.08 | 0.09 |
| Other Diboson + b cross-section | -0.07 | 0.07 |
| Flavor tagging | 0.05 | 0.05 |
| t <bar>t</bar> | -0.05 | 0.05 |
| WZ cross-section - QCD scale | -0.04 | 0.03 |
| Total Systematic Uncertainty | 0.28 | 0.32 |

Table 22: Summary of the most significant sources of systematic uncertainty on the measurement of WZ + b with exactly one associated jet.

¹¹⁰⁸ The ranking and impact of those nuisance parameters with the largest contribution to the

¹¹⁰⁹ overall uncertainty is shown in Figure [15.3](#).

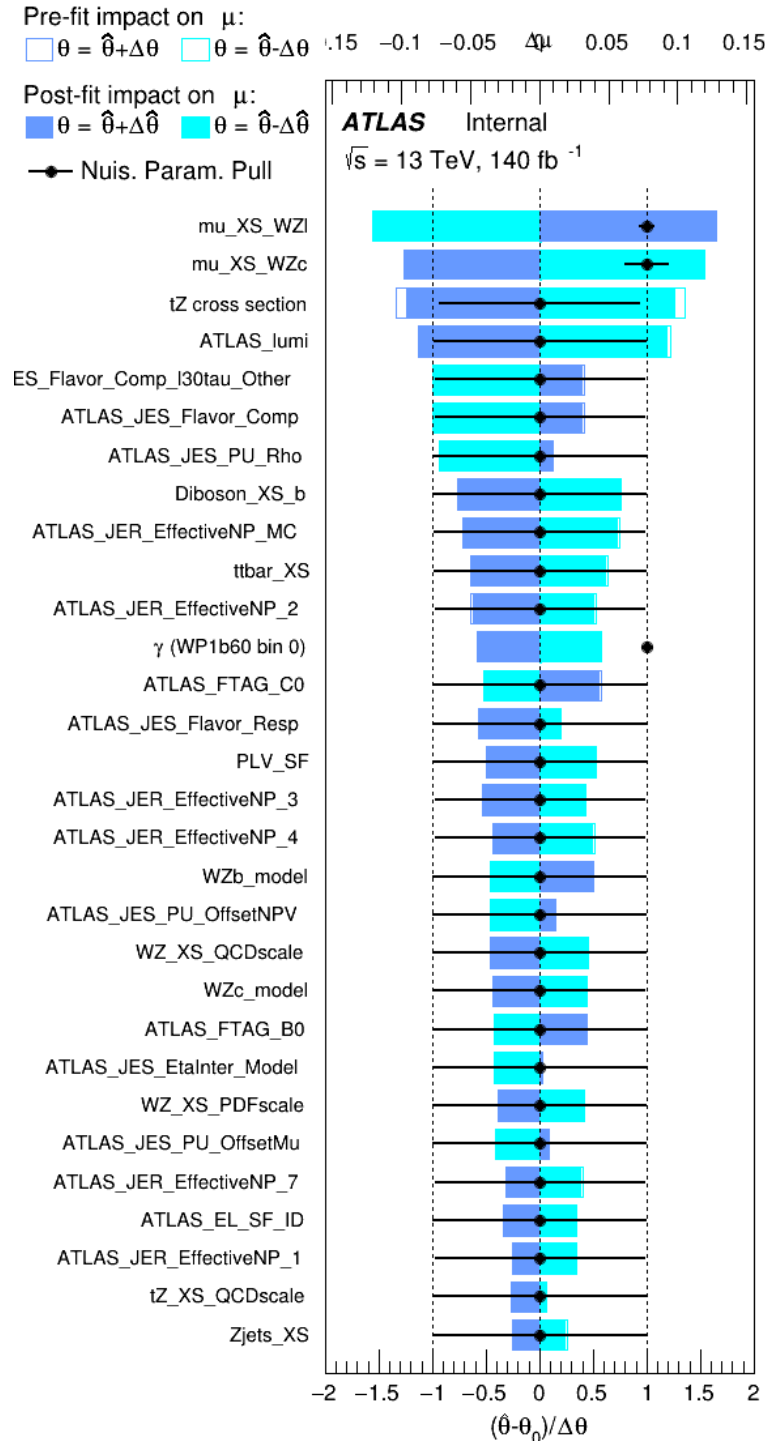


Figure 15.3: Impact of systematic uncertainties on the signal-strength of $WZ + b$ for events with exactly one jet

The large impact of the Jet Energy Scale and Jet Flavor Tagging is unsurprising, as the shape of the fit regions depends heavily on the modeling of the jets. The other major sources of uncertainty come from background modelling and cross-section uncertainty. The pie charts in Figure 15.4 show that for the modelling uncertainties that contribute most correspond to the most significant backgrounds.

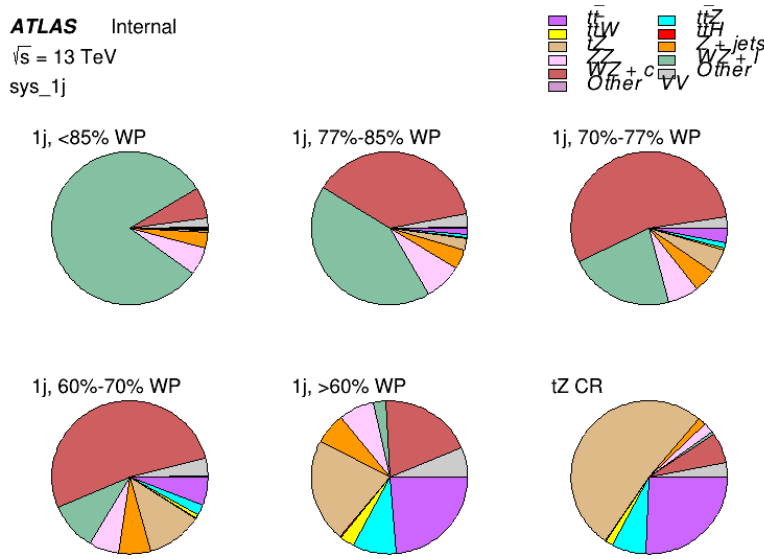


Figure 15.4: Post-fit background composition of the fit regions.

The correlations between these nuisance parameters are summarized in Figure 15.5.

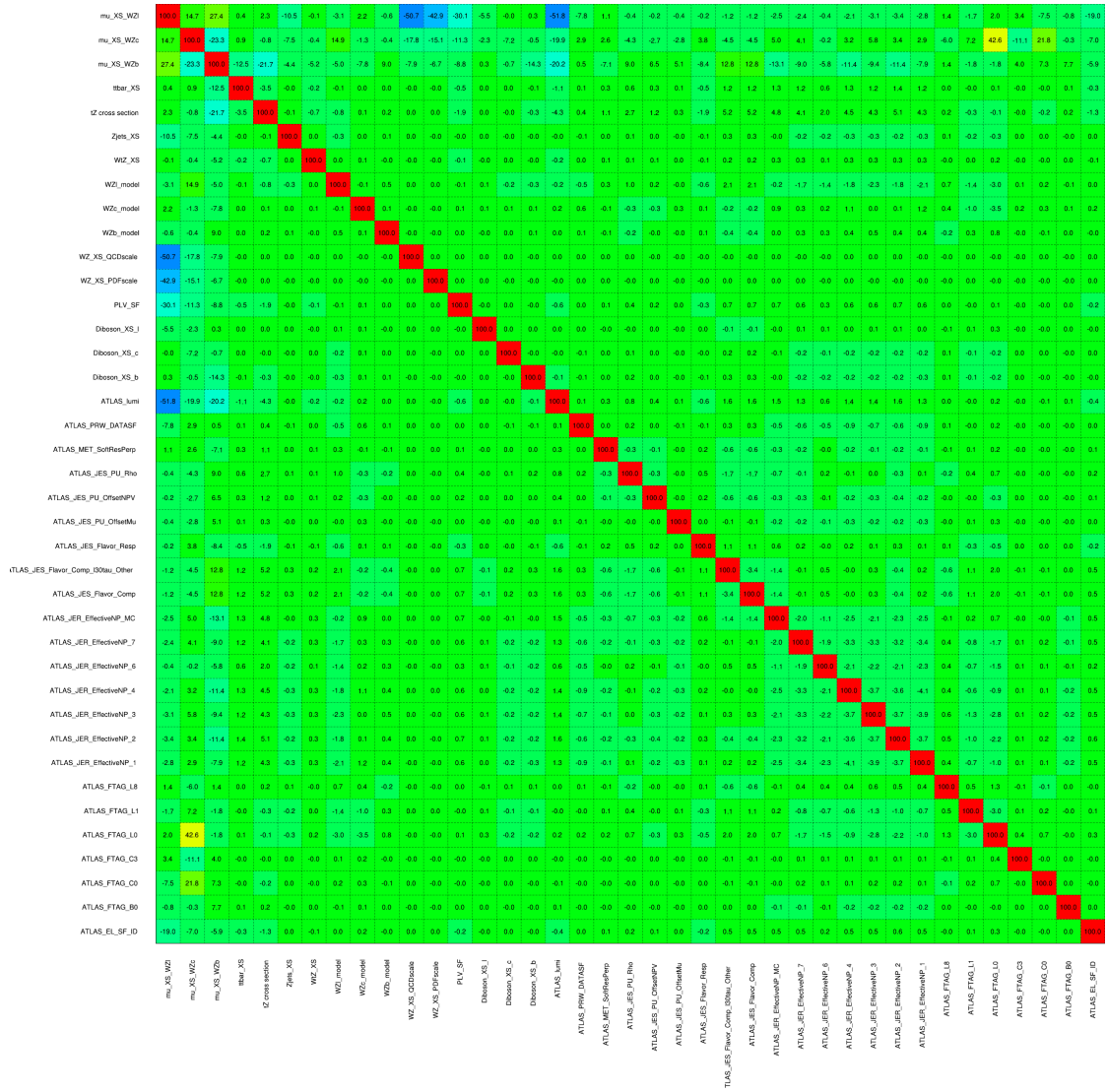


Figure 15.5: Correlations between nuisance parameters

1116 The negative correlations between $\mu_{WZ+charm}$ and μ_{WZ+b} and $\mu_{WZ+light}$ are expected:
1117 WZ + charm is present in both the WZ + b and WZ + light enriched regions, therefore increasing
1118 the fraction of charm requires increasing the fraction of WZ + b and WZ + light. This reasoning
1119 also explains the positive correlation between μ_{WZ+b} and $\mu_{WZ+light}$.

1120 Two of the major backgrounds in the region with the highest purity of $WZ + b$ are tZ and
1121 Other $VV + b$, explaining the negative correlations between μ_{WZ+b} and the tZ cross section, and
1122 the $VV + b$ cross section.

1123 The high correlation between the luminosity and $\mu_{WZ+light}$ arises from the fact that the
1124 uncertainty on $\mu_{WZ+light}$ is very low (around 4%). Small changes in luminosity cause a change
1125 in the yield of $WZ + light$ that is large compared to its uncertainty, producing a large correlation
1126 between these two parameters.

1127 **15.2 2-jet Fit Results**

1128 **The results of the fit are currently blinded.**

1129 Pre-fit yields in each of the 2-jet fit regions are shown in Figure 15.2.

| | 2j, <85% WP | 2j, 77%-85% WP | 2j, 70%-77% WP | 2j, 60%-70% WP | 2j, >60% WP | tZ CR 2j |
|-------------|------------------|-----------------|-----------------|-----------------|-----------------|----------------|
| WZ + b - 2j | 3.1 ± 1.6 | 6.7 ± 0.5 | 5.6 ± 0.4 | 8.0 ± 0.6 | 31 ± 2 | 14 ± 1 |
| WZ + c - 2j | 180 ± 20 | 54 ± 6 | 41 ± 3 | 24 ± 3 | 11 ± 2 | 4.8 ± 0.6 |
| WZ + l - 2j | 1250 ± 150 | 90 ± 14 | 18 ± 3 | 5.8 ± 1.4 | 1.4 ± 0.4 | 0.25 ± 0.1 |
| WZ + b - 1j | 3.4 ± 0.6 | 1.52 ± 0.35 | 1.58 ± 0.23 | 1.95 ± 0.39 | 6.7 ± 1.1 | 1.9 ± 0.6 |
| WZ + c - 1j | 56 ± 14 | 17.6 ± 4.0 | 8.6 ± 2.2 | 6.3 ± 1.8 | 3.0 ± 0.9 | 0.7 ± 0.2 |
| WZ + l - 1j | 427 ± 120 | 24 ± 7 | 4.7 ± 2.3 | 1.6 ± 0.7 | 0.3 ± 0.2 | 0.01 ± 0.0 |
| WZ - Other | 129 ± 29 | 6.1 ± 4.6 | 1.2 ± 0.3 | 0.3 ± 0.2 | 2.9 ± 0.5 | 3.6 ± 0.6 |
| Other VV | 7.63 ± 0.63 | 0.6 ± 0.5 | 0.16 ± 0.03 | 0.01 ± 0.01 | 0.1 ± 0.1 | 0.1 ± 0.1 |
| ZZ | 135 ± 20 | 14.1 ± 3.2 | 4.7 ± 0.8 | 4.0 ± 0.6 | 4.1 ± 0.7 | 3.1 ± 0.5 |
| t̄tW | 0.8 ± 0.2 | 0.4 ± 0.1 | 0.5 ± 0.1 | 0.7 ± 0.2 | 4.3 ± 0.6 | 3.9 ± 0.6 |
| t̄tZ | 14.7 ± 2.2 | 5.6 ± 0.8 | 4.5 ± 0.7 | 6.5 ± 1.1 | 25.4 ± 4.0 | 21.9 ± 3.4 |
| rare Top | 0.14 ± 0.04 | 0.07 ± 0.03 | 0.03 ± 0.02 | 0.09 ± 0.03 | 0.37 ± 0.07 | 0.6 ± 0.1 |
| t̄tWW | 0.04 ± 0.03 | 0.02 ± 0.02 | 0.01 ± 0.01 | 0.01 ± 0.00 | 0.03 ± 0.03 | 0.01 ± 0.0 |
| Z + jets | 110.0 ± 22.9 | 9.6 ± 2.0 | 2.1 ± 0.50 | 1.6 ± 0.4 | 5.1 ± 1.1 | 1.5 ± 0.3 |
| W + jets | 0.0 ± 0.0 | 0.0 ± 0.0 | 0.0 ± 0.0 | 0.0 ± 0.0 | 0.0 ± 0.0 | 0.0 ± 0.0 |
| V + γ | 25 ± 18 | 0.5 ± 0.2 | 0.1 ± 0.1 | 0.1 ± 0.1 | 0.0 ± 0.02 | 0.05 ± 0.0 |
| tZ | 15.9 ± 2.9 | 6.9 ± 1.3 | 5.1 ± 1.0 | 8.0 ± 1.5 | 18.7 ± 3.2 | 36.4 ± 6.1 |
| tW | 0.9 ± 0.7 | 0.2 ± 0.3 | 0.0 ± 0.1 | 0.0 ± 0.0 | 0.8 ± 0.6 | 0.2 ± 0.2 |
| WtZ | 4.9 ± 2.5 | 1.5 ± 0.8 | 1.1 ± 0.6 | 1.3 ± 0.7 | 4.6 ± 2.4 | 3.3 ± 1.7 |
| VVV | 7.4 ± 0.3 | 1.0 ± 0.1 | 0.4 ± 0.1 | 0.2 ± 0.1 | 0.13 ± 0.03 | 0.04 ± 0.0 |
| VH | 19.5 ± 4.2 | 2.8 ± 1.6 | 0.7 ± 0.7 | 0.1 ± 0.2 | 0.0 ± 0.0 | 0.0 ± 0.0 |
| t̄t | 0.7 ± 0.4 | 0.1 ± 0.1 | 0.05 ± 0.06 | 0.15 ± 0.13 | 0.8 ± 0.5 | 2.3 ± 1.2 |
| t̄t | 6.8 ± 1.0 | 2.4 ± 0.5 | 1.8 ± 0.4 | 3.3 ± 0.6 | 8.4 ± 1.2 | 13.6 ± 1.1 |
| t̄tH | 0.4 ± 0.1 | 0.2 ± 0.1 | 0.16 ± 0.02 | 0.23 ± 0.03 | 0.94 ± 0.11 | 1.03 ± 0.1 |
| Total | 2580 ± 160 | 229 ± 24 | 89 ± 13 | 69 ± 11 | 120 ± 15 | 108 ± 11 |

Table 23: Pre-fit yields in each of the 2-jet fit regions.

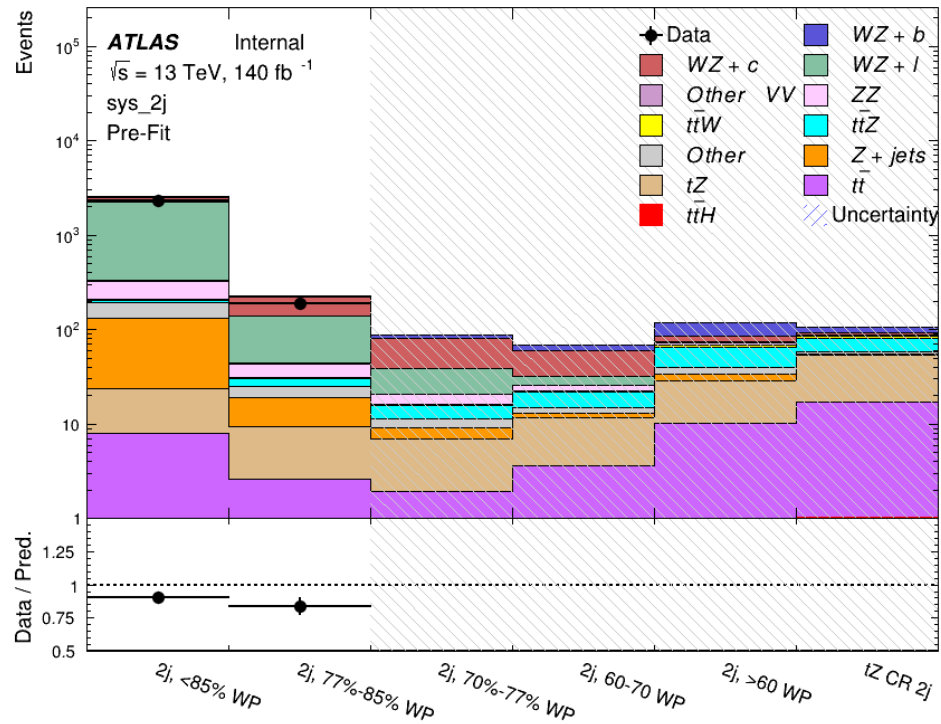


Figure 15.6: Pre-fit summary of the 2-jet fit regions.

1130

The post-fit yields in each region are summarized in Figure 15.2.

| | 2j, <85% WP | 2j, 77%-85% WP | 2j, 70%-77% WP | 2j, 60%-70% WP | 2j, >60% WP | tZ CR 2j |
|-------------|-----------------|-----------------|-----------------|-----------------|-----------------|----------------|
| WZ + b | 13 ± 6 | 6.7 ± 2.9 | 5.8 ± 2.5 | 8.0 ± 3.5 | 31 ± 13 | 14 ± 5 |
| WZ + c | 260 ± 60 | 77 ± 15 | 41 ± 8 | 26 ± 5 | 10.9 ± 2.4 | 4.8 ± 1.1 |
| WZ + l | 1860 ± 90 | 90 ± 12 | 17.6 ± 2.8 | 5.8 ± 1.3 | 1.4 ± 0.4 | 0.3 ± 0.2 |
| WZ + b - 1j | 3.4 ± 0.6 | 1.52 ± 0.35 | 1.58 ± 0.23 | 1.95 ± 0.39 | 6.7 ± 1.1 | 1.9 ± 0.6 |
| WZ + c - 1j | 56 ± 14 | 17.6 ± 4.0 | 8.6 ± 2.2 | 6.3 ± 1.8 | 3.0 ± 0.9 | 0.7 ± 0.2 |
| WZ + l - 1j | 427 ± 120 | 24 ± 7 | 4.7 ± 2.3 | 1.6 ± 0.7 | 0.3 ± 0.2 | 0.01 ± 0.0 |
| WZ - Other | 129 ± 29 | 6.1 ± 4.6 | 1.2 ± 0.3 | 0.3 ± 0.2 | 2.9 ± 0.5 | 3.6 ± 0.6 |
| Other VV | 7.6 ± 0.6 | 0.3 ± 0.3 | 0.3 ± 0.1 | 0.1 ± 0.06 | 0.03 ± 0.02 | 0.1 ± 0.1 |
| ZZ | 145 ± 30 | 11.3 ± 4.4 | 2.7 ± 1.6 | 1.0 ± 0.3 | 4.0 ± 0.1 | 2.4 ± 0.1 |
| t̄tW | 0.8 ± 0.2 | 0.4 ± 0.1 | 0.54 ± 0.12 | 0.74 ± 0.15 | 4.3 ± 0.6 | 3.9 ± 0.6 |
| t̄tZ | 14.7 ± 2.2 | 5.6 ± 0.8 | 4.5 ± 0.7 | 6.5 ± 1.0 | 25.4 ± 3.9 | 21.9 ± 3.0 |
| rare Top | 0.14 ± 0.04 | 0.07 ± 0.03 | 0.03 ± 0.02 | 0.09 ± 0.03 | 0.4 ± 0.1 | 0.6 ± 0.1 |
| t̄tWW | 0.04 ± 0.03 | 0.02 ± 0.02 | 0.01 ± 0.01 | 0.01 ± 0.01 | 0.03 ± 0.03 | 0.01 ± 0.0 |
| Z + jets | 110 ± 23 | 9.6 ± 2.0 | 2.1 ± 0.5 | 1.6 ± 0.4 | 5.1 ± 1.1 | 1.5 ± 0.3 |
| W + jets | 0.0 ± 0.0 | 0.0 ± 0.0 |
| V + γ | 25 ± 19 | 0.5 ± 0.2 | 0.1 ± 0.1 | 0.13 ± 0.14 | 0.0 ± 0.02 | 0.05 ± 0.0 |
| tZ | 15.9 ± 2.7 | 6.9 ± 1.2 | 5.1 ± 0.9 | 8.0 ± 1.4 | 18.7 ± 3.0 | 36 ± 6 |
| tW | 0.1 ± 0.7 | 0.2 ± 0.3 | 0.0 ± 0.1 | 0.0 ± 0.0 | 0.8 ± 0.6 | 0.2 ± 0.2 |
| WtZ | 4.9 ± 2.5 | 1.5 ± 0.8 | 1.1 ± 0.6 | 1.3 ± 0.7 | 4.6 ± 2.3 | 3.3 ± 1.7 |
| VVV | 7.4 ± 0.3 | 1.0 ± 0.1 | 0.36 ± 0.03 | 0.19 ± 0.03 | 0.13 ± 0.03 | 0.04 ± 0.0 |
| VH | 19 ± 4 | 2.8 ± 1.6 | 0.7 ± 0.7 | 0.1 ± 0.2 | 0.0 ± 0.0 | 0.0 ± 0.0 |
| t̄t | 6.8 ± 1.0 | 2.4 ± 0.5 | 1.8 ± 0.4 | 3.3 ± 0.6 | 8.4 ± 1.2 | 13.6 ± 1.7 |
| t̄tH | 0.40 ± 0.05 | 0.19 ± 0.03 | 0.16 ± 0.02 | 0.23 ± 0.03 | 0.94 ± 0.11 | 1.03 ± 0.1 |
| Total | 2580 ± 60 | 229 ± 11 | 89 ± 6 | 69.1 ± 4.1 | 120 ± 10 | 108 ± 6 |

Table 24: Post-fit yields in each of the 2-jet fit regions.

1131

A post-fit summary of the fitted regions is shown in Figure 15.7:

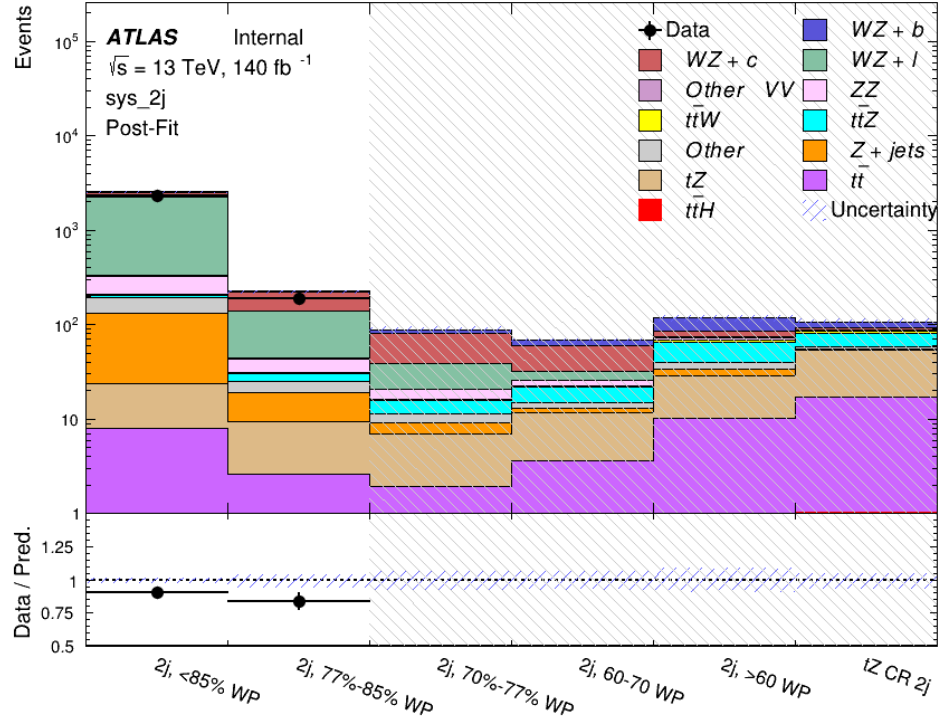


Figure 15.7: Post-fit summary of the fit over 2-jet regions.

1132 The same set of systematic uncertainties consider for the 1-jet fit are included in the 2-jet
 1133 fit as well. The impact of the most significant systematic uncertainties is summarized in Table
 1134 25.

| Uncertainty Source | $\Delta\mu$ | |
|-------------------------------|-------------|-------|
| WZ + c cross-section | -0.1 | 0.14 |
| Luminosity | -0.11 | 0.12 |
| tZ cross-section | -0.11 | 0.11 |
| Jet Energy Scale | -0.11 | 0.11 |
| ttZ cross-section - QCD scale | -0.08 | 0.09 |
| WZ + l cross-section | 0.08 | -0.07 |
| WtZ cross-section | -0.07 | 0.07 |
| Flavor tagging | 0.05 | 0.05 |
| Other VV + b cross-section | -0.05 | 0.05 |
| Jet Energy Resolution | -0.04 | 0.04 |
| Total | 0.29 | 0.31 |

Table 25: Summary of the most significant sources of systematic uncertainty on the measurement of WZ + b 2-jet events.

¹¹³⁵ The ranking and impact of those nuisance parameters with the largest contribution to the
¹¹³⁶ overall uncertainty is shown in Figure 15.8.

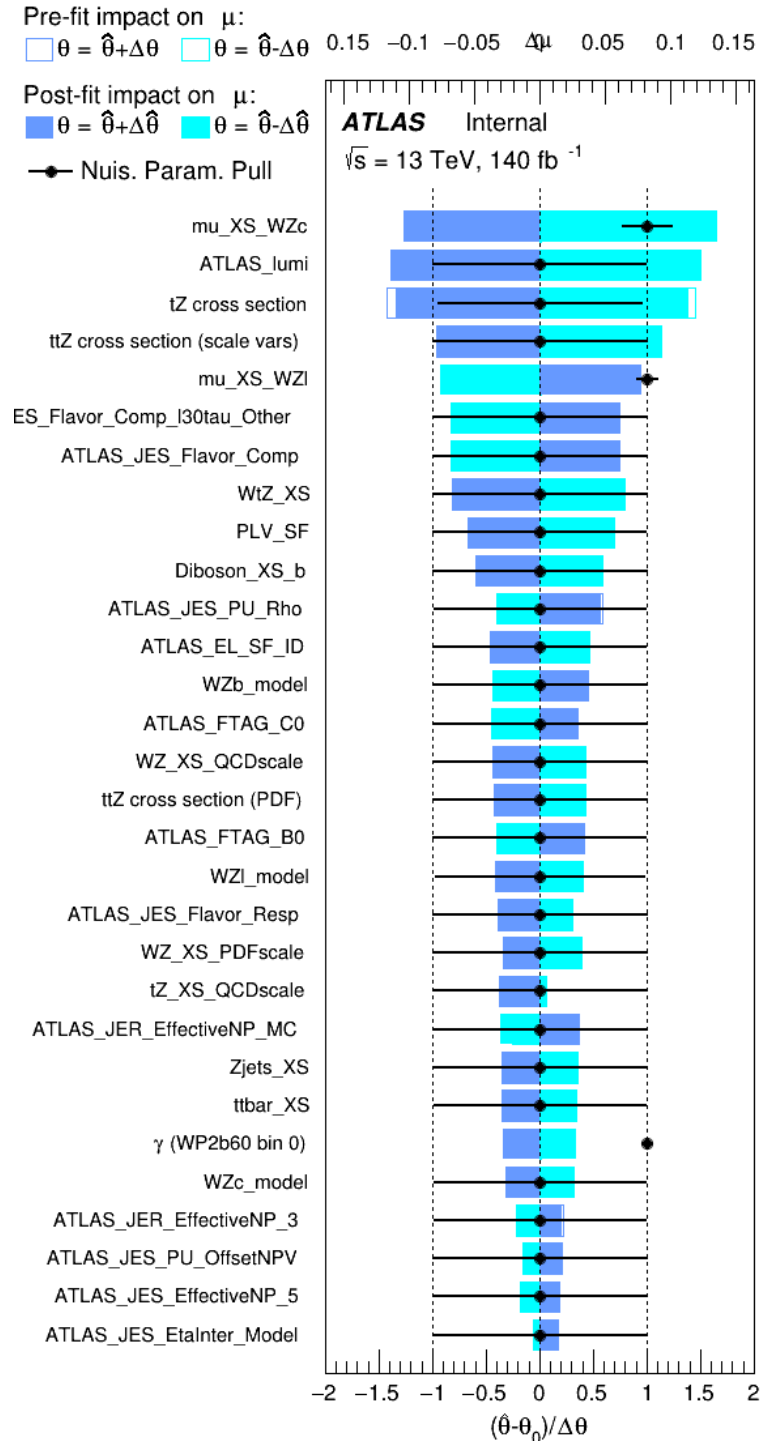


Figure 15.8: Impact of systematic uncertainties on the signal-strength of $WZ + b$ in 2-jet events.

1137 The large impact of the Jet Energy Scale and Jet Flavor Tagging is unsurprising, as the
 1138 shape of the fit regions depends heavily on the modeling of the jets. The other major sources
 1139 of uncertainty come from background modelling and cross-section uncertainty. The pie charts
 1140 in Figure 15.9 show that for the modelling uncertainties that contribute most correspond to the
 1141 most significant backgrounds.

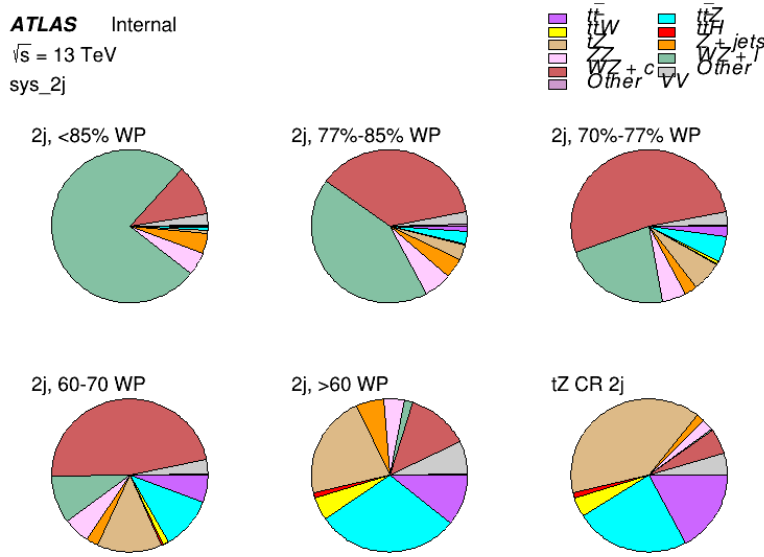


Figure 15.9: Post-fit background composition of the 2-jet fit regions.

1142 The correlations between these nuisance parameters are summarized in Figure 15.10.



Figure 15.10: Correlations between nuisance parameters in the 2-jet fit

As in the 1-jet case, no significant, unexpected correlations are found between nuisance parameters.

Part V**1146 Differential Studies of $t\bar{t}H$ Multilepton****1147 16 Data and Monte Carlo Samples**

1148 For both data and Monte Carlo (MC) simulations, samples were prepared in the `xAOD` format,
1149 which was used to produce a `xAOD` based on the `HIGG8D1` derivation framework. This framework
1150 was designed for the main $t\bar{t}H$ multi-lepton analysis. Because this analysis targets events with
1151 multiple light leptons, as well as tau hadrons, this framework skims the dataset of any events that
1152 do not meet at least one of the following requirements:

- 1153 • at least two light leptons within a range $|\eta| < 2.6$, with leading lepton $p_T > 15$ GeV and
1154 subleading lepton $p_T > 5$ GeV
- 1155 • at least one light lepton with $p_T > 15$ GeV within a range $|\eta| < 2.6$, and at least two hadronic
1156 taus with $p_T > 15$ GeV.

1157 Samples were then generated from these `HIGG8D1` derivations using `AnalysisBase` version
1158 21.2.127. A ptag of `p4133` was used for MC samples, and `p4134` for data.

1159 16.1 Data Samples

1160 The study uses proton-proton collision data collected by the ATLAS detector from 2015 through
1161 2018, which represents an integrated luminosity of 139 fb^{-1} and an energy of $\sqrt{s} = 13 \text{ TeV}$. All
1162 data used in this analysis was included in one of the following Good Run Lists:

- 1163 • data15_13TeV.periodAllYear_DetStatus-v79-repro20-02_DQDefects-00-02-02
1164 _PHYS_StandardGRL_All_Good_25ns.xml

- 1165 • data16_13TeV.periodAllYear_DetStatus-v88-pro20-21_DQDefects-00-02-04
1166 _PHYS_StandardGRL_All_Good_25ns.xml

- 1167 • data17_13TeV.periodAllYear_DetStatus-v97-pro21-13_Unknown_PHYS_StandardGRL
1168 _All_Good_25ns_Triggerno17e33prim.xml

- 1169 • data18_13TeV.periodAllYear_DetStatus-v102-pro22-04_Unknown_PHYS_StandardGRL
1170 _All_Good_25ns_Triggerno17e33prim.xml

1171 16.2 Monte Carlo Samples

1172 Several Monte Carlo (MC) generators were used to simulate both signal and background pro-
1173 cesses. For all of these, the effects of the ATLAS detector are simulated in Geant4. The specific
1174 event generator used for each of these MC samples is listed in Table 26.

Table 26: The configurations used for event generation of signal and background processes, including the event generator, matrix element (ME) order, parton shower algorithm, and parton distribution function (PDF).

| Process | Event generator | ME order | Parton Shower | PDF |
|--|--------------------|---------------|---------------|--------------------|
| $t\bar{t}H$ | MG5_AMC | NLO | PYTHIA 8 | NNPDF 3.0 NLO [11] |
| | (MG5_AMC) | (NLO) | (HERWIG++) | (CT10 [12]) |
| $t\bar{t}W$ | MG5_AMC | NLO | PYTHIA 8 | NNPDF 3.0 NLO |
| | (SHERPA 2.1.1) | (LO multileg) | (SHERPA) | (NNPDF 3.0 NLO) |
| $t\bar{t}(Z/\gamma^* \rightarrow ll)$ | MG5_AMC | NLO | PYTHIA 8 | NNPDF 3.0 NLO |
| | SHERPA 2.2.2 | MEPS NLO | SHERPA | CT10 |
| $t\bar{t}$ | POWHEG-BOX v2 [13] | NLO | PYTHIA 8 | NNPDF 3.0 NLO |
| $t\bar{t}\gamma$ | MG5_AMC | LO | PYTHIA 8 | NNPDF 2.3 LO |
| tZ | MG5_AMC | LO | PYTHIA 6 | CTEQ6L1 |
| $tHqb$ | MG5_AMC | LO | PYTHIA 8 | CT10 |
| tHW | MG5_AMC | NLO | HERWIG++ | CT10 |
| | (SHERPA 2.1.1) | (LO multileg) | (SHERPA) | (NNPDF 3.0 NLO) |
| tWZ | MG5_AMC | NLO | PYTHIA 8 | NNPDF 2.3 LO |
| $t\bar{t}t, t\bar{t}t\bar{t}$ | MG5_AMC | LO | PYTHIA 8 | NNPDF 2.3 LO |
| $t\bar{t}W^+W^-$ | MG5_AMC | LO | PYTHIA 8 | NNPDF 2.3 LO |
| s-, t-channel, Wt single top qqVV, VVV | POWHEG-BOX v1 [14] | NLO | PYTHIA 6 | CT10 |
| | SHERPA 2.2.1 | MEPS NLO | SHERPA | NNPDF 3.0 NLO |
| $Z \rightarrow l^+l^-$ | | | | |

1175 While the main $t\bar{t}H$ analysis uses a more sophisticated data-driven approach to estimating
 1176 the contribution of events with non-prompt leptons (or "fakes"), at the time of this note this
 1177 strategy has not been completely developed for the full Run-2 dataset. Therefore, the non-
 1178 prompt contribution is estimated with MC, while applying conservative systematic uncertainties
 1179 to these processes, as described in Section 21.

1180 The specific DSIDs used in the analysis are listed below:

| Sample | DSID |
|-------------------|--|
| tH | 345873-5, 346343-5 |
| VV | 364250-364254, 364255, 363355-60, 364890 |
| tW | 410155 |
| tZ | 410156, 410157, 410218-20 |
| low mass tZ | 410276-8 |
| Rare Top | 410397, 410398, 410399 |
| single Top | 410658-9, 410644-5 |
| three Top | 304014 |
| four Top | 410080 |
| tWW | 410081 |
| Z + jets | 364100-41 |
| low mass Z + jets | 364198-215 |
| W + jets | 364156-97 |
| V γ | 364500-35 |
| tZ | 410560 |
| tW | 410013-4 |
| WtZ | 410408 |
| VVV | 364242-9 |
| VH | 342284-5 |
| WtH | 341998 |
| t $\bar{\gamma}$ | 410389 |
| t \bar{t} | 410470 |

Table 27: List of Monte Carlo samples by data set ID used in the analysis.

1181 17 Object Reconstruction

1182 All analysis channels considered in this note share a common object selection for leptons and

1183 jets, as well as a shared trigger selection.

1184 **17.1 Trigger Requirements**

1185 Events are required to be selected by dilepton triggers, as summarized in Table 28.

| Dilepton triggers (2015) | |
|-------------------------------|----------------------------|
| $\mu\mu$ (asymm.) | HLT_mu18_mu8noL1 |
| ee (symm.) | HLT_2e12_lhloose_L12EM10VH |
| $e\mu, \mu e$ (\sim symm.) | HLT_e17_lhloose_mu14 |
| Dilepton triggers (2016) | |
| $\mu\mu$ (asymm.) | HLT_mu22_mu8noL1 |
| ee (symm.) | HLT_2e17_lhvloose_nod0 |
| $e\mu, \mu e$ (\sim symm.) | HLT_e17_lhloose_nod0_mu14 |
| Dilepton triggers (2017) | |
| $\mu\mu$ (asymm.) | HLT_mu22_mu8noL1 |
| ee (symm.) | HLT_2e24_lhvloose_nod0 |
| $e\mu, \mu e$ (\sim symm.) | HLT_e17_lhloose_nod0_mu14 |
| Dilepton triggers (2018) | |
| $\mu\mu$ (asymm.) | HLT_mu22_mu8noL1 |
| ee (symm.) | HLT_2e24_lhvloose_nod0 |
| $e\mu, \mu e$ (\sim symm.) | HLT_e17_lhloose_nod0_mu14 |

Table 28: List of lowest p_T -threshold, un-prescaled dilepton triggers used for 2015-2018 data taking.

1186 **17.2 Light Leptons**

1187 Electron candidates are reconstructed from energy clusters in the electromagnetic calorimeter
1188 that are associated with charged particle tracks reconstructed in the inner detector [15]. Electron
1189 candidates are required to have $p_T > 10$ GeV and $|\eta_{\text{cluster}}| < 2.47$. Candidates in the transition
1190 region between different electromagnetic calorimeter components, $1.37 < |\eta_{\text{cluster}}| < 1.52$, are
1191 rejected. A multivariate likelihood discriminant combining shower shape and track information

1192 is used to distinguish prompt electrons from nonprompt leptons, such as those originating from
1193 hadronic showers.

1194 To further reduce the non-prompt contribution, the track of each electron is required to
1195 originate from the primary vertex; requirements are imposed on the transverse impact parameter
1196 significance ($|d_0|/\sigma_{d_0}$) and the longitudinal impact parameter ($|\Delta z_0 \sin \theta_\ell|$).

1197 Muon candidates are reconstructed by combining inner detector tracks with track segments
1198 or full tracks in the muon spectrometer [16]. Muon candidates are required to have $p_T > 10$ GeV
1199 and $|\eta| < 2.5$. All leptons are required to be isolated, and pass a non-prompt BDT selection
1200 described in detail in [5].

1201 **17.3 Jets**

1202 Jets are reconstructed from calibrated topological clusters built from energy deposits in the
1203 calorimeters [18], using the anti- k_t algorithm with a radius parameter $R = 0.4$. Jets with energy
1204 contributions likely arising from noise or detector effects are removed from consideration [19],
1205 and only jets satisfying $p_T > 25$ GeV and $|\eta| < 2.5$ are used in this analysis. For jets with
1206 $p_T < 60$ GeV and $|\eta| < 2.4$, a jet-track association algorithm is used to confirm that the jet
1207 originates from the selected primary vertex, in order to reject jets arising from pileup collisions
1208 [20].

1209 17.4 Missing Transverse Energy

1210 Because all $t\bar{t}H - ML$ channels considered include multiple neutrinos, missing transverse
1211 energy (E_T^{miss}) is present in each event. The missing transverse momentum vector is defined as
1212 the inverse of the sum of the transverse momenta of all reconstructed physics objects as well
1213 as remaining unclustered energy, the latter of which is estimated from low- p_T tracks associated
1214 with the primary vertex but not assigned to a hard object [21].

1215 17.5 Overlap removal

1216 To avoid double counting objects and remove leptons originating from decays of hadrons, overlap
1217 removal is performed in the following order: any electron candidate within $\Delta R = 0.1$ of another
1218 electron candidate with higher p_T is removed; any electron candidate within $\Delta R = 0.1$ of a muon
1219 candidate is removed; any jet within $\Delta R = 0.3$ of an electron candidate is removed; if a muon
1220 candidate and a jet lie within $\Delta R = \min(0.4, 0.04 + 10[\text{GeV}] / p_T(\text{muon}))$ of each other, the jet
1221 is kept and the muon is removed.

1222 This algorithm is applied to the preselected objects. The overlap removal procedure is
1223 summarized in Table 29.

| Keep | Remove | Cone size (ΔR) |
|-------------|-----------------------|---|
| electron | electron (low p_T) | 0.1 |
| muon | electron | 0.1 |
| electron | jet | 0.3 |
| jet | muon | $\min(0.4, 0.04 + 10[\text{GeV}]/p_T(\text{muon}))$ |
| electron | tau | 0.2 |

Table 29: Summary of the overlap removal procedure between electrons, muons, and jets.

1224 18 Higgs Momentum Reconstruction

1225 Reconstructing the momentum of the Higgs boson is a particular challenge for channels with
 1226 leptons in the final state: Because all channels include at least two neutrinos in the final state, the
 1227 Higgs can never be fully reconstructed. However, the momentum spectrum can be well predicted
 1228 by a neural network when provided with the four-vectors of the Higgs Boson decay products, as
 1229 shown in Section 18.1. With this in mind, several layers of MVAs are used to reconstruction the
 1230 Higgs momentum.

1231 The first layer is a model designed to select which jets are most likely to be the b-jets that
 1232 came from the top decay, detailed in Section 18.2. As described in Section 18.3, the kinematics
 1233 of these jets are fed into the second layer, which is designed to identify the decay products of
 1234 the Higgs Boson itself. The kinematics of these particles are then fed into yet another neural-
 1235 network, which predicts the momentum of the Higgs (18.4). MVAs are also used in the analysis
 1236 to determine the decay of the Higgs boson in the 3l channel (18.5).

1237 Models are trained on Monte Carlo simulations of $t\bar{t}H$ events generated using MG5_AMC.
 1238 Specifically, events DSIDs 346343-5, 345873-5, and 345672-4 are used for training.

1239 For all of these models, the Keras neural network framework, with Tensorflow as the
1240 backend, is used, and the number of hidden layers and nodes are determined using grid search
1241 optimization. Each neural network uses the LeakyReLU activation function, a learning rate
1242 of 0.01, and the Adam optimization algorithm, as alternatives are found to either decrease or
1243 have no impact on performance. Batch normalization is applied after each layer. For the
1244 classification algorithms (b-jet matching, Higgs reconstruction, and 3l decay identification)
1245 binary-cross entropy is used as the loss function, while the p_T reconstruction algorithm uses
1246 MSE.

1247 The specific inputs features used for each model are arrived at through a process of trial
1248 and error - features considered potentially useful are tried, and those that are found to increase
1249 performance are included. While each model includes a relatively large number of features,
1250 some using upwards of 30, this inclusive approach is found to maximize the performance of each
1251 model while decreasing the variance compared to a reduced number of inputs. Each input feature
1252 is validated by comparing MC simulations to 80 fb^{-1} of data, as shown in the sections below.

1253 **18.1 Decay Candidate Reconstruction**

1254 Machine Learning algorithms are trained to identify the decay products of the Higgs Boson
1255 using MC simulations of $t\bar{t}H$ events. These include light leptons and jets. Reconstructed
1256 physics objects are matched to truth level particles, in order to identify the parents of these

1257 reconstructed objects. The kinematics of the decay product candidates as well as event level
1258 variables are used as inputs.

1259 Leptons considered as possible Higgs and top decay candidates are required to pass the
1260 selection described in Section 17.2. For jets, however, it is found that a large fraction that
1261 originate from either the top decay or the Higgs decay fall outside the selection described in
1262 Section 17.3. Specifically, jets from the Higgs decay tend to be soft, with 32% having $p_T <$
1263 25 GeV. Therefore jets with $p_T < 15$ GeV are considered as possible candidates in the models
1264 described below. By contrast, less than 5% of the jets originating from the Higgs fall below
1265 this p_T . The jets are found to be well modeled even down to this low p_T threshold, as shown in
1266 Section 20.1. The impact of using different p_T selection for the jet candidates is considered in
1267 detail in Section A.5. As they are expected to originate from the primary vertex, jets are also
1268 required to pass a JVT cut.

1269 18.2 b-jet Identification

1270 Including the kinematics of the b-jets that originate from the top decay is found to improve the
1271 identification of the Higgs decay products, and improve the accuracy with which the Higgs
1272 momentum can be reconstructed. Because these b-jets are reconstructed by the detector with
1273 high efficiency (just over 90% of the time), and can be identified relatively consistently, the first
1274 step in reconstructing the Higgs is selecting the b-jets from the top decay.

1275 Exactly two b-jets are expected in the final state of $t\bar{t}H - ML$ events. However, in both
1276 the 3l and 2lSS channels, only one or more b-tagged jets are required (where the 70% DL1r b-tag
1277 working point is used). Therefore, for events which have exactly one, or more than two, b-tagged
1278 jets, deciding which combination of jets correspond to the top decay is non-trivial. Further,
1279 events with 1 b-tagged jet represent just over half of all $t\bar{t}H - ML$ events. Of those, both b-jets
1280 are reconstructed by the detector 75% of the time. Therefore, rather than adjusting the selection
1281 to require exactly 2 b-tagged jets, and losing more than half of the signal events, a neural network
1282 is used to predict which pair of jets is most likely to correspond to truth b-jets.

1283 Once the network is trained, all possible pairings of jets are fed into the model, and the pair
1284 of jets with the highest output score are taken to be b-jets in successive steps of the analysis.

1285 **18.2.1 2lSS Channel**

1286 For the 2lSS channel, the input features shown in Table 30 are used for training. Here j_0 and j_1
1287 are the two jet candidates, while l_0 and l_1 are the two leptons in the event, both ordered by p_T . jet
1288 DL1r is an integer corresponding to the calibrated b-tagging working points reached by each jet,
1289 where 5 represents the tightest working point and 1 represents the loosest. The variables nJets
1290 DL1r 60% and nJets DL1r 85% represent the number of jets in the event passing the 60% and
1291 85% b-tag working points, respectively.

| | | |
|--------------------------------------|--|--|
| jet p_T 0 | jet p_T 1 | Lepton p_T 0 |
| Lepton p_T 1 | jet η 0 | jet η 1 |
| $\Delta R(j_0)(j_1)$ | $M(j_0 j_1)$ | $\Delta R(l_0)(j_0)$ |
| $\Delta R(l_0)(j_1)$ | $\Delta R(l_1)(j_0)$ | $\Delta R(l_1)(j_1)$ |
| $M(l_0 j_0)$ | $M(l_0 j_1)$ | $M(l_1 j_0)$ |
| $M(l_1 j_1)$ | jet DL1r 0 | jet DL1r 1 |
| nJets OR DL1r 85 | nJets OR DL1r 60 | $\Delta R(j_0 l_0)(j_1 l_1)$ |
| $\Delta R(j_0 l_1)(j_1 l_0)$ | $p_T(j_0 j_1 l_0 l_1 E_T^{\text{miss}})$ | $M(j_0 j_1 l_0 l_1 E_T^{\text{miss}})$ |
| $\Delta\phi(j_0)(E_T^{\text{miss}})$ | $\Delta\phi(j_1)(E_T^{\text{miss}})$ | HT jets |
| nJets | E_T^{miss} | |

Table 30: Input features used in the b-jet identification algorithm for the 2lSS channel

1292 As there are far more incorrect combinations than correct ones, by a factor of more than
 1293 20:1, the training set is resampled to reduce the fraction of incorrect combinations. A random
 1294 sample of 5 million incorrect entries are used for training, along with close 1 million correct
 1295 entries. 10% of the dataset is set aside for testing, leaving around 5 million datapoints for
 1296 training.

1297 The difference between the distributions for a few of these features for the correct(i.e.
 1298 both jets are truth b-jets), and incorrectcombinations are shown in Figure 18.1. The correct and
 1299 incorrect contributions are scaled to the same integral, so as to better demonstrate the differences
 1300 in the distributions.

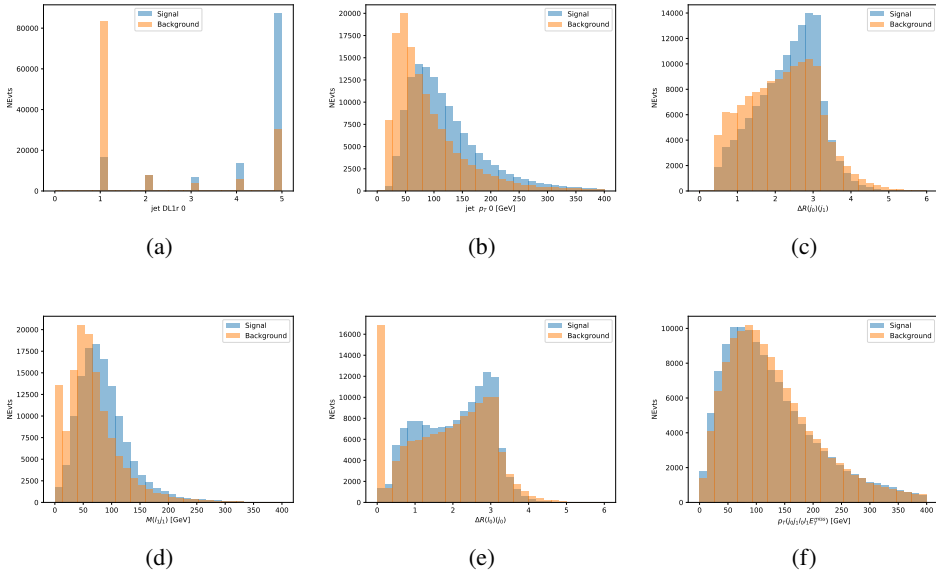


Figure 18.1: Input features for top2lSS training. The signal in blue represents events where both jet candidates are truth b-jets from top decays, and the orange is all other combinations. Each are scaled to the same number of events. (a) shows the DL1r working point of leading jet, (b) shows the p_T of the leading jet, (c) shows the ΔR of the two jets, (d) the invariant mass of lepton 1 and jet 1, (e) the ΔR of lepton 0 and jet 0, and (f) the p_T of both jets, both leptons, and the E_T^{miss} .

1301 The modeling of these inputs is validated against data, with Figure 18.2 showing good
 1302 general agreement between data and MC. Plots for the complete list of features can found in
 1303 Section A.

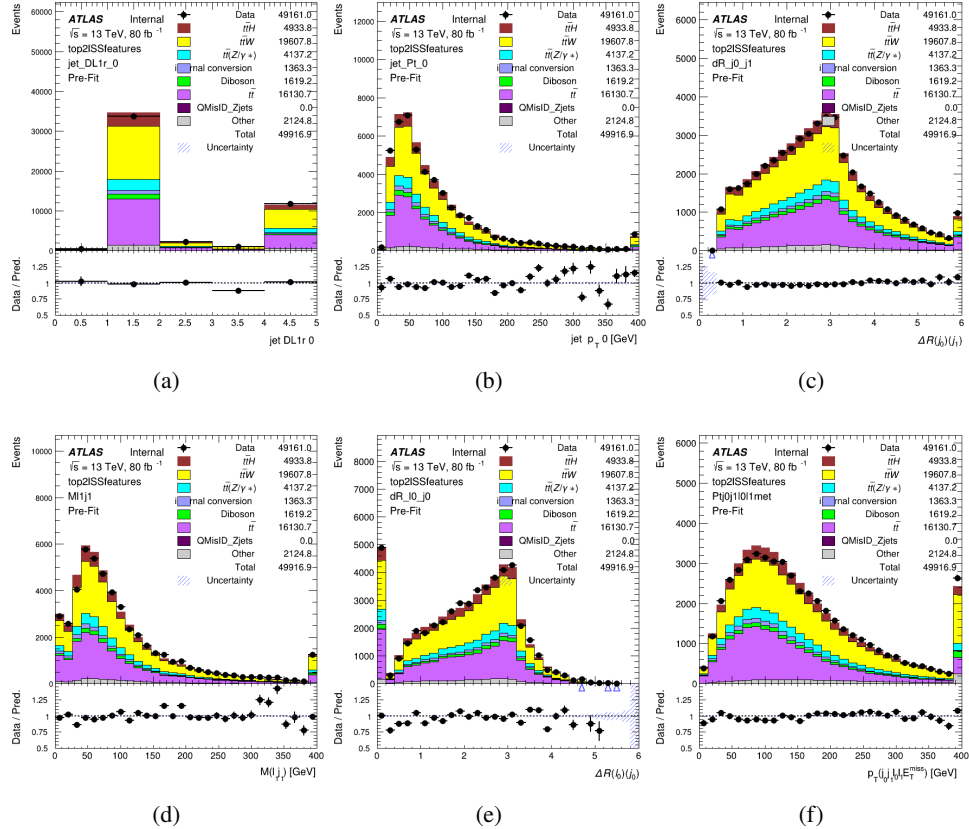


Figure 18.2: Data/MC comparisons of input features for top2ISS training for 80 fb^{-1} of data. (a) shows the DL1r working point of leading jet, (b) shows the p_T of the leading jet, (c) shows the ΔR of the two jets, (d) the invariant mass of lepton 1 and jet 1, (e) the ΔR of lepton 0 and jet 0, and (f) the p_T of both jets, both leptons, and the E_T^{miss} .

1304 Based on the results of grid search evaluation, the optimal architecture is found to include
 1305 5 hidden layers with 40 nodes each. No regularizer or dropout is added to the network, as
 1306 overfitting is found to not be an issue. The output score distribution as well as the ROC curve for
 1307 the trained model are shown in Figure 18.2.1. The model is found to identify the correct pairing
 1308 of jets for 73% of 2lSS signal events on test data.

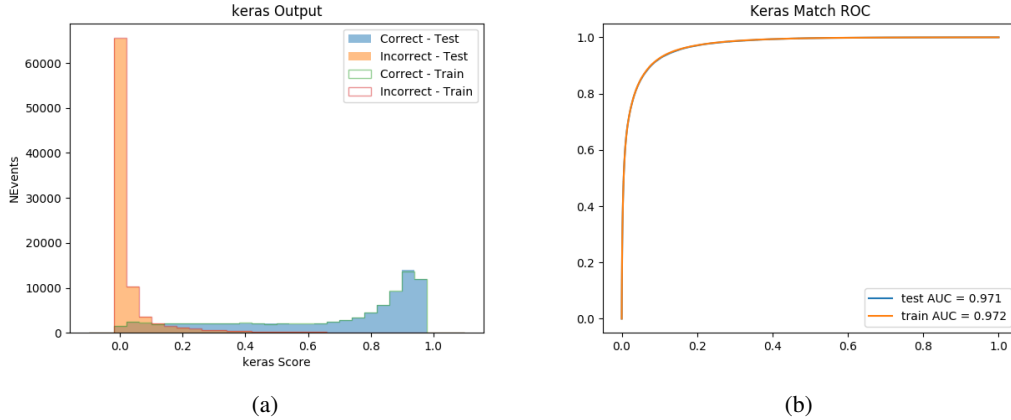


Figure 18.3: Results of the b-jet identification algorithm for the 2lSS channel, showing (a) the output score of the NN for correct and incorrect combinations of jets. (b) the ROC curve of the output, showing background rejection as a function of signal efficiency

1309 For point of comparison, a naïve approach to identify b-jets is used as well: The two jets
 1310 which pass the highest DL1r b-tag working point are assumed to be the b-jets from the top decay.
 1311 In the case that multiple jets meet the same b-tag working point, the jet with higher p_T is used.
 1312 This method identifies the correct jet pair 65% of the time.

1313 The accuracy of the model for different values of n-bjets, compared to this naive approach,
 1314 is shown in Table 31.

| b-jet Selection | Neural Network | Naive |
|-----------------|----------------|-------|
| 1 b-jet | 58.6% | 42.1% |
| 2 b-jets | 88.4% | 87.1% |
| ≥ 3 b-jets | 61.7% | 53.3% |
| Overall | 73.9% | 67.2% |

Table 31: Accuracy of the NN in identifying b-jets from tops in 2lSS events for, compared to the accuracy of taking the two highest b-tagged jets.

1315 **18.2.2 3l Channel**

1316 The input features used in the 3l channel are listed in Table 32, with the same naming convention
1317 as the 2lSS channel.

| | | |
|--|--|--------------------------------------|
| jet p_T 0 | jet p_T 1 | jet η 0 |
| jet η 1 | Lepton p_T 0 | Lepton p_T 1 |
| Lepton p_T 2 | $\Delta R(j_0)(j_1)$ | $M(j_0 j_1)$ |
| $\Delta R(l_0)(j_0)$ | $\Delta R(l_1)(j_0)$ | $\Delta R(l_2)(j_0)$ |
| $\Delta R(l_0)(j_1)$ | $\Delta R(l_1)(j_1)$ | $\Delta R(l_2)(j_1)$ |
| $M(l_0 j_0)$ | $M(l_1 j_0)$ | $M(l_2 j_0)$ |
| $M(l_0 j_1)$ | $M(l_1 j_1)$ | $M(l_2 j_1)$ |
| $\Delta R(j_0 l_0)(j_1 l_1)$ | $\Delta R(j_0 l_0)(j_1 l_2)$ | $\Delta R(j_0 l_1)(j_1 l_0)$ |
| $\Delta R(j_0 l_2)(j_1 l_0)$ | jet DL1r 0 | jet DL1r 1 |
| $p_T(j_0 j_1 l_0 l_1 l_2 E_T^{\text{miss}})$ | $M(t j_0 j_1 l_0 l_1 l_2 E_T^{\text{miss}})$ | $\Delta\phi(j_0)(E_T^{\text{miss}})$ |
| $\Delta\phi(j_1)(E_T^{\text{miss}})$ | HT Lepton | HT jets |
| nJets | E_T^{miss} | nJets OR DL1r 85 |
| nJets OR DL1r 60 | | |

Table 32: Input features for the b-jet identification algorithm in the 3l channel.

1318 A few of these features are shown in Figure 18.4, comparing the distributions for correct
1319 and incorrect combinations of jets.

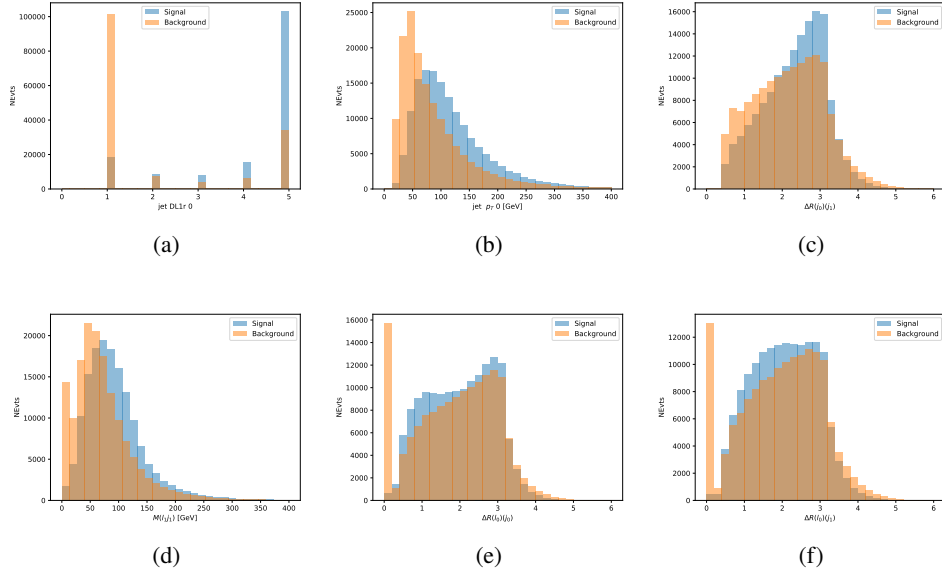


Figure 18.4: Input features for top3l training. The signal in blue represents events where both jet candidates are truth b-jets from top decays, and the orange is all other combinations. Scaled to the same number of events. (a) show the DL1r WP of jet 0, (b) the p_T of jet 0, (c) ΔR between jet 0 and jet 1, (d) the invariant mass of lepton 1 and jet 1, (e) ΔR between lepton 0 and jet 0, and (f) ΔR between lepton 0 and jet 1

1320

The modeling of these inputs is validated against data, with Figure 18.5 showing good

1321

general agreement between data and MC. Plots for the complete list of features can found in

1322

Section A.

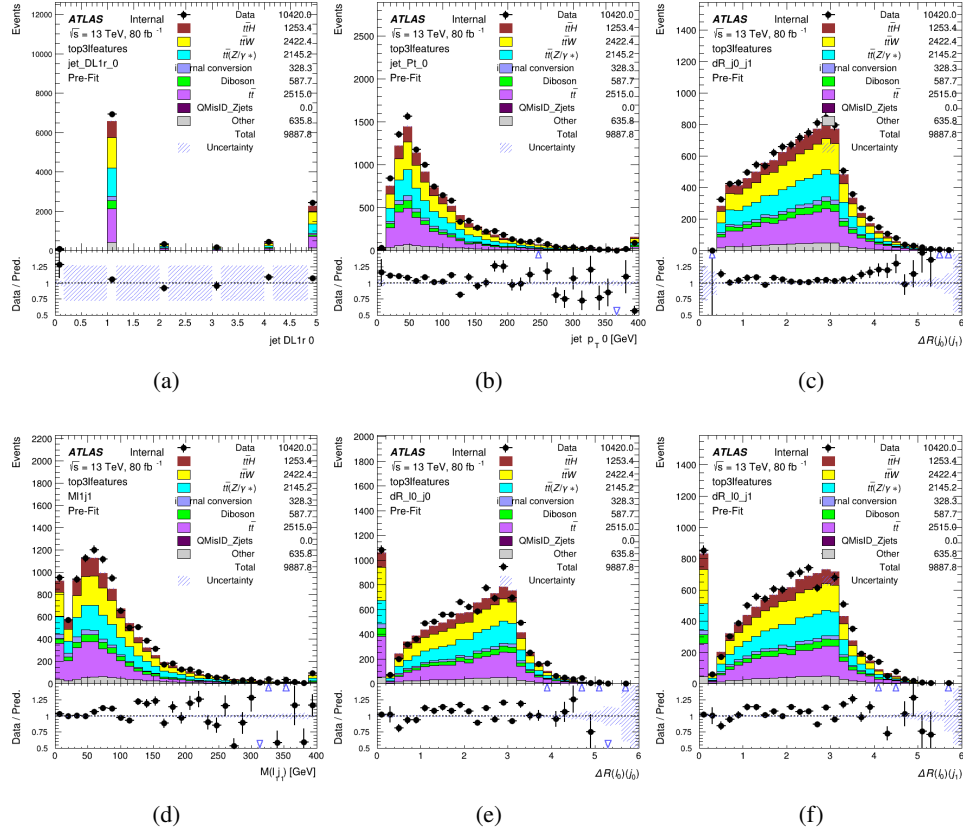


Figure 18.5: Data/MC comparisons of input features for top3l training for 80 fb^{-1} of data. (a) show the DL1r WP of jet 0, (b) the p_T of jet 0, (c) ΔR between jet 0 and jet 1, (d) the invariant mass of lepton 1 and jet 1, (e) ΔR between lepton 0 and jet 0, and (f) ΔR between lepton 0 and jet 1

Again, the dataset is downsized to reduce the ratio of correct and incorrect combination from 20:1, to 5:1. Around 7 million events are used for training, with 10% set aside for testing. Based on the results of grid search evaluation, the optimal architecture is found to include 5 hidden layers with 60 nodes each. The output score distribution as well as the ROC curve for the trained model are shown in Figure 18.2.2.

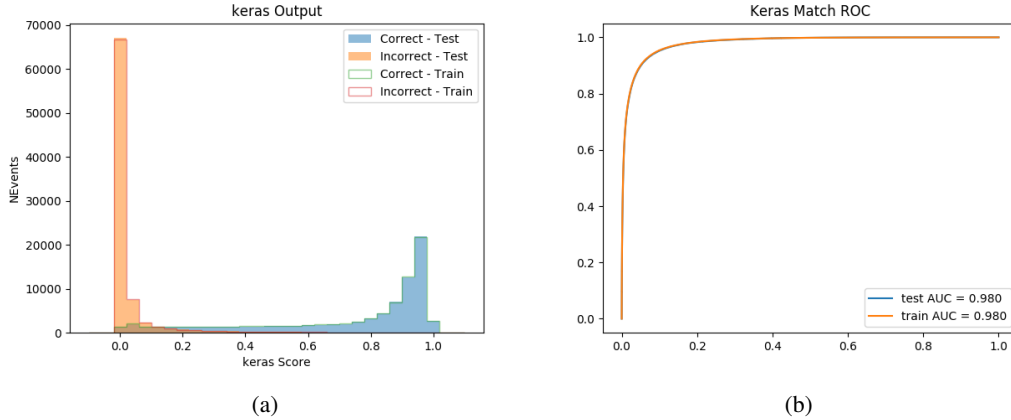


Figure 18.6: Results of the b-jet identification algorithm for the 3l channel, showing (a) the output score of the NN for correct and incorrect combinations of jets. (b) the ROC curve of the output, showing background rejection as a function of signal efficiency

1328 This procedure is found to identify the correct pairing of jets for nearly 80% of 3l signal
 1329 events. The accuracy of the model is summarized in Table 33.

Table 33: Accuracy of the NN in identifying b-jets from tops, compared to the naive method of taking the highest b-tagged jets.

| | NN | Naive |
|-----------------|-------|-------|
| 1 b-jet | 69.0% | 48.9% |
| 2 b-jets | 89.6% | 88.3% |
| ≥ 3 b-jets | 55.7% | 52.3% |
| Overall | 79.8% | 70.2% |

1330 18.3 Higgs Reconstruction

1331 Techniques similar to the b-jet identification algorithms are employed to select the decay products
 1332 of the Higgs: kinematics of all possible combinations of reconstructed objects are fed into a neural
 1333 network to determine which of those is most likely to be the decay products of the Higgs.

1334 Again separate models are used for the 2lSS and 3l channels, while the 3l channel has now
1335 been split into two: $t\bar{t}H$ events with three leptons in the final state include both instances where
1336 the Higgs decays into a lepton (and a neutrino) and a pair of jets, and instances where the Higgs
1337 decays to two leptons.

1338 3l events are therefore categorized as either semi-leptonic (3lS) or fully-leptonic (3lF). In
1339 the semi-leptonic case the reconstructed decay products consist of two jets and a single lepton.
1340 For the fully-leptonic case, the decay products include 2 of the three leptons associated with the
1341 event. For training the models, events are separated into these two categories using truth level
1342 information. A separate MVA, described in Section 18.5, is used to make this distinction at reco
1343 level and determine which model to use.

1344 For all channels, the models described in Section 18.2 are used to identify b-jet candidates,
1345 whose kinematics are used to identify the Higgs decay products. These jets are not considered
1346 as possible candidates for the Higgs decay, justified by the fact that these models are found to
1347 misidentify jets from the Higgs decay as jets from the top decay less than 1% of the time.

1348 18.3.1 2lSS Channel

1349 For the 2lSS channel, the Higgs decay products include one light lepton and two jets. The neural
1350 network is trained on the kinematics of different combinations of leptons and jets, as well as the
1351 b-jets identified in Section 18.2, with the specific input features listed in Table 34.

| Lepton p_T H | Lepton p_T T | jet p_T 0 |
|--|--------------------------|--------------------------|
| jet p_T 1 | top p_T 0 | top p_T 1 |
| top η 0 | top η 1 | jet η 0 |
| jet η 1 | jet Phi 0 | jet Phi 1 |
| Lepton η H | Lepton heta T | $\Delta R(j_0)(j_1)$ |
| $\Delta R(l_H)(j_0)$ | $\Delta R(l_H)(j_1)$ | $M(j_0 j_1)$ |
| $M(l_H j_0)$ | $M(l_H j_1)$ | $\Delta R(l_H)(b_0)$ |
| $\Delta R(l_H)(b_1)$ | $\Delta R(l_T)(b_0)$ | $\Delta R(l_T)(b_1)$ |
| $\Delta R(j_0 j_1)(l_H)$ | $\Delta R(j_0 j_1)(l_T)$ | $\Delta R(j_0 j_1)(b_0)$ |
| $\Delta R(j_0 j_1)(b_1)$ | $\Delta R(j_0)(b_0)$ | $\Delta R(j_0)(b_1)$ |
| $\Delta R(j_1)(b_0)$ | $\Delta R(j_1)(b_1)$ | $M(j_0 j_1 l_H)$ |
| $p_T(j_0 j_1 l_H l_T b_0 b_1 E_T^{\text{miss}})$ | topScore | E_T^{miss} |
| nJets | HT jets | |

Table 34: Input features used to identify the Higgs decay products in 2ISS events

1352 Here j_0 and j_1 , and l_H are the jet and lepton decay candidates, respectively. The other
 1353 lepton in the event is labeled l_T , as it is assumed to have come from the decay of one of the top
 1354 quarks. b_0 and b_1 are the two b-jets identified by the b-jet identification algorithm. The b-jet
 1355 Reco Score is the output of the b-jet reconstruction algorithm.

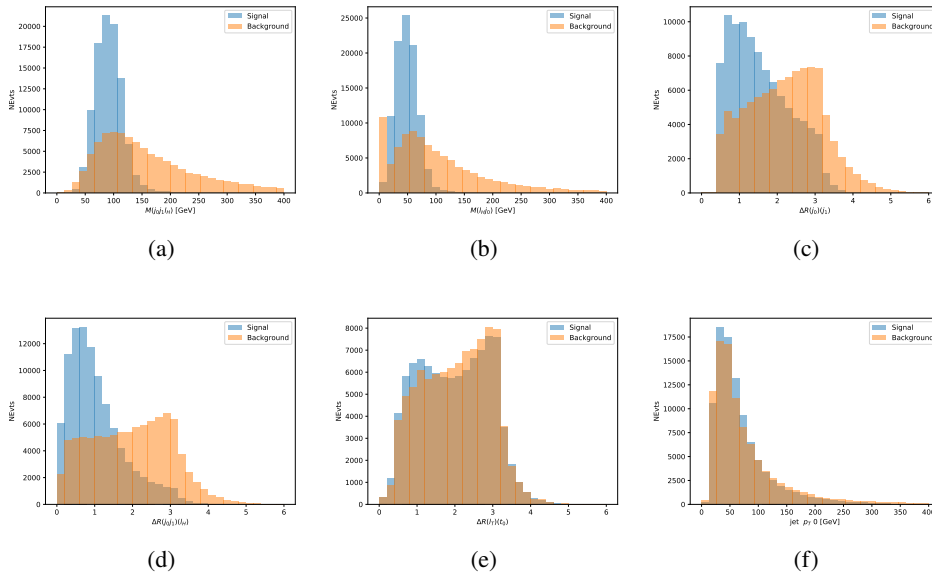


Figure 18.7: Input features for higgs2lSS training. The signal in blue represents events where both jet candidates are truth b-jets from top decays, and the orange is all other combinations. Scaled to the same number of events. (a) shows the invariant mass of the two jet candidates and the lepton candidate, (b) the invariant mass of jet 0 and the lepton candidate, (c) ΔR between the jet candidates, (d) ΔR between jet 0 + jet 1 and the lepton candidate, (e) ΔR between the lepton from the top and the leading b-jet, (f) the p_T of jet 0.

1356 The modeling of these inputs is validated against data, with Figure 18.2 showing good
 1357 general agreement between data and MC. Plots for the complete list of features can found in
 1358 Section A.

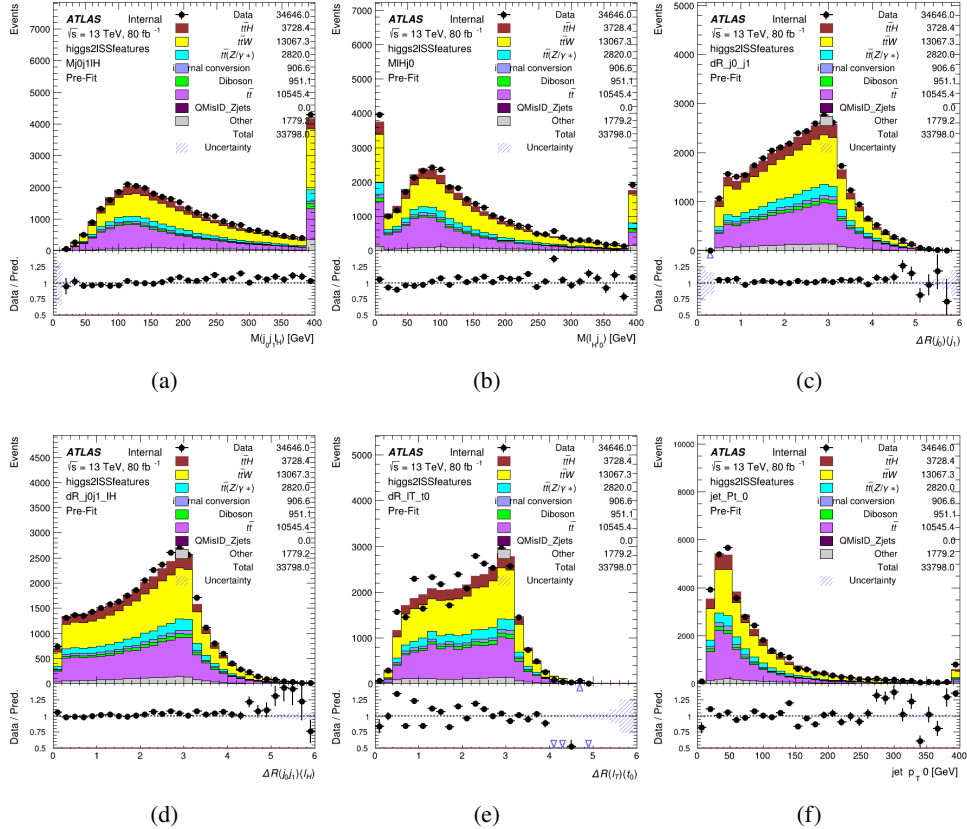


Figure 18.8: Data/MC comparisons of input features for higgs2lSS training for 80 fb^{-1} of data. (a) shows the invariant mass of the two jet candidates and the lepton candidate, (b) the invariant mass of jet 0 and the lepton candidate, (c) ΔR between the jet candidates, (d) ΔR between jet 0 + jet 1 and the lepton candidate, (e) ΔR between the lepton from the top and the leading b-jet, (f) the p_T of jet 0.

1359 A neural network consisting of 7 hidden layers with 60 nodes each is trained on around 2
 1360 million events, with an additional 200,000 reserved for testing the model. In order to compensate
 1361 for large number of incorrect combinations, these have been downsampled such that the correct
 1362 combinations represent over 10% of the training set. The output of the NN is summarized in
 1363 Figure 18.3.1.

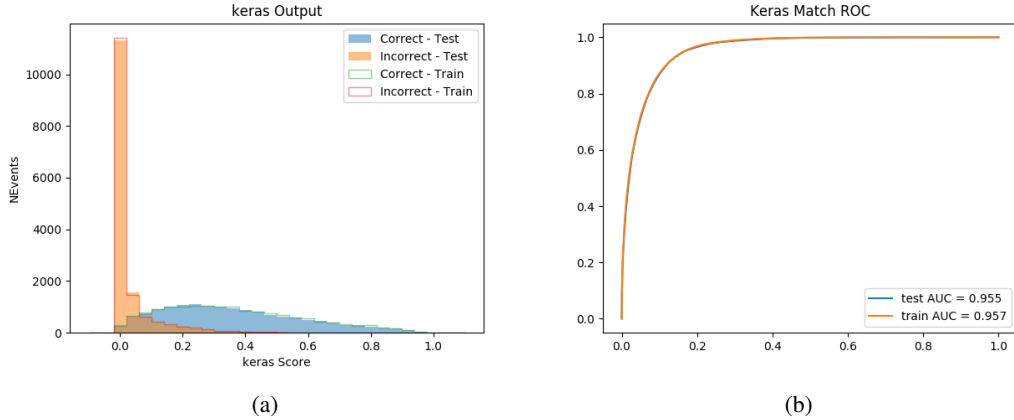


Figure 18.9: Result of the Higgs reconstruction algorithm in the 2lSS channel, showing (a) the output score of the NN for correct and incorrect combinations of jets scaled to an equal number of events, and (b) the ROC curve of the output, showing background rejection as a function of signal efficiency

1364 The neural network identifies the correct combination 55% of the time. It identifies the
 1365 correct lepton 85% of the time, and selects the correct lepton and at least one of the correct jets
 1366 81% of the time.

1367 **18.3.2 3l Semi-leptonic Channel**

1368 For 3l $t\bar{t}H$ where the Higgs decay semi-leptonically, the decay products include one of the three
 1369 leptons and two jets. In this case, the other two leptons originated from the decay of the tops,
 1370 meaning the opposite-sign (OS) lepton cannot have come from the Higgs. This leaves only the two
 1371 same-sign (SS) leptons as possible Higgs decay products.

| Lepton p_T H | Lepton p_T T_0 | Lepton p_T T_1 |
|--|---|--------------------------------|
| jet p_T 0 | jet p_T 1 | top p_T 0 |
| top p_T 1 | jet η 0 | jet η 1 |
| jet ϕ 0 | jet ϕ 1 | $\Delta R(j_0)(j_1)$ |
| $M(j_0j_1)$ | $\Delta R(l_H)(j_0)$ | $\Delta R(l_H)(j_1)$ |
| $\Delta R(j_0j_1)(l_H)$ | $\Delta R(j_0j_1)(l_{T_1})$ | $\Delta R(l_{T_0})(l_{T_1})$ |
| $\Delta R(l_H)(l_{T_1})$ | $M(j_0j_1l_{T_0})$ | $M(j_0j_1l_{T_1})$ |
| $M(j_0j_1l_H)$ | $\Delta R(j_0j_1l_H)(l_{T_0})$ | $\Delta R(j_0j_1l_H)(l_{T_1})$ |
| $\Delta\phi(j_0j_1l_H)(E_T^{\text{miss}})$ | $p_T(j_0j_1l_Hl_{T_0}l_{T_1}b_0b_1E_T^{\text{miss}})$ | $M(j_0j_1b_0)$ |
| $M(j_0j_1b_1)$ | $\Delta R(l_{T_0})(b_0)$ | $\Delta R(l_{T_0})(b_1)$ |
| $\Delta R(l_{T_1})(b_0)$ | $\Delta R(l_{T_1})(b_1)$ | $\Delta R(j_0)(b_0)$ |
| $\Delta R(j_0)(b_1)$ | $\Delta R(j_1)(b_0)$ | $\Delta R(j_1)(b_1)$ |
| topScore | MET | HT jets |
| nJets | | |

Table 35: Input features used to identify the Higgs decay products in 3lS events

1372 Here j_0 and j_1 , and l_H are the jet and lepton decay candidates, respectively. The other
 1373 two leptons in the event are labeled as l_{T0} and l_{T1} . b_0 and b_1 are the two b-jets identified by
 1374 the b-jet identification algorithm. The b-jet Reco Score is the output of the Higgs reconstruction
 1375 algorithm.

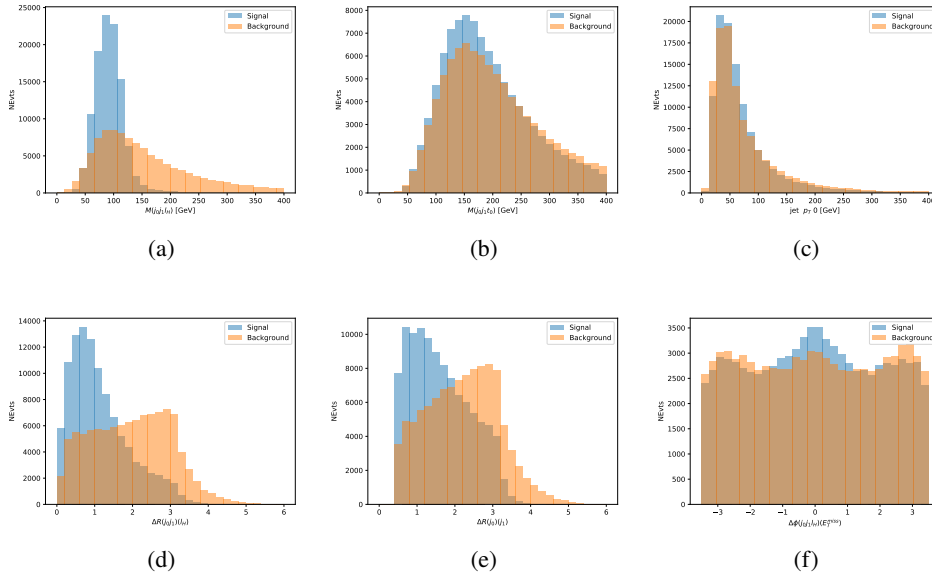


Figure 18.10: Input features for higgs3lS training. The signal in blue represents events where both jet candidates are truth b-jets from top decays, and the orange is all other combinations. Scaled to the same number of events.

1376 The modeling of these inputs is validated against data, with Figure 18.11 showing good
 1377 general agreement between data and MC. Plots for the complete list of features can found in
 1378 appendix A.1.

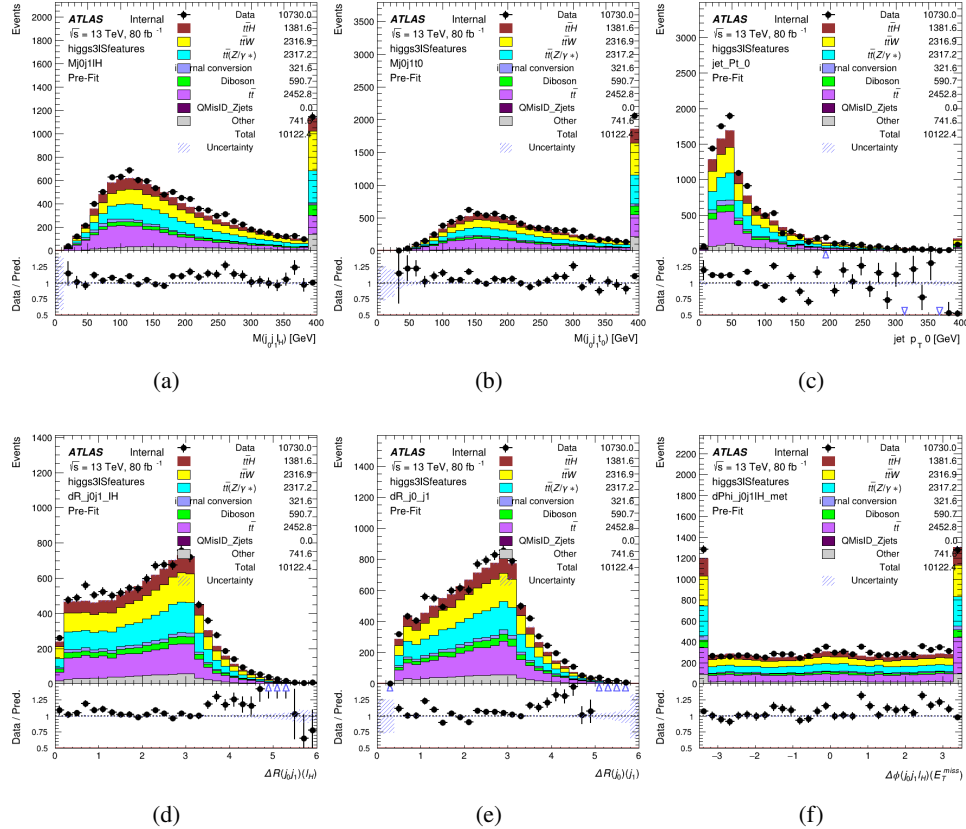


Figure 18.11: Data/MC comparisons of input features for higgs3IS training for 80 fb^{-1} of data.

1379 A neural network of 7 hidden layers with 70 nodes each is trained on 1.8 million events.

1380 Once again, incorrect combinations are downsampled, such that the correct combinations are

1381 around 10% of the training set. 10% of the dataset is reserved for testing. The output of the NN

1382 is summarized in Figure 18.3.2.

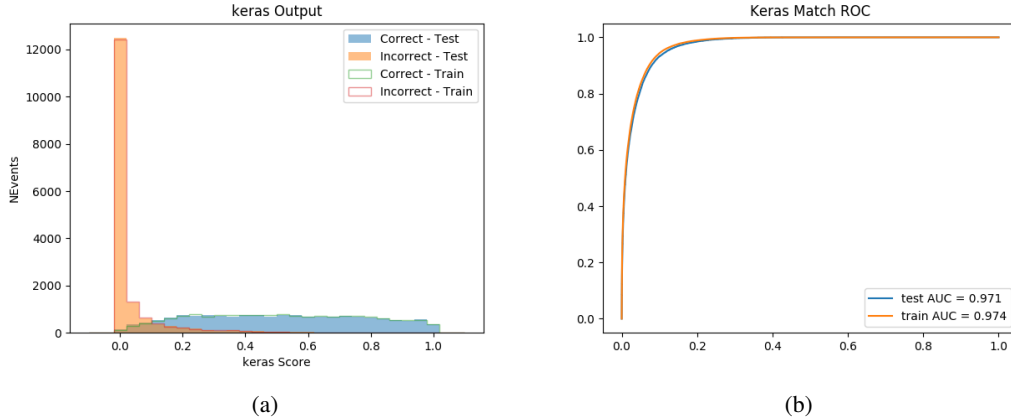


Figure 18.12: Results of the Higgs reconstruction algorithm in the 3lS channel, showing (a) the output score of the NN for correct and incorrect combinations of jets, scaled to an equal number of entries.,. (b) the ROC curve of the output, showing background rejection as a function of signal efficiency

1383 The neural network identifies the correct combination 64% of the time. It identifies the
 1384 correct lepton 85% of the time, and selects the correct lepton and at least one of the correct jets
 1385 83% of the time.

1386 18.3.3 3l Fully-leptonic Channel

1387 In the fully-leptonic 3l case, the goal is identify which two of the three leptons originated from
 1388 the Higgs decay. Since one of these two must be the OS lepton, this problem is reduced to
 1389 determining which of the two SS leptons originated from the Higgs. The kinematics of both
 1390 possibilities are used for training, one where the SS lepton from the Higgs is correctly labeled,
 1391 and one where it is not.

| Lepton $p_T H_1$ | Lepton $p_T H_0$ | Lepton $p_T T$ |
|--------------------------------------|---------------------------------|--|
| top $p_T 0$ | top $p_T 1$ | $\Delta\phi(l_{H_1})(E_T^{\text{miss}})$ |
| $\Delta\phi(l_T)(E_T^{\text{miss}})$ | $M(l_{H_0}l_{H_1})$ | $M(l_{H_1}l_T)$ |
| $M(l_{H_0}l_T)$ | $\Delta R(l_{H_0})(l_{H_1})$ | $\Delta R(l_{H_1})(l_T)$ |
| $\Delta R(l_{H_0})(l_T)$ | $\Delta R(l_{H_0}l_{H_1})(l_T)$ | $\Delta R(l_{H_0}l_T)(l_{H_1})$ |
| $\Delta R(l_{H_0}l_{H_1})(b_0)$ | $\Delta R(l_{H_0}l_{H_1})(b_1)$ | $\Delta R(l_{H_0}b_0)$ |
| $M(l_{H_0}b_0)$ | $\Delta R(l_{H_0}b_1)$ | $M(l_{H_0}b_1)$ |
| $\Delta R(l_{H_1}b_0)$ | $M(l_{H_1}b_0)$ | $\Delta R(l_{H_1}b_1)$ |
| $M(l_{H_1}b_1)$ | E_T^{miss} | topScore |

Table 36: Input features used to identify the Higgs decay products in 3lF events

1392 Here l_{H0} and l_{H1} are the Higgs decay candidates. The other lepton in the event is labeled
 1393 l_T . b_0 and b_1 are the two b-jets identified by the b-jet identification algorithm. The b-jet Reco
 1394 Score is the output of the Higgs reconstruction algorithm.

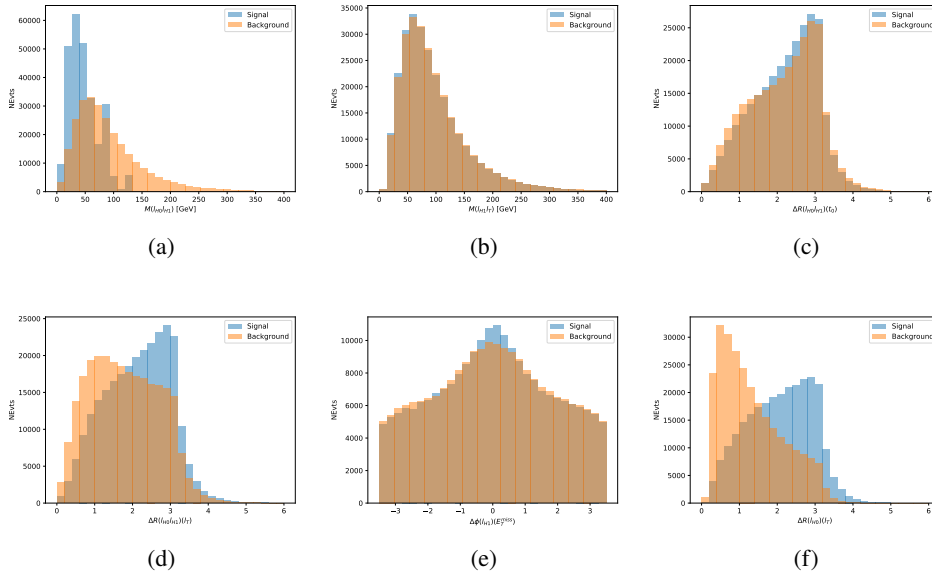


Figure 18.13: Input features for higgs3IF training. The signal in blue represents events where both jet candidates are truth b-jets from top decays, and the orange is all other combinations. Scaled to the same number of events.

1395 The modeling of these inputs is validated against data, with Figure 18.14 showing good
 1396 general agreement between data and MC. Plots for the complete list of features can found in
 1397 Section A.

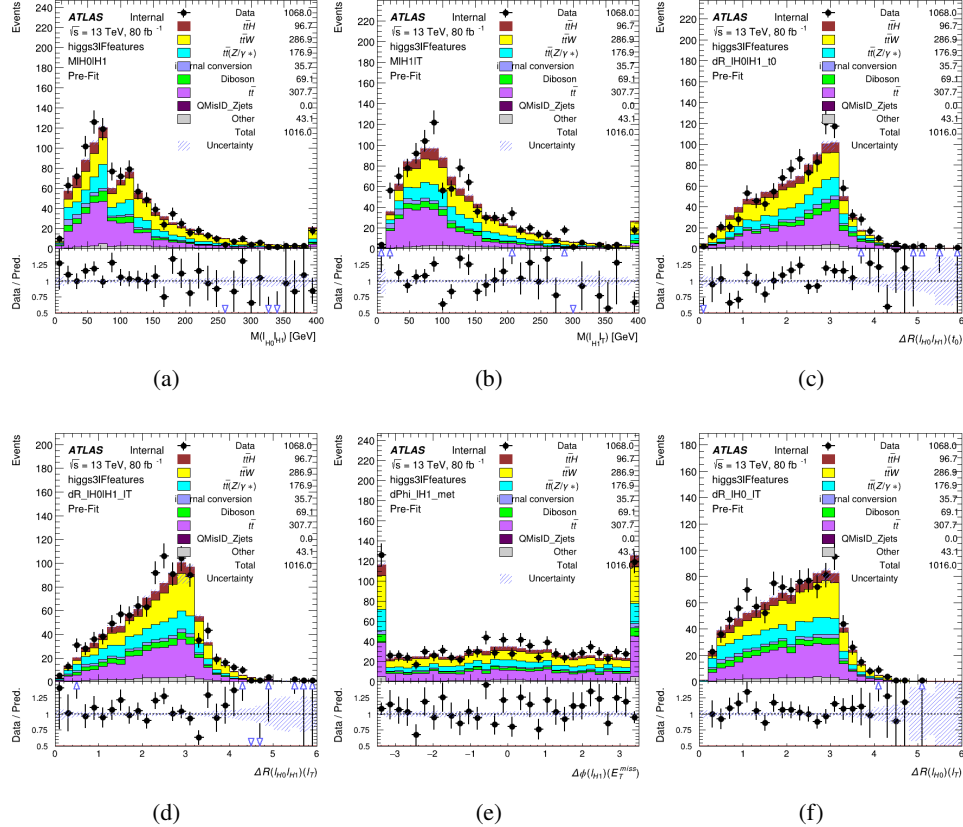


Figure 18.14: Data/MC comparisons of input features for higgs3IF training for 80 fb^{-1} of data.

1398 A neural network consisting of 5 nodes and 60 hidden units is trained on 800,000 events,
 1399 with 10% of the dataset reserved for testing. The output of the model is summarized in Figure
 1400 **18.3.3.**

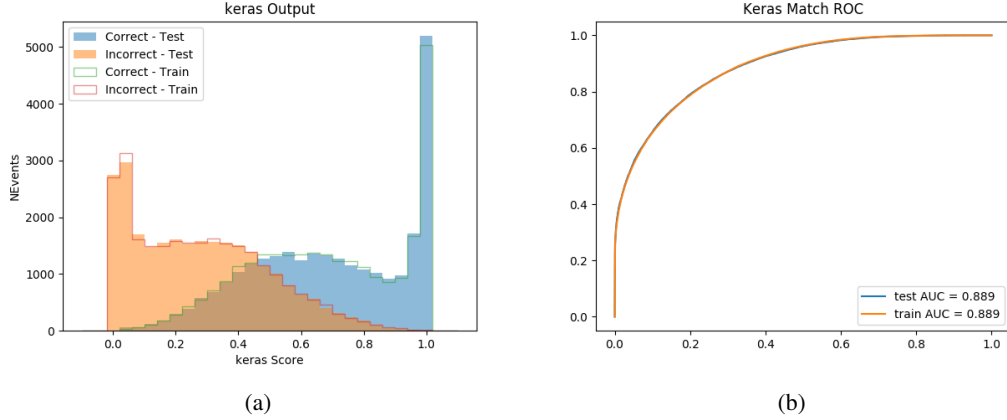


Figure 18.15: (a) the output score of the NN for correct and incorrect combinations of jets. (a) the ROC curve of the output, showing background rejection as a function of signal efficiency

1401 The correct lepton is identified by the model for 80% of events in the testing data set.

1402 **18.4 p_T Prediction**

1403 Once the most probable decay products have been identified, their kinematics are used as inputs
 1404 to a regression model which attempts to predict the momentum of the Higgs Boson. Once again,
 1405 a DNN is used. Input variables representing the b-jets and leptons not from the Higgs decay
 1406 are included as well, as these are found to improve performance. The truth p_T of the Higgs,
 1407 as predicted by MC, are used as labels. Separate models are built for each channel - 2lSS, 3l
 1408 Semi-leptonic and 3l Fully-leptonic.

1409 As a two-bin fit is targeted for the final result, some metrics evaluating the performance
 1410 of the models aim to show how well it distinguished between "high p_T " and "low p_T " events. A

¹⁴¹¹ cutoff point of 150 GeV is used to define these two categories.

¹⁴¹² Because the analysis uses a two bin fit of the Higgs p_T , the momentum reconstruction
¹⁴¹³ could be treated as a binary classification problem, rather than a regression problem. This
¹⁴¹⁴ approach is explored in detail in Section A.4, and is found not to provide any significant increase
¹⁴¹⁵ in sensitivity. The regression approach is used because it provides more flexibility for future
¹⁴¹⁶ analyses, as it is independent of the cutoff between high and low p_T , as well as the number of
¹⁴¹⁷ bins. Further, a regression allows the output of the neural network to be more clearly understood,
¹⁴¹⁸ as it can be directly compared to a physics observable.

¹⁴¹⁹ **18.4.1 2lSS Channel**

¹⁴²⁰ The input variables listed in Table 37 are used to predict the Higgs p_T in the 2lSS channel. Here
¹⁴²¹ j_0 and j_1 are the two jets identified as Higgs decay products. The lepton identified as originating
¹⁴²² from the Higgs is labeled l_H , while the other lepton is labeled l_T , as it is assumed to have come
¹⁴²³ from the decay of one of the top quarks. b_0 and b_1 are the two b-jets identified by the b-jet
¹⁴²⁴ identification algorithm. The Higgs Reco Score and b-jet Reco Score are the outputs of the Higgs
¹⁴²⁵ reconstruction algorithm, and the b-jet identification algorithm, respectively.

| HT | $M(j_0 j_1)$ | $M(j_0 j_1 l_H)$ |
|------------------------------|--|------------------------------|
| $M(l_H j_0)$ | $M(l_H j_1)$ | $p_T(b_0 b_1)$ |
| $p_T(j_0 j_1 l_H)$ | $\Delta\phi(j_0 j_1 l_H)(E_T^{\text{miss}})$ | $\Delta R(j_0)(j_1)$ |
| $\Delta R(j_0 j_1)(l_H)$ | $\Delta R(j_0 j_1 l_H)(l_T)$ | $\Delta R(j_0 j_1 l_H)(b_0)$ |
| $\Delta R(j_0 j_1 l_H)(b_1)$ | $\Delta R(l_H)(j_0)$ | $\Delta R(l_H)(b_0)$ |
| $\Delta R(l_H)(b_1)$ | $\Delta R(l_T)(b_0)$ | $\Delta R(l_T)(b_1)$ |
| $\Delta R(b_0)(b_1)$ | Higgs Reco Score | jet η 0 |
| jet η 1 | jet Phi 0 | jet Phi 1 |
| jet p_T 0 | jet p_T 1 | Lepton η H |
| Lepton ϕ H | Lepton p_T H | Lepton p_T T |
| E_T^{miss} | nJets | b-jet Reco Score |
| b-jet p_T 0 | b-jet p_T 1 | |

Table 37: Input features for reconstructing the Higgs p_T spectrum for 2lSS events

1426 The optimal neural network architecture for this channel is found to consist of 7 hidden
 1427 layers with 60 nodes each. The input data set includes 1.2 million events, 10% of which is used
 1428 for testing, the other 90% for training. Training is found to converge after around 150 epochs.

1429 To evaluate the performance of the model, the predicted p_T spectrum is compared to the
 1430 truth Higgs p_T in Figure 18.16. In order to visualize the model performance more clearly, in (a)
 1431 of that figure, the color of each point is determined by Kernel Density Estimation (KDE). The
 1432 color shown represents the logarithm of the output from KDE, to counteract the large number of
 1433 low p_T events. For that same reason, each column of the histogram shown in (b) of Figure 18.16
 1434 is normalized to unity. This plot therefore demonstrates what the model predicts for each slice
 1435 of truth p_T .

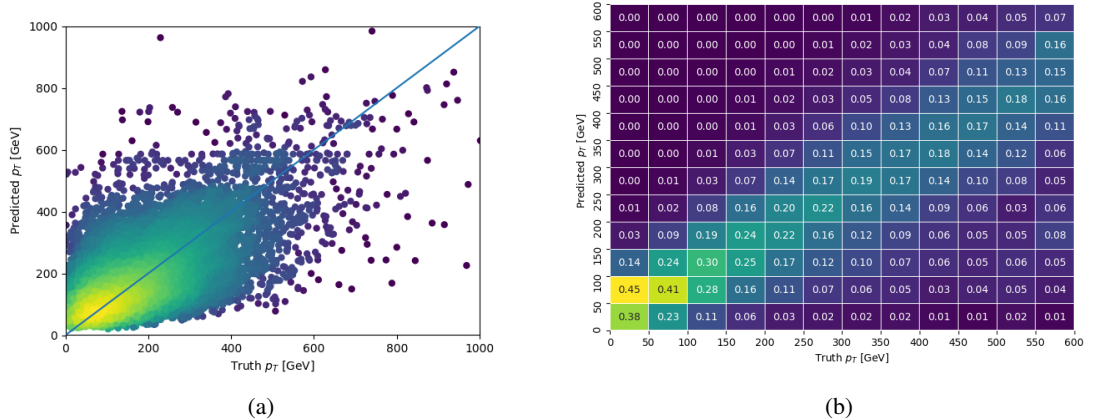


Figure 18.16: The regressed Higgs momentum spectrum as a function of the truth p_T for 2lSS $t\bar{t}H$ events in (a) a scatterplot, where the color of each point represents the log of the point density, based on Gaussian Kernel Density Estimation, and (b) a histogram where each column has been normalized to one.

1436 We are also interested in how well the model distinguishes between events with $p_T < 150$

1437 GeV and >150 GeV. Figure 18.17 demonstrates the NN output for high and low p_T events based
 1438 on this cutoff.

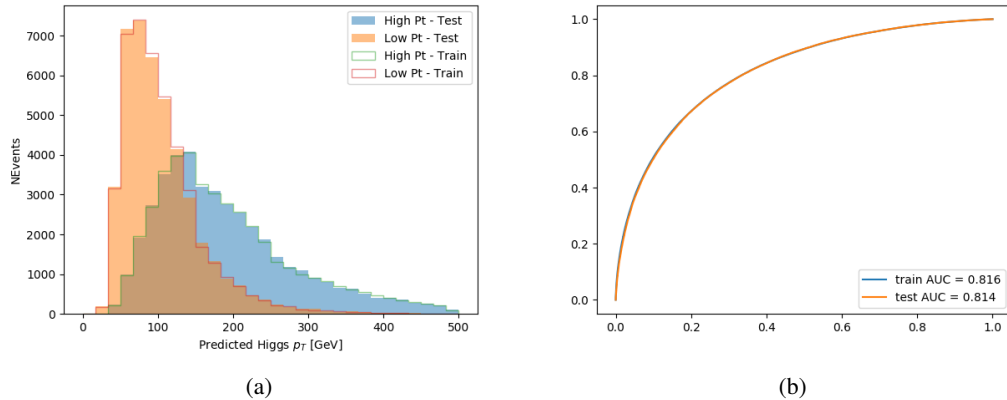


Figure 18.17: (a) shows the reconstructed Higgs p_T for 2lSS events with truth $p_T > 150$ GeV and < 150 GeV, while (b) shows the ROC curve for those two sets of events.

1439 18.4.2 3l Semi-leptonic Channel

1440 The following input features are used to predict the Higgs p_T for events in the 3lS channel:

| HT jets | MET | $M(j_0 j_1)$ |
|--|---------------------------------|------------------------------|
| $M(j_0 j_1 l_H)$ | $M(j_0 j_1 l_{T0})$ | $M(j_0 j_1 l_{T1})$ |
| $M(j_0 j_1 b_0)$ | $M(j_0 j_1 b_1)$ | $M(b_0 l_{T0})$ |
| $M(b_0 l_{T1})$ | $M(b_1 l_{T0})$ | $M(b_1 l_{T1})$ |
| $\Delta\phi(j_0 j_1 l_H)(E_T^{\text{miss}})$ | $\Delta R(j_0)(j_1)$ | $\Delta R(j_0 j_1)(l_H)$ |
| $\Delta R(j_0 j_1)(l_{T1})$ | $\Delta R(j_0 j_1)(b_0)$ | $\Delta R(j_0 j_1)(b_1)$ |
| $\Delta R(j_0 j_1 l_H)(l_{T0})$ | $\Delta R(j_0 j_1 l_H)(l_{T1})$ | $\Delta R(j_0 j_1 l_H)(b_0)$ |
| $\Delta R(j_0 j_1 l_H)(b_1)$ | $\Delta R(l_H)(j_0)$ | $\Delta R(l_H)(j_1)$ |
| $\Delta R(l_H)(l_{T1})$ | $\Delta R(l_{T0})(l_{T1})$ | $\Delta R(l_{T0})(b_0)$ |
| $\Delta R(l_{T0})(b_1)$ | $\Delta R(l_{T1})(b_0)$ | $\Delta R(l_{T1})(b_1)$ |
| higgsScore | jet η 0 | jet η 1 |
| jet ϕ 0 | jet ϕ 1 | jet p_T 0 |
| jet p_T 1 | Lepton η H | Lepton ϕ H |
| Lepton p_T H | Lepton p_T T0 | Lepton p_T T1 |
| nJets | topScore | b-jet p_T 0 |
| b-jet p_T 1 | | |

Table 38: Input features for reconstructing the Higgs p_T spectrum for 3lS events

Again, j_0 and j_1 are the two jets identified as Higgs decay products, ordered by p_T . The lepton identified as originating from the Higgs is labeled l_H , while the other two leptons are labeled l_{T0} and l_{T1} . b_0 and b_1 are the two b-jets identified by the b-jet identification algorithm. The Higgs Reco Score and b-jet Reco Score are the outputs of the Higgs reconstruction algorithm, and the b-jet identification algorithm, respectively.

The optimal neural network architecture for this channel is found to consist of 7 hidden layers with 80 nodes each. The inputdata set includes one million events, 10% of which is used for testing, the other 90% for training. Training is found to converge after around 150 epochs.

To evaluate the performance of the model, the predicted p_T spectrum is compared to the truth Higgs p_T in Figure 18.18. Once again, (a) of 18.18 shows a scatterplots of predicted vs truth p_T , where the color of each point corresponds to the log of the relative KDE at that point. Each column of the the histogram in (b) is normalized to unity, to better demonstrate the output of the NN for each slice of truth p_T .

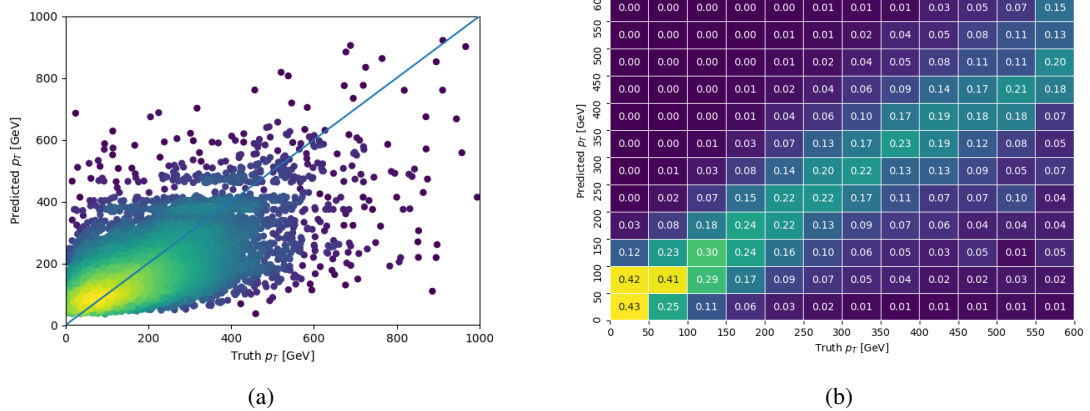


Figure 18.18: The regressed Higgs momentum spectrum as a function of the truth p_T for 3lS $t\bar{t}H$ events in (a) a scatterplot, where the color of each point represents the log of the point density, based on Gaussian Kernel Density Estimation, and (b) a histogram where each column has been normalized to one.

1454 Figure 18.19 shows (a) the output of the NN for events with truth p_T less than and greater
 1455 than 150 GeV and (b) the ROC curve demonstrating how well the NN distinguishes high and low
 1456 p_T events.

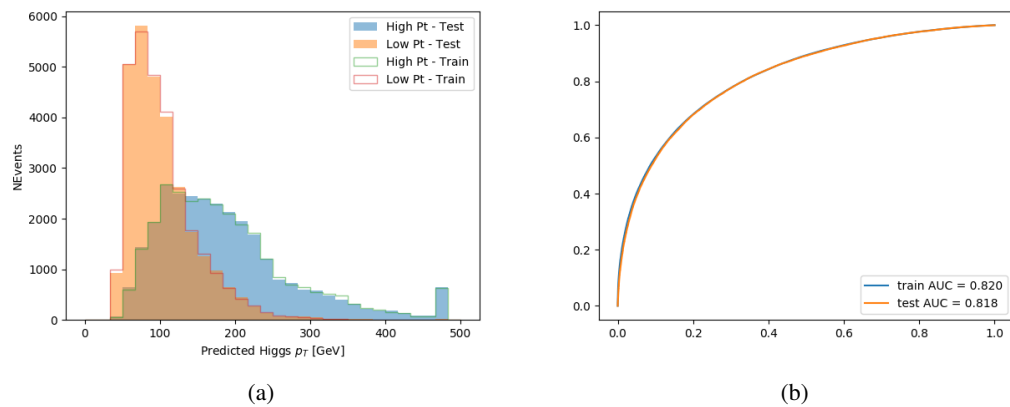


Figure 18.19: (a) shows the reconstructed Higgs p_T for 3lS events with truth $p_T > 150$ GeV and < 150 GeV, while (b) shows the ROC curve for those two sets of events.

18.4.3 3l Fully-leptonic Channel

1457 The features listed in 39 are used to construct a model for predictin the Higgs p_T for 3lF events.

1458 The features listed in 39 are used to construct a model for predictin the Higgs p_T for 3lF events.

| HT | $M(l_{H0}l_{H1})$ | $M(l_{H0}l_T)$ |
|-------------------------|-------------------------------|-------------------------------|
| $M(l_{H0}b_0)$ | $M(l_{H0}b_1)$ | $M(l_{H1}l_T)$ |
| $M(l_{H1}b_0)$ | $M(l_{H1}b_1)$ | $\Delta R(l_{H0})(l_{H1})$ |
| $\Delta R(l_{H0})(l_T)$ | $\Delta R(l_{H0}l_{H1})(l_T)$ | $\Delta R(l_{H0}l_T)(l_{H1})$ |
| $\Delta R(l_{H1})(l_T)$ | $\Delta R(l_{H0}b_0)$ | $\Delta R(l_{H0}b_1)$ |
| $\Delta R(l_{H1}b_1)$ | $\Delta R(l_{H1}b_0)$ | higgsScore |
| Lepton η H_0 | Lepton η H_1 | Lepton η T |
| Lepton p_T H_0 | Lepton p_T H_1 | Lepton p_T T |
| E_T^{miss} | topScore | b-jet p_T 0 |
| b-jet p_T 1 | | |

Table 39: Input features for reconstructing the Higgs p_T spectrum for 3lF events

1459 l_{H0} and l_{H1} represent the two leptons identified by the Higgs reconstruction model as
 1460 originating from the Higgs, while l_T is the other lepton in the event. The Higgs Reco Score and
 1461 b-jet Reco Score are the outputs of the Higgs reconstruction algorithm, and b-jet identification
 1462 algorithm, respectively.

1463 The optimal neural network architecture for this channel is found to consist of 5 hidden
 1464 layers with 40 nodes each. The input data set includes 400,000 events, 10% of which is used for
 1465 testing, the other 90% for training. Training is found to converge after around 150 epochs.

1466 The predicted transverse momentum, as a function of the truth p_T , is shown in Figure
 1467 [18.20](#).

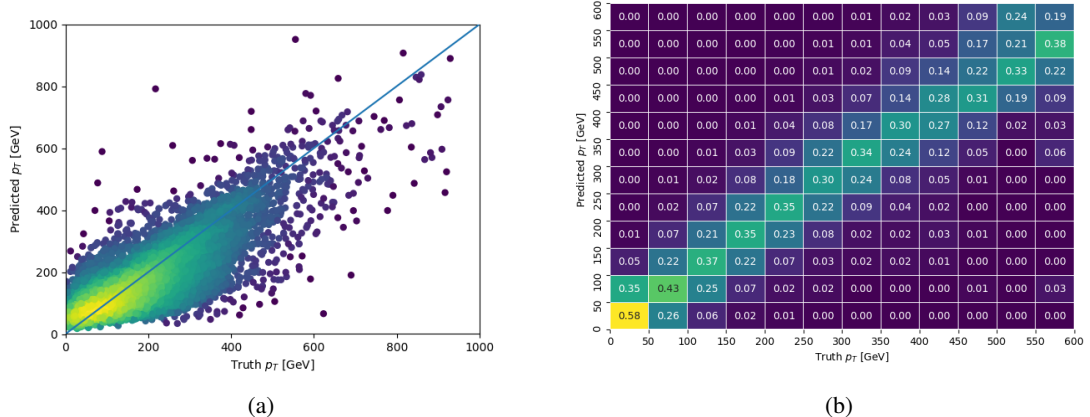


Figure 18.20: The regressed Higgs momentum spectrum as a function of the truth p_T for 3lF $t\bar{t}H$ events in (a) a scatterplot, where the color of each point represents the log of the point density, based on Gaussian Kernel Density Estimation, and (b) a histogram where each column has been normalized to one.

1468 When split into high and low p_T , based on a cutoff of 150 GeV, the

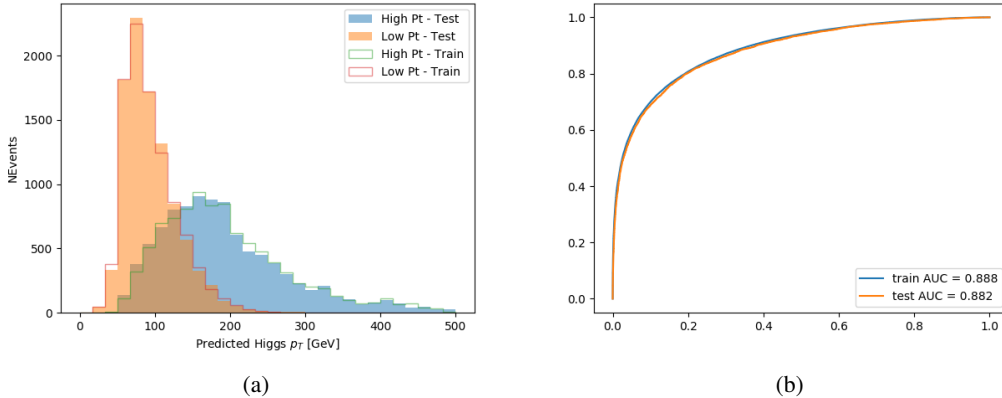


Figure 18.21: (a) shows the reconstructed Higgs p_T for 3lF events with truth $p_T > 150$ GeV and < 150 GeV, while (b) shows the ROC curve for those two sets of events.

18.5 3l Decay Mode

In the 3l channel, there are two possible ways for the Higgs to decay, both involving intermediate W boson pairs: Either both W bosons decay leptonically, in which case the reconstructed decay consists of two leptons (referred as the fully-leptonic 3l channel), or one W decays leptonically and the other hadronically, giving two jets and one lepton in the final state (referred to as the semi-leptonic 3l channel). In order to accurately reconstruct the Higgs, it is necessary to identify which of these decays took place for each 3l event.

The kinematics of each event, along with the output scores of the Higgs and top reconstruction algorithms, are used to distinguish these two possible decay modes. The particular inputs used are listed in Table 40.

| | | |
|---------------------|---------------------|---------------------|
| HT jets | $M(l_0 t_0)$ | $M(l_0 t_1)$ |
| $M(l_1 t_0)$ | $M(l_1 t_1)$ | $M(l_0 l_1)$ |
| $M(l_0 l_2)$ | $M(l_1 l_2)$ | $\Delta R(l_0 t_0)$ |
| $\Delta R(l_0 t_1)$ | $\Delta R(l_1 t_0)$ | $\Delta R(l_1 t_1)$ |
| $\Delta R(l l_0 1)$ | $\Delta R(l l_0 2)$ | $\Delta R(l l_1 2)$ |
| Lepton η 0 | Lepton η 1 | Lepton η 2 |
| Lepton ϕ 0 | Lepton ϕ 1 | Lepton ϕ 2 |
| Lepton p_T 0 | Lepton p_T 1 | Lepton p_T 2 |
| E_T^{miss} | nJets | nJets OR DL1r 60 |
| nJets OR DL1r 85 | score3lF | score3lS |
| topScore | total charge | |

Table 40: Input features used to distinguish semi-leptonic and fully-leptonic Higgs decays in the 3l channel.

1479 Here l_0 is the opposite charge lepton, l_1 and l_2 are the two SS leptons order by ΔR
 1480 from lepton 0. score3lF and score3lS are the outputs of the 3lS and 3lF Higgs reconstruction
 1481 algorithms, while topScore is the output of the b-jet identification algorithm.

1482 A neural network with 5 hidden layers, each with 50 nodes, is trained to distinguish these
 1483 two decay modes. The output of the model is summarized in Figure 18.22.

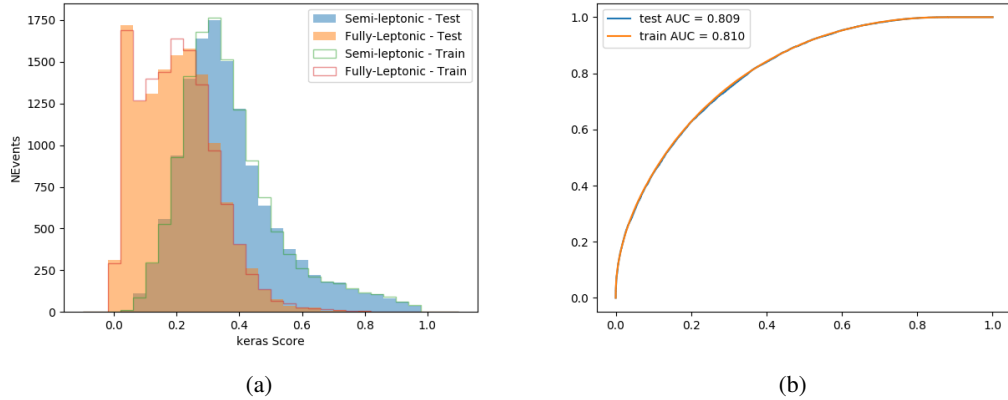


Figure 18.22: (a) shows the output of the decay separation NN for Semi-leptonic (blue) and Fully-leptonic (orange) 3l events, scaled to equal area. (b) shows the ROC curve for those two sets of events.

1484 A cutoff of 0.23 is determined to be optimal for separating 3lS and 3lF in the fit.

1485 19 Signal Region Definitions

1486 Events are divided into two channels based on the number of leptons in the final state: one with
 1487 two same-sign leptons, the other with three leptons. The 3l channel includes events where both
 1488 leptons originated from the Higgs boson as well as events where only one of the leptons

1489 19.1 Pre-MVA Event Selection

1490 A preselection is applied to define orthogonal analysis channels based on the number of leptons
1491 in each event. For the 2lSS channel, the following preselection is used:

- 1492
- Two very tight, same-charge, light leptons with $p_T > 20 \text{ GeV}$

1493

 - ≥ 4 reconstructed jets, ≥ 1 b-tagged jets

1494

 - No reconstructed tau candidates

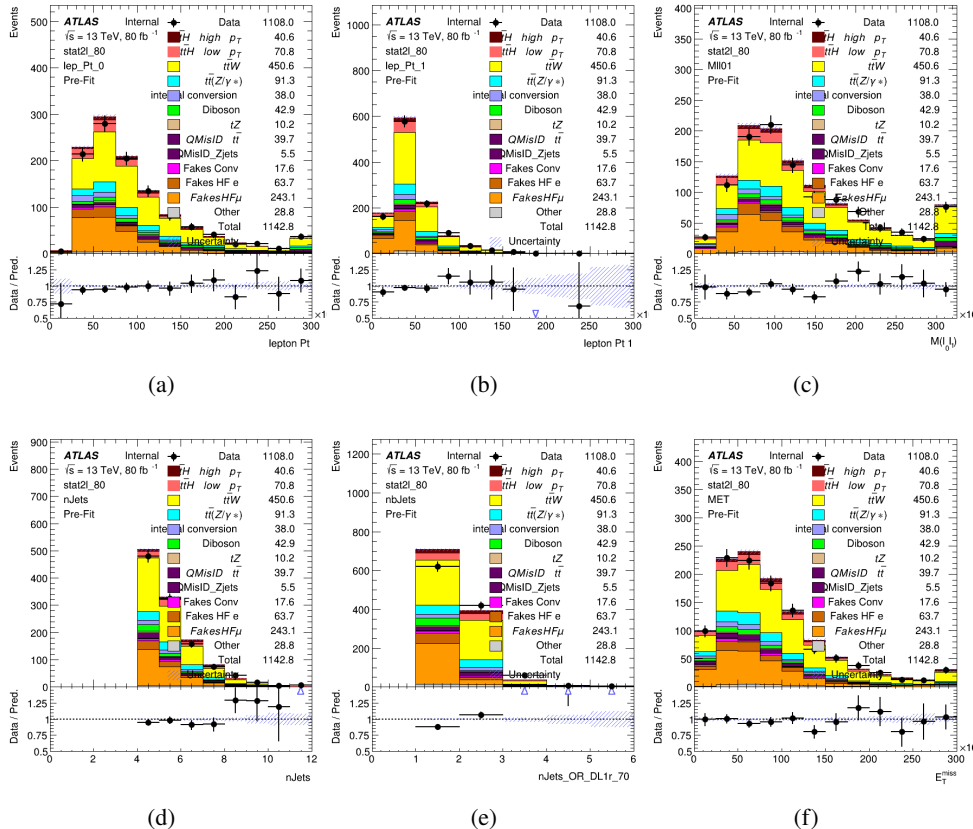
1495 The event yield after the 2lSS preselection has been applied, for MC and data at 80 fb^{-1} ,
1496 is shown in Table 41.

| | Yields |
|-------------------------|------------------|
| t̄H high p _T | 36.19 ± 0.23 |
| t̄H low p _T | 63.58 ± 0.31 |
| t̄W | 440.64 ± 2.32 |
| t̄Z/γ | 91.84 ± 0.79 |
| t̄lllowmass | 8.47 ± 0.28 |
| rareTop | 24.2099 ± 0.40 |
| VV | 38.7927 ± 0.55 |
| tZ | 3e-05 ± 5.47-06 |
| QMISID t̄ | 39.90 ± 2.36 |
| QMISID Zjets | 5.49 ± 0.67 |
| t̄ int. conv. | 12.74 ± 1.40 |
| t̄ + γ int. conv. | 12.09 ± 0.58 |
| t̄ Conv. | 13.55 ± 1.43 |
| t̄ + γ Conv. | 5.35 ± 0.38 |
| t̄ HF e | 59.92 ± 2.89 |
| t̄ + γ HF e | 0.51 ± 0.15 |
| t̄ HF μ | 224.57 ± 5.62 |
| t̄ + γ HF μ | 1.60 ± 0.23 |
| Z + jets internal conv | 3e-05 ± 5.47e-06 |
| Z + jets conv | 0.62 ± 0.21 |
| Z + jets HF e | 0.14 ± 0.13 |
| Z + jets HF μ | 0.82 ± 0.26 |
| Single top Conv | 2.27 ± 0.53 |
| Single top HF e | 2.33 ± 0.50 |
| Single top HF μ | 11.12 ± 1.07 |
| Three top | 2.22 ± 0.02 |
| Four top | 13.09 ± 0.16 |
| t̄WW | 10.985 ± 0.30 |
| tW | 3e-05 ± 5.47-06 |
| WtZ | 9.07 ± 0.44 |
| VVV | 0.30 ± 0.04 |
| VH | 0.59 ± 1.55 |
| Total | 1133.11 ± 7.69 |
| Data | 1108 |

Table 41: Event yield in the 2ISS preselection region.

1497

Figure 20.1. Good general agreement is found.

Figure 19.1: Data/MC comparisons of the 2lSS pre-selection region. (a) and (b) show the p_T of leptons 0 and 1, (c) shows the invariant mass of lepton 0 and 1, (d) shows the jet multiplicity, (e) the b-tagged jet multiplicity, and (f) the missing transverse energy.

1498

For the 3l channel, the following selection is applied:

1499

- Three light leptons with total charge ± 1
- Same charge leptons are required to be very tight, with $p_T > 20 \text{ GeV}$
- Opposite charge lepton must be loose, with $p_T > 10 \text{ GeV}$

1500

- 1502 • ≥ 2 reconstructed jets, ≥ 1 b-tagged jets
- 1503 • No reconstructed tau candidates
- 1504 • $|M(l^+l^-) - 91.2 \text{ GeV}| > 10 \text{ GeV}$ for all opposite-charge, same-flavor lepton pairs
- 1505 The event yield after the 3l preselection has been applied, for MC and data at 80 fb^{-1} , is
- 1506 shown in Table 19.1.

| | Yields |
|-----------------------------|-----------------|
| t̄H high p _T | 18.40 ± 0.13 |
| t̄H low p _T | 29.91 ± 0.16 |
| t̄W | 134.22 ± 1.25 |
| t̄Z/γ | 88.47 ± 0.73 |
| t̄lllowmass | 2.77 ± 0.16 |
| rareTop | 15.05 ± 0.32 |
| VV | 34.54 ± 0.54 |
| tZ | 2e-05 ± 4.47-06 |
| QMisID t̄t | 1.80 ± 0.59 |
| QMisID Zjets | 0.02 ± 0.02 |
| t̄t internal conversion | 4.34 ± 0.43 |
| t̄t + γ internal conversion | 5.83 ± 0.42 |
| t̄t Conv. | 4.71 ± 0.45 |
| t̄t + γ Conv. | 2.64 ± 0.27 |
| t̄t HF e | 27.44 ± 1.05 |
| t̄t + γ HF e | 0.27 ± 0.11 |
| t̄t HF μ | 89.21 ± 1.92 |
| t̄t + γ HF μ | 0.94 ± 0.16 |
| Z + jets conv | 0.09 ± 0.19 |
| Z + jets HF e | 0.25 ± 0.15 |
| Z + jets HF μ | 2.41 ± 0.95 |
| Single top Conv | 0.58 ± 0.61 |
| Single top HF e | 1.50 ± 0.43 |
| Single top HF μ | 4.62 ± 0.85 |
| Three top | 0.96 ± 0.02 |
| Four top | 5.58 ± 0.10 |
| t̄WW | 5.45 ± 0.21 |
| WtZ | 8.71 ± 0.42 |
| VVV | 0.81 ± 0.02 |
| Total | 492.14 ± 3.22 |
| Data | 535 |

Table 42: Yields of the analysis

1507

Comparisons of kinematic distributions for data and MC in this region are shown in Figure

1508 20.2.

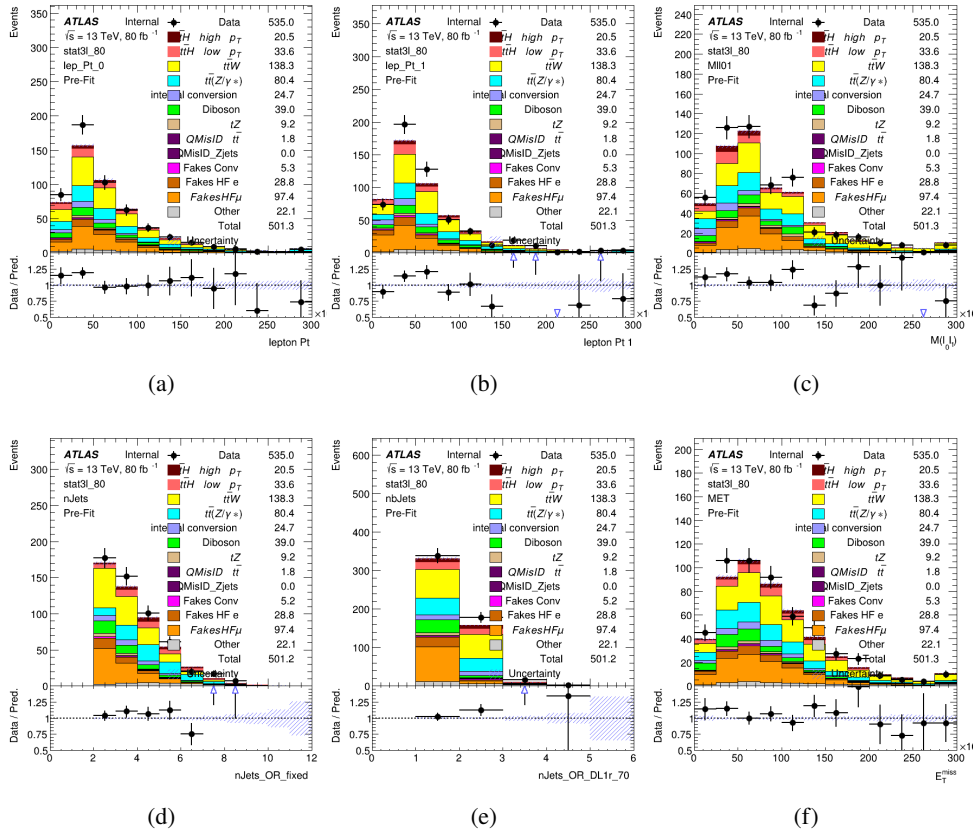


Figure 19.2: Data/MC comparisons of the 3l pre-selection region. (a) and (b) show the p_T of leptons 0 and 1, (c) shows the invariant mass of lepton 0 and 1, (d) shows the jet multiplicity, (e) the b-tagged jet multiplicity, and (f) the missing transverse energy.

1509

19.2 Event MVA

1510

Separate multi-variate analysis techniques (MVAs) are used in order to distinguish signal events from background for each analysis channel - 2lSS, 3l semi-leptonic (3lS), and 3l fully leptonic (3lF). In particular, Boosted Decision Tree (BDT) algorithms are produced with XGBoost

1513 [xgboost] are trained using the kinematics of signal and background events derived from Monte
1514 Carlo simulations. Events are weighted in the BDT training by the weight of each Monte Carlo
1515 event.

1516 Because the background composition differs for events with a high reconstructed Higgs p_T
1517 compared to events with low reconstructed Higgs p_T , separate MVAs are produced for high and
1518 low p_T regions. This is found to provide better significance than attempting to build an inclusive
1519 model, as demonstrated in appendix A.2. A cutoff of 150 GeV is used. This gives a total of 6
1520 background rejection MVAs - explicitly, 2lSS high p_T , 2lSS low p_T , 3lS high p_T , 3lS low p_T ,
1521 3lF high p_T , and 3lF low p_T .

1522 The following features are used in both the high and low p_T 2lSS BDTs:

| HT | $M(\text{lep}, E_T^{\text{miss}})$ | $M(l_0 l_1)$ |
|----------------------------------|---|----------------------------------|
| binHiggs p_T 2ISS | $\Delta R(l_0)(l_1)$ | diLepton type |
| higgsRecoScore | jet η 0 | jet η 1 |
| jet ϕ 0 | jet ϕ 1 | jet p_T 0 |
| jet p_T 1 | Lepton η 0 | Lepton η 1 |
| Lepton ϕ 0 | Lepton ϕ 1 | Lepton p_T 0 |
| Lepton p_T 1 | E_T^{miss} | $\min \Delta R(l_0)(\text{jet})$ |
| $\min \Delta R(l_1)(\text{jet})$ | $\min \Delta R(\text{Lepton})(\text{bjet})$ | mjjMax frwdJet |
| nJets | nJets OR DL1r 60 | nJets OR DL1r 70 |
| nJets OR DL1r 85 | topRecoScore | |

Table 43: Input features used to distinguish signal and background events in the 2ISS channel.

1523

While for each of the 31 BDTs, the features listed below are used for training:

| | | |
|------------------------------------|----------------------------------|---|
| $M(\text{lep}, E_T^{\text{miss}})$ | $M(l_0 l_1)$ | $M(l_0 l_1 l_2)$ |
| $M(l_0 l_2)$ | $M(l_1 l_2)$ | $\text{binHiggs } p_T \text{ 3lF}$ |
| $\text{binHiggs } p_T \text{ 3lS}$ | $\Delta R(l_0)(l_1)$ | $\Delta R(l_0)(l_2)$ |
| $\Delta R(l_1)(l_2)$ | decayScore | higgsRecoScore3lF |
| higgsRecoScore3lS | $\text{jet } \eta \text{ 0}$ | $\text{jet } \eta \text{ 1}$ |
| $\text{jet } \phi \text{ 0}$ | $\text{jet } \phi \text{ 1}$ | $\text{jet } p_T \text{ 0}$ |
| $\text{jet } p_T \text{ 1}$ | $\text{Lepton } \eta \text{ 0}$ | $\text{Lepton } \eta \text{ 1}$ |
| $\text{Lepton } \eta \text{ 2}$ | $\text{Lepton } \phi \text{ 0}$ | $\text{Lepton } \phi \text{ 1}$ |
| $\text{Lepton } \phi \text{ 2}$ | $\text{Lepton } p_T \text{ 0}$ | $\text{Lepton } p_T \text{ 1}$ |
| $\text{Lepton } p_T \text{ 2}$ | E_T^{miss} | $\min \Delta R(l_0)(\text{jet})$ |
| $\min \Delta R(l_1)(\text{jet})$ | $\min \Delta R(l_2)(\text{jet})$ | $\min \Delta R(\text{Lepton})(\text{bjet})$ |
| $mjj\text{Max frwdJet}$ | $n\text{Jets}$ | $n\text{Jets OR DL1r 60}$ |
| $n\text{Jets OR DL1r 70}$ | $n\text{Jets OR DL1r 85}$ | topScore |

Table 44: Input features used to distinguish signal and background events in the 3l channel.

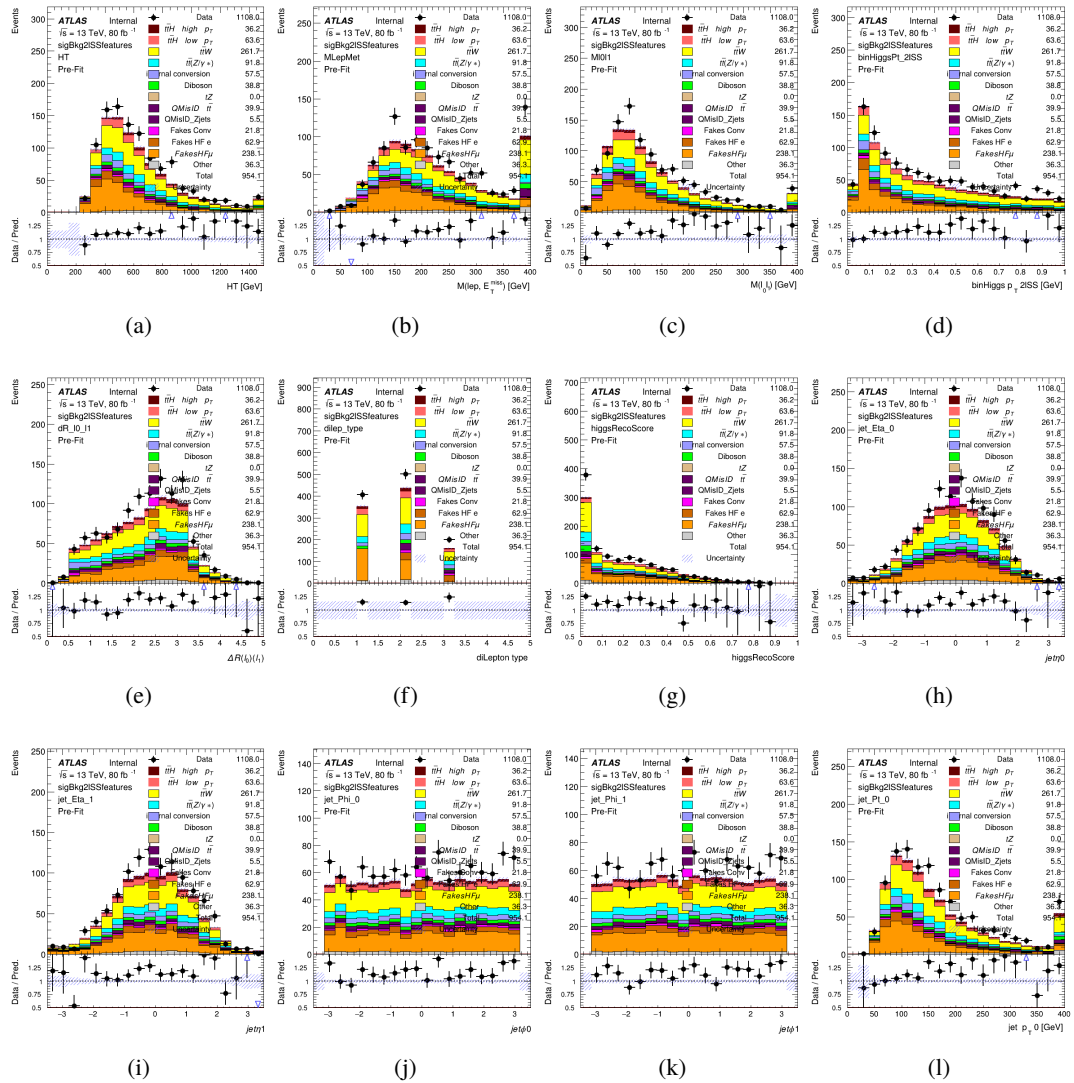


Figure 19.3:

1524

The BDTs are produced with a maximum tree depth of 6, using AUC as the target loss

1525 function.

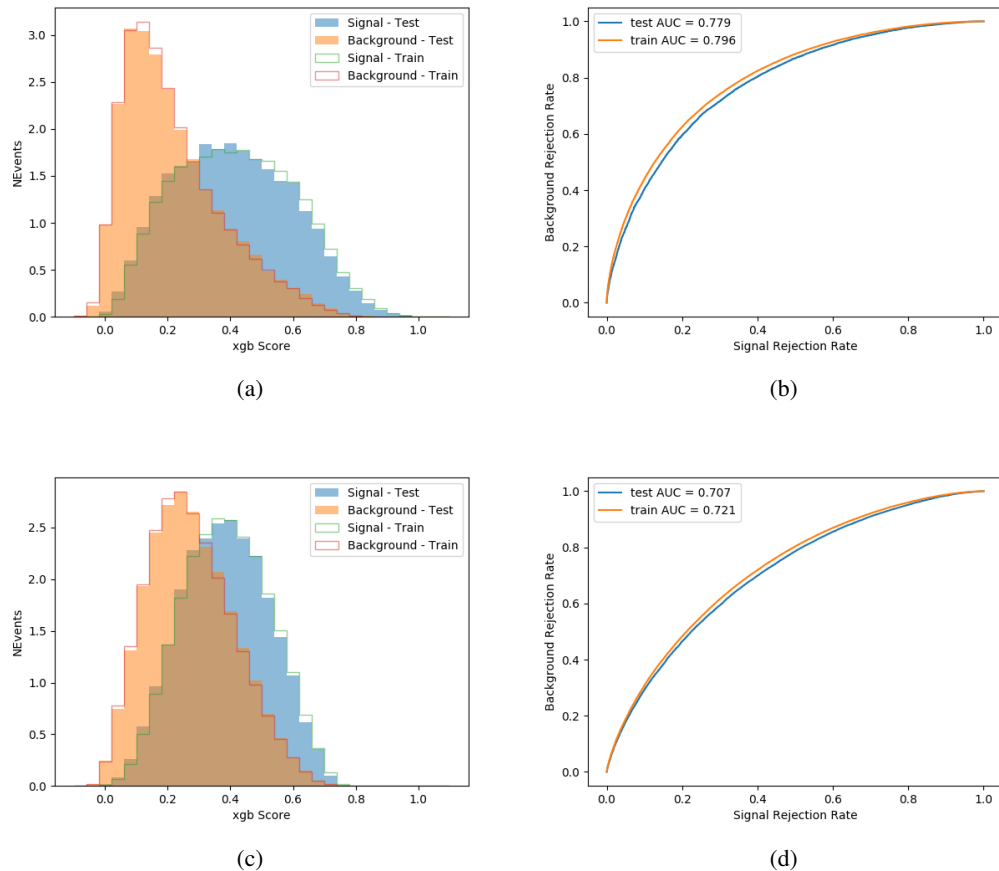


Figure 19.4:

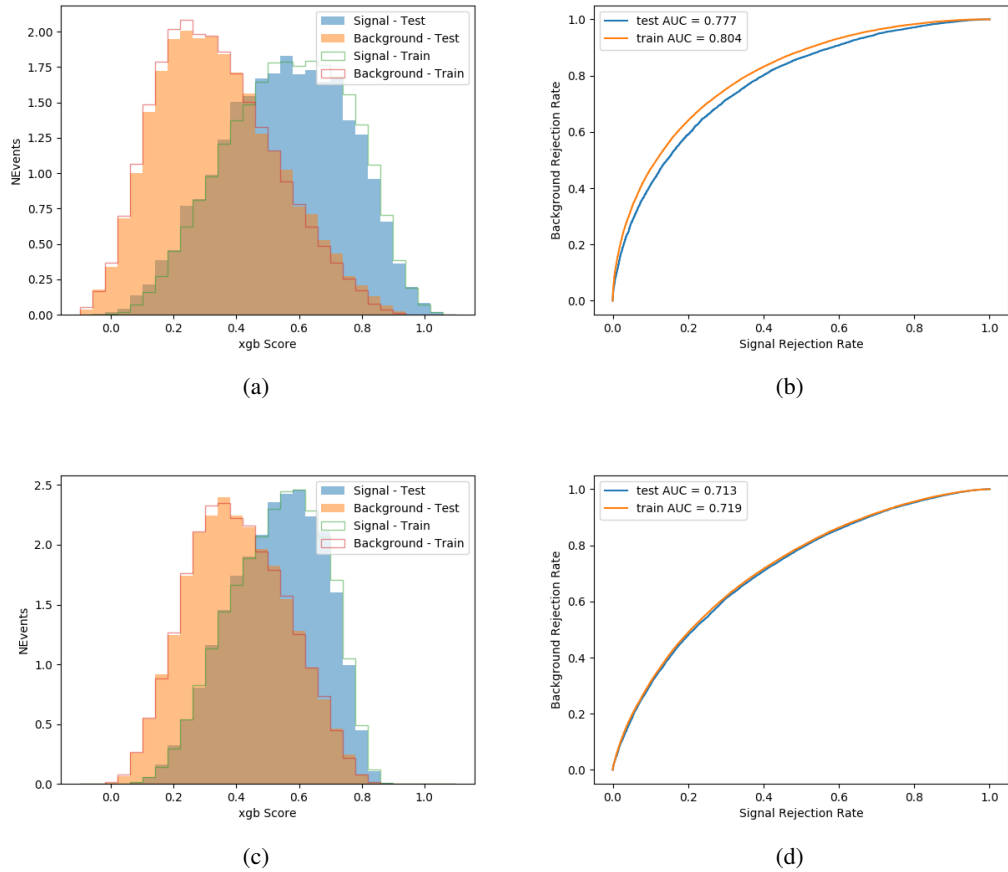


Figure 19.5:

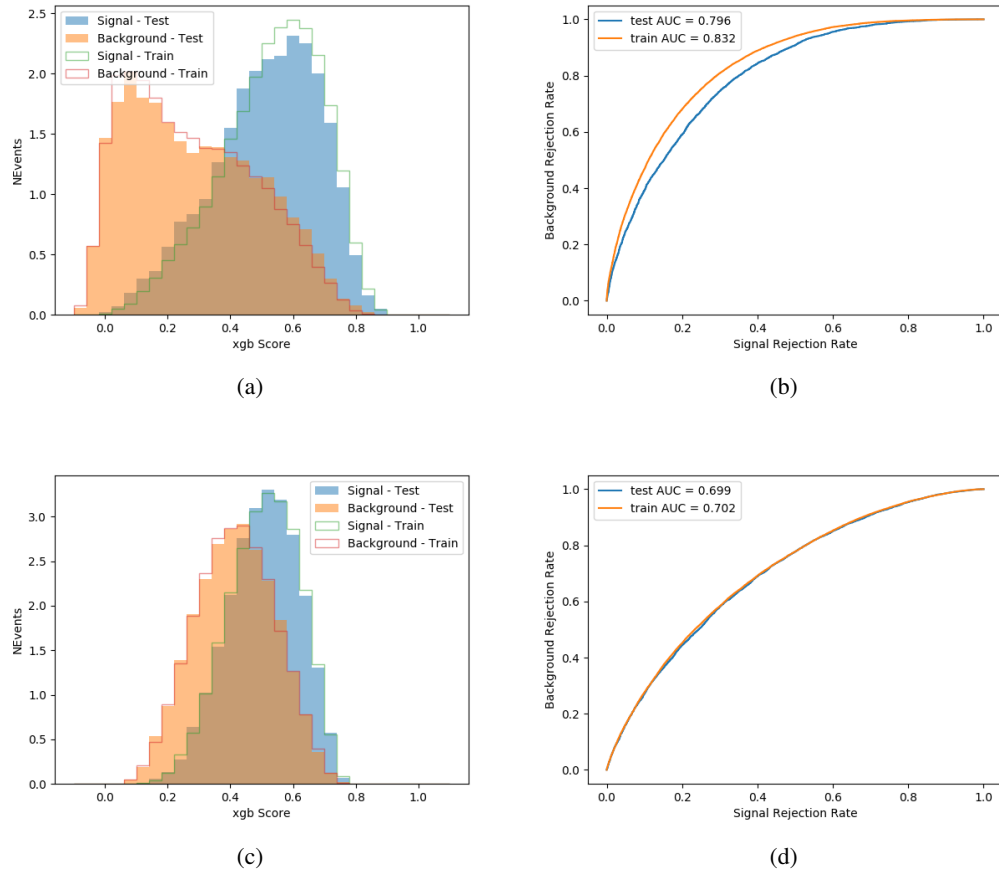


Figure 19.6:

1526 Output distributions of each MVA comparing MC prediction to data at 80 fb^{-1} are shown
 1527 in figures 19.7-19.2.

1528 19.3 Signal Region Definitions

1529 Once pre-selection has been applied, channels are further refined based on the MVAs described
 1530 above. The output of the model described in Section 18.5 is used to separate the three channel

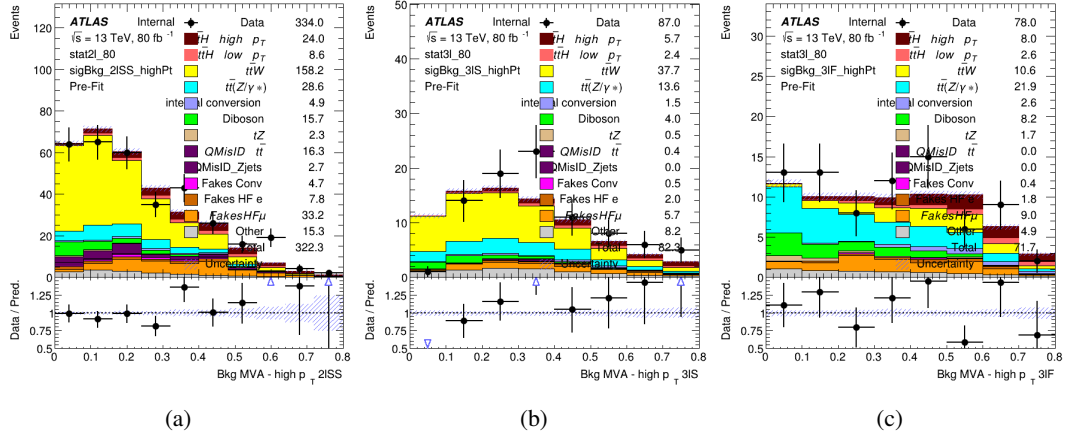


Figure 19.7: Output score of the high p_T BDTs in the (a) 2ISS, (b) 3IS, and (c) 3IF channels

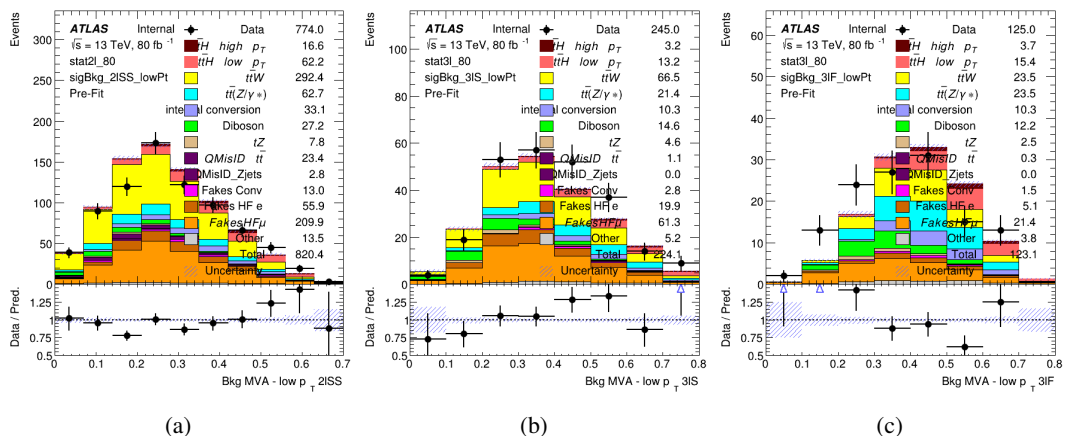


Figure 19.8: Output score of the low p_T BDTs in the (a) 2ISS, (b) 3IS, and (c) 3IF channels

1531 into two - Semi-leptonic and Fully-leptonic - based on the predicted decay mode of the Higgs

1532 boson. This leaves three orthogonal signal regions - 2lSS, 3lS, and 3lF.

1533 For each event, depending on the number of leptons as well as whether the p_T of the Higgs

1534 is predicted to be high (> 150 GeV) or low (< 150 GeV), a cut on the appropriate background

1535 rejection MVA is applied. The particular cut values, listed in Table 45, are determined by

1536 maximizing S/\sqrt{B} in each region.

| Channel | BDT Score |
|-----------------|-----------|
| 2lSS high p_T | 0.36 |
| 2lSS low p_T | 0.34 |
| 3lS high p_T | 0.51 |
| 3lS low p_T | 0.43 |
| 3lF high p_T | 0.33 |
| 3lF low p_T | 0.41 |

Table 45: Cutoff values on background rejection MVA score applied to signal regions.

1537 The event preselection and MVA selection define the three signal regions. These signal

1538 region definitions are summarized in Table 46.

| Region | Selection |
|--------|---|
| 2ISS | Two same charge tight leptons with $p_T > 20 \text{ GeV}$ $N_{\text{jets}} \geq 4, N_{\text{b-jets}} \geq 1$ b-tagged jets Zero τ_{had} $H_{p_T}^{\text{pred}} > 150 \text{ GeV}$ and BDT score > 0.36 or $H_{p_T}^{\text{pred}} < 150 \text{ GeV}$ and BDT score > 0.34 |
| 3IS | Three light leptons with total charge ± 1 Two tight SS leptons, $p_T > 20 \text{ GeV}$ One loose OS lepton, $p_T > 10 \text{ GeV}$ $N_{\text{jets}} \geq 2, N_{\text{b-jets}} \geq 1$ b-tagged jets Zero τ_{had} $ M(l^+l^-) - 91.2 \text{ GeV} > 10 \text{ GeV}$ for all OSSF lepton pairs Decay NN Score < 0.23 $H_{p_T}^{\text{pred}} > 150 \text{ GeV}$ and BDT score > 0.51 or $H_{p_T}^{\text{pred}} > 150 \text{ GeV}$ and BDT score > 0.43 |
| 3IF | Three light leptons with total charge ± 1 Two tight SS leptons, $p_T > 20 \text{ GeV}$ One loose OS lepton, $p_T > 10 \text{ GeV}$ $N_{\text{jets}} \geq 2, N_{\text{b-jets}} \geq 1$ b-tagged jets Zero τ_{had} $ M(l^+l^-) - 91.2 \text{ GeV} > 10 \text{ GeV}$ for all OSSF lepton pairs Decay NN Score > 0.23 $H_{p_T}^{\text{pred}} > 150 \text{ GeV}$ and BDT score > 0.33 or $H_{p_T}^{\text{pred}} > 150 \text{ GeV}$ and BDT score > 0.41 |

Table 46: Selection applied to define the three signal regions used in the fit.

20 Background Rejection MVA

1539 Events are divided into two channels based on the number of leptons in the final state: one with
 1540 two same-sign leptons, the other with three leptons. The 3l channel includes events where both
 1541 leptons originated from the Higgs boson as well as events where only one of the leptons
 1542

1543 20.1 Pre-MVA Event Selection

1544 A preselection is applied to define orthogonal analysis channels based on the number of leptons
 1545 in each event. For the 2lSS channel, the following preselection is used:

- 1546 • Two very tight, same-charge, light leptons with $p_T > 20$ GeV

- 1547 • ≥ 4 reconstructed jets, ≥ 1 b-tagged jets

- 1548 • No reconstructed tau candidates

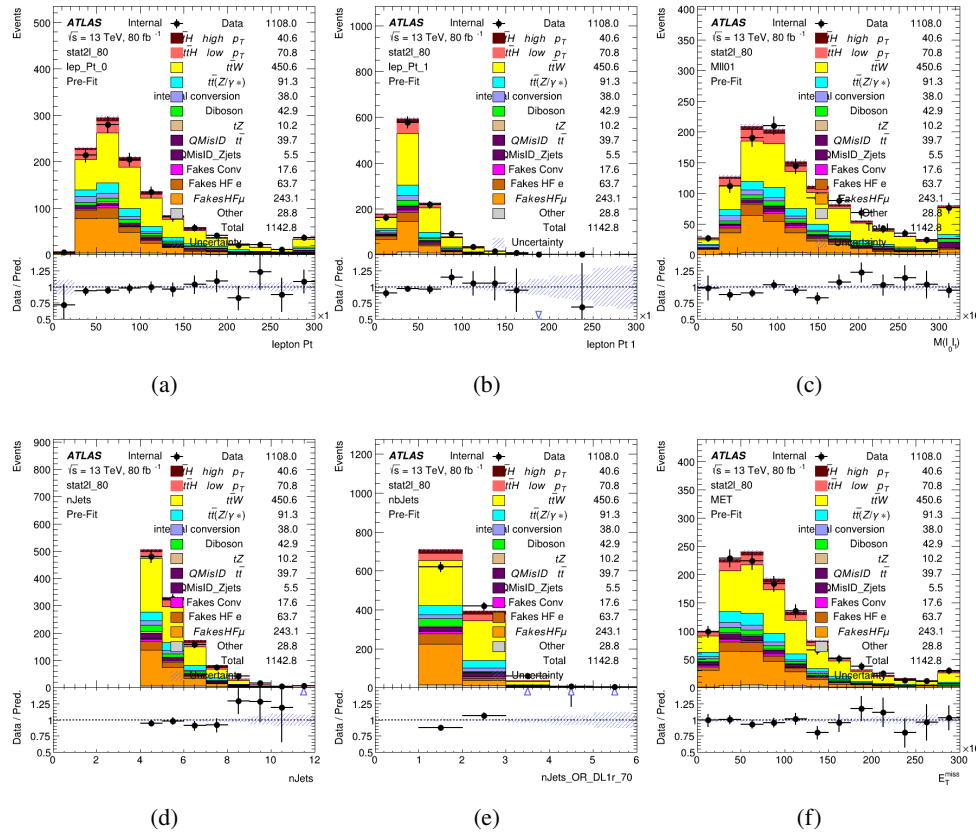


Figure 20.1:

1549 For the 31 channel, the following selection is applied:

1550 • Three light leptons with total charge ± 1

1551 • Same charge leptons are required to be very tight, with $p_T > 20 \text{ GeV}$

1552 • Opposite charge lepton must be loose, with $p_T > 10 \text{ GeV}$

1553 • $>= 2$ reconstructed jets, $>= 1$ b-tagged jets

1554 • No reconstructed tau candidates

1555 • $|M(l^+l^-) - 91.2 \text{ GeV}| > 10 \text{ GeV}$ for all opposite-charge, same-flavor lepton pairs

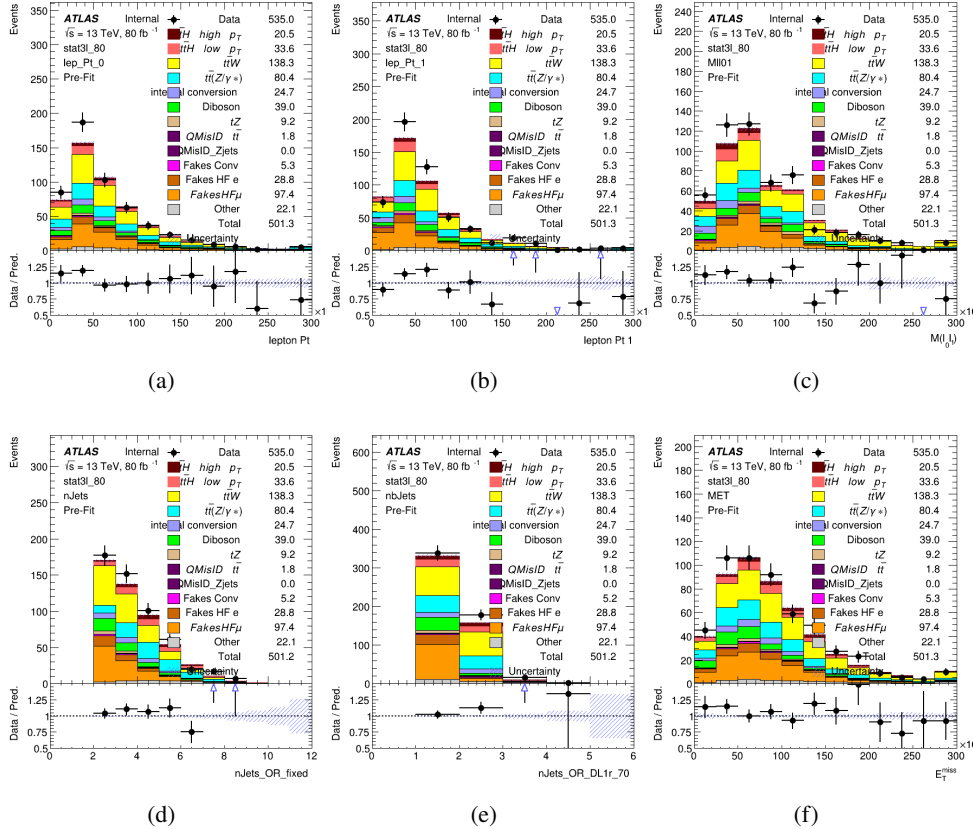


Figure 20.2:

1556 20.2 Event MVA

1557 Separate multi-variate analysis techniques (MVAs) are used in order to distinguish signal events
 1558 from background for each analysis channel - 2lSS, 3l semi-leptonic (3lS), and 3l fully leptonic
 1559 (3lF). In particular, Boosted Decision Tree (BDT) algorithms are produced with XGBoost
 1560 [[xgboost](#)] are trained using the kinematics of signal and background events derived from Monte
 1561 Carlo simulations. Events are weighted in the BDT training by the weight of each Monte Carlo

1562 event.

1563 Because the background composition differs for events with a high reconstructed Higgs p_T
1564 compared to events with low reconstructed Higgs p_T , separate MVAs are produced for high and
1565 low p_T regions. This is found to provide better significance than attempting to build an inclusive
1566 model, as demonstrated in appendix A.2. A cutoff of 150 GeV is used. This gives a total of 6
1567 background rejection MVAs - explicitly, 2lSS high p_T , 2lSS low p_T , 3lS high p_T , 3lS low p_T ,
1568 3lF high p_T , and 3lF low p_T .

1569 The following features are used in both the high and low p_T 2lSS BDTs:

| HT | $M(\text{lep}, E_T^{\text{miss}})$ | $M(l_0 l_1)$ |
|----------------------------------|---|----------------------------------|
| binHiggs p_T 2ISS | $\Delta R(l_0)(l_1)$ | diLepton type |
| higgsRecoScore | jet η 0 | jet η 1 |
| jet ϕ 0 | jet ϕ 1 | jet p_T 0 |
| jet p_T 1 | Lepton η 0 | Lepton η 1 |
| Lepton ϕ 0 | Lepton ϕ 1 | Lepton p_T 0 |
| Lepton p_T 1 | E_T^{miss} | $\min \Delta R(l_0)(\text{jet})$ |
| $\min \Delta R(l_1)(\text{jet})$ | $\min \Delta R(\text{Lepton})(\text{bjet})$ | mjjMax frwdJet |
| nJets | nJets OR DL1r 60 | nJets OR DL1r 70 |
| nJets OR DL1r 85 | topRecoScore | |

Table 47: Input features used to distinguish signal and background events in the 2ISS channel.

1570

While for each of the 31 BDTs, the features listed below are used for training:

| | | |
|------------------------------------|----------------------------------|---|
| $M(\text{lep}, E_T^{\text{miss}})$ | $M(l_0 l_1)$ | $M(l_0 l_1 l_2)$ |
| $M(l_0 l_2)$ | $M(l_1 l_2)$ | $\text{binHiggs } p_T \text{ 3lF}$ |
| $\text{binHiggs } p_T \text{ 3lS}$ | $\Delta R(l_0)(l_1)$ | $\Delta R(l_0)(l_2)$ |
| $\Delta R(l_1)(l_2)$ | decayScore | higgsRecoScore3lF |
| higgsRecoScore3lS | $\text{jet } \eta \text{ 0}$ | $\text{jet } \eta \text{ 1}$ |
| $\text{jet } \phi \text{ 0}$ | $\text{jet } \phi \text{ 1}$ | $\text{jet } p_T \text{ 0}$ |
| $\text{jet } p_T \text{ 1}$ | $\text{Lepton } \eta \text{ 0}$ | $\text{Lepton } \eta \text{ 1}$ |
| $\text{Lepton } \eta \text{ 2}$ | $\text{Lepton } \phi \text{ 0}$ | $\text{Lepton } \phi \text{ 1}$ |
| $\text{Lepton } \phi \text{ 2}$ | $\text{Lepton } p_T \text{ 0}$ | $\text{Lepton } p_T \text{ 1}$ |
| $\text{Lepton } p_T \text{ 2}$ | E_T^{miss} | $\min \Delta R(l_0)(\text{jet})$ |
| $\min \Delta R(l_1)(\text{jet})$ | $\min \Delta R(l_2)(\text{jet})$ | $\min \Delta R(\text{Lepton})(\text{bjet})$ |
| $mjj\text{Max frwdJet}$ | $n\text{Jets}$ | $n\text{Jets OR DL1r 60}$ |
| $n\text{Jets OR DL1r 70}$ | $n\text{Jets OR DL1r 85}$ | topScore |

Table 48: Input features used to distinguish signal and background events in the 3l channel.

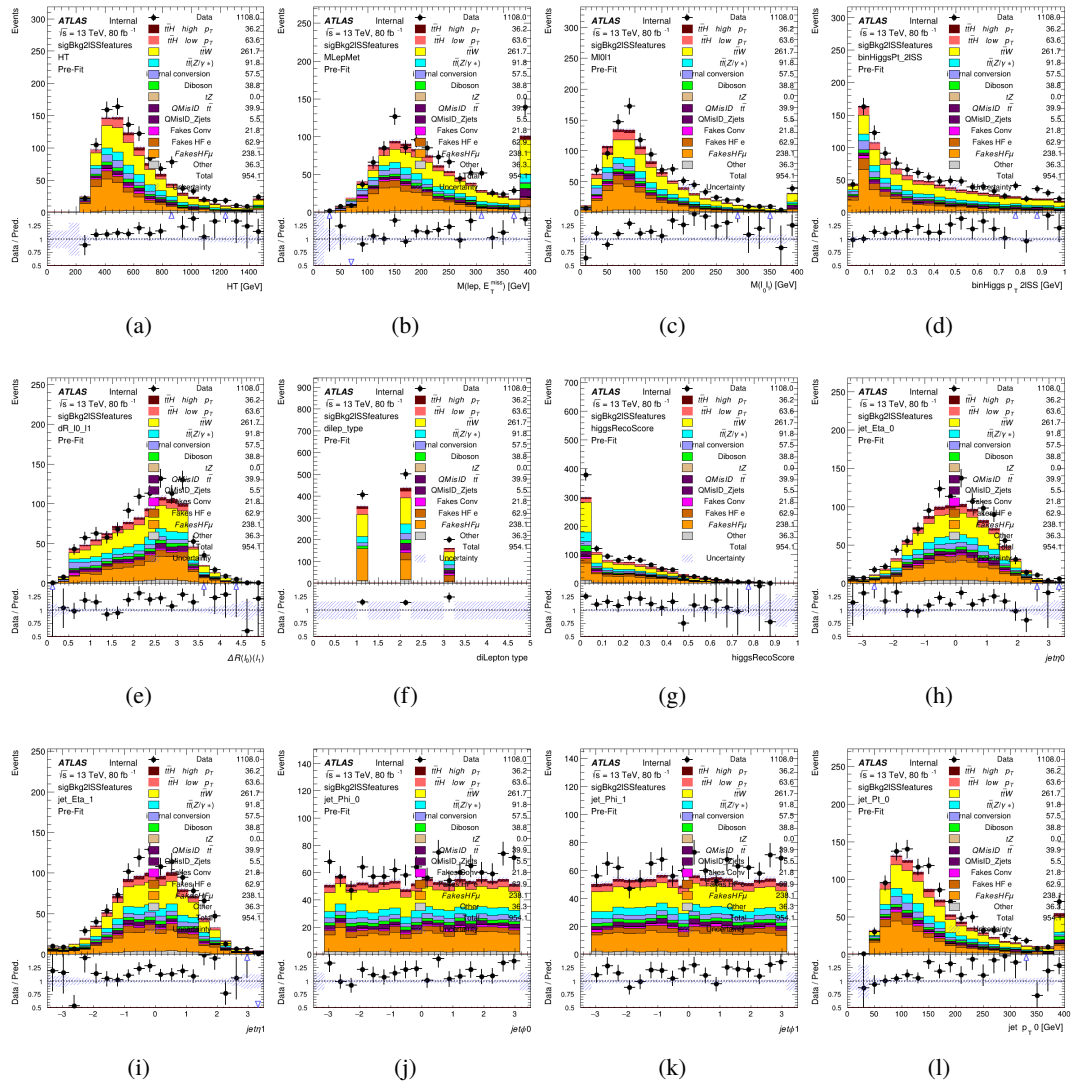


Figure 20.3:

1571

The BDTs are produced with a maximum tree depth of 6, using AUC as the target loss

1572 function.

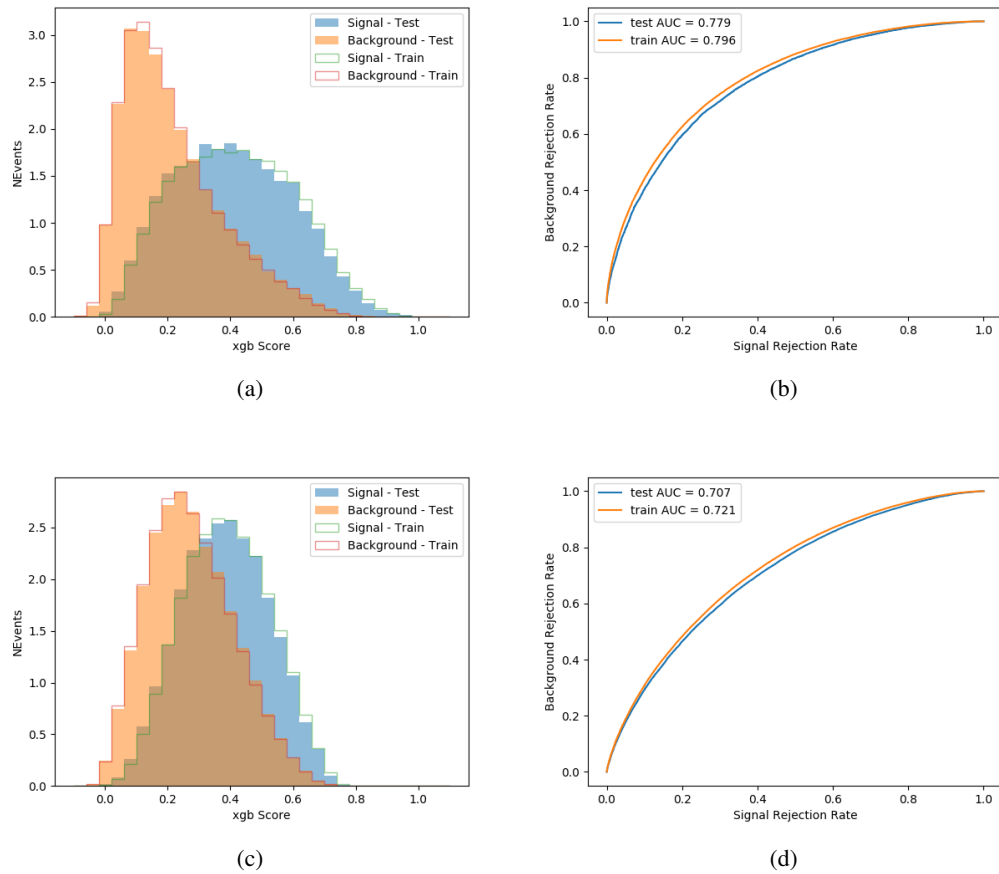


Figure 20.4:

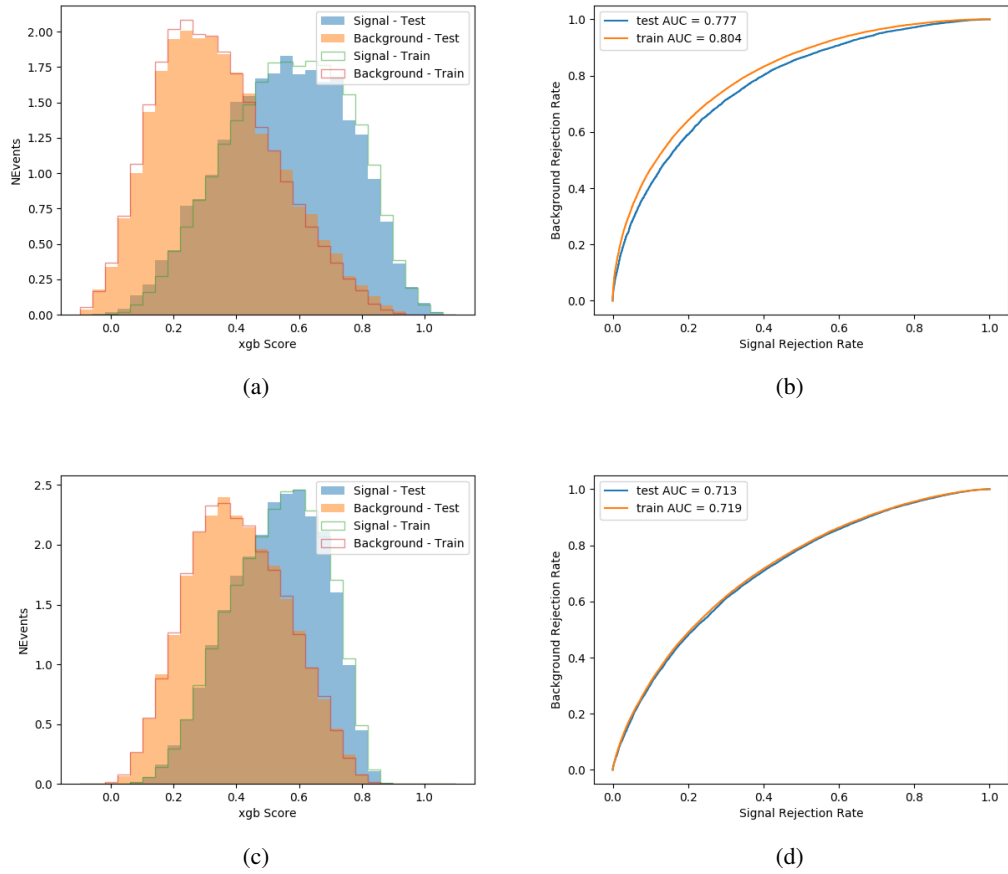


Figure 20.5:

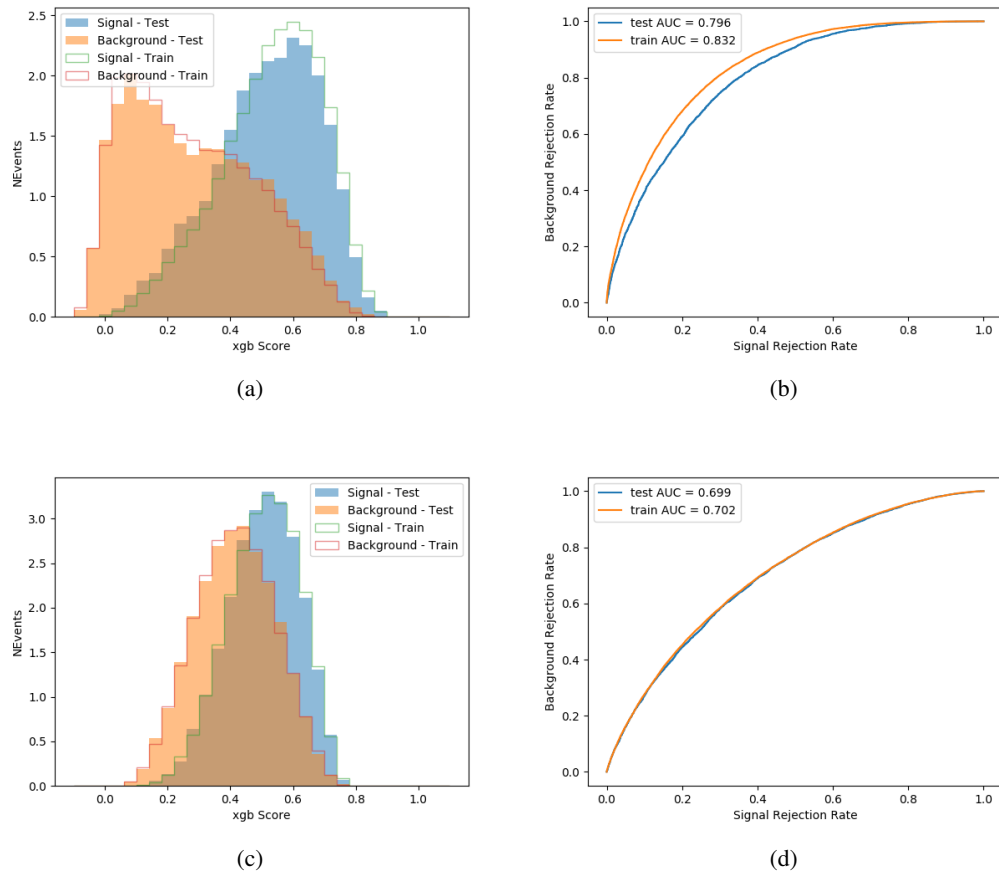


Figure 20.6:

1573 Output distributions of each MVA comparing MC prediction to data at 80 fb^{-1} are shown
 1574 in Figure 20.2.

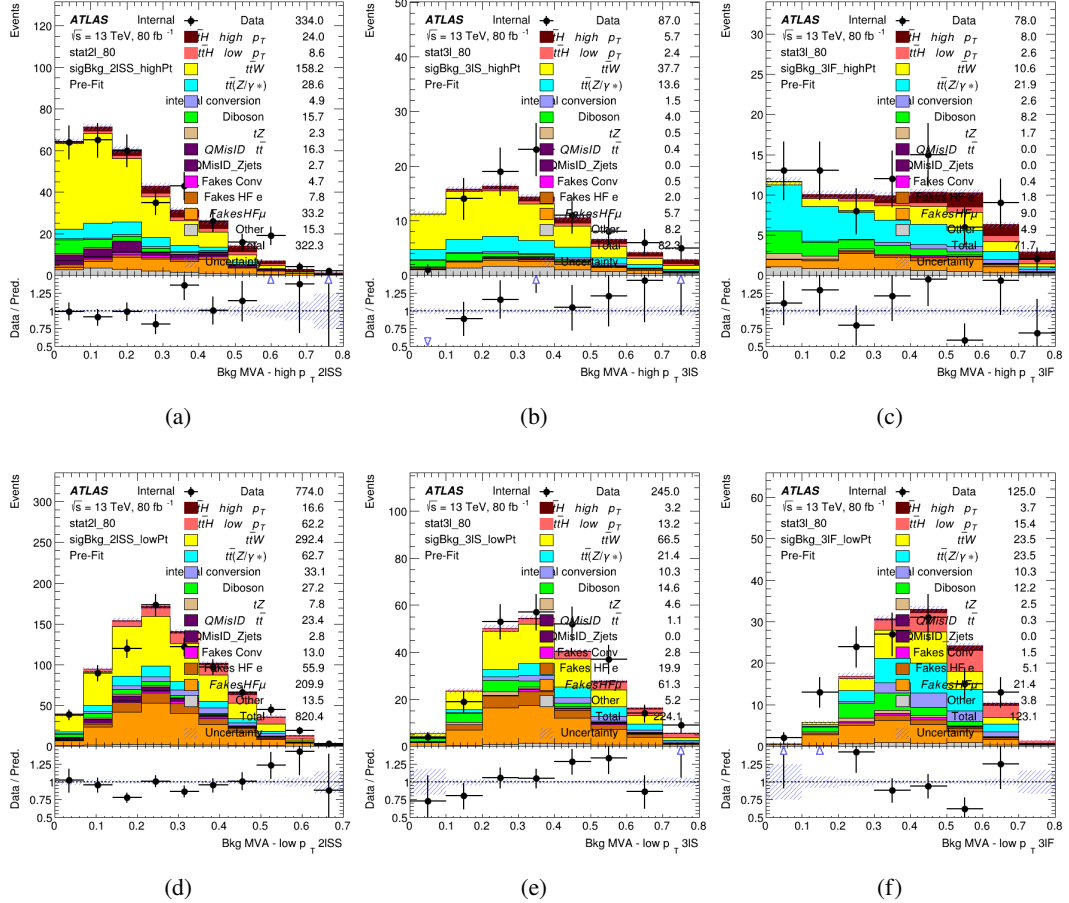


Figure 20.7: scores

1575 20.3 Signal Region Definitions

1576 Once pre-selection has been applied, channels are further refined based on the MVAs described
 1577 above. The output of the model described in Section 18.5 is used to separate the three channel
 1578 into two - Semi-leptonic and Fully-leptonic - based on the predicted decay mode of the Higgs
 1579 boson.

1580 For each event, depending on the channel as well as the predicted p_T of the Higgs derived
1581 from the algorithm described in Section 18.4, a cut on the appropriate background rejection
1582 algorithm is applied. The specific selection used, and the event yield in each channel after this
1583 selection has been applied, is summarized below.

1584 **20.3.1 2lSS**

1585 **20.3.2 3l – Semi – leptonic**

1586 **20.3.3 3l – Fully – leptonic**

1587 **21 Systematic Uncertainties**

1588 The systematic uncertainties that are considered are summarized in Table 49. These are imple-
1589 mented in the fit either as a normalization factors or as a shape variation or both in the signal
1590 and background estimations. The numerical impact of each of these uncertainties is outlined in
1591 section 22.

Table 49: Sources of systematic uncertainty considered in the analysis. Some of the systematic uncertainties are split into several components, as indicated by the number in the rightmost column.

| Systematic uncertainty | Components |
|--|------------|
| Luminosity | 1 |
| Pileup reweighting | 1 |
| Physics Objects | |
| Electron | 6 |
| Muon | 15 |
| Jet energy scale and resolution | 28 |
| Jet vertex fraction | 1 |
| Jet flavor tagging | 131 |
| E_T^{miss} | 3 |
| Total (Experimental) | 186 |
| Background Modeling | |
| Cross section | 24 |
| Renormalization and factorization scales | 10 |
| Parton shower and hadronization model | 2 |
| Shower tune | 4 |
| Total (Signal and background modeling) | 40 |
| Background Modeling | |
| Cross section | 24 |
| Renormalization and factorization scales | 10 |
| Parton shower and hadronization model | 2 |
| Shower tune | 4 |
| Total (Signal and background modeling) | 40 |
| Total (Overall) | 226 |

1592 The uncertainty in the combined 2015+2016 integrated luminosity is derived from a
 1593 calibration of the luminosity scale using x-y beam-separation scans performed in August 2015
 1594 and May 2016 [26].

1595 The experimental uncertainties are related to the reconstruction and identification of light
 1596 leptons and b-tagging of jets, and to the reconstruction of E_T^{miss} . The TOTAL electron ID
 1597 correlation model is used, corresponding to 1 electron ID systematic. Electron ID is found to be

1598 a subleading systematic that is unconstrained by the fit, making it an appropriate choice for this
1599 analysis.

1600 The sources which contribute to the uncertainty in the jet energy scale [28] are decom-
1601 posed into uncorrelated components and treated as independent sources in the analysis. The
1602 CategoryReduction model is used to account for JES uncertainties, which decomposes the uncer-
1603 tainties into 30 nuisance parameters included in the fit. The SimpleJER model is used to account
1604 for jet energy resolution (JER) uncertainties, and 8 JER uncertainty components unclued as
1605 NPs in the fit.

1606 The uncertainties in the b-tagging efficiencies measured in dedicated calibration analyses
1607 [29] are also decomposed into uncorrelated components. The large number of components for
1608 b-tagging is due to the calibration of the distribution of the BDT discriminant.

1609 The systematic uncertainties associated with the signal and background processes are
1610 accounted for by varying the cross-section of each process within its uncertainty.

1611 The full list of systematic uncertainties considered in the analysis is summarized in Tables
1612 50, 51 and 52.

1613

| Experimental Systematics on Leptons and E_T^{miss} | | | |
|---|-------------------------------------|---|-------------------|
| Type | Description | Systematics Name | Application |
| Trigger | | | |
| Scale Factors | Trigger Efficiency | lepSFTrigTight_MU(EL)_SF_Trigger_STAT(SYST) | Event Weight |
| Muons | | | |
| Efficiencies | Reconstruction and Identification | lepSFObjTight_MU_SF_ID_STAT(SYST) | Event Weight |
| | Isolation | lepSFObjTight_MU_SF_Isol_STAT(SYST) | Event Weight |
| | Track To Vertex Association | lepSFObjTight_MU_SF_TTVA_STAT(SYST) | Event Weight |
| p_T Scale | p_T Scale | MUONS_SCALE | p_T Correction |
| Resolution | Inner Detector Energy Resolution | MUONS_ID | p_T Correction |
| | Muon Spectrometer Energy Resolution | MUONS_MS | p_T Correction |
| Electrons | | | |
| Efficiencies | Reconstruction | lepSFObjTight_EL_SF_ID | Event Weight |
| | Identification | lepSFObjTight_EL_SF_Reco | Event Weight |
| | Isolation | lepSFObjTight_EL_SF_Isol | Event Weight |
| Scale Factor | Energy Scale | EG_SCALE_ALL | Energy Correction |
| Resolution | Energy Resolution | EG_RESOLUTION_ALL | Energy Correction |
| E_T^{miss} | | | |
| Soft Tracks Terms | Resolution | MET_SoftTrk_ResoPerp | p_T Correction |
| | Resolution | MET_SoftTrk_ResoPara | p_T Correction |
| | Scale | MET_SoftTrk_ScaleUp | p_T Correction |
| | Scale | MET_SoftTrk_ScaleDown | p_T Correction |

Table 50: Summary of experimental systematics considered for leptons and E_T^{miss} . Includes type, description, name of systematic as used in the fit, and mode of application. The mode of application indicates the systematic evaluation, e.g. as an overall event re-weighting (Event Weight) or rescaling (p_T Correction).

| Experimental Systematics on Jets | | | |
|----------------------------------|--------------------------|--|--|
| Type | Origin | Systematics Name | Application |
| Jet Vertex Tagger | | JVT | Event Weight |
| Energy Scale | Calibration Method | JET_21NP_ JET_EffectiveNP_1-19 | p _T Correction p _T Correction |
| | η inter-calibration | JET_EtaIntercalibration_Modelling JET_EtaIntercalibration_NonClosure JET_EtaIntercalibration_TotalStat | p _T Correction p _T Correction p _T Correction |
| | High p _T jets | JET_SingleParticle_HighPt | p _T Correction |
| | Pile-Up | JET_Pileup_OffsetNPV JET_Pileup_OffsetMu JET_Pileup_PtTerm JET_Pileup_RhoTopology | p _T Correction p _T Correction p _T Correction p _T Correction |
| | Non Closure | JET_PunchThrough_MC15 | p _T Correction |
| | Flavour | JET_Flavor_Response JET_BJES_Response JET_Flavor_Composition | p _T Correction p _T Correction p _T Correction |
| Resolution | | JET_JER_SINGLE_NP | Event Weight |

Table 51: Jet systematics take into account effects of jets calibration method, η inter-calibration, high p_T jets, pile-up, and flavor response. They are all diagonalised into effective parameters.

| Experimental Systematics on b-tagging | | |
|---------------------------------------|---|---|
| Type | Origin | Systematic Name |
| Scale Factors | DL1r b-tagger efficiency on b originated jets in bins of η | DL1r_Continuous_EventWeight_B0-29 |
| | DL1r b-tagger efficiency on c originated jets in bins of η | DL1r_Continuous_EventWeight_C0-19 |
| | DL1r b-tagger efficiency on light flavoured originated jets in bins of η and p_T | DL1r_Continuous_EventWeight_Light0-79 |
| | DL1r b-tagger extrapolation efficiency | DL1r_Continuous_EventWeight_extrapolation DL1r_Continuous_EventWeight_extrapolation_from_charm |

Table 52: Summary of experimental systematics to be included for b-tagging of jets in the analysis, using the continuous DL1r tagging algorithm. All of the b-tagging related systematics are applied as event weights. From left: type, description, and the name of systematic used in the fit.

¹⁶¹⁴ Theoretical uncertainties applied to MC predictions, including cross section, PDF, and
¹⁶¹⁵ scale uncertainties are taken from theory calculations. The theory uncertainties applied to the
¹⁶¹⁶ predominate background estimates are summarized in Table 53.

Table 53: Summary of theoretical uncertainties for MC predictions in the analysis.

¹⁶¹⁷ 22 Results

¹⁶¹⁸ A maximum likelihood fit is performed simultaneously over the reconstructed Higgs p_T spectrum
¹⁶¹⁹ in the three signal regions, 2lSS, 3lS, and 3lF. The signal is split into high and low p_T samples,
¹⁶²⁰ based on whether the truth p_T of the Higgs is above or below 150 GeV. The parameters $\mu_{t\bar{t}Hhighp_T}$

1621 and $\mu_{t\bar{t}H\text{low}p_T}$, where $\mu = \sigma_{\text{observed}}/\sigma_{\text{SM}}$, are extracted from the fit, signifying the difference
1622 between the observed value and the theory prediction. Unblinded results are shown for the 80
1623 fb^{-1} data set, as well as MC only projections of results using the full Run-2, 140 fb^{-1} dataset.

1624 As described in Section 21, there are 229 systematic uncertainties that are considered
1625 as NPs in the fit. These NPs are constrained by Gaussian or log-normal probability density
1626 functions. The latter are used for normalisation factors to ensure that they are always positive.
1627 The expected number of signal and background events are functions of the likelihood. The prior
1628 for each NP is added as a penalty term, decreasing the likelihood as it is shifted away from its
1629 nominal value.

1630 22.1 Results - 80 fb^{-1}

1631 As the data collected from 2015-2017 has been unblinded for $t\bar{t}H$ —ML channels, representing 80
1632 fb^{-1} , those events are unblinded. The predicted Higgs p_T spectrum is fit to data simultaneously
1633 in each of the three signal regions shown in Figure 22.1.

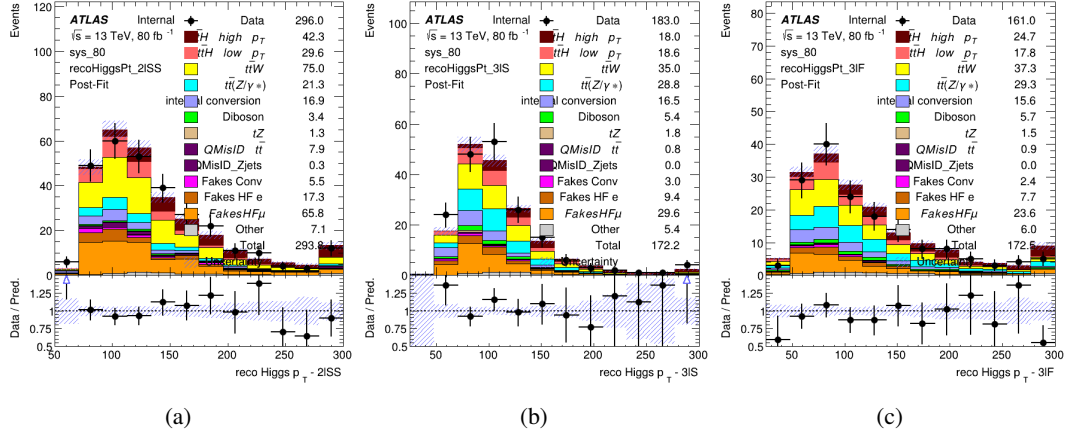


Figure 22.1: Post-fit distributions of the reconstructed Higgs p_T in the three signal regions, (a) 2ISS, (b) 3IS, and (c) 3IF, for 80 fb^{-1} of MC

1634

A post-fit summary of the fitted regions is shown in Figure 22.2.

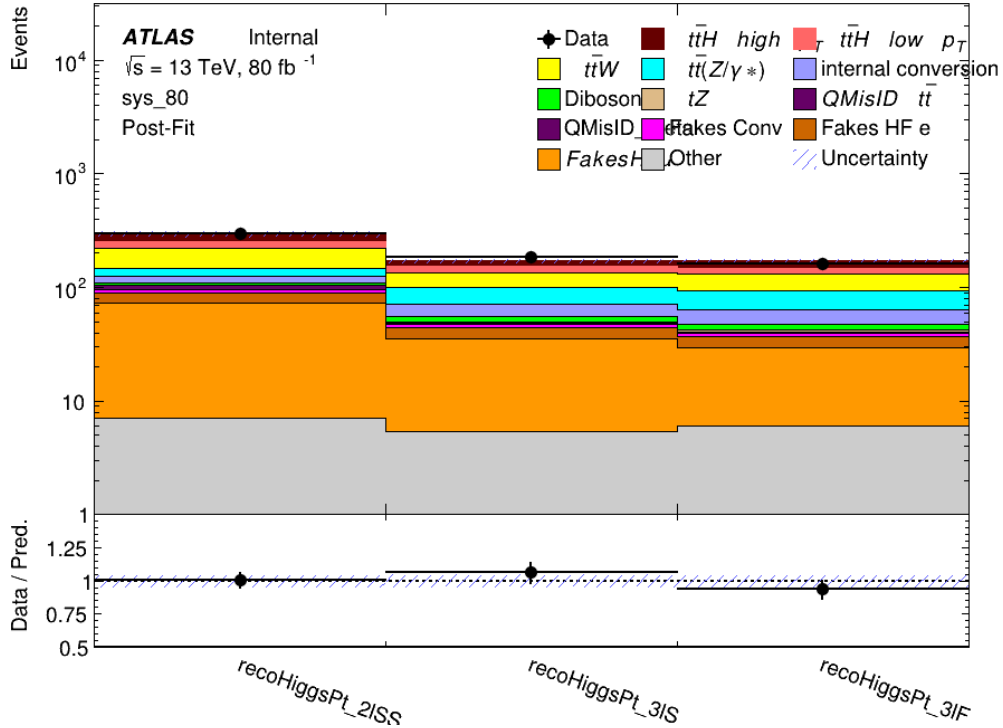


Figure 22.2: Post-fit summary of the yields in each signal region.

1635 The the measured μ values for high and low p_T Higgs production obtained from the fit
 1636 are shown in 54. A significance of 1.7σ is observed for $t\bar{t}H$ high p_T , and 2.1σ is measured for
 1637 $t\bar{t}H$ low p_T .

$$\mu_{t\bar{t}H \text{ high } p_T} = 2.1^{+0.62}_{-0.59}(\text{stat})^{+0.40}_{-0.43}(\text{sys})$$

$$\mu_{t\bar{t}H \text{ low } p_T} = 0.83^{+0.37}_{-0.37}(\text{stat})^{+0.48}_{-0.47}(\text{sys})$$

Table 54: Best fit μ values for $t\bar{t}H$ high p_T and $t\bar{t}H$ low p_T , where $\mu = \sigma_{\text{obs}}/\sigma_{\text{pred}}$

1638 The most prominent sources of systematic uncertainty, as measured by their impact on
 1639 $\mu_{t\bar{t}H \text{ high } p_T}$, are summarized in Table 55.

| Uncertainty Source | $\Delta\mu$ | |
|---------------------------------------|-------------|------|
| Jet Energy Scale | 0.25 | 0.23 |
| $t\bar{t}H$ cross-section (QCD Scale) | -0.11 | 0.21 |
| ATLAS Luminosity | -0.13 | 0.14 |
| Jet Flavor Tagging | 0.14 | 0.13 |
| $t\bar{t}W$ cross-section (QCD Scale) | -0.12 | 0.11 |
| Higgs Branching Ratio | -0.1 | 0.11 |
| $t\bar{t}H$ cross-section (PDF) | -0.07 | 0.08 |
| Electron ID | -0.06 | 0.06 |
| $t\bar{t}$ HF Muon Unc. | -0.05 | 0.06 |
| $t\bar{t}Z$ cross-section (QCD Scale) | -0.05 | 0.05 |
| Diboson cross-section | -0.05 | 0.05 |
| HF Muon Shape - 3l | -0.04 | 0.04 |
| Total Systematic Uncertainty | 0.40 | 0.43 |

Table 55: Summary of the most significant sources of systematic uncertainty on the measurement of $t\bar{t}H$ high p_T .

1640 The ranking and impact of those nuisance parameters with the largest contribution to the
 1641 overall uncertainty is shown in Figure 22.3.

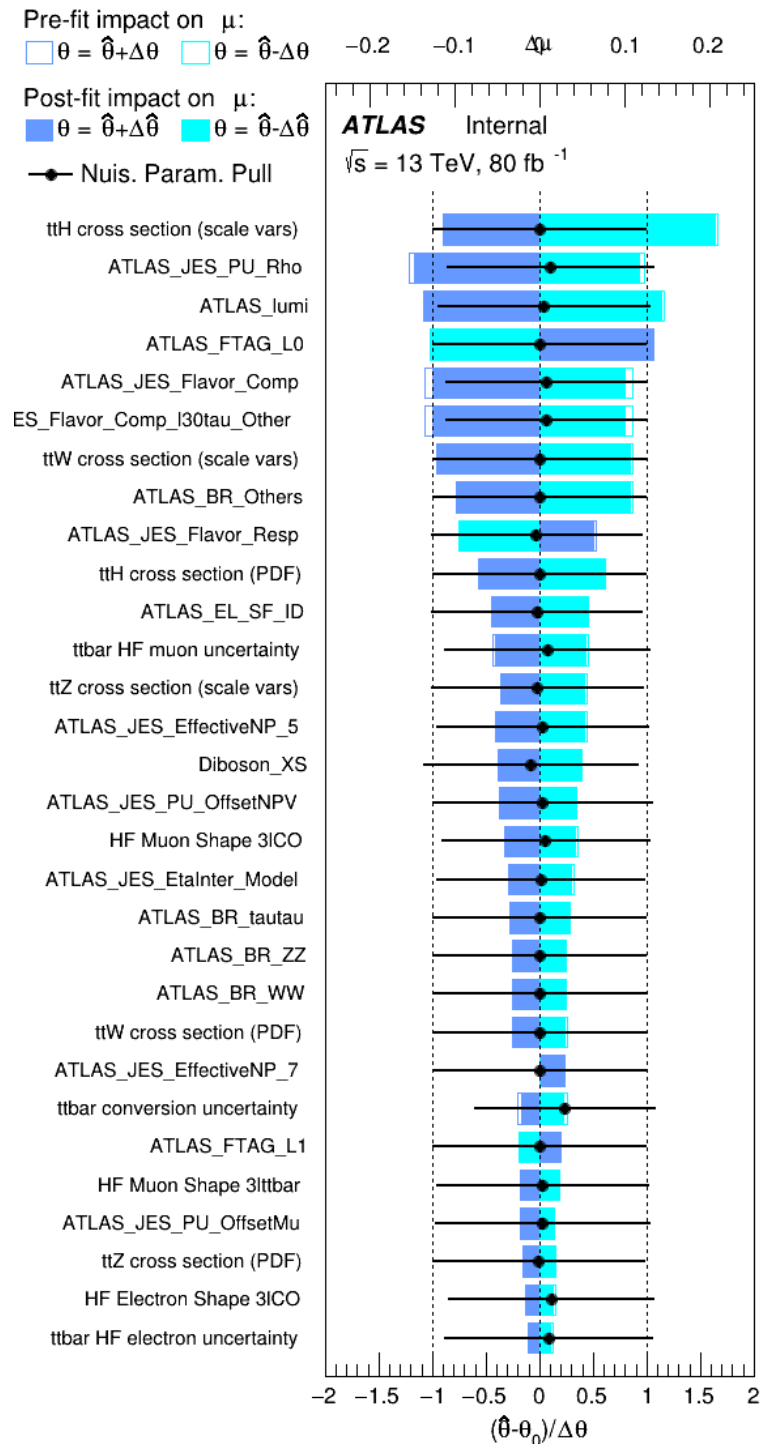


Figure 22.3: Impact of systematic uncertainties on the measurement of high p_T $t\bar{t}H$ events

1642

The background composition of each of the fit regions is shown in Figure 22.4.

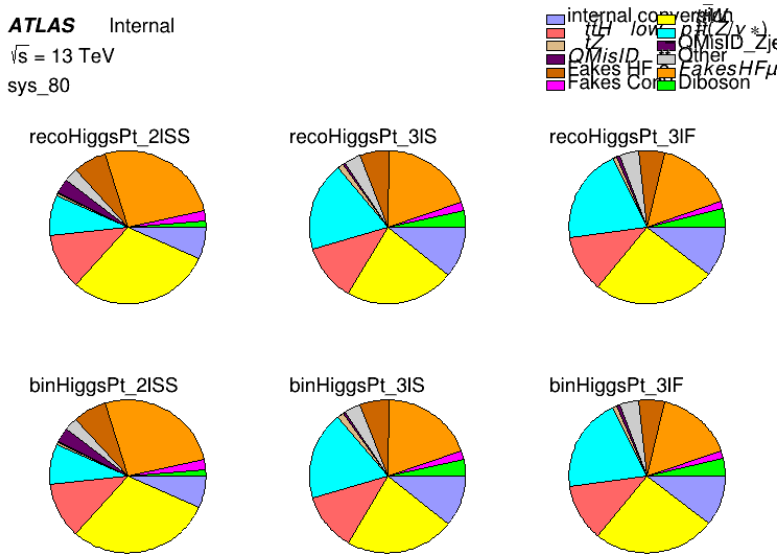


Figure 22.4: Background composition of the fit regions.

1643

22.2 Projected Results - 140 fb^{-1}

1644

As data collected in 2018 has not yet been unblinded for $t\bar{t}H - \text{ML}$ at the time of this note, data

1645

from that year remains blinded. Instead, an Asimov fit is performed - with the MC prediction

1646

being used both as the SM prediction as well as the data in the fit - in order to give expected

1647

results.

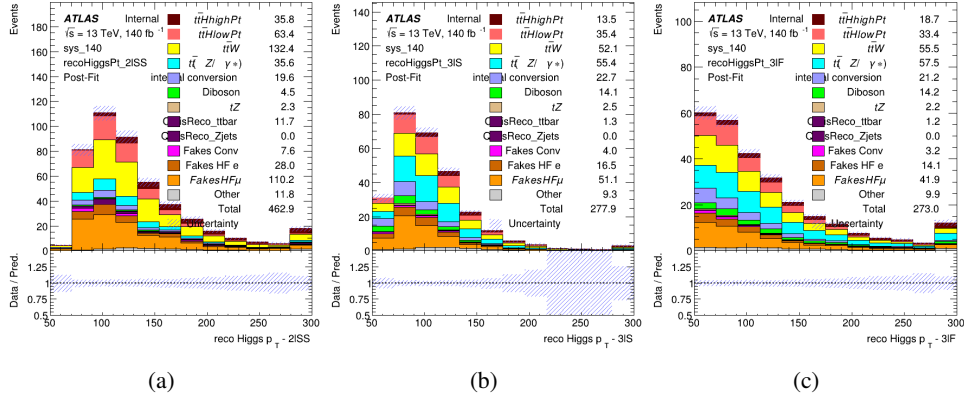


Figure 22.5: Blinded post-fit distributions of the reconstructed Higgs p_T in the three signal regions, (a) 2ISS, (b) 3IS, and (c) 3IF, for 140 fb^{-1} of data

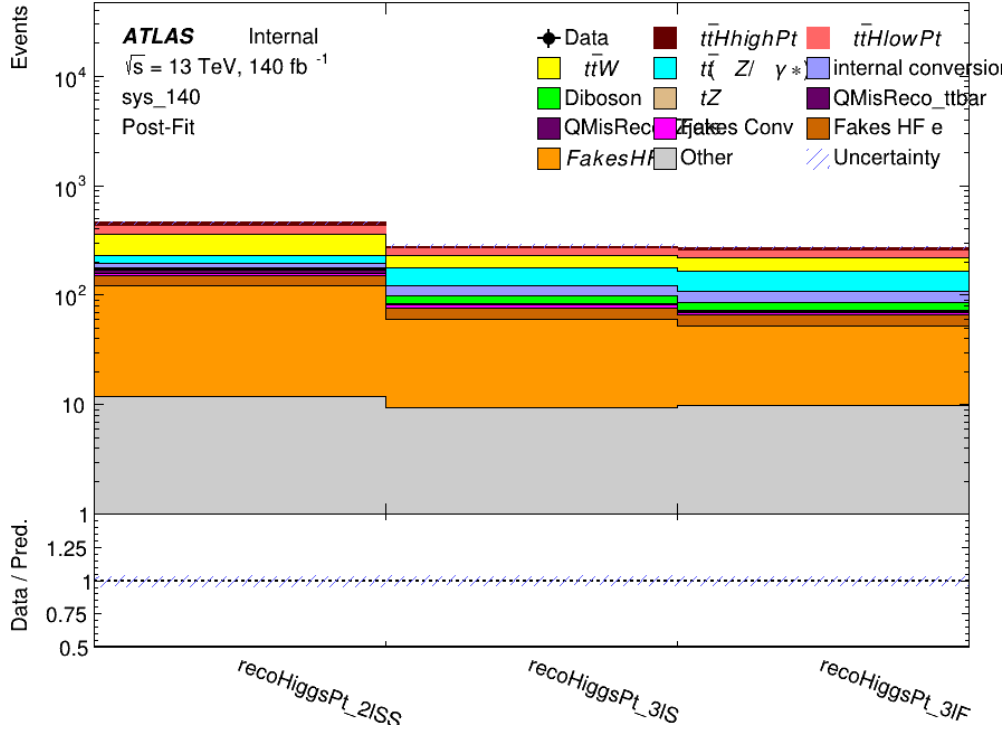


Figure 22.6: Post-fit summary of fit.

¹⁶⁴⁹ shown in [56](#). A significance of 2.0σ is expected for $t\bar{t}H$ high p_T , and a projected significance

¹⁶⁵⁰ 2.3σ is extracted for $t\bar{t}H$ low p_T .

$$\mu_{t\bar{t}H \text{ high } p_T} = 1.00^{+0.45}_{-0.43} (\text{stat})^{+0.31}_{-0.31} (\text{sys})$$

$$\mu_{t\bar{t}H \text{ low } p_T} = 1.00^{+0.29}_{-0.30} (\text{stat})^{+0.47}_{-0.46} (\text{sys})$$

Table 56: Best fit μ values for $t\bar{t}H$ high p_T and $t\bar{t}H$ low p_T , where $\mu = \sigma_{\text{obs}}/\sigma_{\text{pred}}$

¹⁶⁵¹ The most prominent sources of systematic uncertainty, as measured by their impact on

¹⁶⁵² $\mu_{t\bar{t}H \text{ high } p_T}$, are summarized in Table [57](#).

| Uncertainty Source | $\Delta\mu$ | |
|---------------------------------------|-------------|------|
| Jet Energy Scale | 0.2 | 0.18 |
| $t\bar{t}W$ cross-section (QCD Scale) | -0.12 | 0.11 |
| ATLAS Luminosity | -0.11 | 0.11 |
| Jet Flavor Tagging | 0.11 | 0.10 |
| $t\bar{t}H$ cross-section (QCD Scale) | -0.06 | 0.06 |
| Higgs Branching Ratio | -0.1 | 0.11 |
| $t\bar{t}H$ cross-section (PDF) | -0.07 | 0.08 |
| Electron ID | -0.05 | 0.05 |
| $t\bar{t}$ HF Muon Unc. | -0.04 | 0.06 |
| $t\bar{t}Z$ cross-section (QCD Scale) | -0.03 | 0.04 |
| Diboson cross-section | -0.03 | 0.03 |
| HF Muon Shape - 3l | -0.02 | 0.02 |
| Total Systematic Uncertainty | 0.31 | 0.31 |

Table 57: Summary of the most significant sources of systematic uncertainty on the measurement of $t\bar{t}H$ high p_T .

¹⁶⁵³ The ranking and impact of those nuisance parameters with the largest contribution to the

¹⁶⁵⁴ overall uncertainty is shown in Figure [22.7](#).

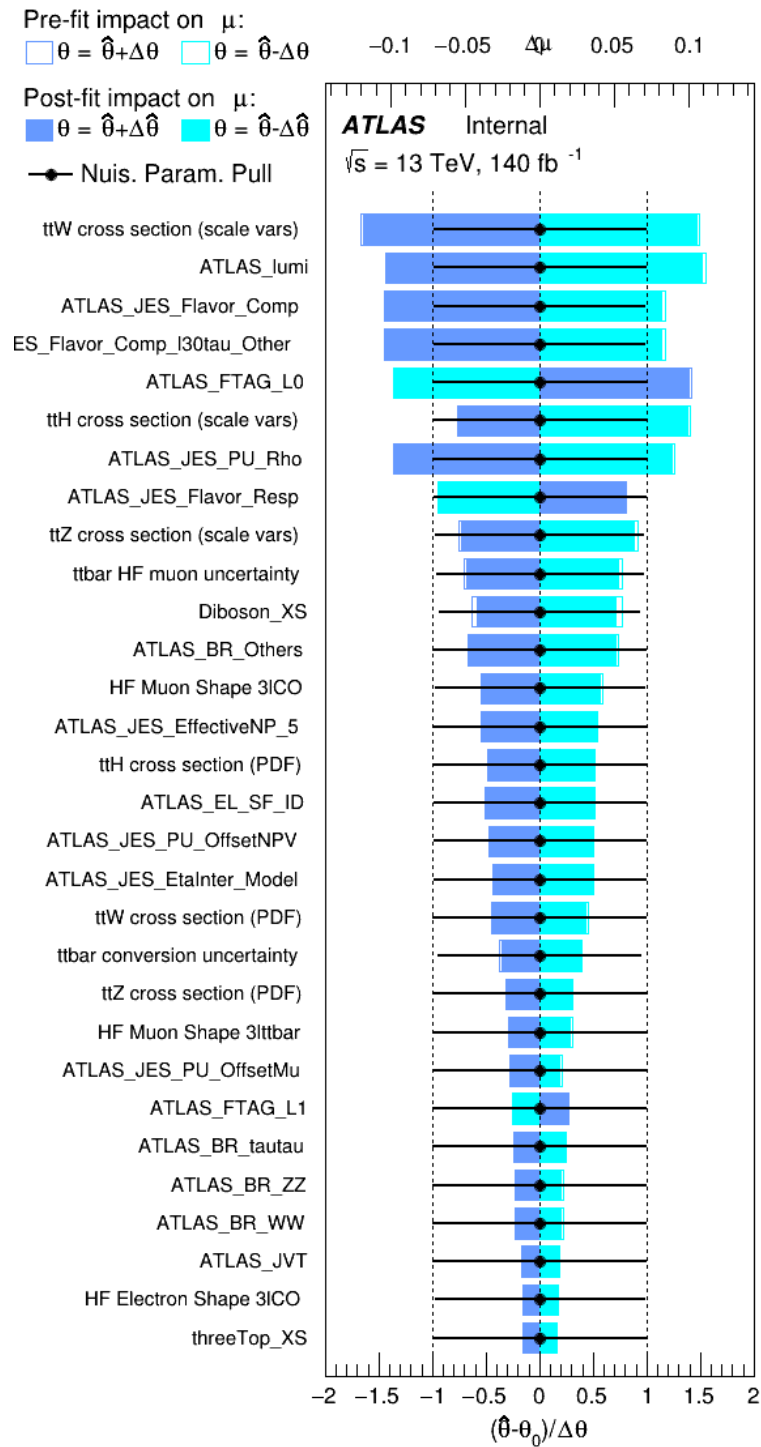


Figure 22.7: Impact of systematic uncertainties on the measurement of high p_T $t\bar{t}H$ events

1655

The background composition of each of the fit regions is shown in Figure 22.8.

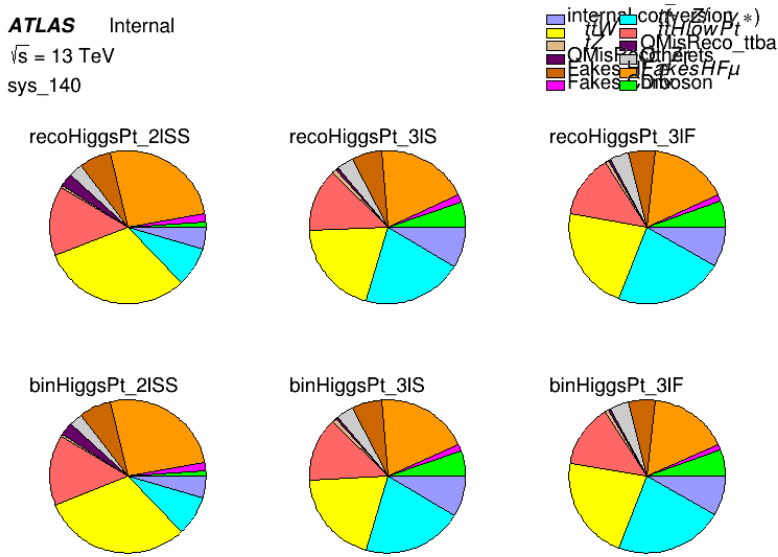


Figure 22.8: Background composition of the fit regions.

1656

Part VI

1657

Conclusion

1658 As search for the effects of dimension-six operators on $t\bar{t}H$ production is performed. An effective
 1659 field theory approached is used to parametrize the effects of high energy physics on the Higgs
 1660 momentum spectrum. The momentum spectrum is reconstructed using various MVA techniques,
 1661 and the limits on dimension-six operators are limited to X.

1662 References

- 1663 [1] R. Oerter, *The theory of almost everything : the Standard Model, the unsung triumph of*
1664 *modern physics*, Pi Press, 2006, ISBN: 978-0-13-236678-6.
- 1665 [2] P. W. Higgs, *Broken Symmetries and the Masses of Gauge Bosons*,
1666 Phys. Rev. Lett. 13 (Oct, 1964) 508-509 ().
- 1667 [3] J. Goldstone, A. Salam and S. Weinberg, *Broken Symmetries*,
1668 Phys. Rev. **127** (3 1962) 965,
1669 URL: <https://link.aps.org/doi/10.1103/PhysRev.127.965>.
- 1670 [4] J. Ellis, *Higgs Physics*,
1671 (2013) 117, 52 pages, 45 figures, Lectures presented at the ESHEP 2013 School of
1672 High-Energy Physics, to appear as part of the proceedings in a CERN Yellow Report,
1673 URL: <https://cds.cern.ch/record/1638469>.
- 1674 [5] *Evidence for the associated production of the Higgs boson and a top quark pair with the*
1675 *ATLAS detector*, tech. rep. ATLAS-CONF-2017-077, CERN, 2017,
1676 URL: <https://cds.cern.ch/record/2291405>.
- 1677 [6] A. M. Sirunyan et al., *Observation of $t\bar{t}H$ Production*,
1678 *Physical Review Letters* **120** (2018), ISSN: 1079-7114,
1679 URL: <http://dx.doi.org/10.1103/PhysRevLett.120.231801>.

- 1680 [7] B. Dumont, S. Fichet and G. von Gersdorff,
1681 *A Bayesian view of the Higgs sector with higher dimensional operators,*
1682 *Journal of High Energy Physics* **2013** (2013), ISSN: 1029-8479,
1683 URL: [http://dx.doi.org/10.1007/JHEP07\(2013\)065](http://dx.doi.org/10.1007/JHEP07(2013)065).
- 1684 [8] S. Banerjee, S. Mukhopadhyay and B. Mukhopadhyaya,
1685 *Higher dimensional operators and the LHC Higgs data: The role of modified kinematics,*
1686 *Physical Review D* **89** (2014), ISSN: 1550-2368,
1687 URL: <http://dx.doi.org/10.1103/PhysRevD.89.053010>.
- 1688 [9] M. Aaboud et al., *Observation of electroweak $W^\pm Z$ boson pair production in association*
1689 *with two jets in pp collisions at $\sqrt{s} = 13$ TeV with the ATLAS detector,*
1690 *Phys. Lett. B* **793** (2019) 469, arXiv: [1812.09740 \[hep-ex\]](https://arxiv.org/abs/1812.09740).
- 1691 [10] T. Gleisberg et al., *Event generation with SHERPA 1.1*, *JHEP* **02** (2009) 007,
1692 arXiv: [0811.4622 \[hep-ph\]](https://arxiv.org/abs/0811.4622).
- 1693 [11] R. D. Ball et al., *Parton distributions for the LHC Run II*, *JHEP* **04** (2015) 040,
1694 arXiv: [1410.8849 \[hep-ph\]](https://arxiv.org/abs/1410.8849).
- 1695 [12] H.-L. Lai et al., *New parton distributions for collider physics*,
1696 *Phys. Rev. D* **82** (2010) 074024, arXiv: [1007.2241 \[hep-ph\]](https://arxiv.org/abs/1007.2241).
- 1697 [13] S. Frixione, G. Ridolfi and P. Nason,
1698 *A positive-weight next-to-leading-order Monte Carlo for heavy flavour hadroproduction*,
1699 *JHEP* **09** (2007) 126, arXiv: [0707.3088 \[hep-ph\]](https://arxiv.org/abs/0707.3088).

- 1700 [14] E. Re, *Single-top Wt-channel production matched with parton showers using the*
1701 *POWHEG method*, Eur. Phys. J. C **71** (2011) 1547, arXiv: [1009.2450](https://arxiv.org/abs/1009.2450) [hep-ph].
- 1702 [15] ATLAS Collaboration, *Electron efficiency measurements with the ATLAS detector using*
1703 *the 2015 LHC proton–proton collision data*, ATLAS-CONF-2016-024, 2016,
1704 URL: <https://cds.cern.ch/record/2157687>.
- 1705 [16] ATLAS Collaboration, *Measurement of the muon reconstruction performance of the*
1706 *ATLAS detector using 2011 and 2012 LHC proton–proton collision data*,
1707 Eur. Phys. J. C **74** (2014) 3130, arXiv: [1407.3935](https://arxiv.org/abs/1407.3935) [hep-ex].
- 1708 [17] R. Narayan et al., *Measurement of the total and differential cross sections of a*
1709 *top-quark-antiquark pair in association with a W boson in proton-proton collisions at a*
1710 *centre-of-mass energy of 13 TeV with ATLAS detector at the Large Hadron Collider*,
1711 tech. rep. ATL-COM-PHYS-2020-217, CERN, 2020,
1712 URL: <https://cds.cern.ch/record/2712986>.
- 1713 [18] ATLAS Collaboration, *Jet Calibration and Systematic Uncertainties for Jets*
1714 *Reconstructed in the ATLAS Detector at $\sqrt{s} = 13 \text{ TeV}$* , ATL-PHYS-PUB-2015-015,
1715 2015, URL: <https://cds.cern.ch/record/2037613>.
- 1716 [19] ATLAS Collaboration,
1717 *Selection of jets produced in 13 TeV proton–proton collisions with the ATLAS detector*,
1718 ATLAS-CONF-2015-029, 2015, URL: <https://cds.cern.ch/record/2037702>.

- 1719 [20] ATLAS Collaboration, *Performance of pile-up mitigation techniques for jets in pp*
1720 *collisions at $\sqrt{s} = 8$ TeV using the ATLAS detector*, *Eur. Phys. J. C* **76** (2016) 581,
1721 arXiv: [1510.03823 \[hep-ex\]](https://arxiv.org/abs/1510.03823).
- 1722 [21] ATLAS Collaboration, *Performance of missing transverse momentum reconstruction*
1723 *with the ATLAS detector in the first proton–proton collisions at $\sqrt{s} = 13$ TeV*,
1724 ATL-PHYS-PUB-2015-027, 2015, URL: <https://cds.cern.ch/record/2037904>.
- 1725 [22] 2021, URL: https://twiki.cern.ch/twiki/bin/view/AtlasProtected/BTagCalibrationRecommendationsRelease21#Tools_for_Flavor_Tagging_Calibra.
- 1726 [23] P. S. A. Hoecker, *TMVA 4 Toolkit for Multivariate Data Analysis with ROOT*,
1727 arXiv:physics/0703039 (2013).
- 1728 [24] F. Cardillo et al., *Measurement of the fiducial and differential cross-section of a top*
1729 *quark pair in association with a Z boson at 13 TeV with the ATLAS detector*, (2019),
1730 URL: <https://cds.cern.ch/record/2672207>.
- 1731 [25] T. Chen and C. Guestrin, ‘XGBoost: A Scalable Tree Boosting System’,
1732 *Proceedings of the 22nd ACM SIGKDD International Conference on Knowledge*
1733 *Discovery and Data Mining*, KDD ’16, ACM, 2016 785, ISBN: 978-1-4503-4232-2,
1734 URL: <http://doi.acm.org/10.1145/2939672.2939785>.
- 1735 [26] ATLAS Collaboration, *Luminosity determination in pp collisions at $\sqrt{s} = 7$ TeV using*
1736 *the ATLAS detector at the LHC*, *Eur. Phys. J. C* **71** (2011) 1630,
1737 arXiv: [1101.2185 \[hep-ex\]](https://arxiv.org/abs/1101.2185).

- 1740 [27] G. Avoni et al.,
1741 *The new LUCID-2 detector for luminosity measurement and monitoring in ATLAS,*
1742 *JINST* **13** (2018) P07017.
1743 [28] G. Aad, T. Abajyan, B. Abbott and etal, *Jet energy resolution in proton-proton collisions*
1744 *at $\sqrt{s} = 7 \text{ TeV}$ recorded in 2010 with the ATLAS detector,*
1745 *The European Physical Journal C* **73** (2013) 2306, ISSN: 1434-6052,
1746 URL: <https://doi.org/10.1140/epjc/s10052-013-2306-0>.
1747 [29] A. Collaboration, *Performance of b -jet identification in the ATLAS experiment,*
1748 *Journal of Instrumentation* **11** (2016) P04008,
1749 URL: <http://stacks.iop.org/1748-0221/11/i=04/a=P04008>.
1750 [30] *Observation of the associated production of a top quark and a Z boson at 13 TeV with*
1751 *ATLAS*, (2020), URL: <https://cds.cern.ch/record/2722504>.

¹⁷⁵² **List of contributions**

1753

1754 **Appendices**

1755 **.1 Non-prompt lepton MVA**

1756 A lepton MVA has been developed to better reject non-prompt leptons than standard cut
1757 based selections based upon impact parameter, isolation and PID. The name of this MVA is
1758 **PromptLeptonIso**. The full set of studies and detailed explanation can be found in [17].

1759 The decays of W and Z bosons are commonly selected by the identification of one or two
1760 electrons or muons. The negligible lifetimes of these bosons mean that the leptons produced in the
1761 decay originate from the interaction vertex and are thus labelled “prompt”. Analyses using these
1762 light leptons impose strict reconstruction quality, isolation and impact parameter requirements
1763 to remove “fake” leptons. A significant source of the fake light leptons are non-prompt leptons
1764 produced in decays of hadrons that contain bottom (b) or charm (c) quarks. Such hadrons
1765 typically have microscopically significant lifetimes that can be detected experimentally.

1766 These non-prompt leptons can also pass the tight selection criteria. In analyses that
1767 involve top (t) quarks, which decay almost exclusively into a W boson and a b quark, non-
1768 prompt leptons from the semileptonic decay of bottom and charm hadrons can be a significant
1769 source of background events. This is particularly the case in the selection of same-sign dilepton
1770 and multilepton final states.

1771 The main idea is to identify non-prompt light leptons using lifetime information associated
1772 with a track jet that matches the selected light lepton. This lifetime information is computed
1773 using tracks contained within the jet. Typically, lepton lifetime is determined using the impact
1774 parameter of the track reconstructed by the inner tracking detector which is matched to the recon-
1775 structed lepton. Using additional reconstructed charged particle tracks increases the precision of

1776 identifying the displaced decay vertex of bottom or charm hadrons that produced a non-prompt
 1777 light lepton. The MVA also includes information related to the isolation of the lepton to reject
 1778 non-prompt leptons.

1779 **PromptLeptonIso** is a gradient boosted BDT. The training of the BDT is performed on
 1780 leptons selected from the PowHEG+PYTHIA6 non-allhad $t\bar{t}$ MC sample. Eight variables are used
 1781 to train the BDT in order to discriminate between prompt and non-prompt leptons. The track
 1782 jets that are matched to the non-prompt leptons correspond to jets initiated by b or c quarks, and
 1783 may contain a displaced vertex. Consequently, three of the selected variables are used to identify
 1784 b-tag jets by standard ATLAS flavour tagging algorithms. Two variables use the relationship
 1785 between the track jet and lepton: the ratio of the lepton p_T with respect to the track jet p_T and
 1786 ΔR between the lepton and the track jet axis. Finally three additional variables test whether the
 1787 reconstructed lepton is isolated: the number of tracks collected by the track jet and the lepton
 1788 track and calorimeter isolation variables. Table 58 describes the variables used to train the BDT
 1789 algorithm. The choice of input variables has been extensively discussed with Egamma, Muon,
 1790 Tracking, and Flavour Tagging CP groups.

| Variable | Description |
|--|---|
| N_{track} in track jet | Number of tracks collected by the track jet |
| $\text{IP2 log}(P_b/P_{\text{light}})$ | Log-likelihood ratio between the b and light jet hypotheses with the IP2D algorithm |
| $\text{IP3 log}(P_b/P_{\text{light}})$ | Log-likelihood ratio between the b and light jet hypotheses with the IP3D algorithm |
| $N_{\text{TrkAtVtx}} \text{ SV + JF}$ | Number of tracks used in the secondary vertex found by the SV1 algorithm in addition to the number of tracks from secondary vertices found by the JetFitter algorithm with at least two tracks |
| $p_T^{\text{lepton}}/p_T^{\text{track jet}}$ | The ratio of the lepton p_T and the track jet p_T |
| $\Delta R(\text{lepton}, \text{track jet})$ | ΔR between the lepton and the track jet axis |
| $p_T^{\text{VarCone30}}/p_T$ | Lepton track isolation, with track collecting radius of $\Delta R < 0.3$ |
| $E_T^{\text{TopoCone30}}/p_T$ | Lepton calorimeter isolation, with topological cluster collecting radius of $\Delta R < 0.3$ |

Table 58: A table of the variables used in the training of **PromptLeptonIso**.

1791 The output distribution of the BDT is shown in Figure .1.

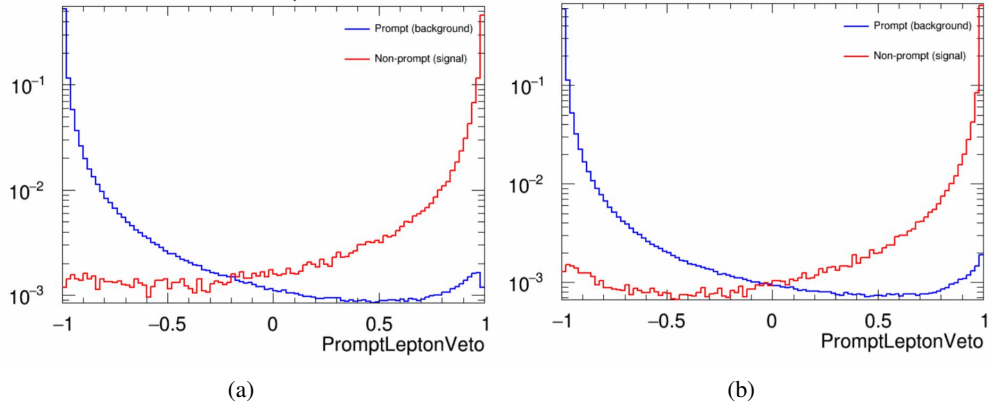


Figure .9: Distribution of the PLV BDT discriminant for (a) electrons and (b) muons

1792 The ROC curve for the BDT response, compared to the standard `FixedCutTight` WP, is
 1793 shown in figure .1, which shows a clear improvement when using this alternate training.

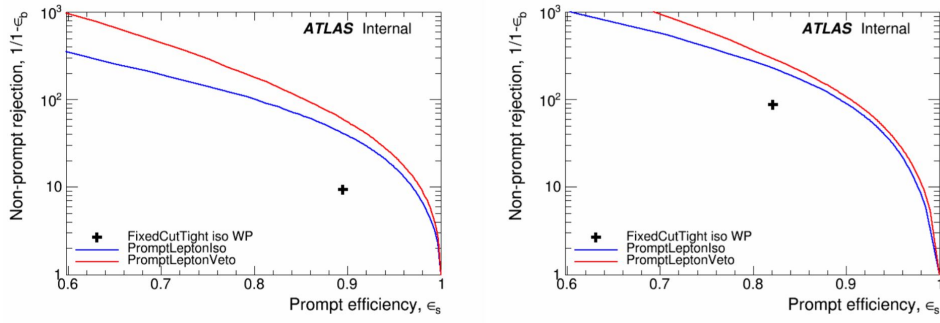


Figure .10: ROC curves for the PLV as well as the performance of the standard `FixedCutTight` WP for (left) electrons and (right) muons

1794 A cutoff value of -0.7 for electrons and -0.5 for muons are chosen as the WPs for this
 1795 MVA, based on an optimisation of S/\sqrt{B} performed in the preselection regions of the $t\bar{t}H - ML$
 1796 analysis, which have a signature similar to that of this analysis.

1797 The efficiency of the tight `PromptLeptonIso` working point is measured using the tag
1798 and probe method with $Z \rightarrow \ell^+ \ell^-$ events. Such calibration are performed by analysers from
1799 this analysis in communication with the Egamma and Muon combined performance groups. The
1800 scale factor are approximately 0.92 for $10 < p_T < 15$ GeV, and averaging at 0.98 to 0.99 for
1801 higher p_T leptons. An extra systematic is applied to muons within $\Delta R < 0.6$ of a calorimeter
1802 jet, since there is a strong dependence on the scale factor due to the presence of these jets. For
1803 electrons, the dominant systematics is coming from pile-up dependence. Overall the systematics
1804 are a maximum of 3% at low p_T and decreasing at a function of p_T .

1805 **.2 Non-prompt CR Modelling**

1806 In order to further validate the modeling in each of the non-prompt CRs, additional
 1807 kinematic plots are made in the Z+jets CR and $t\bar{t}$ CR in each of the continuous b-tag regions,
 1808 after the correction factors detailed in Section 12.3 have been applied.

1809 In the case of the Z+jets CR, the p_T spectrum of the lepton originating from the W
 1810 candidate is shown, as this is the distribution used to extract the scale factor applied to Z+jets.
 1811 These plots are shown in Figures .11 and .12.

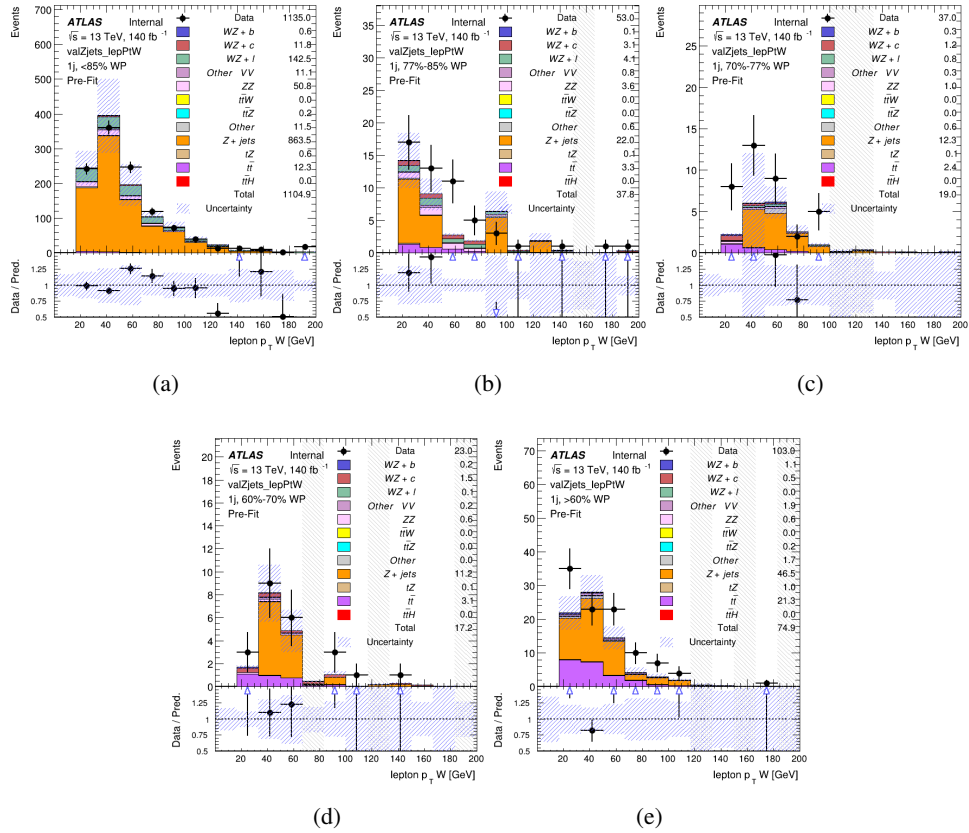


Figure .11: Comparisons between the data and MC distributions of the p_T of the lepton originating from the W-candidate in the Z+jets CR for each of the 1-jet b-tag working point regions

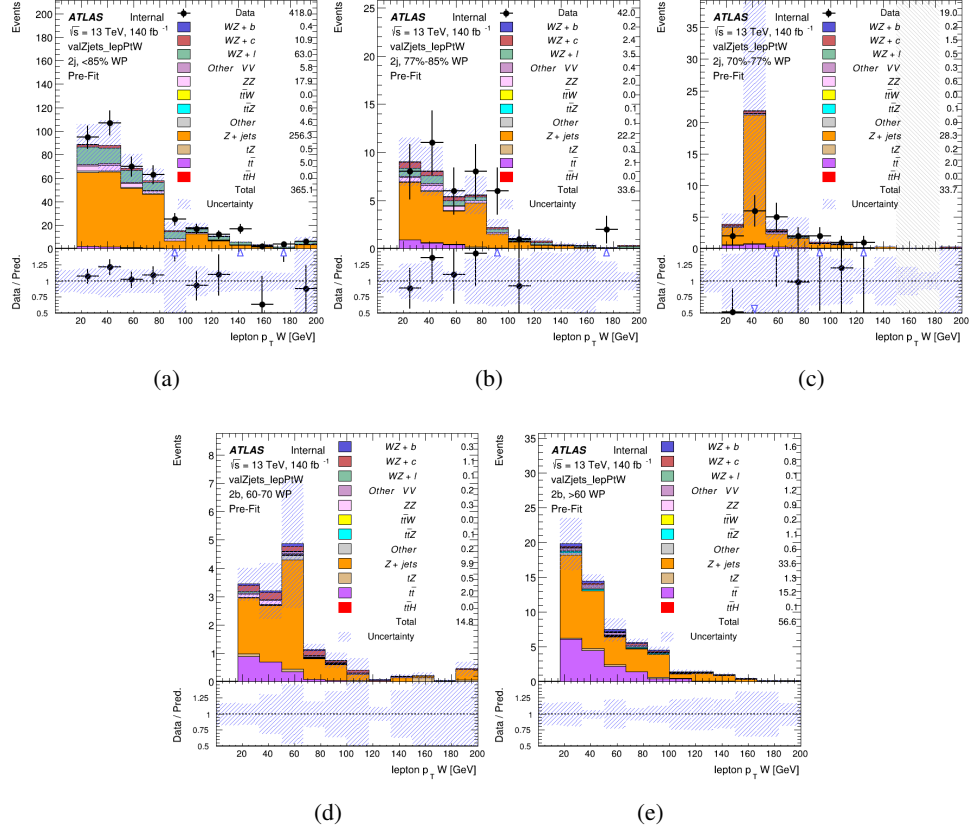


Figure .12: Comparisons between the data and MC distributions of the p_T of the lepton originating from the W-candidate in the Z+jets CR for each of the 2-jet b-tag working point regions

1812 The same is shown for the $t\bar{t}$ CR, but the p_T of the OS lepton is used instead as a
 1813 representation of the modeling, as the lepton from the W is not well defined for $t\bar{t}$ events. These
 1814 plots are shown in Figures .13 and .14.

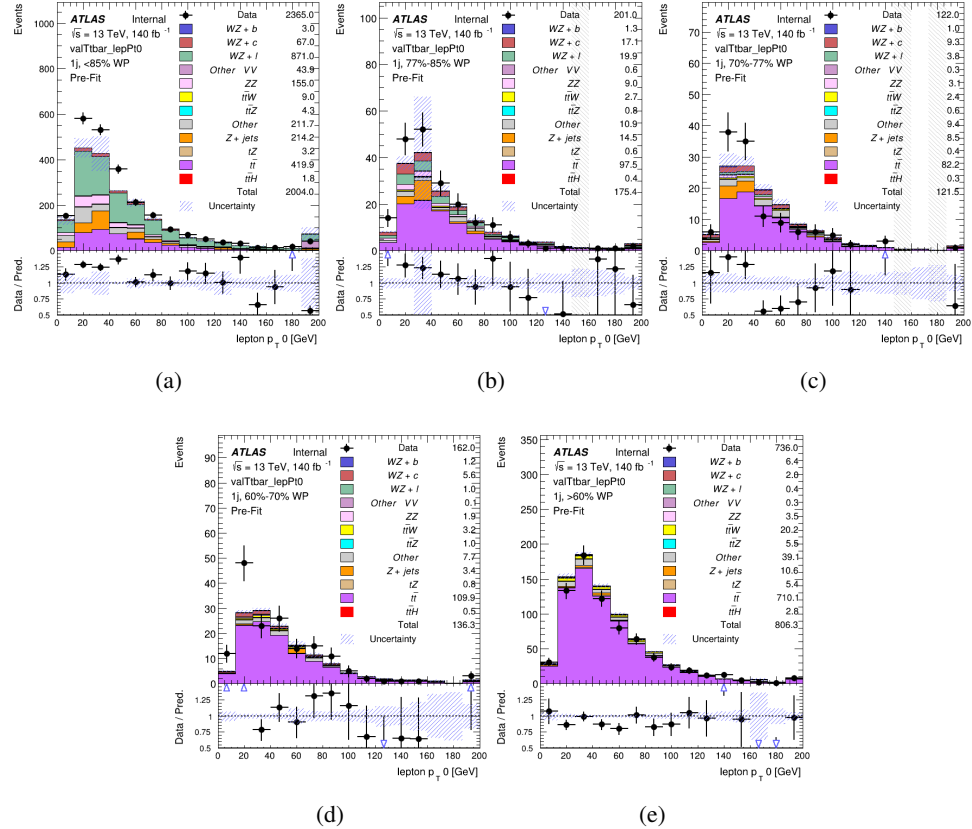


Figure .13: Comparisons between the data and MC distributions of the p_T of the OS lepton in the $t\bar{t}$ CR for each of the 1-jet b-tag working point regions

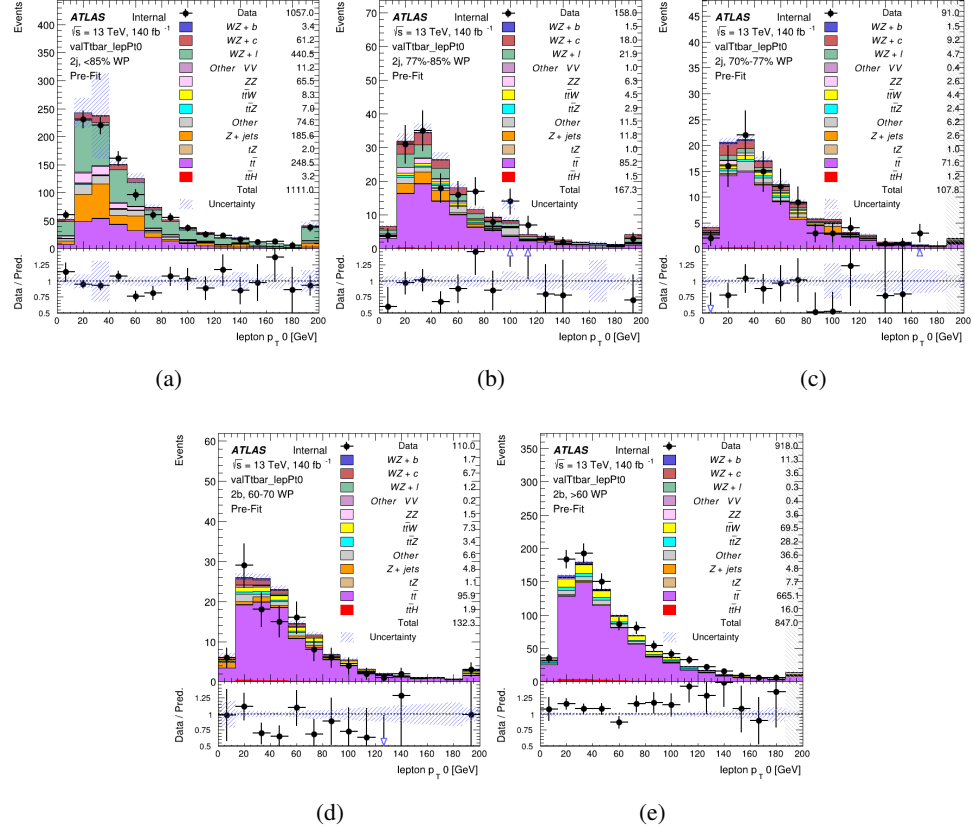


Figure 14: Comparisons between the data and MC distributions of the p_T of the OS lepton in the $t\bar{t}$ CR for each of the 2-jet b-tag working point regions

1815 .3 tZ Interference Studies

1816 Because it includes an on-shell Z boson as well as a b-jet and W from the top decay, tZ
1817 production represents an identical final state to WZ + b-jet. This implies the possibility of matrix
1818 level interference between these two processes not accounted for in the Monte Carlo simulations,
1819 which consider the two processes independently. Truth level studies are performed in order to
1820 estimate the impact of these interference effects.

1821 In order to estimate the matrix level interference effects between tZ and WZ + b-jet, two
1822 different sets of simulations are produced using MadGraph 5 [**Madgraph**] - one which simulates
1823 these two processes independently, and another where they are produced simultaneously, such
1824 that interference effects are present. These two sets of samples are then compared, and the
1825 difference between them can be taken to represent any interference effects.

1826 MadGraph simulations of 10,000 tZ and 10,000 WZ + b-jet events are produced, along
1827 with 20,000 events where both are present, in the fiducial region where three leptons and at least
1828 one jet are produced.

1829 A selection mimicking the preselection used in the main analysis is applied to the samples:
1830 The SS leptons are required to have $p_T > 20$ GeV, and > 10 GeV is required for the OS lepton.
1831 The associated b-jet is required to have $p_T > 25$ GeV, and all physics objects are required to fall
1832 in a range of $|\eta| < 2.5$.

1833 The kinematics of these samples after the selection has been applied are shown below:

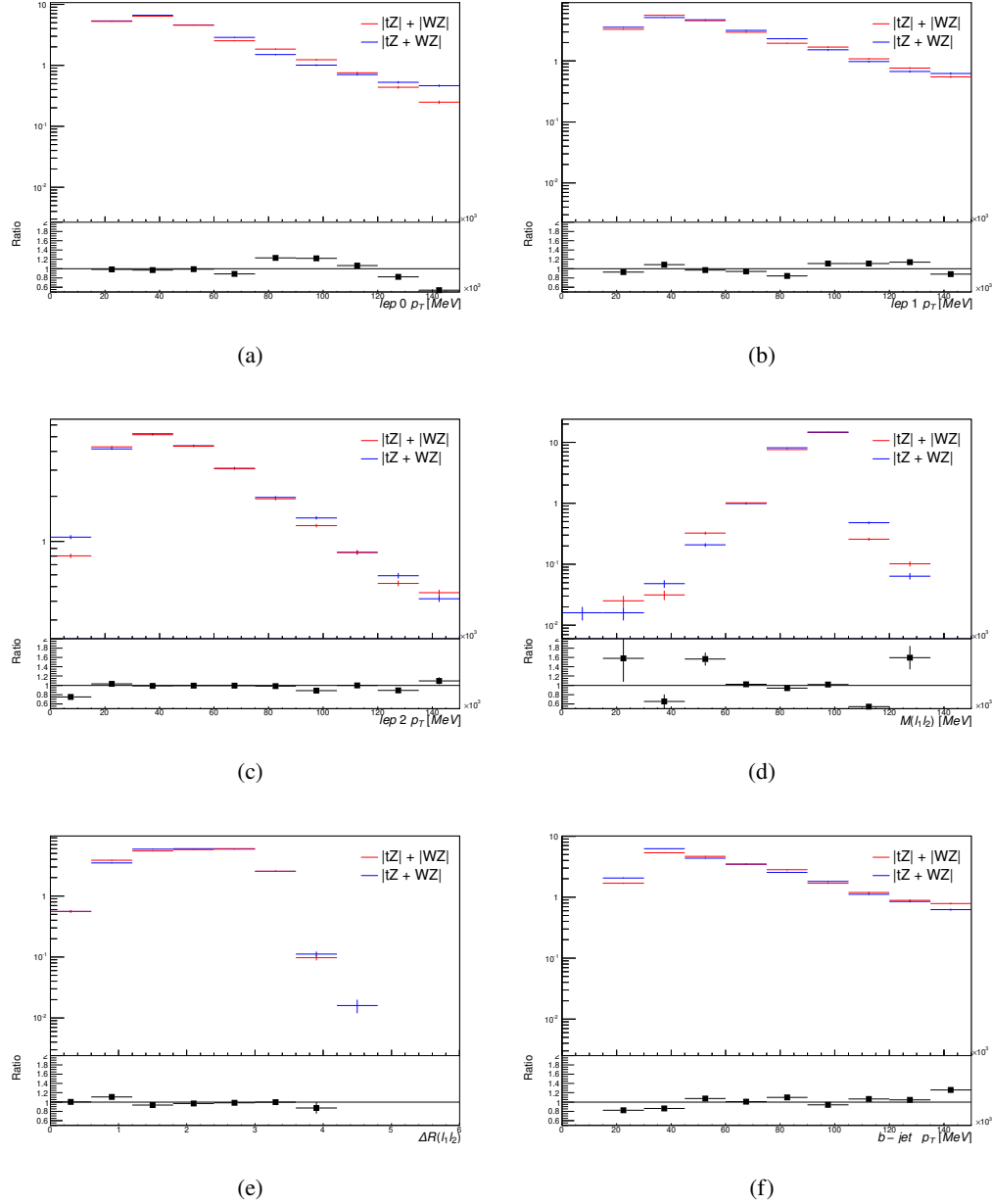


Figure .15: Comparisons between (a) the p_T of the lepton from the W, (b) and (c) show the p_T of the lepton from the Z, (d) the invariant mass of the Z-candidate, (e) ΔR of the leptons from the Z, and (f) the p_T of the b-jet, for WZ and tZ events generated with interference effects (blue) and without interference effects (red).

1834 The overall cross-section of the two methods agree within error, and no significant differ-
1835 ences in the kinematic distributions are seen. It is therefore concluded that interference effects
1836 do not significantly impact the results.

¹⁸³⁷ **.4 Alternate tZ Inclusive Fit**

1838 **.4.1 tZ Inclusive Fit**

1839 While tZ is often considered as a distinct process from WZ + b, this could also be considered part
1840 of the signal. Alternate studies are performed where, using the same framework as the nominal
1841 analysis, a measurement of WZ + b is performed that includes tZ as part of WZ+b.

1842 Because of this change, the tZ CR is no longer necessary, and only the five pseudo-
1843 continuous b-tag regions are used in the fit. Further, systematics related to the tZ cross-section
1844 are removed from the fit, as they are now encompassed by the normalization measurement of
1845 WZ + b. All other systematic uncertainties are carried over from the nominal analysis.

1846 An expected WZ + b cross-section of $4.1^{+0.78}_{-0.74}(\text{stat})^{+0.53}_{-0.52}(\text{sys}) \text{ fb}$ is extracted from the fit,
1847 with an expected significance of 4.0σ .

1848 The impact of the predominate systematics are summarized in Table 59.

| Uncertainty Source | $\Delta\mu$ | |
|---------------------------------|-------------|-------|
| WZ + light cross-section | 0.08 | -0.08 |
| Jet Energy Scale | -0.06 | 0.08 |
| Luminosity | -0.05 | 0.06 |
| WZ + charm cross-section | -0.04 | 0.05 |
| Other Diboson + b cross-section | -0.04 | 0.04 |
| WZ cross-section - QCD scale | -0.04 | 0.03 |
| t̄ cross-section | -0.03 | 0.03 |
| Jet Energy Resolution | -0.03 | 0.03 |
| Flavor tagging | -0.03 | 0.03 |
| Z+jets cross section | -0.02 | 0.02 |
| Total Systematic Uncertainty | -0.15 | 0.16 |

Table 59: Summary of the most significant sources of systematic uncertainty on the measurement of WZ + b with exactly one associated jet.

1849 .4.2 Floating tZ

1850 In order to quantify the impact of the tZ uncertainty on the fit, an alternate fit strategy is used
1851 where the tZ normalization is allowed to float. This normalization factor replaces the cross-
1852 section uncertainty on tZ, and all other parameters of the fit remain the same.

1853 An uncertainty of 17% on the normalization of tZ is extracted from the fit, compared to a
1854 theory uncertainty of 15% applied to the tZ cross-section. The measured uncertainties on WZ
1855 remain the same.

1856 .5 DSID list

Data:

```
data15_13TeV.AllYear.physics_Main.PhysCont.DAOD_HIGG8D1.grp15_v01_p4134
data16_13TeV.AllYear.physics_Main.PhysCont.DAOD_HIGG8D1.grp16_v01_p4134
data17_13TeV.AllYear.physics_Main.PhysCont.DAOD_HIGG8D1.grp17_v01_p4134
data18_13TeV.AllYear.physics_Main.PhysCont.DAOD_HIGG8D1.grp18_v01_p4134
```

mc16a:

```
mc16_13TeV.361603.PowhegPy8EG_CT10nloME_AZNLOCTEQ6L1_ZZllll_mll4.deriv.DAOD_HIGG8D1.e4475_s3126_r9364_r9315_p4133
mc16_13TeV.361602.PowhegPy8EG_CT10nloME_AZNLOCTEQ6L1_WZlvvv_mll4.deriv.DAOD_HIGG8D1.e4054_s3126_r9364_r9315_p4133
mc16_13TeV.361604.PowhegPy8EG_CT10nloME_AZNLOCTEQ6L1_ZZvvll_mll4.deriv.DAOD_HIGG8D1.e4475_s3126_r9364_r9315_p4133
mc16_13TeV.361600.PowhegPy8EG_CT10nloME_AZNLOCTEQ6L1_WWlvvv.deriv.DAOD_HIGG8D1.e4616_s3126_r9364_r9315_p4133
mc16_13TeV.361605.PowhegPy8EG_CT10nloME_AZNLOCTEQ6L1_ZZvvvv_mll4.deriv.DAOD_HIGG8D1.e4054_s3126_s3136_r9364_r9315_p4133
mc16_13TeV.361601.PowhegPy8EG_CT10nloME_AZNLOCTEQ6L1_WZlVll_mll4.deriv.DAOD_HIGG8D1.e4475_s3126_r9364_r9315_p4133
mc16_13TeV.364286.Sherpa_222_NNPDF30NNLO_llvjj_ss_EW4.deriv.DAOD_HIGG8D1.e6055_e5984_s3126_r9364_r9315_p3983 mc16_13TeV.364285.Sherpa_222_NNPDF30NNLO_llvjj_EW6_OFPlus.deriv.DAOD_HIGG8D1.e7421_e5984_s3126_r9364_r9315_p4133
mc16_13TeV.364740.MGPy8EG_NNPDF30NLO_A14NNPDF23LO_lvlljj_EW6_SFPlus.deriv.DAOD_HIGG8D1.e7421_e5984_s3126_r9364_r9315_p4133
mc16_13TeV.364742.MGPy8EG_NNPDF30NLO_A14NNPDF23LO_lvlljj_EW6_SFPlus.deriv.DAOD_HIGG8D1.e7421_e5984_s3126_r9364_r9315_p4133
mc16_13TeV.364253.Sherpa_222_NNPDF30NNLO_llv.deriv.DAOD_HIGG8D1.e5916_s3126_r9364_r9315_p4133
mc16_13TeV.364250.Sherpa_222_NNPDF30NNLO_lll.deriv.DAOD_HIGG8D1.e5894_s3126_r9364_r9315_p4133
mc16_13TeV.364254.Sherpa_222_NNPDF30NNLO_llv.deriv.DAOD_HIGG8D1.e5916_s3126_r9364_r9315_p4133
mc16_13TeV.364255.Sherpa_222_NNPDF30NNLO_lvvv.deriv.DAOD_HIGG8D1.e5916_s3126_r9364_r9315_p4133
mc16_13TeV.410155.aMcAtNloPythia8EvtGen_MEN30NLO_A14N23LO_ttW.deriv.DAOD_HIGG8D1.e5070_s3126_r9364_r9315_p4133
mc16_13TeV.410156.aMcAtNloPythia8EvtGen_MEN30NLO_A14N23LO_ttZnunu.deriv.DAOD_HIGG8D1.e5070_s3126_r9364_r9315_p4133
mc16_13TeV.410157.aMcAtNloPythia8EvtGen_MEN30NLO_A14N23LO_ttZqq.deriv.DAOD_HIGG8D1.e5070_s3126_r9364_r9315_p4133
mc16_13TeV.410218.aMcAtNloPythia8EvtGen_MEN30NLO_A14N23LO_ttee.deriv.DAOD_HIGG8D1.e5070_s3126_r9364_r9315_p4133
mc16_13TeV.410219.aMcAtNloPythia8EvtGen_MEN30NLO_A14N23LO_ttmumu.deriv.DAOD_HIGG8D1.e5070_s3126_r9364_r9315_p4133
mc16_13TeV.410220.aMcAtNloPythia8EvtGen_MEN30NLO_A14N23LO_ttautau.deriv.DAOD_HIGG8D1.e5070_s3126_r9364_r9315_p4133
mc16_13TeV.412063.aMcAtNloPythia8EvtGen_tllq_NNPDF30_nf4_A14.deriv.DAOD_TOPQ1.e7054_e5984_s3126_r9364_r9315_p4174
mc16_13TeV.410276.aMcAtNloPythia8EvtGen_MEN30NLO_A14N23LO_ttee_mll_1_5.deriv.DAOD_HIGG8D1.e6087_e5984_s3126_r9364_r9315_p4133
mc16_13TeV.410277.aMcAtNloPythia8EvtGen_MEN30NLO_A14N23LO_ttmumu_mll_1_5.deriv.DAOD_HIGG8D1.e6087_e5984_s3126_r9364_r9315_p4133
mc16_13TeV.410278.aMcAtNloPythia8EvtGen_MEN30NLO_A14N23LO_ttautau_mll_1_5.deriv.DAOD_HIGG8D1.e6087_e5984_s3126_r9364_r9315_p4133
mc16_13TeV.410397.MadGraphPythia8EvtGen_ttbar_wbee_MEN30LO_A14N23LO.deriv.DAOD_HIGG8D1.e6086_e5984_s3126_r9364_r9315_p4133
```

mc16_13TeV.410398.MadGraphPythia8EvtGen_ttbar_wbmumu_MEN30LO_A14N23LO.deriv.DAOD_HIGG8D1.e6086_e5984_s3126_r9364_r9315_p4133
 mc16_13TeV.410399.MadGraphPythia8EvtGen_ttbar_wbtautau_MEN30LO_A14N23LO.deriv.DAOD_HIGG8D1.e6086_e5984_s3126_r9364_r9315_p4133
 mc16_13TeV.410658.PhPy8EG_A14_tchan_BW50_lept_top.deriv.DAOD_HIGG8D1.e6671_e5984_s3126_r9364_r9315_p4133
 mc16_13TeV.410659.PhPy8EG_A14_tchan_BW50_lept_antitop.deriv.DAOD_HIGG8D1.e6671_e5984_s3126_r9364_r9315_p4133
 mc16_13TeV.410644.PowhegPythia8EvtGen_A14_singletop_schan_lept_top.deriv.DAOD_HIGG8D1.e6527_e5984_s3126_r9364_r9315_p4133
 mc16_13TeV.410645.PowhegPythia8EvtGen_A14_singletop_schan_lept_antitop.deriv.DAOD_HIGG8D1.e6527_e5984_s3126_r9364_r9315_p4133
 mc16_13TeV.304014.MadGraphPythia8EvtGen_A14NNPDF23_3top_SM.deriv.DAOD_HIGG8D1.e4324_s3126_r9364_r9315_p4133
 mc16_13TeV.410080.MadGraphPythia8EvtGen_A14NNPDF23_4topSM.deriv.DAOD_HIGG8D1.e4111_s3126_r9364_r9315_p4133
 mc16_13TeV.410081.MadGraphPythia8EvtGen_A14NNPDF23_ttbarWW.deriv.DAOD_HIGG8D1.e4111_s3126_r9364_r9315_p4133
 mc16_13TeV.364100.Sherpa_221_NNPDF30NNLO_Zmumu_MAXHTPTV0_70_CVetoBVeto.deriv.DAOD_HIGG8D1.e5271_s3126_r9364_r9315_p4133
 mc16_13TeV.364101.Sherpa_221_NNPDF30NNLO_Zmumu_MAXHTPTV0_70_CFilterBVeto.deriv.DAOD_HIGG8D1.e5271_s3126_r9364_r9315_p4133
 mc16_13TeV.364102.Sherpa_221_NNPDF30NNLO_Zmumu_MAXHTPTV0_70_BFilter.deriv.DAOD_HIGG8D1.e5271_s3126_r9364_r9315_p4133
 mc16_13TeV.364103.Sherpa_221_NNPDF30NNLO_Zmumu_MAXHTPTV70_140_CVetoBVeto.deriv.DAOD_HIGG8D1.e5271_s3126_r9364_r9315_p4133
 mc16_13TeV.364104.Sherpa_221_NNPDF30NNLO_Zmumu_MAXHTPTV70_140_CFilterBVeto.deriv.DAOD_HIGG8D1.e5271_s3126_r9364_r9315_p4133
 mc16_13TeV.364106.Sherpa_221_NNPDF30NNLO_Zmumu_MAXHTPTV140_280_CVetoBVeto.deriv.DAOD_HIGG8D1.e5271_s3126_r9364_r9315_p4133
 mc16_13TeV.364107.Sherpa_221_NNPDF30NNLO_Zmumu_MAXHTPTV140_280_CFilterBVeto.deriv.DAOD_HIGG8D1.e5271_s3126_r9364_r9315_p4133
 mc16_13TeV.364108.Sherpa_221_NNPDF30NNLO_Zmumu_MAXHTPTV140_280_BFilter.deriv.DAOD_HIGG8D1.e5271_s3126_r9364_r9315_p4133
 mc16_13TeV.364109.Sherpa_221_NNPDF30NNLO_Zmumu_MAXHTPTV280_500_CVetoBVeto.deriv.DAOD_HIGG8D1.e5271_s3126_r9364_r9315_p4133
 mc16_13TeV.364110.Sherpa_221_NNPDF30NNLO_Zmumu_MAXHTPTV280_500_CFilterBVeto.deriv.DAOD_HIGG8D1.e5271_s3126_r9364_r9315_p4133
 mc16_13TeV.364111.Sherpa_221_NNPDF30NNLO_Zmumu_MAXHTPTV280_500_BFilter.deriv.DAOD_HIGG8D1.e5271_e5984_s3126_r9364_r9315_p4133
 mc16_13TeV.364111.Sherpa_221_NNPDF30NNLO_Zmumu_MAXHTPTV280_500_BFilter.deriv.DAOD_HIGG8D1.e5271_s3126_r9364_r9315_p4133
 mc16_13TeV.364112.Sherpa_221_NNPDF30NNLO_Zmumu_MAXHTPTV500_1000.deriv.DAOD_HIGG8D1.e5271_s3126_r9364_r9315_p4133
 mc16_13TeV.364113.Sherpa_221_NNPDF30NNLO_Zmumu_MAXHTPTV1000_E_CMS.deriv.DAOD_HIGG8D1.e5271_s3126_r9364_r9315_p4133
 mc16_13TeV.364114.Sherpa_221_NNPDF30NNLO_Zee_MAXHTPTV0_70_CVetoBVeto.deriv.DAOD_HIGG8D1.e5299_s3126_r9364_r9315_p4133
 mc16_13TeV.364115.Sherpa_221_NNPDF30NNLO_Zee_MAXHTPTV0_70_CFilterBVeto.deriv.DAOD_HIGG8D1.e5299_s3126_r9364_r9315_p4133
 mc16_13TeV.364116.Sherpa_221_NNPDF30NNLO_Zee_MAXHTPTV0_70_BFilter.deriv.DAOD_HIGG8D1.e5299_s3126_r9364_r9315_p4133
 mc16_13TeV.364117.Sherpa_221_NNPDF30NNLO_Zee_MAXHTPTV70_140_CVetoBVeto.deriv.DAOD_HIGG8D1.e5299_s3126_r9364_r9315_p4133
 mc16_13TeV.364118.Sherpa_221_NNPDF30NNLO_Zee_MAXHTPTV70_140_CFilterBVeto.deriv.DAOD_HIGG8D1.e5299_s3126_r9364_r9315_p4133
 mc16_13TeV.364119.Sherpa_221_NNPDF30NNLO_Zee_MAXHTPTV70_140_BFilter.deriv.DAOD_HIGG8D1.e5299_s3126_r9364_r9315_p4133
 mc16_13TeV.364120.Sherpa_221_NNPDF30NNLO_Zee_MAXHTPTV140_280_CVetoBVeto.deriv.DAOD_HIGG8D1.e5299_s3126_r9364_r9315_p4133
 mc16_13TeV.364121.Sherpa_221_NNPDF30NNLO_Zee_MAXHTPTV140_280_CFilterBVeto.deriv.DAOD_HIGG8D1.e5299_s3126_r9364_r9315_p4133

mc16_13TeV.364122.Sherpa_221_NNPDF30NNLO_Zee_MAXHTPTV140_280_BFilter.deriv.DAOD_HIGG8D1.e5299_s3126_r9364_r9315_p4133
 mc16_13TeV.364123.Sherpa_221_NNPDF30NNLO_Zee_MAXHTPTV280_500_CVetoBVeto.deriv.DAOD_HIGG8D1.e5299_s3126_r9364_r9315_p4133
 mc16_13TeV.364124.Sherpa_221_NNPDF30NNLO_Zee_MAXHTPTV280_500_CFilterBVeto.deriv.DAOD_HIGG8D1.e5299_s3126_r9364_r9315_p4133
 mc16_13TeV.364125.Sherpa_221_NNPDF30NNLO_Zee_MAXHTPTV280_500_BFilter.deriv.DAOD_HIGG8D1.e5299_s3126_r9364_r9315_p4133
 mc16_13TeV.364125.Sherpa_221_NNPDF30NNLO_Zee_MAXHTPTV280_500_BFilter.deriv.DAOD_HIGG8D1.e5299_e5984_s3126_r9364_r9315_p4133
 mc16_13TeV.364126.Sherpa_221_NNPDF30NNLO_Zee_MAXHTPTV500_1000.deriv.DAOD_HIGG8D1.e5299_s3126_r9364_r9315_p4133
 mc16_13TeV.364127.Sherpa_221_NNPDF30NNLO_Zee_MAXHTPTV1000_E_CMS.deriv.DAOD_HIGG8D1.e5299_s3126_r9364_r9315_p4133
 mc16_13TeV.364128.Sherpa_221_NNPDF30NNLO_Ztautau_MAXHTPTV0_70_CVetoBVeto.deriv.DAOD_HIGG8D1.e5307_s3126_r9364_r9315_p4133
 mc16_13TeV.364129.Sherpa_221_NNPDF30NNLO_Ztautau_MAXHTPTV0_70_CFilterBVeto.deriv.DAOD_HIGG8D1.e5307_s3126_r9364_r9315_p4133
 mc16_13TeV.364130.Sherpa_221_NNPDF30NNLO_Ztautau_MAXHTPTV0_70_BFilter.deriv.DAOD_HIGG8D1.e5307_s3126_r9364_r9315_p4133
 mc16_13TeV.364131.Sherpa_221_NNPDF30NNLO_Ztautau_MAXHTPTV70_140_CVetoBVeto.deriv.DAOD_HIGG8D1.e5307_s3126_r9364_r9315_p4133
 mc16_13TeV.364132.Sherpa_221_NNPDF30NNLO_Ztautau_MAXHTPTV70_140_CFilterBVeto.deriv.DAOD_HIGG8D1.e5307_s3126_r9364_r9315_p4133
 mc16_13TeV.364133.Sherpa_221_NNPDF30NNLO_Ztautau_MAXHTPTV70_140_BFilter.deriv.DAOD_HIGG8D1.e5307_s3126_r9364_r9315_p4133
 mc16_13TeV.364134.Sherpa_221_NNPDF30NNLO_Ztautau_MAXHTPTV140_280_CVetoBVeto.deriv.DAOD_HIGG8D1.e5307_s3126_r9364_r9315_p4133
 mc16_13TeV.364135.Sherpa_221_NNPDF30NNLO_Ztautau_MAXHTPTV140_280_CFilterBVeto.deriv.DAOD_HIGG8D1.e5307_s3126_r9364_r9315_p4133
 mc16_13TeV.364136.Sherpa_221_NNPDF30NNLO_Ztautau_MAXHTPTV140_280_BFilter.deriv.DAOD_HIGG8D1.e5307_s3126_r9364_r9315_p4133
 mc16_13TeV.364137.Sherpa_221_NNPDF30NNLO_Ztautau_MAXHTPTV280_500_CVetoBVeto.deriv.DAOD_HIGG8D1.e5307_e5984_s3126_r9364_r9315_p4133
 mc16_13TeV.364137.Sherpa_221_NNPDF30NNLO_Ztautau_MAXHTPTV280_500_CVetoBVeto.deriv.DAOD_HIGG8D1.e5307_s3126_r9364_r9315_p4133
 mc16_13TeV.364138.Sherpa_221_NNPDF30NNLO_Ztautau_MAXHTPTV280_500_CFilterBVeto.deriv.DAOD_HIGG8D1.e5313_s3126_r9364_r9315_p4133
 mc16_13TeV.364139.Sherpa_221_NNPDF30NNLO_Ztautau_MAXHTPTV280_500_BFilter.deriv.DAOD_HIGG8D1.e5313_s3126_r9364_r9315_p4133
 mc16_13TeV.364140.Sherpa_221_NNPDF30NNLO_Ztautau_MAXHTPTV500_1000.deriv.DAOD_HIGG8D1.e5307_s3126_r9364_r9315_p4133
 mc16_13TeV.364141.Sherpa_221_NNPDF30NNLO_Ztautau_MAXHTPTV1000_E_CMS.deriv.DAOD_HIGG8D1.e5307_s3126_r9364_r9315_p4133
 mc16_13TeV.364198.Sherpa_221_NN30NNLO_Zmm_Mll10_40_MAXHTPTV0_70_BVeto.deriv.DAOD_HIGG8D1.e5421_s3126_r9364_r9315_p4133
 mc16_13TeV.364199.Sherpa_221_NN30NNLO_Zmm_Mll10_40_MAXHTPTV0_70_BFilter.deriv.DAOD_HIGG8D1.e5421_s3126_r9364_r9315_p4133
 mc16_13TeV.364200.Sherpa_221_NN30NNLO_Zmm_Mll10_40_MAXHTPTV70_280_BVeto.deriv.DAOD_HIGG8D1.e5421_s3126_r9364_r9315_p4133
 mc16_13TeV.364201.Sherpa_221_NN30NNLO_Zmm_Mll10_40_MAXHTPTV70_280_BFilter.deriv.DAOD_HIGG8D1.e5421_s3126_r9364_r9315_p4133
 mc16_13TeV.364202.Sherpa_221_NN30NNLO_Zmm_Mll10_40_MAXHTPTV280_E_CMS_BVeto.deriv.DAOD_HIGG8D1.e5421_s3126_r9364_r9315_p4133
 mc16_13TeV.364203.Sherpa_221_NN30NNLO_Zmm_Mll10_40_MAXHTPTV280_E_CMS_BFilter.deriv.DAOD_HIGG8D1.e5421_s3126_r9364_r9315_p4133
 mc16_13TeV.364204.Sherpa_221_NN30NNLO_Zee_Mll10_40_MAXHTPTV0_70_BVeto.deriv.DAOD_HIGG8D1.e5421_s3126_r9364_r9315_p4133
 mc16_13TeV.364205.Sherpa_221_NN30NNLO_Zee_Mll10_40_MAXHTPTV0_70_BFilter.deriv.DAOD_HIGG8D1.e5421_s3126_r9364_r9315_p4133
 mc16_13TeV.364206.Sherpa_221_NN30NNLO_Zee_Mll10_40_MAXHTPTV70_280_BVeto.deriv.DAOD_HIGG8D1.e5421_s3126_r9364_r9315_p4133

mc16_13TeV.364207.Sherpa_221_NN30NNLO_Zee_Mll10_40_MAXHTPTV70_280_BFilter.deriv.DAOD_HIGG8D1.e5421_s3126_r9364_r9315_p4133
 mc16_13TeV.364208.Sherpa_221_NN30NNLO_Zee_Mll10_40_MAXHTPTV280_E_CMS_BVeto.deriv.DAOD_HIGG8D1.e5421_s3126_r9364_r9315_p4133
 mc16_13TeV.364209.Sherpa_221_NN30NNLO_Zee_Mll10_40_MAXHTPTV280_E_CMS_BFilter.deriv.DAOD_HIGG8D1.e5421_s3126_r9364_r9315_p4133
 mc16_13TeV.364210.Sherpa_221_NN30NNLO_Ztt_Mll10_40_MAXHTPTV0_70_BVeto.deriv.DAOD_HIGG8D1.e5421_s3126_r9364_r9315_p4133
 mc16_13TeV.364211.Sherpa_221_NN30NNLO_Ztt_Mll10_40_MAXHTPTV0_70_BFilter.deriv.DAOD_HIGG8D1.e5421_s3126_r9364_r9315_p4133
 mc16_13TeV.364212.Sherpa_221_NN30NNLO_Ztt_Mll10_40_MAXHTPTV70_280_BVeto.deriv.DAOD_HIGG8D1.e5421_s3126_r9364_r9315_p4133
 mc16_13TeV.364213.Sherpa_221_NN30NNLO_Ztt_Mll10_40_MAXHTPTV70_280_BFilter.deriv.DAOD_HIGG8D1.e5421_s3126_r9364_r9315_p4133
 mc16_13TeV.364214.Sherpa_221_NN30NNLO_Ztt_Mll10_40_MAXHTPTV280_E_CMS_BVeto.deriv.DAOD_HIGG8D1.e5421_s3126_r9364_r9315_p4133
 mc16_13TeV.364215.Sherpa_221_NN30NNLO_Ztt_Mll10_40_MAXHTPTV280_E_CMS_BFilter.deriv.DAOD_HIGG8D1.e5421_s3126_r9364_r9315_p4133
 mc16_13TeV.364156.Sherpa_221_NNPDF30NNLO_Wmunu_MAXHTPTV0_70_CVetoBVeto.deriv.DAOD_HIGG8D1.e5340_s3126_r9364_r9315_p4133
 mc16_13TeV.364157.Sherpa_221_NNPDF30NNLO_Wmunu_MAXHTPTV0_70_CFilterBVeto.deriv.DAOD_HIGG8D1.e5340_s3126_r9364_r9315_p4133
 mc16_13TeV.364157.Sherpa_221_NNPDF30NNLO_Wmunu_MAXHTPTV0_70_CFilterBVeto.deriv.DAOD_HIGG8D1.e5340_e5984_s3126_r9364_r9315_p4133
 mc16_13TeV.364158.Sherpa_221_NNPDF30NNLO_Wmunu_MAXHTPTV0_70_BFilter.deriv.DAOD_HIGG8D1.e5340_s3126_r9364_r9315_p4133
 mc16_13TeV.364159.Sherpa_221_NNPDF30NNLO_Wmunu_MAXHTPTV70_140_CVetoBVeto.deriv.DAOD_HIGG8D1.e5340_s3126_r9364_r9315_p4133
 mc16_13TeV.364160.Sherpa_221_NNPDF30NNLO_Wmunu_MAXHTPTV70_140_CFilterBVeto.deriv.DAOD_HIGG8D1.e5340_s3126_r9364_r9315_p4133
 mc16_13TeV.364161.Sherpa_221_NNPDF30NNLO_Wmunu_MAXHTPTV70_140_BFilter.deriv.DAOD_HIGG8D1.e5340_s3126_r9364_r9315_p4133
 mc16_13TeV.364162.Sherpa_221_NNPDF30NNLO_Wmunu_MAXHTPTV140_280_CVetoBVeto.deriv.DAOD_HIGG8D1.e5340_s3126_r9364_r9315_p4133
 mc16_13TeV.364163.Sherpa_221_NNPDF30NNLO_Wmunu_MAXHTPTV140_280_CFilterBVeto.deriv.DAOD_HIGG8D1.e5340_s3126_r9364_r9315_p4133
 mc16_13TeV.364163.Sherpa_221_NNPDF30NNLO_Wmunu_MAXHTPTV140_280_CFilterBVeto.deriv.DAOD_HIGG8D1.e5340_e5984_s3126_s3136_r9364_r9315_p4133
 mc16_13TeV.364164.Sherpa_221_NNPDF30NNLO_Wmunu_MAXHTPTV140_280_BFilter.deriv.DAOD_HIGG8D1.e5340_s3126_r9364_r9315_p4133
 mc16_13TeV.364165.Sherpa_221_NNPDF30NNLO_Wmunu_MAXHTPTV280_500_CVetoBVeto.deriv.DAOD_HIGG8D1.e5340_s3126_r9364_r9315_p4133
 mc16_13TeV.364166.Sherpa_221_NNPDF30NNLO_Wmunu_MAXHTPTV280_500_CFilterBVeto.deriv.DAOD_HIGG8D1.e5340_s3126_r9364_r9315_p4133
 mc16_13TeV.364167.Sherpa_221_NNPDF30NNLO_Wmunu_MAXHTPTV280_500_BFilter.deriv.DAOD_HIGG8D1.e5340_e5984_s3126_r9364_r9315_p4133
 mc16_13TeV.364167.Sherpa_221_NNPDF30NNLO_Wmunu_MAXHTPTV280_500_BFilter.deriv.DAOD_HIGG8D1.e5340_s3126_r9364_r9315_p4133
 mc16_13TeV.364168.Sherpa_221_NNPDF30NNLO_Wmunu_MAXHTPTV500_1000.deriv.DAOD_HIGG8D1.e5340_s3126_r9364_r9315_p4133
 mc16_13TeV.364169.Sherpa_221_NNPDF30NNLO_Wmunu_MAXHTPTV1000_E_CMS.deriv.DAOD_HIGG8D1.e5340_s3126_r9364_r9315_p4133
 mc16_13TeV.364170.Sherpa_221_NNPDF30NNLO_Wenu_MAXHTPTV0_70_CVetoBVeto.deriv.DAOD_HIGG8D1.e5340_s3126_r9364_r9315_p4133
 mc16_13TeV.364171.Sherpa_221_NNPDF30NNLO_Wenu_MAXHTPTV0_70_CFilterBVeto.deriv.DAOD_HIGG8D1.e5340_e5984_s3126_r9364_r9315_p4133
 mc16_13TeV.364171.Sherpa_221_NNPDF30NNLO_Wenu_MAXHTPTV0_70_CFilterBVeto.deriv.DAOD_HIGG8D1.e5340_s3126_r9364_r9315_p4133
 mc16_13TeV.364172.Sherpa_221_NNPDF30NNLO_Wenu_MAXHTPTV0_70_BFilter.deriv.DAOD_HIGG8D1.e5340_s3126_r9364_r9315_p4133
 mc16_13TeV.364173.Sherpa_221_NNPDF30NNLO_Wenu_MAXHTPTV70_140_CVetoBVeto.deriv.DAOD_HIGG8D1.e5340_s3126_r9364_r9315_p4133

mc16_13TeV.364174.Sherpa_221_NNPDF30NNLO_Wenu_MAXHTPTV70_140_CFilterBVeto.deriv.DAOD_HIGG8D1.e5340_s3126_r9364_r9315_p4133
 mc16_13TeV.364175.Sherpa_221_NNPDF30NNLO_Wenu_MAXHTPTV70_140_BFilter.deriv.DAOD_HIGG8D1.e5340_e5984_s3126_s3136_r9364_r9315_p4133
 mc16_13TeV.364175.Sherpa_221_NNPDF30NNLO_Wenu_MAXHTPTV70_140_BFilter.deriv.DAOD_HIGG8D1.e5340_s3126_r9364_r9315_p4133
 mc16_13TeV.364176.Sherpa_221_NNPDF30NNLO_Wenu_MAXHTPTV140_280_CVetoBVeto.deriv.DAOD_HIGG8D1.e5340_s3126_r9364_r9315_p4133
 mc16_13TeV.364177.Sherpa_221_NNPDF30NNLO_Wenu_MAXHTPTV140_280_CFilterBVeto.deriv.DAOD_HIGG8D1.e5340_s3126_r9364_r9315_p4133
 mc16_13TeV.364177.Sherpa_221_NNPDF30NNLO_Wenu_MAXHTPTV140_280_CFilterBVeto.deriv.DAOD_HIGG8D1.e5340_e5984_s3126_s3136_r9364_r9315_p4133
 mc16_13TeV.364178.Sherpa_221_NNPDF30NNLO_Wenu_MAXHTPTV140_280_BFilter.deriv.DAOD_HIGG8D1.e5340_s3126_r9364_r9315_p4133
 mc16_13TeV.364179.Sherpa_221_NNPDF30NNLO_Wenu_MAXHTPTV280_500_CVetoBVeto.deriv.DAOD_HIGG8D1.e5340_s3126_r9364_r9315_p4133
 mc16_13TeV.364180.Sherpa_221_NNPDF30NNLO_Wenu_MAXHTPTV280_500_CFilterBVeto.deriv.DAOD_HIGG8D1.e5340_s3126_r9364_r9315_p4133
 mc16_13TeV.364181.Sherpa_221_NNPDF30NNLO_Wenu_MAXHTPTV280_500_BFilter.deriv.DAOD_HIGG8D1.e5340_e5984_s3126_r9364_r9315_p4133
 mc16_13TeV.364181.Sherpa_221_NNPDF30NNLO_Wenu_MAXHTPTV280_500_BFilter.deriv.DAOD_HIGG8D1.e5340_s3126_r9364_r9315_p4133
 mc16_13TeV.364182.Sherpa_221_NNPDF30NNLO_Wenu_MAXHTPTV500_1000.deriv.DAOD_HIGG8D1.e5340_s3126_r9364_r9315_p4133
 mc16_13TeV.364183.Sherpa_221_NNPDF30NNLO_Wenu_MAXHTPTV1000_E_CMS.deriv.DAOD_HIGG8D1.e5340_s3126_r9364_r9315_p4133
 mc16_13TeV.364184.Sherpa_221_NNPDF30NNLO_Wtaunu_MAXHTPTV0_70_CVetoBVeto.deriv.DAOD_HIGG8D1.e5340_s3126_r9364_r9315_p4133
 mc16_13TeV.364185.Sherpa_221_NNPDF30NNLO_Wtaunu_MAXHTPTV0_70_CFilterBVeto.deriv.DAOD_HIGG8D1.e5340_e5984_s3126_r9364_r9315_p4133
 mc16_13TeV.364185.Sherpa_221_NNPDF30NNLO_Wtaunu_MAXHTPTV0_70_CFilterBVeto.deriv.DAOD_HIGG8D1.e5340_s3126_r9364_r9315_p4133
 mc16_13TeV.364186.Sherpa_221_NNPDF30NNLO_Wtaunu_MAXHTPTV0_70_BFilter.deriv.DAOD_HIGG8D1.e5340_s3126_r9364_r9315_p4133
 mc16_13TeV.364187.Sherpa_221_NNPDF30NNLO_Wtaunu_MAXHTPTV70_140_CVetoBVeto.deriv.DAOD_HIGG8D1.e5340_s3126_r9364_r9315_p4133
 mc16_13TeV.364188.Sherpa_221_NNPDF30NNLO_Wtaunu_MAXHTPTV70_140_CFilterBVeto.deriv.DAOD_HIGG8D1.e5340_s3126_r9364_r9315_p4133
 mc16_13TeV.364189.Sherpa_221_NNPDF30NNLO_Wtaunu_MAXHTPTV70_140_BFilter.deriv.DAOD_HIGG8D1.e5340_s3126_r9364_r9315_p4133
 mc16_13TeV.364190.Sherpa_221_NNPDF30NNLO_Wtaunu_MAXHTPTV140_280_CVetoBVeto.deriv.DAOD_HIGG8D1.e5340_e5984_s3126_r9364_r9315_p4133
 mc16_13TeV.364190.Sherpa_221_NNPDF30NNLO_Wtaunu_MAXHTPTV140_280_CVetoBVeto.deriv.DAOD_HIGG8D1.e5340_s3126_r9364_r9315_p4133
 mc16_13TeV.364191.Sherpa_221_NNPDF30NNLO_Wtaunu_MAXHTPTV140_280_CFilterBVeto.deriv.DAOD_HIGG8D1.e5340_s3126_r9364_r9315_p4133
 mc16_13TeV.364191.Sherpa_221_NNPDF30NNLO_Wtaunu_MAXHTPTV140_280_CFilterBVeto.deriv.DAOD_HIGG8D1.e5340_e5984_s3126_s3136_r9364_r9315_p4133
 mc16_13TeV.364192.Sherpa_221_NNPDF30NNLO_Wtaunu_MAXHTPTV140_280_BFilter.deriv.DAOD_HIGG8D1.e5340_s3126_r9364_r9315_p4133
 mc16_13TeV.364193.Sherpa_221_NNPDF30NNLO_Wtaunu_MAXHTPTV280_500_CVetoBVeto.deriv.DAOD_HIGG8D1.e5340_s3126_r9364_r9315_p4133
 mc16_13TeV.364193.Sherpa_221_NNPDF30NNLO_Wtaunu_MAXHTPTV280_500_CVetoBVeto.deriv.DAOD_HIGG8D1.e5340_e5984_s3126_s3136_r9364_r9315_p4133
 mc16_13TeV.364194.Sherpa_221_NNPDF30NNLO_Wtaunu_MAXHTPTV280_500_CFilterBVeto.deriv.DAOD_HIGG8D1.e5340_e5984_s3126_s3136_r9364_r9315_p4133
 mc16_13TeV.364195.Sherpa_221_NNPDF30NNLO_Wtaunu_MAXHTPTV280_500_BFilter.deriv.DAOD_HIGG8D1.e5340_s3126_r9364_r9315_p4133
 mc16_13TeV.364196.Sherpa_221_NNPDF30NNLO_Wtaunu_MAXHTPTV500_1000.deriv.DAOD_HIGG8D1.e5340_s3126_r9364_r9315_p4133

mc16_13TeV.364197.Sherpa_221_NNPDF30NNLO_Wtaunu_MAXHTPTV1000_E_CMS.deriv.DAOD_HIGG8D1.e5340_s3126_r9364_r9315_p4133
 mc16_13TeV.364500.Sherpa_222_NNPDF30NNLO_eegamma_pty_7_15.deriv.DAOD_HIGG8D1.e5928_e5984_s3126_r9364_r9315_p4133
 mc16_13TeV.364501.Sherpa_222_NNPDF30NNLO_eegamma_pty_15_35.deriv.DAOD_HIGG8D1.e5928_e5984_s3126_r9364_r9315_p4133
 mc16_13TeV.364502.Sherpa_222_NNPDF30NNLO_eegamma_pty_35_70.deriv.DAOD_HIGG8D1.e5928_e5984_s3126_r9364_r9315_p4133
 mc16_13TeV.364503.Sherpa_222_NNPDF30NNLO_eegamma_pty_70_140.deriv.DAOD_HIGG8D1.e5928_e5984_s3126_r9364_r9315_p4133
 mc16_13TeV.364504.Sherpa_222_NNPDF30NNLO_eegamma_pty_140_E_CMS.deriv.DAOD_HIGG8D1.e5928_e5984_s3126_r9364_r9315_p4133
 mc16_13TeV.364505.Sherpa_222_NNPDF30NNLO_mumugamma_pty_7_15.deriv.DAOD_HIGG8D1.e5928_e5984_s3126_r9364_r9315_p4133
 mc16_13TeV.364506.Sherpa_222_NNPDF30NNLO_mumugamma_pty_15_35.deriv.DAOD_HIGG8D1.e5988_e5984_s3126_r9364_r9315_p4133
 mc16_13TeV.364507.Sherpa_222_NNPDF30NNLO_mumugamma_pty_35_70.deriv.DAOD_HIGG8D1.e5928_e5984_s3126_r9364_r9315_p4133
 mc16_13TeV.364508.Sherpa_222_NNPDF30NNLO_mumugamma_pty_70_140.deriv.DAOD_HIGG8D1.e5928_e5984_s3126_r9364_r9315_p4133
 mc16_13TeV.364509.Sherpa_222_NNPDF30NNLO_mumugamma_pty_140_E_CMS.deriv.DAOD_HIGG8D1.e5928_e5984_s3126_r9364_r9315_p4133
 mc16_13TeV.364510.Sherpa_222_NNPDF30NNLO_tautaugamma_pty_7_15.deriv.DAOD_HIGG8D1.e5928_s3126_r9364_r9315_p4133
 mc16_13TeV.364511.Sherpa_222_NNPDF30NNLO_tautaugamma_pty_15_35.deriv.DAOD_HIGG8D1.e5928_s3126_r9364_r9315_p4133
 mc16_13TeV.364512.Sherpa_222_NNPDF30NNLO_tautaugamma_pty_35_70.deriv.DAOD_HIGG8D1.e5928_s3126_r9364_r9315_p4133
 mc16_13TeV.364513.Sherpa_222_NNPDF30NNLO_tautaugamma_pty_70_140.deriv.DAOD_HIGG8D1.e5982_s3126_r9364_r9315_p4133
 mc16_13TeV.364514.Sherpa_222_NNPDF30NNLO_tautaugamma_pty_140_E_CMS.deriv.DAOD_HIGG8D1.e5928_s3126_r9364_r9315_p4133
 mc16_13TeV.364521.Sherpa_222_NNPDF30NNLO_enugamma_pty_7_15.deriv.DAOD_HIGG8D1.e5928_s3126_r9364_r9315_p4133
 mc16_13TeV.364522.Sherpa_222_NNPDF30NNLO_enugamma_pty_15_35.deriv.DAOD_HIGG8D1.e5928_s3126_r9364_r9315_p4133
 mc16_13TeV.364523.Sherpa_222_NNPDF30NNLO_enugamma_pty_35_70.deriv.DAOD_HIGG8D1.e5928_s3126_r9364_r9315_p4133
 mc16_13TeV.364524.Sherpa_222_NNPDF30NNLO_enugamma_pty_70_140.deriv.DAOD_HIGG8D1.e5928_s3126_r9364_r9315_p4133
 mc16_13TeV.364525.Sherpa_222_NNPDF30NNLO_enugamma_pty_140_E_CMS.deriv.DAOD_HIGG8D1.e5928_s3126_r9364_r9315_p4133
 mc16_13TeV.364526.Sherpa_222_NNPDF30NNLO_munugamma_pty_7_15.deriv.DAOD_HIGG8D1.e5928_s3126_r9364_r9315_p4133
 mc16_13TeV.364527.Sherpa_222_NNPDF30NNLO_munugamma_pty_15_35.deriv.DAOD_HIGG8D1.e5928_s3126_r9364_r9315_p4133
 mc16_13TeV.364528.Sherpa_222_NNPDF30NNLO_munugamma_pty_35_70.deriv.DAOD_HIGG8D1.e5928_s3126_r9364_r9315_p4133
 mc16_13TeV.364529.Sherpa_222_NNPDF30NNLO_munugamma_pty_70_140.deriv.DAOD_HIGG8D1.e5928_s3126_r9364_r9315_p4133
 mc16_13TeV.364530.Sherpa_222_NNPDF30NNLO_munugamma_pty_140_E_CMS.deriv.DAOD_HIGG8D1.e5928_s3126_r9364_r9315_p4133
 mc16_13TeV.364530.Sherpa_222_NNPDF30NNLO_munugamma_pty_140_E_CMS.deriv.DAOD_HIGG8D1.e5928_e5984_s3126_r9364_r9315_p4133
 mc16_13TeV.364531.Sherpa_222_NNPDF30NNLO_taunugamma_pty_7_15.deriv.DAOD_HIGG8D1.e5928_s3126_r9364_r9315_p4133
 mc16_13TeV.364532.Sherpa_222_NNPDF30NNLO_taunugamma_pty_15_35.deriv.DAOD_HIGG8D1.e5928_s3126_r9364_r9315_p4133
 mc16_13TeV.364533.Sherpa_222_NNPDF30NNLO_taunugamma_pty_35_70.deriv.DAOD_HIGG8D1.e5928_s3126_r9364_r9315_p4133

mc16_13TeV.364534.Sherpa_222_NNPDF30NNLO_taunugamma_pty_70_140.deriv.DAOD_HIGG8D1.e5928_s3126_r9364_r9315_p4133
 mc16_13TeV.364535.Sherpa_222_NNPDF30NNLO_taunugamma_pty_140_E_CMS.deriv.DAOD_HIGG8D1.e5928_s3126_r9364_r9315_p4133
 mc16_13TeV.364535.Sherpa_222_NNPDF30NNLO_taunugamma_pty_140_E_CMS.deriv.DAOD_HIGG8D1.e5928_e5984_s3126_r9364_r9315_p4133
 mc16_13TeV.410560.MadGraphPythia8EvtGen_A14_tZ_4fl_tchan_noAllHad.deriv.DAOD_HIGG8D1.e5803_s3126_r9364_r9315_p4133
 mc16_13TeV.410013.PowhegPythiaEvtGen_P2012_Wt_inclusive_top.deriv.DAOD_HIGG8D1.e3753_s3126_r9364_r9315_p4133
 mc16_13TeV.410014.PowhegPythiaEvtGen_P2012_Wt_inclusive_antitop.deriv.DAOD_HIGG8D1.e3753_s3126_r9364_r9315_p4133
 mc16_13TeV.410408.aMcAtNloPythia8EvtGen_tWZ_Ztoll_minDR1.deriv.DAOD_HIGG8D1.e6423_e5984_s3126_r9364_r9315_p4133
 mc16_13TeV.364242.Sherpa_222_NNPDF30NNLO_WWW_3l3v_EW6.deriv.DAOD_HIGG8D1.e5887_s3126_r9364_r9315_p4133
 mc16_13TeV.364243.Sherpa_222_NNPDF30NNLO_WWZ_4l2v_EW6.deriv.DAOD_HIGG8D1.e5887_s3126_r9364_r9315_p4133
 mc16_13TeV.364244.Sherpa_222_NNPDF30NNLO_WWZ_2l4v_EW6.deriv.DAOD_HIGG8D1.e5887_s3126_r9364_r9315_p4133
 mc16_13TeV.364245.Sherpa_222_NNPDF30NNLO_WZZ_5l1v_EW6.deriv.DAOD_HIGG8D1.e5887_s3126_r9364_r9315_p4133
 mc16_13TeV.364246.Sherpa_222_NNPDF30NNLO_WZZ_3l3v_EW6.deriv.DAOD_HIGG8D1.e5887_s3126_r9364_r9315_p4133
 mc16_13TeV.364247.Sherpa_222_NNPDF30NNLO_ZZZ_6l0v_EW6.deriv.DAOD_HIGG8D1.e5887_s3126_r9364_r9315_p4133
 mc16_13TeV.364248.Sherpa_222_NNPDF30NNLO_ZZZ_4l2v_EW6.deriv.DAOD_HIGG8D1.e5887_s3126_r9364_r9315_p4133
 mc16_13TeV.364249.Sherpa_222_NNPDF30NNLO_ZZZ_2l4v_EW6.deriv.DAOD_HIGG8D1.e5887_s3126_r9364_r9315_p4133
 mc16_13TeV.342284.Pythia8EvtGen_A14NNPDF23LO_WH125_inc.deriv.DAOD_HIGG8D1.e4246_s3126_r9364_r9315_p4133
 mc16_13TeV.342285.Pythia8EvtGen_A14NNPDF23LO_ZH125_inc.deriv.DAOD_HIGG8D1.e4246_s3126_r9364_r9315_p4133
 mc16_13TeV.341998.aMcAtNloHppEG_UEEE5_CTEQ6L1_CT10ME_tWH125_gamgam_yt_plus1.deriv.DAOD_HIGG8D1.e4394_e5984_s3126_r9364_r9315_p4133
 mc16_13TeV.410389.MadGraphPythia8EvtGen_A14NNPDF23_ttgamma_nonallhadronic.deriv.DAOD_HIGG8D1.e6155_e5984_s3126_r9364_r9315_p4133
 mc16_13TeV.410470.PhPy8EG_A14_ttbar_hdamp258p75_nonallhad.deriv.DAOD_HIGG8D1.e6337_e5984_s3126_r9364_r9315_p4133
 mc16_13TeV.410472.PhPy8EG_A14_ttbar_hdamp258p75_dil.deriv.DAOD_HIGG8D1.e6348_e5984_s3126_r9364_r9315_p4133
 mc16_13TeV.346343.PhPy8EG_A14NNPDF23_NNPDF30ME_ttH125_allhad.deriv.DAOD_HIGG8D1.e7148_e5984_s3126_r9364_r9315_p4133
 mc16_13TeV.346344.PhPy8EG_A14NNPDF23_NNPDF30ME_ttH125_semilep.deriv.DAOD_HIGG8D1.e7148_e5984_s3126_r9364_r9315_p4133
 mc16_13TeV.346345.PhPy8EG_A14NNPDF23_NNPDF30ME_ttH125_dilep.deriv.DAOD_HIGG8D1.e7148_e5984_s3126_r9364_r9315_p4133

mc16d:

mc16_13TeV.364253.Sherpa_222_NNPDF30NNLO_lllv.deriv.DAOD_HIGG8D1.e5916_e5984_s3126_r10201_r10210_p4133
 mc16_13TeV.364250.Sherpa_222_NNPDF30NNLO_llll.deriv.DAOD_HIGG8D1.e5894_e5984_s3126_r10201_r10210_p4133
 mc16_13TeV.364254.Sherpa_222_NNPDF30NNLO_llvv.deriv.DAOD_HIGG8D1.e5916_e5984_s3126_r10201_r10210_p4133
 mc16_13TeV.364255.Sherpa_222_NNPDF30NNLO_lvvv.deriv.DAOD_HIGG8D1.e5916_e5984_s3126_r10201_r10210_p4133
 mc16_13TeV.410155.aMcAtNloPythia8EvtGen_MEN30NLO_A14N23LO_ttW.deriv.DAOD_HIGG8D1.e5070_e5984_s3126_r10201_r10210_p4133

mc16_13TeV.410156.aMcAtNloPythia8EvtGen_MEN30NLO_A14N23LO_ttZnunu.deriv.DAOD_HIGG8D1.e5070_e5984_s3126_r10201_r10210_p4133
 mc16_13TeV.410157.aMcAtNloPythia8EvtGen_MEN30NLO_A14N23LO_ttZqq.deriv.DAOD_HIGG8D1.e5070_e5984_s3126_r10201_r10210_p4133
 mc16_13TeV.410218.aMcAtNloPythia8EvtGen_MEN30NLO_A14N23LO_ttee.deriv.DAOD_HIGG8D1.e5070_e5984_s3126_r10201_r10210_p4133
 mc16_13TeV.410219.aMcAtNloPythia8EvtGen_MEN30NLO_A14N23LO_ttmumu.deriv.DAOD_HIGG8D1.e5070_e5984_s3126_r10201_r10210_p4133
 mc16_13TeV.410220.aMcAtNloPythia8EvtGen_MEN30NLO_A14N23LO_ttautau.deriv.DAOD_HIGG8D1.e5070_e5984_s3126_r10201_r10210_p4133
 mc16_13TeV.410276.aMcAtNloPythia8EvtGen_MEN30NLO_A14N23LO_ttee_mll_1_5.deriv.DAOD_HIGG8D1.e6087_e5984_s3126_r10201_r10210_p4133
 mc16_13TeV.410277.aMcAtNloPythia8EvtGen_MEN30NLO_A14N23LO_ttmumu_mll_1_5.deriv.DAOD_HIGG8D1.e6087_e5984_s3126_r10201_r10210_p4133
 mc16_13TeV.410278.aMcAtNloPythia8EvtGen_MEN30NLO_A14N23LO_ttautau_mll_1_5.deriv.DAOD_HIGG8D1.e6087_e5984_s3126_r10201_r10210_p4133
 mc16_13TeV.410397.MadGraphPythia8EvtGen_ttbar_wbee_MEN30LO_A14N23LO.deriv.DAOD_HIGG8D1.e6086_e5984_s3126_r10201_r10210_p4133
 mc16_13TeV.410398.MadGraphPythia8EvtGen_ttbar_wbmumu_MEN30LO_A14N23LO.deriv.DAOD_HIGG8D1.e6086_e5984_s3126_r10201_r10210_p4133
 mc16_13TeV.410399.MadGraphPythia8EvtGen_ttbar_wbttau_MEN30LO_A14N23LO.deriv.DAOD_HIGG8D1.e6086_e5984_s3126_r10201_r10210_p4133
 mc16_13TeV.410658.PhPy8EG_A14_tchan_BW50_lept_top.deriv.DAOD_HIGG8D1.e6671_e5984_s3126_r10201_r10210_p4133
 mc16_13TeV.410659.PhPy8EG_A14_tchan_BW50_lept_antitop.deriv.DAOD_HIGG8D1.e6671_e5984_s3126_r10201_r10210_p4133
 mc16_13TeV.410644.PowhegPythia8EvtGen_A14_singletop_schan_lept_top.deriv.DAOD_HIGG8D1.e6527_e5984_s3126_r10201_r10210_p4133
 mc16_13TeV.410645.PowhegPythia8EvtGen_A14_singletop_schan_lept_antitop.deriv.DAOD_HIGG8D1.e6527_s3126_r10201_r10210_p4133
 mc16_13TeV.412063.aMcAtNloPythia8EvtGen_tllq_NNPDF30_nf4_A14.deriv.DAOD_TOPQ1.e7054_e5984_s3126_r10201_r10210_p4174
 mc16_13TeV.304014.MadGraphPythia8EvtGen_A14NNPDF23_3top_SM.deriv.DAOD_HIGG8D1.e4324_e5984_s3126_r10201_r10210_p4133
 mc16_13TeV.410080.MadGraphPythia8EvtGen_A14NNPDF23_4topSM.deriv.DAOD_HIGG8D1.e4111_e5984_s3126_r10201_r10210_p4133
 mc16_13TeV.410081.MadGraphPythia8EvtGen_A14NNPDF23_ttbarWW.deriv.DAOD_HIGG8D1.e4111_e5984_s3126_r10201_r10210_p4133
 mc16_13TeV.364100.Sherpa_221_NNPDF30NNLO_Zmumu_MAXHTPTV0_70_CVetoBVeto.deriv.DAOD_HIGG8D1.e5271_s3126_r10201_r10210_p4133
 mc16_13TeV.364101.Sherpa_221_NNPDF30NNLO_Zmumu_MAXHTPTV0_70_CFfilterBVeto.deriv.DAOD_HIGG8D1.e5271_s3126_r10201_r10210_p4133
 mc16_13TeV.364101.Sherpa_221_NNPDF30NNLO_Zmumu_MAXHTPTV0_70_CFfilterBVeto.deriv.DAOD_HIGG8D1.e5271_e5984_s3126_r10201_r10210_p4133
 mc16_13TeV.364102.Sherpa_221_NNPDF30NNLO_Zmumu_MAXHTPTV0_70_BFilter.deriv.DAOD_HIGG8D1.e5271_s3126_r10201_r10210_p4133
 mc16_13TeV.364103.Sherpa_221_NNPDF30NNLO_Zmumu_MAXHTPTV70_140_CVetoBVeto.deriv.DAOD_HIGG8D1.e5271_s3126_r10201_r10210_p4133
 mc16_13TeV.364104.Sherpa_221_NNPDF30NNLO_Zmumu_MAXHTPTV70_140_CFfilterBVeto.deriv.DAOD_HIGG8D1.e5271_s3126_r10201_r10210_p4133
 mc16_13TeV.364106.Sherpa_221_NNPDF30NNLO_Zmumu_MAXHTPTV140_280_CVetoBVeto.deriv.DAOD_HIGG8D1.e5271_s3126_r10201_r10210_p4133
 mc16_13TeV.364107.Sherpa_221_NNPDF30NNLO_Zmumu_MAXHTPTV140_280_CFfilterBVeto.deriv.DAOD_HIGG8D1.e5271_s3126_r10201_r10210_p4133
 mc16_13TeV.364108.Sherpa_221_NNPDF30NNLO_Zmumu_MAXHTPTV140_280_BFilter.deriv.DAOD_HIGG8D1.e5271_e5984_s3126_r10201_r10210_p4133
 mc16_13TeV.364109.Sherpa_221_NNPDF30NNLO_Zmumu_MAXHTPTV280_500_CVetoBVeto.deriv.DAOD_HIGG8D1.e5271_e5984_s3126_r10201_r10210_p4133
 mc16_13TeV.364109.Sherpa_221_NNPDF30NNLO_Zmumu_MAXHTPTV280_500_CVetoBVeto.deriv.DAOD_HIGG8D1.e5271_s3126_r10201_r10210_p4133

mc16_13TeV.364110.Sherpa_221_NNPDF30NNLO_Zmumu_MAXHTPTV280_500_CFilterBVeto.deriv.DAOD_HIGG8D1.e5271_s3126_r10201_r10210_p4133
 mc16_13TeV.364111.Sherpa_221_NNPDF30NNLO_Zmumu_MAXHTPTV280_500_BFilter.deriv.DAOD_HIGG8D1.e5271_e5984_s3126_r10201_r10210_p4133
 mc16_13TeV.364111.Sherpa_221_NNPDF30NNLO_Zmumu_MAXHTPTV280_500_BFilter.deriv.DAOD_HIGG8D1.e5271_s3126_r10201_r10210_p4133
 mc16_13TeV.364112.Sherpa_221_NNPDF30NNLO_Zmumu_MAXHTPTV500_1000.deriv.DAOD_HIGG8D1.e5271_e5984_s3126_r10201_r10210_p4133
 mc16_13TeV.364112.Sherpa_221_NNPDF30NNLO_Zmumu_MAXHTPTV500_1000.deriv.DAOD_HIGG8D1.e5271_s3126_r10201_r10210_p4133
 mc16_13TeV.364113.Sherpa_221_NNPDF30NNLO_Zmumu_MAXHTPTV1000_E_CMS.deriv.DAOD_HIGG8D1.e5271_s3126_r10201_r10210_p4133
 mc16_13TeV.364114.Sherpa_221_NNPDF30NNLO_Zee_MAXHTPTV0_70_CVetoBVeto.deriv.DAOD_HIGG8D1.e5299_s3126_r10201_r10210_p4133
 mc16_13TeV.364115.Sherpa_221_NNPDF30NNLO_Zee_MAXHTPTV0_70_CFilterBVeto.deriv.DAOD_HIGG8D1.e5299_e5984_s3126_r10201_r10210_p4133
 mc16_13TeV.364116.Sherpa_221_NNPDF30NNLO_Zee_MAXHTPTV0_70_BFilter.deriv.DAOD_HIGG8D1.e5299_e5984_s3126_r10201_r10210_p4133
 mc16_13TeV.364117.Sherpa_221_NNPDF30NNLO_Zee_MAXHTPTV70_140_CVetoBVeto.deriv.DAOD_HIGG8D1.e5299_e5984_s3126_r10201_r10210_p4133
 mc16_13TeV.364118.Sherpa_221_NNPDF30NNLO_Zee_MAXHTPTV70_140_CFilterBVeto.deriv.DAOD_HIGG8D1.e5299_e5984_s3126_r10201_r10210_p4133
 mc16_13TeV.364119.Sherpa_221_NNPDF30NNLO_Zee_MAXHTPTV70_140_BFilter.deriv.DAOD_HIGG8D1.e5299_e5984_s3126_r10201_r10210_p4133
 mc16_13TeV.364120.Sherpa_221_NNPDF30NNLO_Zee_MAXHTPTV140_280_CVetoBVeto.deriv.DAOD_HIGG8D1.e5299_e5984_s3126_r10201_r10210_p4133
 mc16_13TeV.364121.Sherpa_221_NNPDF30NNLO_Zee_MAXHTPTV140_280_CFilterBVeto.deriv.DAOD_HIGG8D1.e5299_e5984_s3126_r10201_r10210_p4133
 mc16_13TeV.364122.Sherpa_221_NNPDF30NNLO_Zee_MAXHTPTV140_280_BFilter.deriv.DAOD_HIGG8D1.e5299_e5984_s3126_r10201_r10210_p4133
 mc16_13TeV.364123.Sherpa_221_NNPDF30NNLO_Zee_MAXHTPTV280_500_CVetoBVeto.deriv.DAOD_HIGG8D1.e5299_e5984_s3126_r10201_r10210_p4133
 mc16_13TeV.364124.Sherpa_221_NNPDF30NNLO_Zee_MAXHTPTV280_500_CFilterBVeto.deriv.DAOD_HIGG8D1.e5299_e5984_s3126_r10201_r10210_p4133
 mc16_13TeV.364125.Sherpa_221_NNPDF30NNLO_Zee_MAXHTPTV280_500_BFilter.deriv.DAOD_HIGG8D1.e5299_e5984_s3126_r10201_r10210_p4133
 mc16_13TeV.364126.Sherpa_221_NNPDF30NNLO_Zee_MAXHTPTV500_1000.deriv.DAOD_HIGG8D1.e5299_e5984_s3126_r10201_r10210_p4133
 mc16_13TeV.364127.Sherpa_221_NNPDF30NNLO_Zee_MAXHTPTV1000_E_CMS.deriv.DAOD_HIGG8D1.e5299_e5984_s3126_r10201_r10210_p4133
 mc16_13TeV.364128.Sherpa_221_NNPDF30NNLO_Ztautau_MAXHTPTV0_70_CVetoBVeto.deriv.DAOD_HIGG8D1.e5307_e5984_s3126_r10201_r10210_p4133
 mc16_13TeV.364129.Sherpa_221_NNPDF30NNLO_Ztautau_MAXHTPTV0_70_CFilterBVeto.deriv.DAOD_HIGG8D1.e5307_e5984_s3126_r10201_r10210_p4133
 mc16_13TeV.364130.Sherpa_221_NNPDF30NNLO_Ztautau_MAXHTPTV0_70_BFilter.deriv.DAOD_HIGG8D1.e5307_e5984_s3126_r10201_r10210_p4133
 mc16_13TeV.364131.Sherpa_221_NNPDF30NNLO_Ztautau_MAXHTPTV70_140_CVetoBVeto.deriv.DAOD_HIGG8D1.e5307_e5984_s3126_r10201_r10210_p4133
 mc16_13TeV.364132.Sherpa_221_NNPDF30NNLO_Ztautau_MAXHTPTV70_140_CFilterBVeto.deriv.DAOD_HIGG8D1.e5307_e5984_s3126_r10201_r10210_p4133
 mc16_13TeV.364133.Sherpa_221_NNPDF30NNLO_Ztautau_MAXHTPTV70_140_BFilter.deriv.DAOD_HIGG8D1.e5307_e5984_s3126_r10201_r10210_p4133
 mc16_13TeV.364134.Sherpa_221_NNPDF30NNLO_Ztautau_MAXHTPTV140_280_CVetoBVeto.deriv.DAOD_HIGG8D1.e5307_e5984_s3126_r10201_r10210_p4133
 mc16_13TeV.364135.Sherpa_221_NNPDF30NNLO_Ztautau_MAXHTPTV140_280_CFilterBVeto.deriv.DAOD_HIGG8D1.e5307_e5984_s3126_r10201_r10210_p4133
 mc16_13TeV.364136.Sherpa_221_NNPDF30NNLO_Ztautau_MAXHTPTV140_280_BFilter.deriv.DAOD_HIGG8D1.e5307_e5984_s3126_r10201_r10210_p4133
 mc16_13TeV.364137.Sherpa_221_NNPDF30NNLO_Ztautau_MAXHTPTV280_500_CVetoBVeto.deriv.DAOD_HIGG8D1.e5307_e5984_s3126_r10201_r10210_p4133
 mc16_13TeV.364138.Sherpa_221_NNPDF30NNLO_Ztautau_MAXHTPTV280_500_CFilterBVeto.deriv.DAOD_HIGG8D1.e5313_e5984_s3126_r10201_r10210_p4133

mc16_13TeV.364139.Sherpa_221_NNPDF30NNLO_Ztautau_MAXHTPTV280_500_BFilter.deriv.DAOD_HIGG8D1.e5313_e5984_s3126_r10201_r10210_p4133
 mc16_13TeV.364140.Sherpa_221_NNPDF30NNLO_Ztautau_MAXHTPTV500_1000.deriv.DAOD_HIGG8D1.e5307_e5984_s3126_r10201_r10210_p4133
 mc16_13TeV.364141.Sherpa_221_NNPDF30NNLO_Ztautau_MAXHTPTV1000_E_CMS.deriv.DAOD_HIGG8D1.e5307_e5984_s3126_r10201_r10210_p4133
 mc16_13TeV.364198.Sherpa_221_NN30NNLO_Zmm_Mll10_40_MAXHTPTV0_70_BVeto.deriv.DAOD_HIGG8D1.e5421_e5984_s3126_r10201_r10210_p4133
 mc16_13TeV.364199.Sherpa_221_NN30NNLO_Zmm_Mll10_40_MAXHTPTV0_70_BFilter.deriv.DAOD_HIGG8D1.e5421_e5984_s3126_r10201_r10210_p4133
 mc16_13TeV.364200.Sherpa_221_NN30NNLO_Zmm_Mll10_40_MAXHTPTV70_280_BVeto.deriv.DAOD_HIGG8D1.e5421_e5984_s3126_r10201_r10210_p4133
 mc16_13TeV.364201.Sherpa_221_NN30NNLO_Zmm_Mll10_40_MAXHTPTV70_280_BFilter.deriv.DAOD_HIGG8D1.e5421_e5984_s3126_r10201_r10210_p4133
 mc16_13TeV.364202.Sherpa_221_NN30NNLO_Zmm_Mll10_40_MAXHTPTV280_E_CMS_BVeto.deriv.DAOD_HIGG8D1.e5421_e5984_s3126_r10201_r10210_p4133
 mc16_13TeV.364203.Sherpa_221_NN30NNLO_Zmm_Mll10_40_MAXHTPTV280_E_CMS_BFilter.deriv.DAOD_HIGG8D1.e5421_e5984_s3126_r10201_r10210_p4133
 mc16_13TeV.364204.Sherpa_221_NN30NNLO_Zee_Mll10_40_MAXHTPTV0_70_BVeto.deriv.DAOD_HIGG8D1.e5421_e5984_s3126_r10201_r10210_p4133
 mc16_13TeV.364205.Sherpa_221_NN30NNLO_Zee_Mll10_40_MAXHTPTV0_70_BFilter.deriv.DAOD_HIGG8D1.e5421_e5984_s3126_r10201_r10210_p4133
 mc16_13TeV.364206.Sherpa_221_NN30NNLO_Zee_Mll10_40_MAXHTPTV70_280_BVeto.deriv.DAOD_HIGG8D1.e5421_e5984_s3126_r10201_r10210_p4133
 mc16_13TeV.364207.Sherpa_221_NN30NNLO_Zee_Mll10_40_MAXHTPTV70_280_BFilter.deriv.DAOD_HIGG8D1.e5421_e5984_s3126_r10201_r10210_p4133
 mc16_13TeV.364208.Sherpa_221_NN30NNLO_Zee_Mll10_40_MAXHTPTV280_E_CMS_BVeto.deriv.DAOD_HIGG8D1.e5421_e5984_s3126_r10201_r10210_p4133
 mc16_13TeV.364209.Sherpa_221_NN30NNLO_Zee_Mll10_40_MAXHTPTV280_E_CMS_BFilter.deriv.DAOD_HIGG8D1.e5421_e5984_s3126_r10201_r10210_p4133
 mc16_13TeV.364210.Sherpa_221_NN30NNLO_Ztt_Mll10_40_MAXHTPTV0_70_BVeto.deriv.DAOD_HIGG8D1.e5421_e5984_s3126_r10201_r10210_p4133
 mc16_13TeV.364211.Sherpa_221_NN30NNLO_Ztt_Mll10_40_MAXHTPTV0_70_BFilter.deriv.DAOD_HIGG8D1.e5421_e5984_s3126_r10201_r10210_p4133
 mc16_13TeV.364212.Sherpa_221_NN30NNLO_Ztt_Mll10_40_MAXHTPTV70_280_BVeto.deriv.DAOD_HIGG8D1.e5421_e5984_s3126_r10201_r10210_p4133
 mc16_13TeV.364213.Sherpa_221_NN30NNLO_Ztt_Mll10_40_MAXHTPTV70_280_BFilter.deriv.DAOD_HIGG8D1.e5421_e5984_s3126_r10201_r10210_p4133
 mc16_13TeV.364214.Sherpa_221_NN30NNLO_Ztt_Mll10_40_MAXHTPTV280_E_CMS_BVeto.deriv.DAOD_HIGG8D1.e5421_e5984_s3126_r10201_r10210_p4133
 mc16_13TeV.364215.Sherpa_221_NN30NNLO_Ztt_Mll10_40_MAXHTPTV280_E_CMS_BFilter.deriv.DAOD_HIGG8D1.e5421_e5984_s3126_r10201_r10210_p4133
 mc16_13TeV.364156.Sherpa_221_NNPDF30NNLO_Wmunu_MAXHTPTV0_70_CVetoBVeto.deriv.DAOD_HIGG8D1.e5340_s3126_r10201_r10210_p4133
 mc16_13TeV.364156.Sherpa_221_NNPDF30NNLO_Wmunu_MAXHTPTV0_70_CVetoBVeto.deriv.DAOD_HIGG8D1.e5340_e5984_s3126_s3136_r10201_r10210_p4133
 mc16_13TeV.364157.Sherpa_221_NNPDF30NNLO_Wmunu_MAXHTPTV0_70_CFilterBVeto.deriv.DAOD_HIGG8D1.e5340_e5984_s3126_s3136_r10201_r10210_p4133
 mc16_13TeV.364157.Sherpa_221_NNPDF30NNLO_Wmunu_MAXHTPTV0_70_CFilterBVeto.deriv.DAOD_HIGG8D1.e5340_s3126_r10201_r10210_p4133
 mc16_13TeV.364158.Sherpa_221_NNPDF30NNLO_Wmunu_MAXHTPTV0_70_BFilter.deriv.DAOD_HIGG8D1.e5340_e5984_s3126_s3136_r10201_r10210_p4133
 mc16_13TeV.364158.Sherpa_221_NNPDF30NNLO_Wmunu_MAXHTPTV0_70_BFilter.deriv.DAOD_HIGG8D1.e5340_s3126_r10201_r10210_p4133
 mc16_13TeV.364159.Sherpa_221_NNPDF30NNLO_Wmunu_MAXHTPTV70_140_CVetoBVeto.deriv.DAOD_HIGG8D1.e5340_s3126_r10201_r10210_p4133
 mc16_13TeV.364159.Sherpa_221_NNPDF30NNLO_Wmunu_MAXHTPTV70_140_CVetoBVeto.deriv.DAOD_HIGG8D1.e5340_e5984_s3126_r10201_r10210_p4133
 mc16_13TeV.364159.Sherpa_221_NNPDF30NNLO_Wmunu_MAXHTPTV70_140_CVetoBVeto.deriv.DAOD_HIGG8D1.e5340_e5984_s3126_s3136_r10201_r10210_p4133

mc16_13TeV.364160.Sherpa_221_NNPDF30NNLO_Wmunu_MAXHTPTV70_140_CFilterBVeto.deriv.DAOD_HIGG8D1.e5340_e5984_s3126_r10201_r10210_p4133
 mc16_13TeV.364160.Sherpa_221_NNPDF30NNLO_Wmunu_MAXHTPTV70_140_CFilterBVeto.deriv.DAOD_HIGG8D1.e5340_s3126_r10201_r10210_p4133
 mc16_13TeV.364161.Sherpa_221_NNPDF30NNLO_Wmunu_MAXHTPTV70_140_BFilter.deriv.DAOD_HIGG8D1.e5340_s3126_r10201_r10210_p4133
 mc16_13TeV.364161.Sherpa_221_NNPDF30NNLO_Wmunu_MAXHTPTV70_140_BFilter.deriv.DAOD_HIGG8D1.e5340_e5984_s3126_s3136_r10201_r10210_p4133
 mc16_13TeV.364162.Sherpa_221_NNPDF30NNLO_Wmunu_MAXHTPTV140_280_CVetoBVeto.deriv.DAOD_HIGG8D1.e5340_s3126_r10201_r10210_p4133
 mc16_13TeV.364162.Sherpa_221_NNPDF30NNLO_Wmunu_MAXHTPTV140_280_CVetoBVeto.deriv.DAOD_HIGG8D1.e5340_e5984_s3126_s3136_r10201_r10210_p4133
 mc16_13TeV.364163.Sherpa_221_NNPDF30NNLO_Wmunu_MAXHTPTV140_280_CFilterBVeto.deriv.DAOD_HIGG8D1.e5340_s3126_r10201_r10210_p4133
 mc16_13TeV.364163.Sherpa_221_NNPDF30NNLO_Wmunu_MAXHTPTV140_280_CFilterBVeto.deriv.DAOD_HIGG8D1.e5340_e5984_s3126_s3136_r10201_r10210_p4133
 mc16_13TeV.364163.Sherpa_221_NNPDF30NNLO_Wmunu_MAXHTPTV140_280_CFilterBVeto.deriv.DAOD_HIGG8D1.e5340_e5984_s3126_r10201_r10210_p4133
 mc16_13TeV.364164.Sherpa_221_NNPDF30NNLO_Wmunu_MAXHTPTV140_280_BFilter.deriv.DAOD_HIGG8D1.e5340_s3126_r10201_r10210_p4133
 mc16_13TeV.364164.Sherpa_221_NNPDF30NNLO_Wmunu_MAXHTPTV140_280_BFilter.deriv.DAOD_HIGG8D1.e5340_e5984_s3126_s3136_r10201_r10210_p4133
 mc16_13TeV.364165.Sherpa_221_NNPDF30NNLO_Wmunu_MAXHTPTV280_500_CVetoBVeto.deriv.DAOD_HIGG8D1.e5340_e5984_s3126_s3136_r10201_r10210_p4133
 mc16_13TeV.364166.Sherpa_221_NNPDF30NNLO_Wmunu_MAXHTPTV280_500_CFilterBVeto.deriv.DAOD_HIGG8D1.e5340_s3126_r10201_r10210_p4133
 mc16_13TeV.364166.Sherpa_221_NNPDF30NNLO_Wmunu_MAXHTPTV280_500_CFilterBVeto.deriv.DAOD_HIGG8D1.e5340_e5984_s3126_s3136_r10201_r10210_p4133
 mc16_13TeV.364167.Sherpa_221_NNPDF30NNLO_Wmunu_MAXHTPTV280_500_BFilter.deriv.DAOD_HIGG8D1.e5340_s3126_r10201_r10210_p4133
 mc16_13TeV.364167.Sherpa_221_NNPDF30NNLO_Wmunu_MAXHTPTV280_500_BFilter.deriv.DAOD_HIGG8D1.e5340_e5984_s3126_r10201_r10210_p4133
 mc16_13TeV.364168.Sherpa_221_NNPDF30NNLO_Wmunu_MAXHTPTV500_1000.deriv.DAOD_HIGG8D1.e5340_s3126_r10201_r10210_p4133
 mc16_13TeV.364168.Sherpa_221_NNPDF30NNLO_Wmunu_MAXHTPTV500_1000.deriv.DAOD_HIGG8D1.e5340_e5984_s3126_s3136_r10201_r10210_p4133
 mc16_13TeV.364169.Sherpa_221_NNPDF30NNLO_Wmunu_MAXHTPTV1000_E_CMS.deriv.DAOD_HIGG8D1.e5340_s3126_r10201_r10210_p4133
 mc16_13TeV.364169.Sherpa_221_NNPDF30NNLO_Wmunu_MAXHTPTV1000_E_CMS.deriv.DAOD_HIGG8D1.e5340_e5984_s3126_s3136_r10201_r10210_p4133
 mc16_13TeV.364170.Sherpa_221_NNPDF30NNLO_Wenu_MAXHTPTV0_70_CVetoBVeto.deriv.DAOD_HIGG8D1.e5340_e5984_s3126_s3136_r10201_r10210_p4133
 mc16_13TeV.364170.Sherpa_221_NNPDF30NNLO_Wenu_MAXHTPTV0_70_CVetoBVeto.deriv.DAOD_HIGG8D1.e5340_s3126_r10201_r10210_p4133
 mc16_13TeV.364171.Sherpa_221_NNPDF30NNLO_Wenu_MAXHTPTV0_70_CFilterBVeto.deriv.DAOD_HIGG8D1.e5340_e5984_s3126_r10201_r10210_p4133
 mc16_13TeV.364171.Sherpa_221_NNPDF30NNLO_Wenu_MAXHTPTV0_70_CFilterBVeto.deriv.DAOD_HIGG8D1.e5340_s3126_r10201_r10210_p4133
 mc16_13TeV.364171.Sherpa_221_NNPDF30NNLO_Wenu_MAXHTPTV0_70_CFilterBVeto.deriv.DAOD_HIGG8D1.e5340_e5984_s3126_s3136_r10201_r10210_p4133
 mc16_13TeV.364172.Sherpa_221_NNPDF30NNLO_Wenu_MAXHTPTV0_70_BFilter.deriv.DAOD_HIGG8D1.e5340_e5984_s3126_s3136_r10201_r10210_p4133
 mc16_13TeV.364172.Sherpa_221_NNPDF30NNLO_Wenu_MAXHTPTV0_70_BFilter.deriv.DAOD_HIGG8D1.e5340_e5984_s3126_r10201_r10210_p4133
 mc16_13TeV.364173.Sherpa_221_NNPDF30NNLO_Wenu_MAXHTPTV70_140_CVetoBVeto.deriv.DAOD_HIGG8D1.e5340_s3126_r10201_r10210_p4133
 mc16_13TeV.364173.Sherpa_221_NNPDF30NNLO_Wenu_MAXHTPTV70_140_CVetoBVeto.deriv.DAOD_HIGG8D1.e5340_e5984_s3126_r10201_r10210_p4133

mc16_13TeV.364174.Sherpa_221_NNPDF30NNLO_Wenu_MAXHTPTV70_140_CFilterBVeto.deriv.DAOD_HIGG8D1.e5340_s3126_r10201_r10210_p4133
 mc16_13TeV.364174.Sherpa_221_NNPDF30NNLO_Wenu_MAXHTPTV70_140_CFilterBVeto.deriv.DAOD_HIGG8D1.e5340_e5984_s3126_r10201_r10210_p4133
 mc16_13TeV.364175.Sherpa_221_NNPDF30NNLO_Wenu_MAXHTPTV70_140_BFilter.deriv.DAOD_HIGG8D1.e5340_e5984_s3126_r10201_r10210_p4133
 mc16_13TeV.364175.Sherpa_221_NNPDF30NNLO_Wenu_MAXHTPTV70_140_BFilter.deriv.DAOD_HIGG8D1.e5340_e5984_s3126_s3136_r10201_r10210_p4133
 mc16_13TeV.364175.Sherpa_221_NNPDF30NNLO_Wenu_MAXHTPTV70_140_BFilter.deriv.DAOD_HIGG8D1.e5340_s3126_r10201_r10210_p4133
 mc16_13TeV.364176.Sherpa_221_NNPDF30NNLO_Wenu_MAXHTPTV140_280_CVetoBVeto.deriv.DAOD_HIGG8D1.e5340_e5984_s3126_s3136_r10201_r10210_p4133
 mc16_13TeV.364176.Sherpa_221_NNPDF30NNLO_Wenu_MAXHTPTV140_280_CVetoBVeto.deriv.DAOD_HIGG8D1.e5340_s3126_r10201_r10210_p4133
 mc16_13TeV.364177.Sherpa_221_NNPDF30NNLO_Wenu_MAXHTPTV140_280_CFilterBVeto.deriv.DAOD_HIGG8D1.e5340_s3126_r10201_r10210_p4133
 mc16_13TeV.364177.Sherpa_221_NNPDF30NNLO_Wenu_MAXHTPTV140_280_CFilterBVeto.deriv.DAOD_HIGG8D1.e5340_e5984_s3126_s3136_r10201_r10210_p4133
 mc16_13TeV.364177.Sherpa_221_NNPDF30NNLO_Wenu_MAXHTPTV140_280_CFilterBVeto.deriv.DAOD_HIGG8D1.e5340_e5984_s3126_s3136_r10201_r10210_p4133
 mc16_13TeV.364177.Sherpa_221_NNPDF30NNLO_Wenu_MAXHTPTV140_280_CFilterBVeto.deriv.DAOD_HIGG8D1.e5340_e5984_s3126_r10201_r10210_p4133
 mc16_13TeV.364178.Sherpa_221_NNPDF30NNLO_Wenu_MAXHTPTV140_280_BFilter.deriv.DAOD_HIGG8D1.e5340_s3126_r10201_r10210_p4133
 mc16_13TeV.364179.Sherpa_221_NNPDF30NNLO_Wenu_MAXHTPTV280_500_CVetoBVeto.deriv.DAOD_HIGG8D1.e5340_s3126_r10201_r10210_p4133
 mc16_13TeV.364179.Sherpa_221_NNPDF30NNLO_Wenu_MAXHTPTV280_500_CVetoBVeto.deriv.DAOD_HIGG8D1.e5340_e5984_s3126_r10201_r10210_p4133
 mc16_13TeV.364180.Sherpa_221_NNPDF30NNLO_Wenu_MAXHTPTV280_500_CFilterBVeto.deriv.DAOD_HIGG8D1.e5340_e5984_s3126_s3136_r10201_r10210_p4133
 mc16_13TeV.364180.Sherpa_221_NNPDF30NNLO_Wenu_MAXHTPTV280_500_CFilterBVeto.deriv.DAOD_HIGG8D1.e5340_s3126_r10201_r10210_p4133
 mc16_13TeV.364181.Sherpa_221_NNPDF30NNLO_Wenu_MAXHTPTV280_500_BFilter.deriv.DAOD_HIGG8D1.e5340_e5984_s3126_r10201_r10210_p4133
 mc16_13TeV.364181.Sherpa_221_NNPDF30NNLO_Wenu_MAXHTPTV280_500_BFilter.deriv.DAOD_HIGG8D1.e5340_s3126_r10201_r10210_p4133
 mc16_13TeV.364182.Sherpa_221_NNPDF30NNLO_Wenu_MAXHTPTV500_1000.deriv.DAOD_HIGG8D1.e5340_s3126_r10201_r10210_p4133
 mc16_13TeV.364182.Sherpa_221_NNPDF30NNLO_Wenu_MAXHTPTV500_1000.deriv.DAOD_HIGG8D1.e5340_e5984_s3126_s3136_r10201_r10210_p4133
 mc16_13TeV.364183.Sherpa_221_NNPDF30NNLO_Wenu_MAXHTPTV1000_E_CMS.deriv.DAOD_HIGG8D1.e5340_e5984_s3126_r10201_r10210_p4133
 mc16_13TeV.364184.Sherpa_221_NNPDF30NNLO_Wtaunu_MAXHTPTV0_70_CVetoBVeto.deriv.DAOD_HIGG8D1.e5340_e5984_s3126_r10201_r10210_p4133
 mc16_13TeV.364184.Sherpa_221_NNPDF30NNLO_Wtaunu_MAXHTPTV0_70_CVetoBVeto.deriv.DAOD_HIGG8D1.e5340_s3126_r10201_r10210_p4133
 mc16_13TeV.364185.Sherpa_221_NNPDF30NNLO_Wtaunu_MAXHTPTV0_70_CFilterBVeto.deriv.DAOD_HIGG8D1.e5340_e5984_s3126_r10201_r10210_p4133
 mc16_13TeV.364186.Sherpa_221_NNPDF30NNLO_Wtaunu_MAXHTPTV0_70_BFilter.deriv.DAOD_HIGG8D1.e5340_e5984_s3126_r10201_r10210_p4133
 mc16_13TeV.364187.Sherpa_221_NNPDF30NNLO_Wtaunu_MAXHTPTV70_140_CVetoBVeto.deriv.DAOD_HIGG8D1.e5340_e5984_s3126_r10201_r10210_p4133
 mc16_13TeV.364188.Sherpa_221_NNPDF30NNLO_Wtaunu_MAXHTPTV70_140_CFilterBVeto.deriv.DAOD_HIGG8D1.e5340_e5984_s3126_r10201_r10210_p4133
 mc16_13TeV.364189.Sherpa_221_NNPDF30NNLO_Wtaunu_MAXHTPTV70_140_BFilter.deriv.DAOD_HIGG8D1.e5340_s3126_r10201_r10210_p4133
 mc16_13TeV.364190.Sherpa_221_NNPDF30NNLO_Wtaunu_MAXHTPTV140_280_CVetoBVeto.deriv.DAOD_HIGG8D1.e5340_s3126_r10201_r10210_p4133
 mc16_13TeV.364190.Sherpa_221_NNPDF30NNLO_Wtaunu_MAXHTPTV140_280_CVetoBVeto.deriv.DAOD_HIGG8D1.e5340_e5984_s3126_s3136_r10201_r10210_p4133

mc16_13TeV.364191.Sherpa_221_NNPDF30NNLO_Wtaunu_MAXHTPTV140_280_CFilterBVeto.deriv.DAOD_HIGG8D1.e5340_e5984_s3126_s3136_r10201_r10210_p4133
 mc16_13TeV.364191.Sherpa_221_NNPDF30NNLO_Wtaunu_MAXHTPTV140_280_CFilterBVeto.deriv.DAOD_HIGG8D1.e5340_s3126_r10201_r10210_p4133
 mc16_13TeV.364192.Sherpa_221_NNPDF30NNLO_Wtaunu_MAXHTPTV140_280_BFilter.deriv.DAOD_HIGG8D1.e5340_e5984_s3126_r10201_r10210_p4133
 mc16_13TeV.364193.Sherpa_221_NNPDF30NNLO_Wtaunu_MAXHTPTV280_500_CVetoBVeto.deriv.DAOD_HIGG8D1.e5340_e5984_s3126_r10201_r10210_p4133
 mc16_13TeV.364193.Sherpa_221_NNPDF30NNLO_Wtaunu_MAXHTPTV280_500_CVetoBVeto.deriv.DAOD_HIGG8D1.e5340_e5984_s3126_s3136_r10201_r10210_p4133
 mc16_13TeV.364194.Sherpa_221_NNPDF30NNLO_Wtaunu_MAXHTPTV280_500_CFilterBVeto.deriv.DAOD_HIGG8D1.e5340_e5984_s3126_r10201_r10210_p4133
 mc16_13TeV.364194.Sherpa_221_NNPDF30NNLO_Wtaunu_MAXHTPTV280_500_CFilterBVeto.deriv.DAOD_HIGG8D1.e5340_s3126_r10201_r10210_p4133
 mc16_13TeV.364194.Sherpa_221_NNPDF30NNLO_Wtaunu_MAXHTPTV280_500_BFilter.deriv.DAOD_HIGG8D1.e5340_e5984_s3126_r10201_r10210_p4133
 mc16_13TeV.364195.Sherpa_221_NNPDF30NNLO_Wtaunu_MAXHTPTV280_500_BFilter.deriv.DAOD_HIGG8D1.e5340_e5984_s3126_r10201_r10210_p4133
 mc16_13TeV.364195.Sherpa_221_NNPDF30NNLO_Wtaunu_MAXHTPTV280_500_BFilter.deriv.DAOD_HIGG8D1.e5340_s3126_r10201_r10210_p4133
 mc16_13TeV.364196.Sherpa_221_NNPDF30NNLO_Wtaunu_MAXHTPTV500_1000.deriv.DAOD_HIGG8D1.e5340_e5984_s3126_s3136_r10201_r10210_p4133
 mc16_13TeV.364196.Sherpa_221_NNPDF30NNLO_Wtaunu_MAXHTPTV500_1000.deriv.DAOD_HIGG8D1.e5340_s3126_r10201_r10210_p4133
 mc16_13TeV.364197.Sherpa_221_NNPDF30NNLO_Wtaunu_MAXHTPTV1000_E_CMS.deriv.DAOD_HIGG8D1.e5340_e5984_s3126_r10201_r10210_p4133
 mc16_13TeV.364500.Sherpa_222_NNPDF30NNLO_eegamma_pty_7_15.deriv.DAOD_HIGG8D1.e5928_e5984_s3126_r10201_r10210_p4133
 mc16_13TeV.364501.Sherpa_222_NNPDF30NNLO_eegamma_pty_15_35.deriv.DAOD_HIGG8D1.e5928_e5984_s3126_r10201_r10210_p4133
 mc16_13TeV.364502.Sherpa_222_NNPDF30NNLO_eegamma_pty_35_70.deriv.DAOD_HIGG8D1.e5928_e5984_s3126_r10201_r10210_p4133
 mc16_13TeV.364503.Sherpa_222_NNPDF30NNLO_eegamma_pty_70_140.deriv.DAOD_HIGG8D1.e5928_e5984_s3126_r10201_r10210_p4133
 mc16_13TeV.364504.Sherpa_222_NNPDF30NNLO_eegamma_pty_140_E_CMS.deriv.DAOD_HIGG8D1.e5928_e5984_s3126_r10201_r10210_p4133
 mc16_13TeV.364505.Sherpa_222_NNPDF30NNLO_mumugamma_pty_7_15.deriv.DAOD_HIGG8D1.e5928_e5984_s3126_r10201_r10210_p4133
 mc16_13TeV.364506.Sherpa_222_NNPDF30NNLO_mumugamma_pty_15_35.deriv.DAOD_HIGG8D1.e5928_e5984_s3126_r10201_r10210_p4133
 mc16_13TeV.364507.Sherpa_222_NNPDF30NNLO_mumugamma_pty_35_70.deriv.DAOD_HIGG8D1.e5928_e5984_s3126_r10201_r10210_p4133
 mc16_13TeV.364508.Sherpa_222_NNPDF30NNLO_mumugamma_pty_70_140.deriv.DAOD_HIGG8D1.e5928_e5984_s3126_r10201_r10210_p4133
 mc16_13TeV.364509.Sherpa_222_NNPDF30NNLO_mumugamma_pty_140_E_CMS.deriv.DAOD_HIGG8D1.e5928_e5984_s3126_r10201_r10210_p4133
 mc16_13TeV.364510.Sherpa_222_NNPDF30NNLO_tautaugamma_pty_7_15.deriv.DAOD_HIGG8D1.e5928_e5984_s3126_r10201_r10210_p4133
 mc16_13TeV.364511.Sherpa_222_NNPDF30NNLO_tautaugamma_pty_15_35.deriv.DAOD_HIGG8D1.e5928_e5984_s3126_r10201_r10210_p4133
 mc16_13TeV.364512.Sherpa_222_NNPDF30NNLO_tautaugamma_pty_35_70.deriv.DAOD_HIGG8D1.e5928_e5984_s3126_r10201_r10210_p4133
 mc16_13TeV.364513.Sherpa_222_NNPDF30NNLO_tautaugamma_pty_70_140.deriv.DAOD_HIGG8D1.e5982_e5984_s3126_r10201_r10210_p4133
 mc16_13TeV.364513.Sherpa_222_NNPDF30NNLO_tautaugamma_pty_70_140.deriv.DAOD_HIGG8D1.e5928_e5984_s3126_r10201_r10210_p4133
 mc16_13TeV.364514.Sherpa_222_NNPDF30NNLO_tautaugamma_pty_140_E_CMS.deriv.DAOD_HIGG8D1.e5928_e5984_s3126_r10201_r10210_p4133
 mc16_13TeV.364521.Sherpa_222_NNPDF30NNLO_enugamma_pty_7_15.deriv.DAOD_HIGG8D1.e5928_e5984_s3126_r10201_r10210_p4133
 mc16_13TeV.364522.Sherpa_222_NNPDF30NNLO_enugamma_pty_15_35.deriv.DAOD_HIGG8D1.e5928_e5984_s3126_r10201_r10210_p4133

mc16_13TeV.364523.Sherpa_222_NNPDF30NNLO_enugamma_pty_35_70.deriv.DAOD_HIGG8D1.e5928_e5984_s3126_r10201_r10210_p4133
 mc16_13TeV.364524.Sherpa_222_NNPDF30NNLO_enugamma_pty_70_140.deriv.DAOD_HIGG8D1.e5928_e5984_s3126_r10201_r10210_p4133
 mc16_13TeV.364525.Sherpa_222_NNPDF30NNLO_enugamma_pty_140_E_CMS.deriv.DAOD_HIGG8D1.e5928_e5984_s3126_r10201_r10210_p4133
 mc16_13TeV.364526.Sherpa_222_NNPDF30NNLO_munugamma_pty_7_15.deriv.DAOD_HIGG8D1.e5928_e5984_s3126_r10201_r10210_p4133
 mc16_13TeV.364527.Sherpa_222_NNPDF30NNLO_munugamma_pty_15_35.deriv.DAOD_HIGG8D1.e5928_e5984_s3126_r10201_r10210_p4133
 mc16_13TeV.364528.Sherpa_222_NNPDF30NNLO_munugamma_pty_35_70.deriv.DAOD_HIGG8D1.e5928_e5984_s3126_r10201_r10210_p4133
 mc16_13TeV.364529.Sherpa_222_NNPDF30NNLO_munugamma_pty_70_140.deriv.DAOD_HIGG8D1.e5928_e5984_s3126_r10201_r10210_p4133
 mc16_13TeV.364530.Sherpa_222_NNPDF30NNLO_munugamma_pty_140_E_CMS.deriv.DAOD_HIGG8D1.e5928_e5984_s3126_r10201_r10210_p4133
 mc16_13TeV.364531.Sherpa_222_NNPDF30NNLO_taunugamma_pty_7_15.deriv.DAOD_HIGG8D1.e5928_e5984_s3126_r10201_r10210_p4133
 mc16_13TeV.364532.Sherpa_222_NNPDF30NNLO_taunugamma_pty_15_35.deriv.DAOD_HIGG8D1.e5928_e5984_s3126_r10201_r10210_p4133
 mc16_13TeV.364533.Sherpa_222_NNPDF30NNLO_taunugamma_pty_35_70.deriv.DAOD_HIGG8D1.e5928_e5984_s3126_r10201_r10210_p4133
 mc16_13TeV.364534.Sherpa_222_NNPDF30NNLO_taunugamma_pty_70_140.deriv.DAOD_HIGG8D1.e5928_e5984_s3126_r10201_r10210_p4133
 mc16_13TeV.364535.Sherpa_222_NNPDF30NNLO_taunugamma_pty_140_E_CMS.deriv.DAOD_HIGG8D1.e5928_e5984_s3126_r10201_r10210_p4133
 mc16_13TeV.410560.MadGraphPythia8EvtGen_A14_tZ_4fl_tchan_noAllHad.deriv.DAOD_HIGG8D1.e5803_e5984_s3126_r10201_r10210_p4133
 mc16_13TeV.410013.PowhegPythiaEvtGen_P2012_Wt_inclusive_top.deriv.DAOD_HIGG8D1.e3753_s3126_r10201_r10210_p4133
 mc16_13TeV.410014.PowhegPythiaEvtGen_P2012_Wt_inclusive_antitop.deriv.DAOD_HIGG8D1.e3753_s3126_r10201_r10210_p4133
 mc16_13TeV.410408.aMcAtNloPythia8EvtGen_tWZ_Ztoll_minDR1.deriv.DAOD_HIGG8D1.e6423_e5984_s3126_r10201_r10210_p4133
 mc16_13TeV.364242.Sherpa_222_NNPDF30NNLO_WWW_3l3v_EW6.deriv.DAOD_HIGG8D1.e5887_e5984_s3126_r10201_r10210_p4133
 mc16_13TeV.364243.Sherpa_222_NNPDF30NNLO_WWZ_4l2v_EW6.deriv.DAOD_HIGG8D1.e5887_e5984_s3126_r10201_r10210_p4133
 mc16_13TeV.364244.Sherpa_222_NNPDF30NNLO_WWZ_2l4v_EW6.deriv.DAOD_HIGG8D1.e5887_e5984_s3126_r10201_r10210_p4133
 mc16_13TeV.364245.Sherpa_222_NNPDF30NNLO_WZZ_5l1v_EW6.deriv.DAOD_HIGG8D1.e5887_e5984_s3126_r10201_r10210_p4133
 mc16_13TeV.364246.Sherpa_222_NNPDF30NNLO_WZZ_3l3v_EW6.deriv.DAOD_HIGG8D1.e5887_e5984_s3126_r10201_r10210_p4133
 mc16_13TeV.364247.Sherpa_222_NNPDF30NNLO_ZZZ_6l0v_EW6.deriv.DAOD_HIGG8D1.e5887_e5984_s3126_r10201_r10210_p4133
 mc16_13TeV.364248.Sherpa_222_NNPDF30NNLO_ZZZ_4l2v_EW6.deriv.DAOD_HIGG8D1.e5887_e5984_s3126_r10201_r10210_p4133
 mc16_13TeV.364249.Sherpa_222_NNPDF30NNLO_ZZZ_2l4v_EW6.deriv.DAOD_HIGG8D1.e5887_e5984_s3126_r10201_r10210_p4133
 mc16_13TeV.342284.Pythia8EvtGen_A14NNPDF23LO_WH125_inc.deriv.DAOD_HIGG8D1.e4246_e5984_s3126_r10201_r10210_p4133
 mc16_13TeV.342285.Pythia8EvtGen_A14NNPDF23LO_ZH125_inc.deriv.DAOD_HIGG8D1.e4246_e5984_s3126_r10201_r10210_p4133
 mc16_13TeV.341998.aMcAtNloHppEG_UEEE5_CTEQ6L1_CT10ME_tWH125_gamgam_yt_plus1.deriv.DAOD_HIGG8D1.e4394_e5984_s3126_r10201_r10210_p4133
 mc16_13TeV.410470.PhPy8EG_A14_ttbar_hdamp258p75_nonallhad.deriv.DAOD_HIGG8D1.e6337_e5984_s3126_r10201_r10210_p4133
 mc16_13TeV.410472.PhPy8EG_A14_ttbar_hdamp258p75_dil.deriv.DAOD_HIGG8D1.e6348_e5984_s3126_r10201_r10210_p4133
 mc16_13TeV.346343.PhPy8EG_A14NNPDF23_NNPDF30ME_ttH125_allhad.deriv.DAOD_HIGG8D1.e7148_e5984_s3126_r10201_r10210_p4133

mc16_13TeV.346344.PhPy8EG_A14NNPDF23_NNPDF30ME_ttH125_semilep.deriv.DAOD_HIGG8D1.e7148_e5984_a875_r10201_r10210_p4133

mc16_13TeV.346345.PhPy8EG_A14NNPDF23_NNPDF30ME_ttH125_dilep.deriv.DAOD_HIGG8D1.e7148_e5984_a875_r10201_r10210_p4133

mc16e:

mc16_13TeV.361605.PowhegPy8EG_CT10nloME_AZNLOCTEQ6L1_ZZvvvv_mll4.deriv.DAOD_HIGG8D1.e4054_e5984_s3126_r10724_r10726_p4133

mc16_13TeV.361602.PowhegPy8EG_CT10nloME_AZNLOCTEQ6L1_WZlvvv_mll4.deriv.DAOD_HIGG8D1.e4054_e5984_s3126_r10724_r10726_p4133

mc16_13TeV.361601.PowhegPy8EG_CT10nloME_AZNLOCTEQ6L1_WZlvl_l_mll4.deriv.DAOD_HIGG8D1.e4475_e5984_s3126_r10724_r10726_p4133

mc16_13TeV.361600.PowhegPy8EG_CT10nloME_AZNLOCTEQ6L1_WWlvvv.deriv.DAOD_HIGG8D1.e4616_e5984_s3126_r10724_r10726_p4133

mc16_13TeV.361603.PowhegPy8EG_CT10nloME_AZNLOCTEQ6L1_ZZllll_mll4.deriv.DAOD_HIGG8D1.e4475_e5984_s3126_r10724_r10726_p4133

mc16_13TeV.361604.PowhegPy8EG_CT10nloME_AZNLOCTEQ6L1_ZZvvll_mll4.deriv.DAOD_HIGG8D1.e4475_e5984_s3126_r10724_r10726_p4133

mc16_13TeV.364288.Sherpa_222_NNPDF30NNLO_llll_lowMllPtComplement.deriv.DAOD_HIGG8D1.e6096_s3126_r10724_p3983 mc16_13TeV.364287.Sherpa_222_NNPDF

mc16_13TeV.364285.Sherpa_222_NNPDF30NNLO_llvjj_EW6.deriv.DAOD_HIGG8D1.e6055_e5984_s3126_r10724_r10726_p3983

mc16_13TeV.364284.Sherpa_222_NNPDF30NNLO_llvjj_EW6.deriv.DAOD_HIGG8D1.e6055_s3126_r10724_p3983

mc16_13TeV.364283.Sherpa_222_NNPDF30NNLO_lllljj_EW6.deriv.DAOD_HIGG8D1.e6055_s3126_r10724_p3983

mc16_13TeV.364739.MGPy8EG_NNPDF30NLO_A14NNPDF23LO_lvlljjEW6_OFMinus.deriv.DAOD_HIGG8D1.e7421_e5984_s3126_r10724_r10726_p4133

mc16_13TeV.364742.MGPy8EG_NNPDF30NLO_A14NNPDF23LO_lvlljjEW6_SFPlus.deriv.DAOD_HIGG8D1.e7421_e5984_s3126_r10724_r10726_p4133

mc16_13TeV.364740.MGPy8EG_NNPDF30NLO_A14NNPDF23LO_lvlljjEW6_OFPlus.deriv.DAOD_HIGG8D1.e7421_e5984_s3126_r10724_r10726_p4133

mc16_13TeV.364741.MGPy8EG_NNPDF30NLO_A14NNPDF23LO_lvlljjEW6_SFMinus.deriv.DAOD_HIGG8D1.e7421_e5984_s3126_r10724_r10726_p4133

mc16_13TeV.364253.Sherpa_222_NNPDF30NNLO_llv.deriv.DAOD_HIGG8D1.e5916_e5984_s3126_r10724_r10726_p4133

mc16_13TeV.364250.Sherpa_222_NNPDF30NNLO_llll.deriv.DAOD_HIGG8D1.e5894_e5984_s3126_r10724_r10726_p4133

mc16_13TeV.364254.Sherpa_222_NNPDF30NNLO_llv.deriv.DAOD_HIGG8D1.e5916_e5984_s3126_r10724_r10726_p4133

mc16_13TeV.364255.Sherpa_222_NNPDF30NNLO_lvvv.deriv.DAOD_HIGG8D1.e5916_e5984_s3126_r10724_r10726_p4133

mc16_13TeV.410155.aMcAtNloPythia8EvtGen_MEN30NLO_A14N23LO_ttW.deriv.DAOD_HIGG8D1.e5070_e5984_s3126_r10724_r10726_p4133

mc16_13TeV.410156.aMcAtNloPythia8EvtGen_MEN30NLO_A14N23LO_ttZnuuu.deriv.DAOD_HIGG8D1.e5070_e5984_s3126_r10724_r10726_p4133

mc16_13TeV.410157.aMcAtNloPythia8EvtGen_MEN30NLO_A14N23LO_ttZqq.deriv.DAOD_HIGG8D1.e5070_e5984_s3126_r10724_r10726_p4133

mc16_13TeV.410218.aMcAtNloPythia8EvtGen_MEN30NLO_A14N23LO_ttee.deriv.DAOD_HIGG8D1.e5070_e5984_s3126_r10724_r10726_p4133

mc16_13TeV.410219.aMcAtNloPythia8EvtGen_MEN30NLO_A14N23LO_ttmumu.deriv.DAOD_HIGG8D1.e5070_e5984_s3126_r10724_r10726_p4133

mc16_13TeV.410220.aMcAtNloPythia8EvtGen_MEN30NLO_A14N23LO_ttautau.deriv.DAOD_HIGG8D1.e5070_e5984_s3126_r10724_r10726_p4133

mc16_13TeV.410276.aMcAtNloPythia8EvtGen_MEN30NLO_A14N23LO_ttee_mll_1_5.deriv.DAOD_HIGG8D1.e6087_e5984_s3126_r10724_r10726_p4133

mc16_13TeV.410277.aMcAtNloPythia8EvtGen_MEN30NLO_A14N23LO_ttmumu_mll_1_5.deriv.DAOD_HIGG8D1.e6087_e5984_s3126_r10724_r10726_p4133

mc16_13TeV.410278.aMcAtNloPythia8EvtGen_MEN30NLO_A14N23LO_ttautau_mll_1_5.deriv.DAOD_HIGG8D1.e6087_e5984_s3126_r10724_r10726_p4133

mc16_13TeV.410397.MadGraphPythia8EvtGen_ttbar_wbee_MEN30LO_A14N23LO.deriv.DAOD_HIGG8D1.e6086_e5984_s3126_r10724_r10726_p4133
 mc16_13TeV.410398.MadGraphPythia8EvtGen_ttbar_wbmumu_MEN30LO_A14N23LO.deriv.DAOD_HIGG8D1.e6086_e5984_s3126_r10724_r10726_p4133
 mc16_13TeV.410399.MadGraphPythia8EvtGen_ttbar_wbttau_MEN30LO_A14N23LO.deriv.DAOD_HIGG8D1.e6086_e5984_s3126_r10724_r10726_p4133
 mc16_13TeV.410658.PhPy8EG_A14_tchan_BW50_lept_top.deriv.DAOD_HIGG8D1.e6671_e5984_s3126_s3136_r10724_r10726_p4133
 mc16_13TeV.410659.PhPy8EG_A14_tchan_BW50_lept_antitop.deriv.DAOD_HIGG8D1.e6671_e5984_s3126_s3136_r10724_r10726_p4133
 mc16_13TeV.410644.PowhegPythia8EvtGen_A14_singletop_schan_lept_top.deriv.DAOD_HIGG8D1.e6527_e5984_s3126_r10724_r10726_p4133
 mc16_13TeV.410645.PowhegPythia8EvtGen_A14_singletop_schan_lept_antitop.deriv.DAOD_HIGG8D1.e6527_e5984_s3126_r10724_r10726_p4133
 mc16_13TeV.412063.aMcAtNloPythia8EvtGen_llq_NNPDF30_nf4_A14.deriv.DAOD_TOPQ1.e7054_e5984_s3126_r10724_r10726_p4174
 mc16_13TeV.304014.MadGraphPythia8EvtGen_A14NNPDF23_3top_SM.deriv.DAOD_HIGG8D1.e4324_e5984_s3126_r10724_r10726_p4133
 mc16_13TeV.410080.MadGraphPythia8EvtGen_A14NNPDF23_4topSM.deriv.DAOD_HIGG8D1.e4111_e5984_s3126_r10724_r10726_p4133
 mc16_13TeV.410081.MadGraphPythia8EvtGen_A14NNPDF23_ttbarWW.deriv.DAOD_HIGG8D1.e4111_e5984_s3126_r10724_r10726_p4133
 mc16_13TeV.364100.Sherpa_221_NNPDF30NNLO_Zmumu_MAXHTPTV0_70_CVetoBVeto.deriv.DAOD_HIGG8D1.e5271_e5984_s3126_s3136_r10724_r10726_p4133
 mc16_13TeV.364100.Sherpa_221_NNPDF30NNLO_Zmumu_MAXHTPTV0_70_CVetoBVeto.deriv.DAOD_HIGG8D1.e5271_e5984_s3126_r10724_r10726_p4133
 mc16_13TeV.364101.Sherpa_221_NNPDF30NNLO_Zmumu_MAXHTPTV0_70_CFilterBVeto.deriv.DAOD_HIGG8D1.e5271_e5984_s3126_r10724_r10726_p4133
 mc16_13TeV.364102.Sherpa_221_NNPDF30NNLO_Zmumu_MAXHTPTV0_70_BFilter.deriv.DAOD_HIGG8D1.e5271_e5984_s3126_s3136_r10724_r10726_p4133
 mc16_13TeV.364102.Sherpa_221_NNPDF30NNLO_Zmumu_MAXHTPTV0_70_BFilter.deriv.DAOD_HIGG8D1.e5271_e5984_s3126_r10724_r10726_p4133
 mc16_13TeV.364103.Sherpa_221_NNPDF30NNLO_Zmumu_MAXHTPTV70_140_CVetoBVeto.deriv.DAOD_HIGG8D1.e5271_e5984_s3126_r10724_r10726_p4133
 mc16_13TeV.364103.Sherpa_221_NNPDF30NNLO_Zmumu_MAXHTPTV70_140_CVetoBVeto.deriv.DAOD_HIGG8D1.e5271_e5984_s3126_s3136_r10724_r10726_p4133
 mc16_13TeV.364104.Sherpa_221_NNPDF30NNLO_Zmumu_MAXHTPTV70_140_CFilterBVeto.deriv.DAOD_HIGG8D1.e5271_e5984_s3126_r10724_r10726_p4133
 mc16_13TeV.364104.Sherpa_221_NNPDF30NNLO_Zmumu_MAXHTPTV70_140_CFilterBVeto.deriv.DAOD_HIGG8D1.e5271_e5984_s3126_s3136_r10724_r10726_p4133
 mc16_13TeV.364106.Sherpa_221_NNPDF30NNLO_Zmumu_MAXHTPTV140_280_CVetoBVeto.deriv.DAOD_HIGG8D1.e5271_e5984_s3126_s3136_r10724_r10726_p4133
 mc16_13TeV.364107.Sherpa_221_NNPDF30NNLO_Zmumu_MAXHTPTV140_280_CFilterBVeto.deriv.DAOD_HIGG8D1.e5271_e5984_s3126_r10724_r10726_p4133
 mc16_13TeV.364107.Sherpa_221_NNPDF30NNLO_Zmumu_MAXHTPTV140_280_CFilterBVeto.deriv.DAOD_HIGG8D1.e5271_e5984_s3126_s3136_r10724_r10726_p4133
 mc16_13TeV.364108.Sherpa_221_NNPDF30NNLO_Zmumu_MAXHTPTV140_280_BFilter.deriv.DAOD_HIGG8D1.e5271_e5984_s3126_r10724_r10726_p4133
 mc16_13TeV.364109.Sherpa_221_NNPDF30NNLO_Zmumu_MAXHTPTV280_500_CVetoBVeto.deriv.DAOD_HIGG8D1.e5271_e5984_s3126_r10724_r10726_p4133
 mc16_13TeV.364110.Sherpa_221_NNPDF30NNLO_Zmumu_MAXHTPTV280_500_CFilterBVeto.deriv.DAOD_HIGG8D1.e5271_e5984_s3126_r10724_r10726_p4133
 mc16_13TeV.364110.Sherpa_221_NNPDF30NNLO_Zmumu_MAXHTPTV280_500_CFilterBVeto.deriv.DAOD_HIGG8D1.e5271_e5984_s3126_s3136_r10724_r10726_p4133
 mc16_13TeV.364111.Sherpa_221_NNPDF30NNLO_Zmumu_MAXHTPTV280_500_BFilter.deriv.DAOD_HIGG8D1.e5271_e5984_s3126_s3136_r10724_r10726_p4133
 mc16_13TeV.364111.Sherpa_221_NNPDF30NNLO_Zmumu_MAXHTPTV280_500_BFilter.deriv.DAOD_HIGG8D1.e5271_e5984_s3126_r10724_r10726_p4133
 mc16_13TeV.364112.Sherpa_221_NNPDF30NNLO_Zmumu_MAXHTPTV500_1000.deriv.DAOD_HIGG8D1.e5271_e5984_s3126_r10724_r10726_p4133

mc16_13TeV.364113.Sherpa_221_NNPDF30NNLO_Zmumu_MAXHTPTV1000_E_CMS.deriv.DAOD_HIGG8D1.e5271_e5984_s3126_r10724_r10726_p4133
 mc16_13TeV.364113.Sherpa_221_NNPDF30NNLO_Zmumu_MAXHTPTV1000_E_CMS.deriv.DAOD_HIGG8D1.e5271_e5984_s3126_s3136_r10724_r10726_p4133
 mc16_13TeV.364114.Sherpa_221_NNPDF30NNLO_Zee_MAXHTPTV0_70_CVetoBVeto.deriv.DAOD_HIGG8D1.e5299_e5984_s3126_s3136_r10724_r10726_p4133
 mc16_13TeV.364114.Sherpa_221_NNPDF30NNLO_Zee_MAXHTPTV0_70_CVetoBVeto.deriv.DAOD_HIGG8D1.e5299_e5984_s3126_r10724_r10726_p4133
 mc16_13TeV.364115.Sherpa_221_NNPDF30NNLO_Zee_MAXHTPTV0_70_CFilterBVeto.deriv.DAOD_HIGG8D1.e5299_e5984_s3126_s3136_r10724_r10726_p4133
 mc16_13TeV.364115.Sherpa_221_NNPDF30NNLO_Zee_MAXHTPTV0_70_CFilterBVeto.deriv.DAOD_HIGG8D1.e5299_e5984_s3126_r10724_r10726_p4133
 mc16_13TeV.364116.Sherpa_221_NNPDF30NNLO_Zee_MAXHTPTV0_70_BFilter.deriv.DAOD_HIGG8D1.e5299_e5984_s3126_r10724_r10726_p4133
 mc16_13TeV.364117.Sherpa_221_NNPDF30NNLO_Zee_MAXHTPTV70_140_CVetoBVeto.deriv.DAOD_HIGG8D1.e5299_e5984_s3126_s3136_r10724_r10726_p4133
 mc16_13TeV.364117.Sherpa_221_NNPDF30NNLO_Zee_MAXHTPTV70_140_CVetoBVeto.deriv.DAOD_HIGG8D1.e5299_e5984_s3126_r10724_r10726_p4133
 mc16_13TeV.364118.Sherpa_221_NNPDF30NNLO_Zee_MAXHTPTV70_140_CFilterBVeto.deriv.DAOD_HIGG8D1.e5299_e5984_s3126_s3136_r10724_r10726_p4133
 mc16_13TeV.364118.Sherpa_221_NNPDF30NNLO_Zee_MAXHTPTV70_140_CFilterBVeto.deriv.DAOD_HIGG8D1.e5299_e5984_s3126_r10724_r10726_p4133
 mc16_13TeV.364119.Sherpa_221_NNPDF30NNLO_Zee_MAXHTPTV70_140_BFilter.deriv.DAOD_HIGG8D1.e5299_e5984_s3126_r10724_r10726_p4133
 mc16_13TeV.364120.Sherpa_221_NNPDF30NNLO_Zee_MAXHTPTV140_280_CVetoBVeto.deriv.DAOD_HIGG8D1.e5299_e5984_s3126_r10724_r10726_p4133
 mc16_13TeV.364121.Sherpa_221_NNPDF30NNLO_Zee_MAXHTPTV140_280_CFilterBVeto.deriv.DAOD_HIGG8D1.e5299_e5984_s3126_r10724_r10726_p4133
 mc16_13TeV.364122.Sherpa_221_NNPDF30NNLO_Zee_MAXHTPTV140_280_BFilter.deriv.DAOD_HIGG8D1.e5299_e5984_s3126_s3136_r10724_r10726_p4133
 mc16_13TeV.364122.Sherpa_221_NNPDF30NNLO_Zee_MAXHTPTV140_280_BFilter.deriv.DAOD_HIGG8D1.e5299_e5984_s3126_r10724_r10726_p4133
 mc16_13TeV.364123.Sherpa_221_NNPDF30NNLO_Zee_MAXHTPTV280_500_CVetoBVeto.deriv.DAOD_HIGG8D1.e5299_e5984_s3126_r10724_r10726_p4133
 mc16_13TeV.364124.Sherpa_221_NNPDF30NNLO_Zee_MAXHTPTV280_500_CFilterBVeto.deriv.DAOD_HIGG8D1.e5299_e5984_s3126_r10724_r10726_p4133
 mc16_13TeV.364125.Sherpa_221_NNPDF30NNLO_Zee_MAXHTPTV280_500_BFilter.deriv.DAOD_HIGG8D1.e5299_e5984_s3126_s3136_r10724_r10726_p4133
 mc16_13TeV.364125.Sherpa_221_NNPDF30NNLO_Zee_MAXHTPTV280_500_BFilter.deriv.DAOD_HIGG8D1.e5299_e5984_s3126_r10724_r10726_p4133
 mc16_13TeV.364126.Sherpa_221_NNPDF30NNLO_Zee_MAXHTPTV500_1000.deriv.DAOD_HIGG8D1.e5299_e5984_s3126_r10724_r10726_p4133
 mc16_13TeV.364126.Sherpa_221_NNPDF30NNLO_Zee_MAXHTPTV500_1000.deriv.DAOD_HIGG8D1.e5299_e5984_s3126_s3136_r10724_r10726_p4133
 mc16_13TeV.364127.Sherpa_221_NNPDF30NNLO_Zee_MAXHTPTV1000_E_CMS.deriv.DAOD_HIGG8D1.e5299_e5984_s3126_s3136_r10724_r10726_p4133
 mc16_13TeV.364127.Sherpa_221_NNPDF30NNLO_Zee_MAXHTPTV1000_E_CMS.deriv.DAOD_HIGG8D1.e5299_e5984_s3126_r10724_r10726_p4133
 mc16_13TeV.364128.Sherpa_221_NNPDF30NNLO_Ztautau_MAXHTPTV0_70_CVetoBVeto.deriv.DAOD_HIGG8D1.e5307_e5984_s3126_s3136_r10724_r10726_p4133
 mc16_13TeV.364128.Sherpa_221_NNPDF30NNLO_Ztautau_MAXHTPTV0_70_CVetoBVeto.deriv.DAOD_HIGG8D1.e5307_e5984_s3126_r10724_r10726_p4133
 mc16_13TeV.364129.Sherpa_221_NNPDF30NNLO_Ztautau_MAXHTPTV0_70_CFilterBVeto.deriv.DAOD_HIGG8D1.e5307_e5984_s3126_r10724_r10726_p4133
 mc16_13TeV.364129.Sherpa_221_NNPDF30NNLO_Ztautau_MAXHTPTV0_70_CFilterBVeto.deriv.DAOD_HIGG8D1.e5307_e5984_s3126_s3136_r10724_r10726_p4133
 mc16_13TeV.364130.Sherpa_221_NNPDF30NNLO_Ztautau_MAXHTPTV0_70_BFilter.deriv.DAOD_HIGG8D1.e5307_e5984_s3126_s3136_r10724_r10726_p4133
 mc16_13TeV.364130.Sherpa_221_NNPDF30NNLO_Ztautau_MAXHTPTV0_70_BFilter.deriv.DAOD_HIGG8D1.e5307_e5984_s3126_r10724_r10726_p4133
 mc16_13TeV.364131.Sherpa_221_NNPDF30NNLO_Ztautau_MAXHTPTV70_140_CVetoBVeto.deriv.DAOD_HIGG8D1.e5307_e5984_s3126_r10724_r10726_p4133

mc16_13TeV.364132.Sherpa_221_NNPDF30NNLO_Ztautau_MAXHTPTV70_140_CFilterBVeto.deriv.DAOD_HIGG8D1.e5307_e5984_s3126_r10724_r10726_p4133
 mc16_13TeV.364132.Sherpa_221_NNPDF30NNLO_Ztautau_MAXHTPTV70_140_CFilterBVeto.deriv.DAOD_HIGG8D1.e5307_e5984_s3126_s3136_r10724_r10726_p4133
 mc16_13TeV.364133.Sherpa_221_NNPDF30NNLO_Ztautau_MAXHTPTV70_140_BFilter.deriv.DAOD_HIGG8D1.e5307_e5984_s3126_r10724_r10726_p4133
 mc16_13TeV.364134.Sherpa_221_NNPDF30NNLO_Ztautau_MAXHTPTV140_280_CVetoBVeto.deriv.DAOD_HIGG8D1.e5307_e5984_s3126_r10724_r10726_p4133
 mc16_13TeV.364135.Sherpa_221_NNPDF30NNLO_Ztautau_MAXHTPTV140_280_CFilterBVeto.deriv.DAOD_HIGG8D1.e5307_e5984_s3126_r10724_r10726_p4133
 mc16_13TeV.364135.Sherpa_221_NNPDF30NNLO_Ztautau_MAXHTPTV140_280_CFilterBVeto.deriv.DAOD_HIGG8D1.e5307_e5984_s3126_s3136_r10724_r10726_p4133
 mc16_13TeV.364136.Sherpa_221_NNPDF30NNLO_Ztautau_MAXHTPTV140_280_BFilter.deriv.DAOD_HIGG8D1.e5307_e5984_s3126_r10724_r10726_p4133
 mc16_13TeV.364137.Sherpa_221_NNPDF30NNLO_Ztautau_MAXHTPTV280_500_CVetoBVeto.deriv.DAOD_HIGG8D1.e5307_e5984_s3126_r10724_r10726_p4133
 mc16_13TeV.364138.Sherpa_221_NNPDF30NNLO_Ztautau_MAXHTPTV280_500_CFilterBVeto.deriv.DAOD_HIGG8D1.e5313_e5984_s3126_s3136_r10724_r10726_p4133
 mc16_13TeV.364138.Sherpa_221_NNPDF30NNLO_Ztautau_MAXHTPTV280_500_CFilterBVeto.deriv.DAOD_HIGG8D1.e5313_e5984_s3126_r10724_r10726_p4133
 mc16_13TeV.364139.Sherpa_221_NNPDF30NNLO_Ztautau_MAXHTPTV280_500_BFilter.deriv.DAOD_HIGG8D1.e5313_e5984_s3126_r10724_r10726_p4133
 mc16_13TeV.364139.Sherpa_221_NNPDF30NNLO_Ztautau_MAXHTPTV280_500_BFilter.deriv.DAOD_HIGG8D1.e5313_e5984_s3126_s3136_r10724_r10726_p4133
 mc16_13TeV.364140.Sherpa_221_NNPDF30NNLO_Ztautau_MAXHTPTV500_1000.deriv.DAOD_HIGG8D1.e5307_e5984_s3126_r10724_r10726_p4133
 mc16_13TeV.364140.Sherpa_221_NNPDF30NNLO_Ztautau_MAXHTPTV500_1000.deriv.DAOD_HIGG8D1.e5307_e5984_s3126_s3136_r10724_r10726_p4133
 mc16_13TeV.364141.Sherpa_221_NNPDF30NNLO_Ztautau_MAXHTPTV1000_E_CMS.deriv.DAOD_HIGG8D1.e5307_e5984_s3126_s3136_r10724_r10726_p4133
 mc16_13TeV.364141.Sherpa_221_NNPDF30NNLO_Ztautau_MAXHTPTV1000_E_CMS.deriv.DAOD_HIGG8D1.e5307_e5984_s3126_r10724_r10726_p4133
 mc16_13TeV.364198.Sherpa_221_NN30NNLO_Zmm_Mll10_40_MAXHTPTV0_70_BVeto.deriv.DAOD_HIGG8D1.e5421_e5984_s3126_r10724_r10726_p4133
 mc16_13TeV.364199.Sherpa_221_NN30NNLO_Zmm_Mll10_40_MAXHTPTV0_70_BFilter.deriv.DAOD_HIGG8D1.e5421_e5984_s3126_r10724_r10726_p4133
 mc16_13TeV.364200.Sherpa_221_NN30NNLO_Zmm_Mll10_40_MAXHTPTV70_280_BVeto.deriv.DAOD_HIGG8D1.e5421_e5984_s3126_r10724_r10726_p4133
 mc16_13TeV.364201.Sherpa_221_NN30NNLO_Zmm_Mll10_40_MAXHTPTV70_280_BFilter.deriv.DAOD_HIGG8D1.e5421_e5984_s3126_r10724_r10726_p4133
 mc16_13TeV.364202.Sherpa_221_NN30NNLO_Zmm_Mll10_40_MAXHTPTV280_E_CMS_BVeto.deriv.DAOD_HIGG8D1.e5421_e5984_s3126_r10724_r10726_p4133
 mc16_13TeV.364203.Sherpa_221_NN30NNLO_Zmm_Mll10_40_MAXHTPTV280_E_CMS_BFilter.deriv.DAOD_HIGG8D1.e5421_e5984_s3126_r10724_r10726_p4133
 mc16_13TeV.364204.Sherpa_221_NN30NNLO_Zee_Mll10_40_MAXHTPTV0_70_BVeto.deriv.DAOD_HIGG8D1.e5421_e5984_s3126_r10724_r10726_p4133
 mc16_13TeV.364205.Sherpa_221_NN30NNLO_Zee_Mll10_40_MAXHTPTV0_70_BFilter.deriv.DAOD_HIGG8D1.e5421_e5984_s3126_r10724_r10726_p4133
 mc16_13TeV.364206.Sherpa_221_NN30NNLO_Zee_Mll10_40_MAXHTPTV70_280_BVeto.deriv.DAOD_HIGG8D1.e5421_e5984_s3126_r10724_r10726_p4133
 mc16_13TeV.364207.Sherpa_221_NN30NNLO_Zee_Mll10_40_MAXHTPTV70_280_BFilter.deriv.DAOD_HIGG8D1.e5421_e5984_s3126_r10724_r10726_p4133
 mc16_13TeV.364208.Sherpa_221_NN30NNLO_Zee_Mll10_40_MAXHTPTV280_E_CMS_BVeto.deriv.DAOD_HIGG8D1.e5421_e5984_s3126_r10724_r10726_p4133
 mc16_13TeV.364209.Sherpa_221_NN30NNLO_Zee_Mll10_40_MAXHTPTV280_E_CMS_BFilter.deriv.DAOD_HIGG8D1.e5421_e5984_s3126_r10724_r10726_p4133
 mc16_13TeV.364210.Sherpa_221_NN30NNLO_Ztt_Mll10_40_MAXHTPTV0_70_BVeto.deriv.DAOD_HIGG8D1.e5421_e5984_s3126_r10724_r10726_p4133
 mc16_13TeV.364211.Sherpa_221_NN30NNLO_Ztt_Mll10_40_MAXHTPTV0_70_BFilter.deriv.DAOD_HIGG8D1.e5421_e5984_s3126_r10724_r10726_p4133
 mc16_13TeV.364212.Sherpa_221_NN30NNLO_Ztt_Mll10_40_MAXHTPTV70_280_BVeto.deriv.DAOD_HIGG8D1.e5421_e5984_s3126_r10724_r10726_p4133

mc16_13TeV.364213.Sherpa_221_NN30NNLO_Ztt_Mll10_40_MAXHTPTV70_280_BFilter.deriv.DAOD_HIGG8D1.e5421_e5984_s3126_r10724_r10726_p4133
 mc16_13TeV.364214.Sherpa_221_NN30NNLO_Ztt_Mll10_40_MAXHTPTV280_E_CMS_BVeto.deriv.DAOD_HIGG8D1.e5421_e5984_s3126_r10724_r10726_p4133
 mc16_13TeV.364215.Sherpa_221_NN30NNLO_Ztt_Mll10_40_MAXHTPTV280_E_CMS_BFilter.deriv.DAOD_HIGG8D1.e5421_e5984_s3126_r10724_r10726_p4133
 mc16_13TeV.364156.Sherpa_221_NNPDF30NNLO_Wmunu_MAXHTPTV0_70_CVetoBVeto.deriv.DAOD_HIGG8D1.e5340_e5984_s3126_r10724_r10726_p4133
 mc16_13TeV.364157.Sherpa_221_NNPDF30NNLO_Wmunu_MAXHTPTV0_70_CFilterBVeto.deriv.DAOD_HIGG8D1.e5340_e5984_s3126_r10724_r10726_p4133
 mc16_13TeV.364158.Sherpa_221_NNPDF30NNLO_Wmunu_MAXHTPTV0_70_BFilter.deriv.DAOD_HIGG8D1.e5340_e5984_s3126_s3136_r10724_r10726_p4133
 mc16_13TeV.364158.Sherpa_221_NNPDF30NNLO_Wmunu_MAXHTPTV0_70_BFilter.deriv.DAOD_HIGG8D1.e5340_e5984_s3126_r10724_r10726_p4133
 mc16_13TeV.364159.Sherpa_221_NNPDF30NNLO_Wmunu_MAXHTPTV70_140_CVetoBVeto.deriv.DAOD_HIGG8D1.e5340_e5984_s3126_s3136_r10724_r10726_p4133
 mc16_13TeV.364160.Sherpa_221_NNPDF30NNLO_Wmunu_MAXHTPTV70_140_CFilterBVeto.deriv.DAOD_HIGG8D1.e5340_e5984_s3126_s3136_r10724_r10726_p4133
 mc16_13TeV.364160.Sherpa_221_NNPDF30NNLO_Wmunu_MAXHTPTV70_140_CFilterBVeto.deriv.DAOD_HIGG8D1.e5340_e5984_s3126_r10724_r10726_p4133
 mc16_13TeV.364161.Sherpa_221_NNPDF30NNLO_Wmunu_MAXHTPTV70_140_BFilter.deriv.DAOD_HIGG8D1.e5340_e5984_s3126_r10724_r10726_p4133
 mc16_13TeV.364162.Sherpa_221_NNPDF30NNLO_Wmunu_MAXHTPTV140_280_CVetoBVeto.deriv.DAOD_HIGG8D1.e5340_e5984_s3126_r10724_r10726_p4133
 mc16_13TeV.364163.Sherpa_221_NNPDF30NNLO_Wmunu_MAXHTPTV140_280_CFilterBVeto.deriv.DAOD_HIGG8D1.e5340_e5984_s3126_s3136_r10724_r10726_p4133
 mc16_13TeV.364163.Sherpa_221_NNPDF30NNLO_Wmunu_MAXHTPTV140_280_CFilterBVeto.deriv.DAOD_HIGG8D1.e5340_e5984_s3126_r10724_r10726_p4133
 mc16_13TeV.364164.Sherpa_221_NNPDF30NNLO_Wmunu_MAXHTPTV140_280_BFilter.deriv.DAOD_HIGG8D1.e5340_e5984_s3126_r10724_r10726_p4133
 mc16_13TeV.364165.Sherpa_221_NNPDF30NNLO_Wmunu_MAXHTPTV280_500_CVetoBVeto.deriv.DAOD_HIGG8D1.e5340_e5984_s3126_r10724_r10726_p4133
 mc16_13TeV.364165.Sherpa_221_NNPDF30NNLO_Wmunu_MAXHTPTV280_500_CVetoBVeto.deriv.DAOD_HIGG8D1.e5340_e5984_s3126_s3136_r10724_r10726_p4133
 mc16_13TeV.364166.Sherpa_221_NNPDF30NNLO_Wmunu_MAXHTPTV280_500_CFilterBVeto.deriv.DAOD_HIGG8D1.e5340_e5984_s3126_s3136_r10724_r10726_p4133
 mc16_13TeV.364166.Sherpa_221_NNPDF30NNLO_Wmunu_MAXHTPTV280_500_CFilterBVeto.deriv.DAOD_HIGG8D1.e5340_e5984_s3126_r10724_r10726_p4133
 mc16_13TeV.364167.Sherpa_221_NNPDF30NNLO_Wmunu_MAXHTPTV280_500_BFilter.deriv.DAOD_HIGG8D1.e5340_e5984_s3126_r10724_r10726_p4133
 mc16_13TeV.364167.Sherpa_221_NNPDF30NNLO_Wmunu_MAXHTPTV280_500_BFilter.deriv.DAOD_HIGG8D1.e5340_e5984_s3126_s3136_r10724_r10726_p4133
 mc16_13TeV.364168.Sherpa_221_NNPDF30NNLO_Wmunu_MAXHTPTV500_1000.deriv.DAOD_HIGG8D1.e5340_e5984_s3126_r10724_r10726_p4133
 mc16_13TeV.364168.Sherpa_221_NNPDF30NNLO_Wmunu_MAXHTPTV500_1000.deriv.DAOD_HIGG8D1.e5340_e5984_s3126_s3136_r10724_r10726_p4133
 mc16_13TeV.364169.Sherpa_221_NNPDF30NNLO_Wmunu_MAXHTPTV1000_E_CMS.deriv.DAOD_HIGG8D1.e5340_e5984_s3126_s3136_r10724_r10726_p4133
 mc16_13TeV.364169.Sherpa_221_NNPDF30NNLO_Wmunu_MAXHTPTV1000_E_CMS.deriv.DAOD_HIGG8D1.e5340_e5984_s3126_r10724_r10726_p4133
 mc16_13TeV.364170.Sherpa_221_NNPDF30NNLO_Wenu_MAXHTPTV0_70_CVetoBVeto.deriv.DAOD_HIGG8D1.e5340_e5984_s3126_r10724_r10726_p4133
 mc16_13TeV.364171.Sherpa_221_NNPDF30NNLO_Wenu_MAXHTPTV0_70_CFilterBVeto.deriv.DAOD_HIGG8D1.e5340_e5984_s3126_r10724_r10726_p4133
 mc16_13TeV.364172.Sherpa_221_NNPDF30NNLO_Wenu_MAXHTPTV0_70_BFilter.deriv.DAOD_HIGG8D1.e5340_e5984_s3126_r10724_r10726_p4133
 mc16_13TeV.364173.Sherpa_221_NNPDF30NNLO_Wenu_MAXHTPTV70_140_CVetoBVeto.deriv.DAOD_HIGG8D1.e5340_e5984_s3126_s3136_r10724_r10726_p4133
 mc16_13TeV.364174.Sherpa_221_NNPDF30NNLO_Wenu_MAXHTPTV70_140_CFilterBVeto.deriv.DAOD_HIGG8D1.e5340_e5984_s3126_r10724_r10726_p4133
 mc16_13TeV.364175.Sherpa_221_NNPDF30NNLO_Wenu_MAXHTPTV70_140_BFilter.deriv.DAOD_HIGG8D1.e5340_e5984_s3126_s3136_r10724_r10726_p4133

mc16_13TeV.364176.Sherpa_221_NNPDF30NNLO_Wenu_MAXHTPTV140_280_CVetoBVeto.deriv.DAOD_HIGG8D1.e5340_e5984_s3126_r10724_r10726_p4133
 mc16_13TeV.364177.Sherpa_221_NNPDF30NNLO_Wenu_MAXHTPTV140_280_CFilterBVeto.deriv.DAOD_HIGG8D1.e5340_e5984_s3126_r10724_r10726_p4133
 mc16_13TeV.364177.Sherpa_221_NNPDF30NNLO_Wenu_MAXHTPTV140_280_CFilterBVeto.deriv.DAOD_HIGG8D1.e5340_e5984_s3126_s3136_r10724_r10726_p4133
 mc16_13TeV.364178.Sherpa_221_NNPDF30NNLO_Wenu_MAXHTPTV140_280_BFilter.deriv.DAOD_HIGG8D1.e5340_e5984_s3126_r10724_r10726_p4133
 mc16_13TeV.364179.Sherpa_221_NNPDF30NNLO_Wenu_MAXHTPTV280_500_CVetoBVeto.deriv.DAOD_HIGG8D1.e5340_e5984_s3126_r10724_r10726_p4133
 mc16_13TeV.364179.Sherpa_221_NNPDF30NNLO_Wenu_MAXHTPTV280_500_CVetoBVeto.deriv.DAOD_HIGG8D1.e5340_e5984_s3126_s3136_r10724_r10726_p4133
 mc16_13TeV.364180.Sherpa_221_NNPDF30NNLO_Wenu_MAXHTPTV280_500_CFilterBVeto.deriv.DAOD_HIGG8D1.e5340_e5984_s3126_s3136_r10724_r10726_p4133
 mc16_13TeV.364180.Sherpa_221_NNPDF30NNLO_Wenu_MAXHTPTV280_500_CFilterBVeto.deriv.DAOD_HIGG8D1.e5340_e5984_s3126_r10724_r10726_p4133
 mc16_13TeV.364181.Sherpa_221_NNPDF30NNLO_Wenu_MAXHTPTV280_500_BFilter.deriv.DAOD_HIGG8D1.e5340_e5984_s3126_s3136_r10724_r10726_p4133
 mc16_13TeV.364181.Sherpa_221_NNPDF30NNLO_Wenu_MAXHTPTV280_500_BFilter.deriv.DAOD_HIGG8D1.e5340_e5984_s3126_r10724_r10726_p4133
 mc16_13TeV.364182.Sherpa_221_NNPDF30NNLO_Wenu_MAXHTPTV500_1000.deriv.DAOD_HIGG8D1.e5340_e5984_s3126_s3136_r10724_r10726_p4133
 mc16_13TeV.364182.Sherpa_221_NNPDF30NNLO_Wenu_MAXHTPTV500_1000.deriv.DAOD_HIGG8D1.e5340_e5984_s3126_r10724_r10726_p4133
 mc16_13TeV.364183.Sherpa_221_NNPDF30NNLO_Wenu_MAXHTPTV1000_E_CMS.deriv.DAOD_HIGG8D1.e5340_e5984_s3126_r10724_r10726_p4133
 mc16_13TeV.364183.Sherpa_221_NNPDF30NNLO_Wenu_MAXHTPTV1000_E_CMS.deriv.DAOD_HIGG8D1.e5340_e5984_s3126_s3136_r10724_r10726_p4133
 mc16_13TeV.364184.Sherpa_221_NNPDF30NNLO_Wtaunu_MAXHTPTV0_70_CVetoBVeto.deriv.DAOD_HIGG8D1.e5340_e5984_s3126_r10724_r10726_p4133
 mc16_13TeV.364185.Sherpa_221_NNPDF30NNLO_Wtaunu_MAXHTPTV0_70_CFilterBVeto.deriv.DAOD_HIGG8D1.e5340_e5984_s3126_r10724_r10726_p4133
 mc16_13TeV.364186.Sherpa_221_NNPDF30NNLO_Wtaunu_MAXHTPTV0_70_BFilter.deriv.DAOD_HIGG8D1.e5340_e5984_s3126_s3136_r10724_r10726_p4133
 mc16_13TeV.364186.Sherpa_221_NNPDF30NNLO_Wtaunu_MAXHTPTV0_70_BFilter.deriv.DAOD_HIGG8D1.e5340_e5984_s3126_r10724_r10726_p4133
 mc16_13TeV.364187.Sherpa_221_NNPDF30NNLO_Wtaunu_MAXHTPTV70_140_CVetoBVeto.deriv.DAOD_HIGG8D1.e5340_e5984_s3126_r10724_r10726_p4133
 mc16_13TeV.364188.Sherpa_221_NNPDF30NNLO_Wtaunu_MAXHTPTV70_140_CFilterBVeto.deriv.DAOD_HIGG8D1.e5340_e5984_s3126_r10724_r10726_p4133
 mc16_13TeV.364189.Sherpa_221_NNPDF30NNLO_Wtaunu_MAXHTPTV70_140_BFilter.deriv.DAOD_HIGG8D1.e5340_e5984_s3126_r10724_r10726_p4133
 mc16_13TeV.364189.Sherpa_221_NNPDF30NNLO_Wtaunu_MAXHTPTV70_140_BFilter.deriv.DAOD_HIGG8D1.e5340_e5984_s3126_s3136_r10724_r10726_p4133
 mc16_13TeV.364190.Sherpa_221_NNPDF30NNLO_Wtaunu_MAXHTPTV140_280_CVetoBVeto.deriv.DAOD_HIGG8D1.e5340_e5984_s3126_r10724_r10726_p4133
 mc16_13TeV.364190.Sherpa_221_NNPDF30NNLO_Wtaunu_MAXHTPTV140_280_CVetoBVeto.deriv.DAOD_HIGG8D1.e5340_e5984_s3126_s3136_r10724_r10726_p4133
 mc16_13TeV.364191.Sherpa_221_NNPDF30NNLO_Wtaunu_MAXHTPTV140_280_CFilterBVeto.deriv.DAOD_HIGG8D1.e5340_e5984_s3126_r10724_r10726_p4133
 mc16_13TeV.364191.Sherpa_221_NNPDF30NNLO_Wtaunu_MAXHTPTV140_280_CFilterBVeto.deriv.DAOD_HIGG8D1.e5340_e5984_s3126_s3136_r10724_r10726_p4133
 mc16_13TeV.364192.Sherpa_221_NNPDF30NNLO_Wtaunu_MAXHTPTV140_280_BFilter.deriv.DAOD_HIGG8D1.e5340_e5984_s3126_s3136_r10724_r10726_p4133
 mc16_13TeV.364192.Sherpa_221_NNPDF30NNLO_Wtaunu_MAXHTPTV140_280_BFilter.deriv.DAOD_HIGG8D1.e5340_e5984_s3126_r10724_r10726_p4133
 mc16_13TeV.364193.Sherpa_221_NNPDF30NNLO_Wtaunu_MAXHTPTV280_500_CVetoBVeto.deriv.DAOD_HIGG8D1.e5340_e5984_s3126_r10724_r10726_p4133
 mc16_13TeV.364193.Sherpa_221_NNPDF30NNLO_Wtaunu_MAXHTPTV280_500_CVetoBVeto.deriv.DAOD_HIGG8D1.e5340_e5984_s3126_s3136_r10724_r10726_p4133
 mc16_13TeV.364194.Sherpa_221_NNPDF30NNLO_Wtaunu_MAXHTPTV280_500_CFilterBVeto.deriv.DAOD_HIGG8D1.e5340_e5984_s3126_s3136_r10724_r10726_p4133

mc16_13TeV.364194.Sherpa_221_NNPDF30NNLO_Wtaunu_MAXHTPTV280_500_CFilterBVeto.deriv.DAOD_HIGG8D1.e5340_e5984_s3126_r10724_r10726_p4133
 mc16_13TeV.364195.Sherpa_221_NNPDF30NNLO_Wtaunu_MAXHTPTV280_500_BFilter.deriv.DAOD_HIGG8D1.e5340_e5984_s3126_s3136_r10724_r10726_p4133
 mc16_13TeV.364195.Sherpa_221_NNPDF30NNLO_Wtaunu_MAXHTPTV280_500_BFilter.deriv.DAOD_HIGG8D1.e5340_e5984_s3126_r10724_r10726_p4133
 mc16_13TeV.364196.Sherpa_221_NNPDF30NNLO_Wtaunu_MAXHTPTV500_1000.deriv.DAOD_HIGG8D1.e5340_e5984_s3126_s3136_r10724_r10726_p4133
 mc16_13TeV.364196.Sherpa_221_NNPDF30NNLO_Wtaunu_MAXHTPTV500_1000.deriv.DAOD_HIGG8D1.e5340_e5984_s3126_r10724_r10726_p4133
 mc16_13TeV.364197.Sherpa_221_NNPDF30NNLO_Wtaunu_MAXHTPTV1000_E_CMS.deriv.DAOD_HIGG8D1.e5340_e5984_s3126_s3136_r10724_r10726_p4133
 mc16_13TeV.364197.Sherpa_221_NNPDF30NNLO_Wtaunu_MAXHTPTV1000_E_CMS.deriv.DAOD_HIGG8D1.e5340_e5984_s3126_r10724_r10726_p4133
 mc16_13TeV.364500.Sherpa_222_NNPDF30NNLO_eegamma_pty_7_15.deriv.DAOD_HIGG8D1.e5928_e5984_s3126_r10724_r10726_p4133
 mc16_13TeV.364501.Sherpa_222_NNPDF30NNLO_eegamma_pty_15_35.deriv.DAOD_HIGG8D1.e5928_e5984_s3126_r10724_r10726_p4133
 mc16_13TeV.364502.Sherpa_222_NNPDF30NNLO_eegamma_pty_35_70.deriv.DAOD_HIGG8D1.e5928_e5984_s3126_r10724_r10726_p4133
 mc16_13TeV.364503.Sherpa_222_NNPDF30NNLO_eegamma_pty_70_140.deriv.DAOD_HIGG8D1.e5928_e5984_s3126_r10724_r10726_p4133
 mc16_13TeV.364504.Sherpa_222_NNPDF30NNLO_eegamma_pty_140_E_CMS.deriv.DAOD_HIGG8D1.e5928_e5984_s3126_r10724_r10726_p4133
 mc16_13TeV.364505.Sherpa_222_NNPDF30NNLO_mumugamma_pty_7_15.deriv.DAOD_HIGG8D1.e5928_e5984_s3126_r10724_r10726_p4133
 mc16_13TeV.364506.Sherpa_222_NNPDF30NNLO_mumugamma_pty_15_35.deriv.DAOD_HIGG8D1.e5928_e5984_s3126_r10724_r10726_p4133
 mc16_13TeV.364507.Sherpa_222_NNPDF30NNLO_mumugamma_pty_35_70.deriv.DAOD_HIGG8D1.e5928_e5984_s3126_r10724_r10726_p4133
 mc16_13TeV.364508.Sherpa_222_NNPDF30NNLO_mumugamma_pty_70_140.deriv.DAOD_HIGG8D1.e5928_e5984_s3126_r10724_r10726_p4133
 mc16_13TeV.364509.Sherpa_222_NNPDF30NNLO_mumugamma_pty_140_E_CMS.deriv.DAOD_HIGG8D1.e5928_e5984_s3126_r10724_r10726_p4133
 mc16_13TeV.364511.Sherpa_222_NNPDF30NNLO_tautaugamma_pty_15_35.deriv.DAOD_HIGG8D1.e5928_e5984_s3126_r10724_r10726_p4133
 mc16_13TeV.364512.Sherpa_222_NNPDF30NNLO_tautaugamma_pty_35_70.deriv.DAOD_HIGG8D1.e5928_e5984_s3126_r10724_r10726_p4133
 mc16_13TeV.364513.Sherpa_222_NNPDF30NNLO_tautaugamma_pty_70_140.deriv.DAOD_HIGG8D1.e5982_e5984_s3126_r10724_r10726_p4133
 mc16_13TeV.364514.Sherpa_222_NNPDF30NNLO_tautaugamma_pty_140_E_CMS.deriv.DAOD_HIGG8D1.e5928_e5984_s3126_r10724_r10726_p4133
 mc16_13TeV.364522.Sherpa_222_NNPDF30NNLO_enugamma_pty_15_35.deriv.DAOD_HIGG8D1.e5928_e5984_s3126_r10724_r10726_p4133
 mc16_13TeV.364523.Sherpa_222_NNPDF30NNLO_enugamma_pty_35_70.deriv.DAOD_HIGG8D1.e5928_e5984_s3126_r10724_r10726_p4133
 mc16_13TeV.364524.Sherpa_222_NNPDF30NNLO_enugamma_pty_70_140.deriv.DAOD_HIGG8D1.e5928_e5984_s3126_r10724_r10726_p4133
 mc16_13TeV.364525.Sherpa_222_NNPDF30NNLO_enugamma_pty_140_E_CMS.deriv.DAOD_HIGG8D1.e5928_e5984_s3126_r10724_r10726_p4133
 mc16_13TeV.364527.Sherpa_222_NNPDF30NNLO_munugamma_pty_15_35.deriv.DAOD_HIGG8D1.e5928_e5984_s3126_r10724_r10726_p4133
 mc16_13TeV.364528.Sherpa_222_NNPDF30NNLO_munugamma_pty_35_70.deriv.DAOD_HIGG8D1.e5928_e5984_s3126_r10724_r10726_p4133
 mc16_13TeV.364529.Sherpa_222_NNPDF30NNLO_munugamma_pty_70_140.deriv.DAOD_HIGG8D1.e5928_e5984_s3126_r10724_r10726_p4133
 mc16_13TeV.364530.Sherpa_222_NNPDF30NNLO_munugamma_pty_140_E_CMS.deriv.DAOD_HIGG8D1.e5928_e5984_s3126_r10724_r10726_p4133
 mc16_13TeV.364532.Sherpa_222_NNPDF30NNLO_taunugamma_pty_15_35.deriv.DAOD_HIGG8D1.e5928_e5984_s3126_r10724_r10726_p4133
 mc16_13TeV.364533.Sherpa_222_NNPDF30NNLO_taunugamma_pty_35_70.deriv.DAOD_HIGG8D1.e5928_e5984_s3126_r10724_r10726_p4133

mc16_13TeV.364534.Sherpa_222_NNPDF30NNLO_taunugamma_pty_70_140.deriv.DAOD_HIGG8D1.e5928_e5984_s3126_r10724_r10726_p4133
mc16_13TeV.364535.Sherpa_222_NNPDF30NNLO_taunugamma_pty_140_E_CMS.deriv.DAOD_HIGG8D1.e5928_e5984_s3126_r10724_r10726_p4133
mc16_13TeV.410560.MadGraphPythia8EvtGen_A14_tZ_4fl_tchan_noAllHad.deriv.DAOD_HIGG8D1.e5803_e5984_s3126_r10724_r10726_p4133
mc16_13TeV.410408.aMcAtNloPythia8EvtGen_tWZ_Ztoll_minDR1.deriv.DAOD_HIGG8D1.e6423_e5984_s3126_r10724_r10726_p4133
mc16_13TeV.364242.Sherpa_222_NNPDF30NNLO_WWW_3l3v_EW6.deriv.DAOD_HIGG8D1.e5887_e5984_s3126_r10724_r10726_p4133
mc16_13TeV.364243.Sherpa_222_NNPDF30NNLO_WWZ_4l2v_EW6.deriv.DAOD_HIGG8D1.e5887_e5984_s3126_r10724_r10726_p4133
mc16_13TeV.364244.Sherpa_222_NNPDF30NNLO_WWZ_2l4v_EW6.deriv.DAOD_HIGG8D1.e5887_e5984_s3126_r10724_r10726_p4133
mc16_13TeV.364245.Sherpa_222_NNPDF30NNLO_WZZ_5l1v_EW6.deriv.DAOD_HIGG8D1.e5887_e5984_s3126_r10724_r10726_p4133
mc16_13TeV.364246.Sherpa_222_NNPDF30NNLO_WZZ_3l3v_EW6.deriv.DAOD_HIGG8D1.e5887_e5984_s3126_r10724_r10726_p4133
mc16_13TeV.364247.Sherpa_222_NNPDF30NNLO_ZZZ_6l0v_EW6.deriv.DAOD_HIGG8D1.e5887_e5984_s3126_r10724_r10726_p4133
mc16_13TeV.364248.Sherpa_222_NNPDF30NNLO_ZZZ_4l2v_EW6.deriv.DAOD_HIGG8D1.e5887_e5984_s3126_r10724_r10726_p4133
mc16_13TeV.364249.Sherpa_222_NNPDF30NNLO_ZZZ_2l4v_EW6.deriv.DAOD_HIGG8D1.e5887_e5984_s3126_r10724_r10726_p4133
mc16_13TeV.342284.Pythia8EvtGen_A14NNPDF23LO_WH125_inc.deriv.DAOD_HIGG8D1.e4246_e5984_s3126_r10724_r10726_p4133
mc16_13TeV.342285.Pythia8EvtGen_A14NNPDF23LO_ZH125_inc.deriv.DAOD_HIGG8D1.e4246_e5984_s3126_r10724_r10726_p4133
mc16_13TeV.341998.aMcAtNloHppEG_UEEE5_CTEQ6L1_CT10ME_tWH125_gamgam_yt_plus1.deriv.DAOD_HIGG8D1.e4394_e5984_s3126_r10724_r10726_p4133
mc16_13TeV.410389.MadGraphPythia8EvtGen_A14NNPDF23_ttgamma_nonallhadronic.deriv.DAOD_HIGG8D1.e6155_e5984_s3126_r10724_r10726_p4133
mc16_13TeV.410470.PhPy8EG_A14_ttbar_hdamp258p75_nonallhad.deriv.DAOD_HIGG8D1.e6337_e5984_s3126_r10724_r10726_p4133
mc16_13TeV.410472.PhPy8EG_A14_ttbar_hdamp258p75_dil.deriv.DAOD_HIGG8D1.e6348_e5984_s3126_r10724_r10726_p4133
mc16_13TeV.346343.PhPy8EG_A14NNPDF23_NNPDF30ME_ttH125_allhad.deriv.DAOD_HIGG8D1.e7148_e5984_s3126_r10724_r10726_p4133
mc16_13TeV.346343.PhPy8EG_A14NNPDF23_NNPDF30ME_ttH125_allhad.deriv.DAOD_HIGG8D1.e7148_e5984_a875_r10724_r10726_p4133
mc16_13TeV.346344.PhPy8EG_A14NNPDF23_NNPDF30ME_ttH125_semilep.deriv.DAOD_HIGG8D1.e7148_e5984_a875_r10724_r10726_p4133
mc16_13TeV.346344.PhPy8EG_A14NNPDF23_NNPDF30ME_ttH125_semilep.deriv.DAOD_HIGG8D1.e7148_e5984_s3126_r10724_r10726_p4133
mc16_13TeV.346345.PhPy8EG_A14NNPDF23_NNPDF30ME_ttH125_dilep.deriv.DAOD_HIGG8D1.e7148_e5984_a875_r10724_r10726_p4133
mc16_13TeV.346345.PhPy8EG_A14NNPDF23_NNPDF30ME_ttH125_dilep.deriv.DAOD_HIGG8D1.e7148_e5984_s3126_r10724_r10726_p4133

1857 **A Machine Learning Models**

1858 The following section provides details of the various MVAs as well as a few studies performed
1859 in support of this analysis, exploring alternate decisions and strategies.

1860 **A.1 Higgs Reconstruction Models**

1861 **A.1.1 b-jet Identification Features - 2lSS**

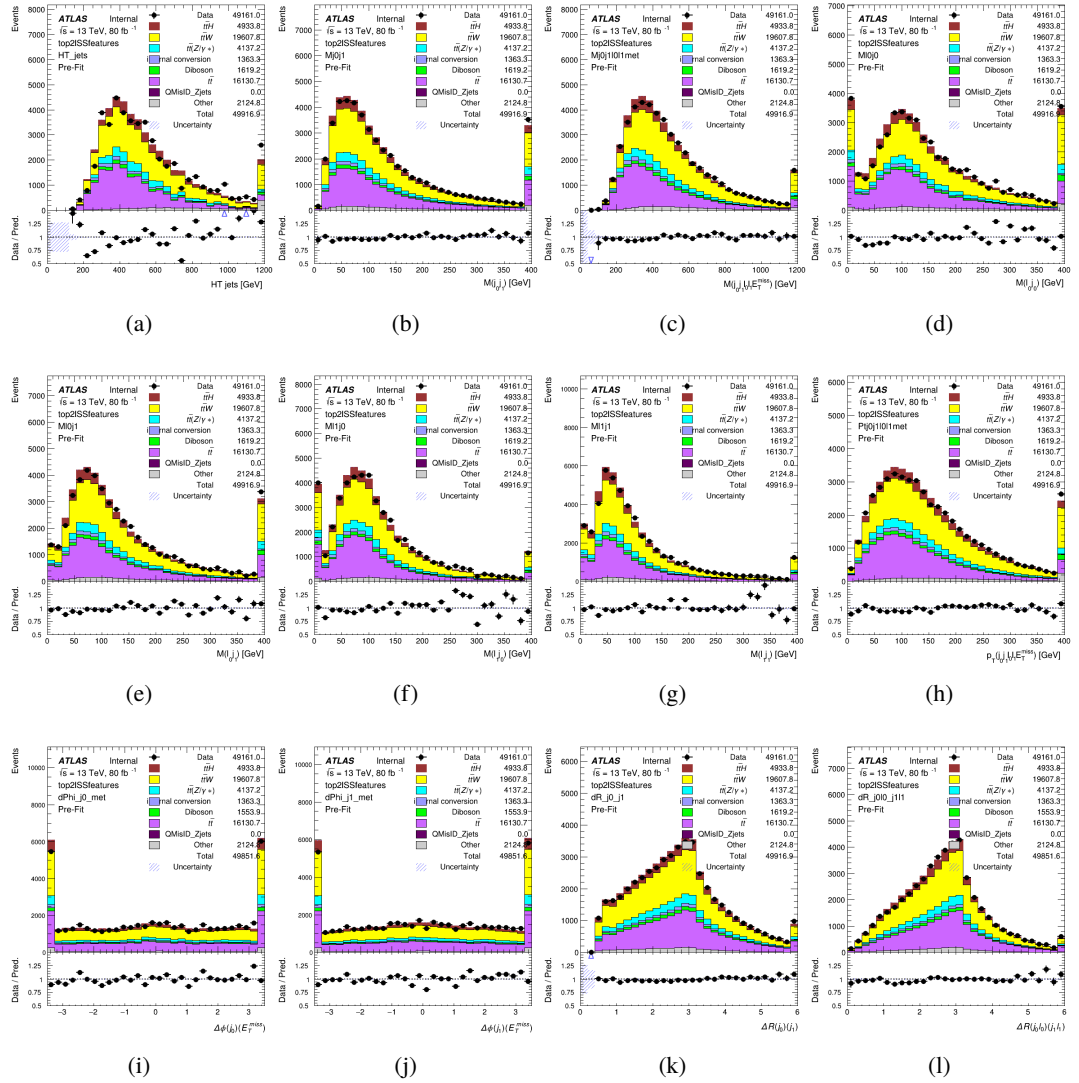


Figure A.1: Input features for top2lSS

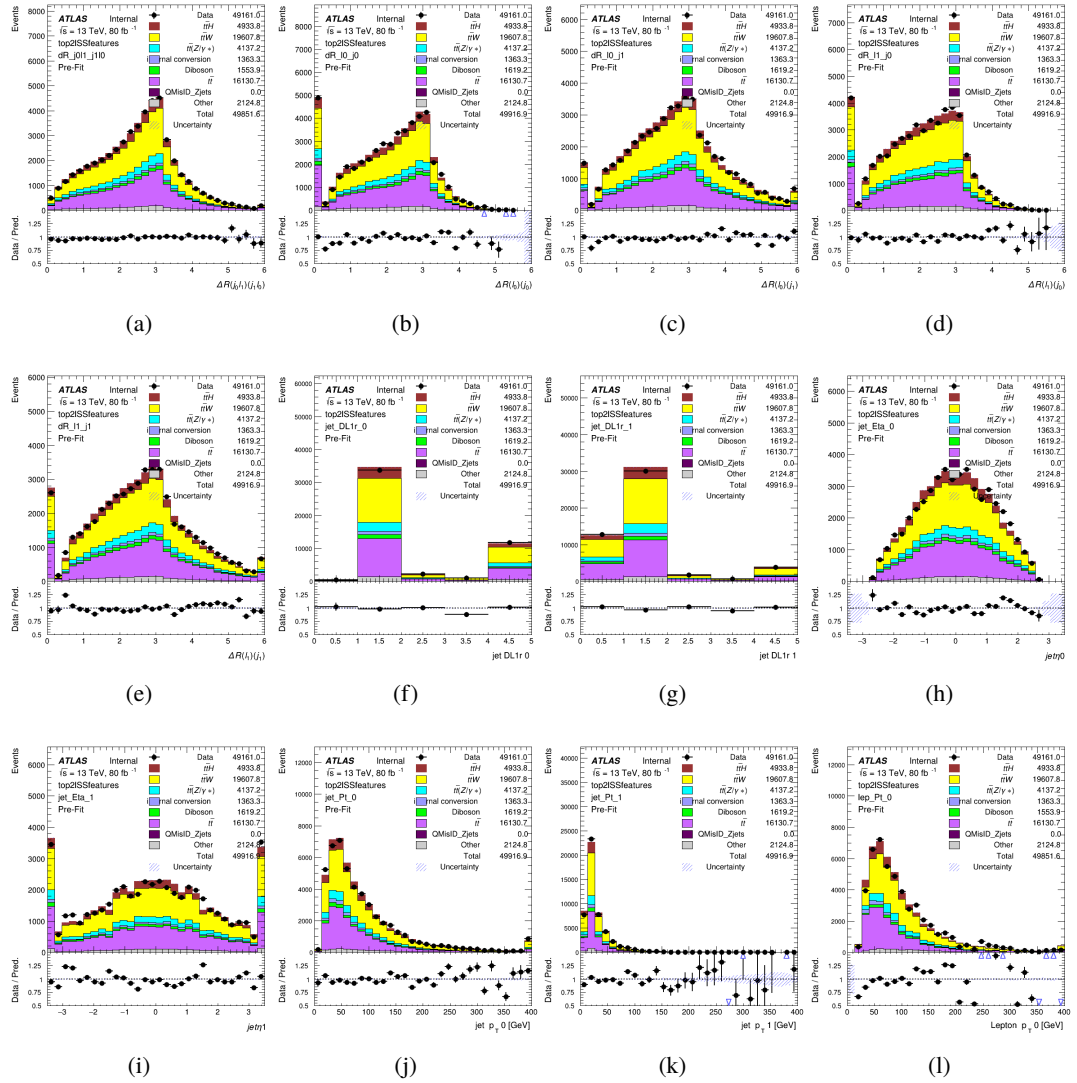


Figure A.2: Input features for top2lSS

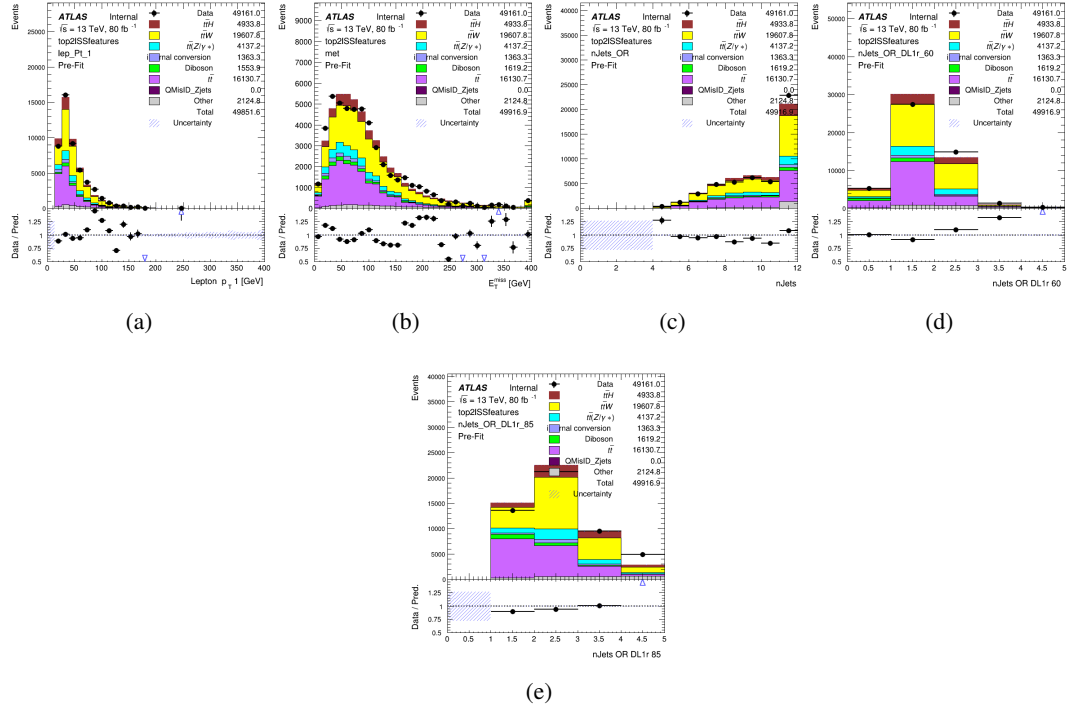


Figure A.3: Input features for top2ISS

1862 **A.1.2 b-jet Identification Features - 3l**

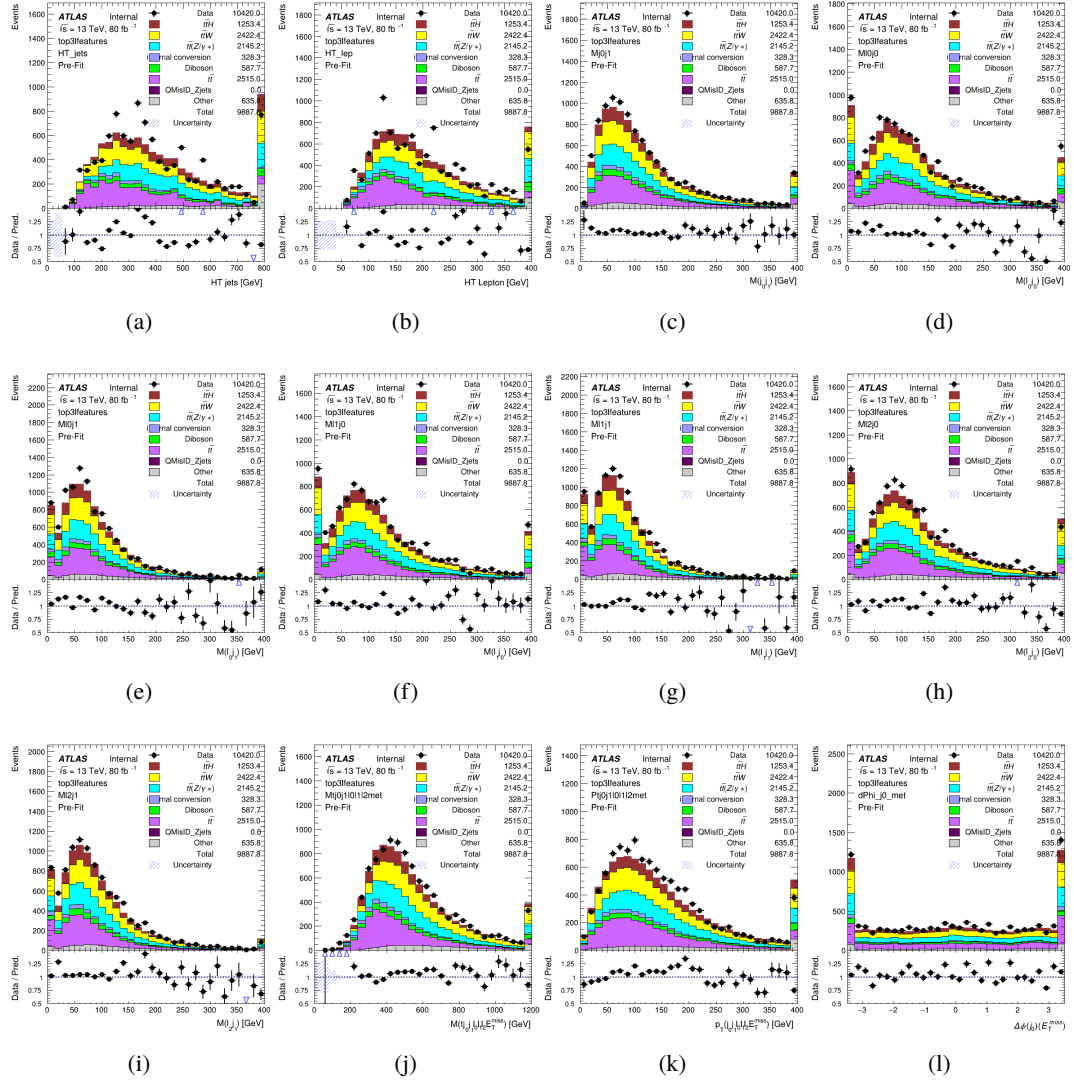


Figure A.4: Input features for top31

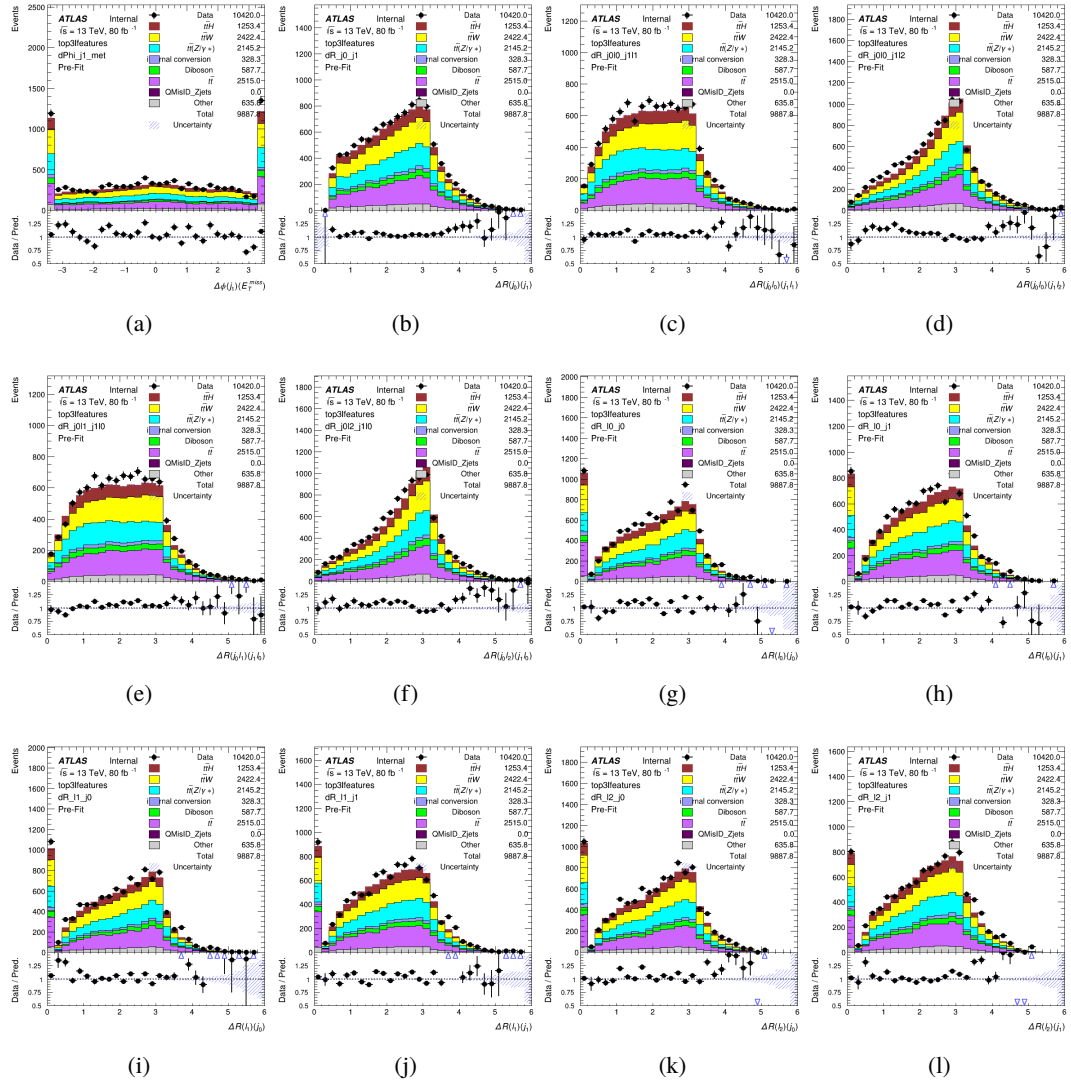


Figure A.5: Input features for top31

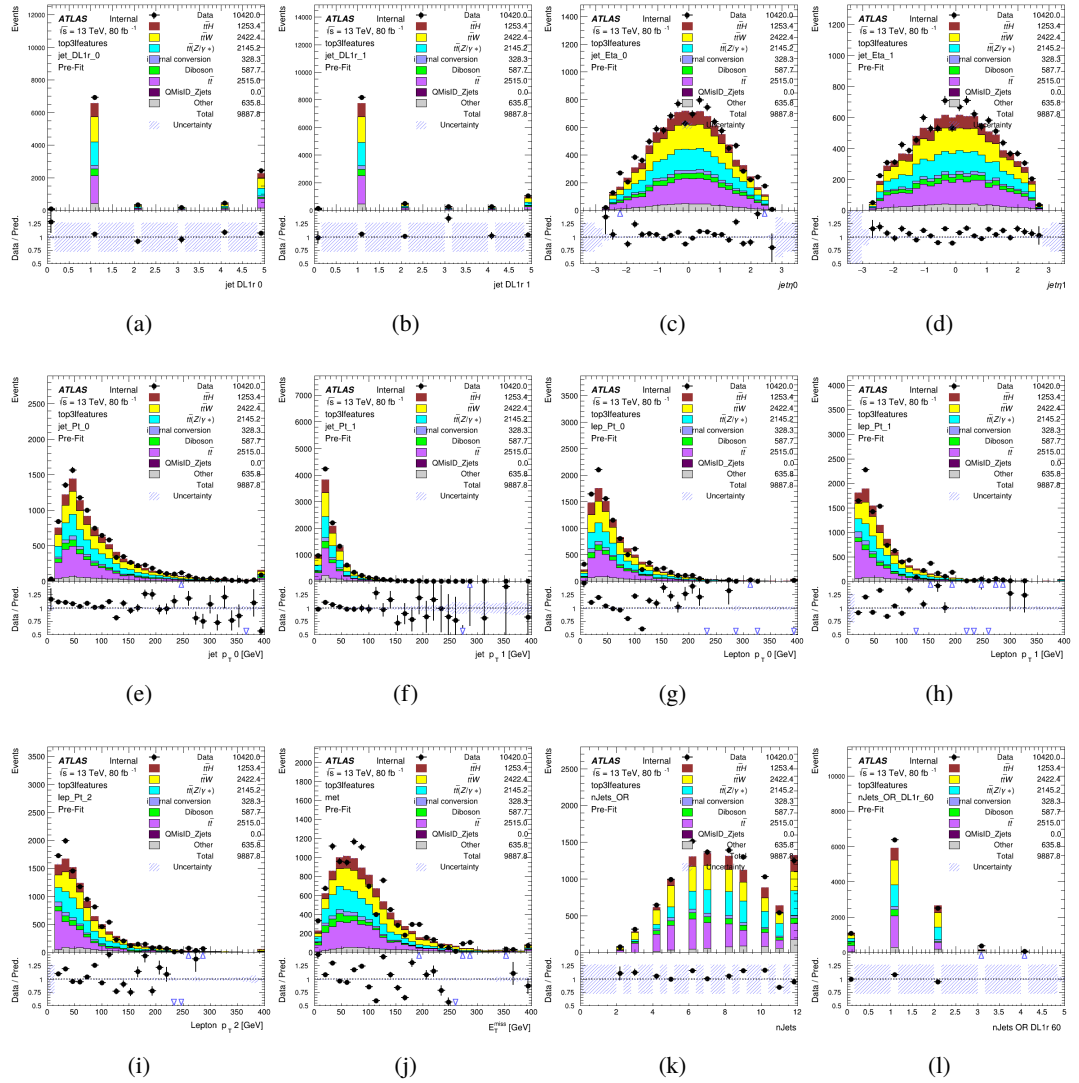
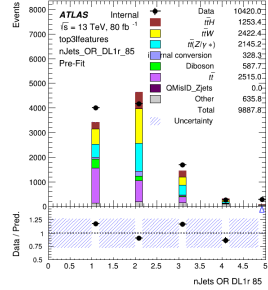


Figure A.6: Input features for top31



(a)

Figure A.7: Input features for top31

1863 **A.1.3 Higgs Reconstruction Features - 2lSS**

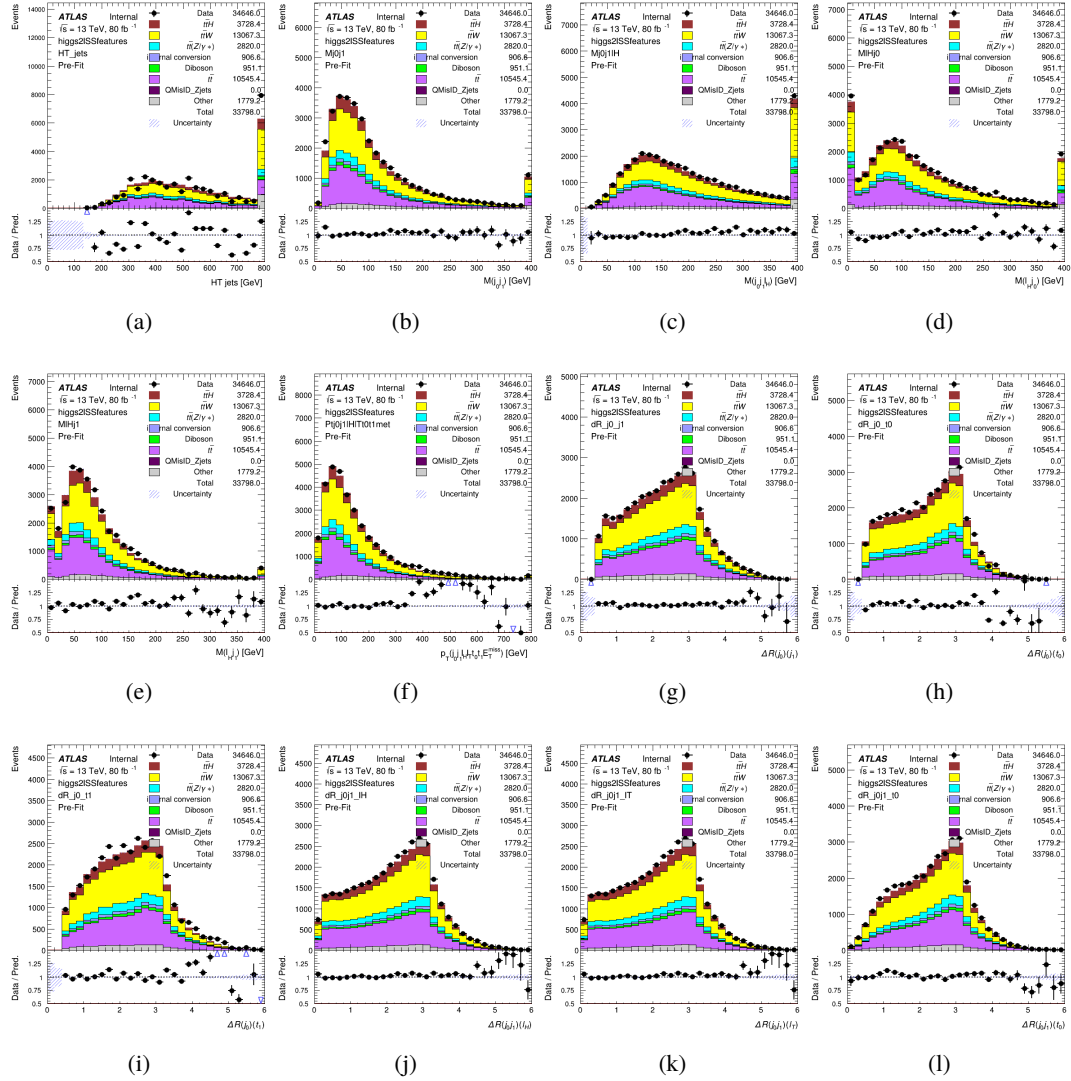


Figure A.8: Input features for higgs2lSS

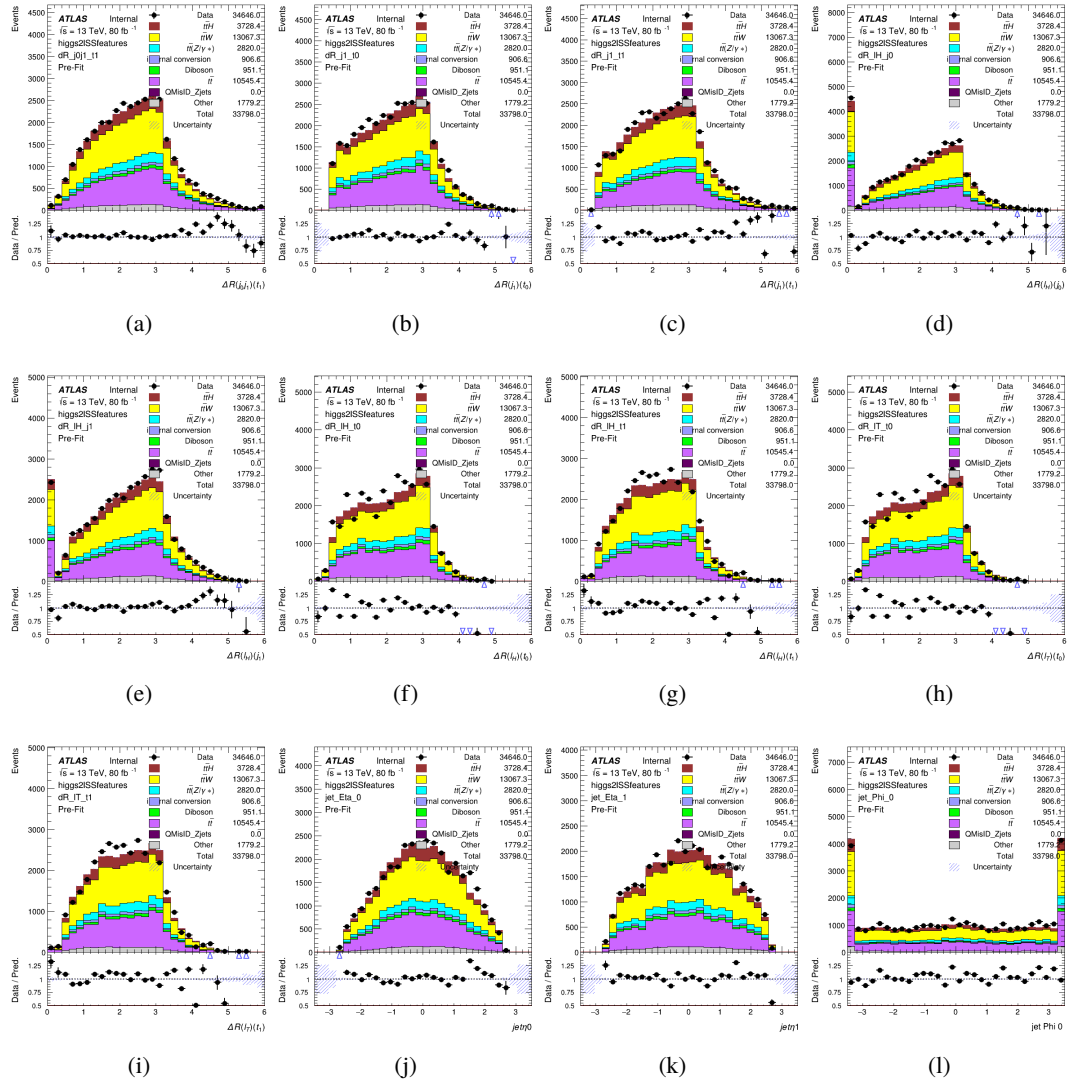


Figure A.9: Input features for higgs2lSS

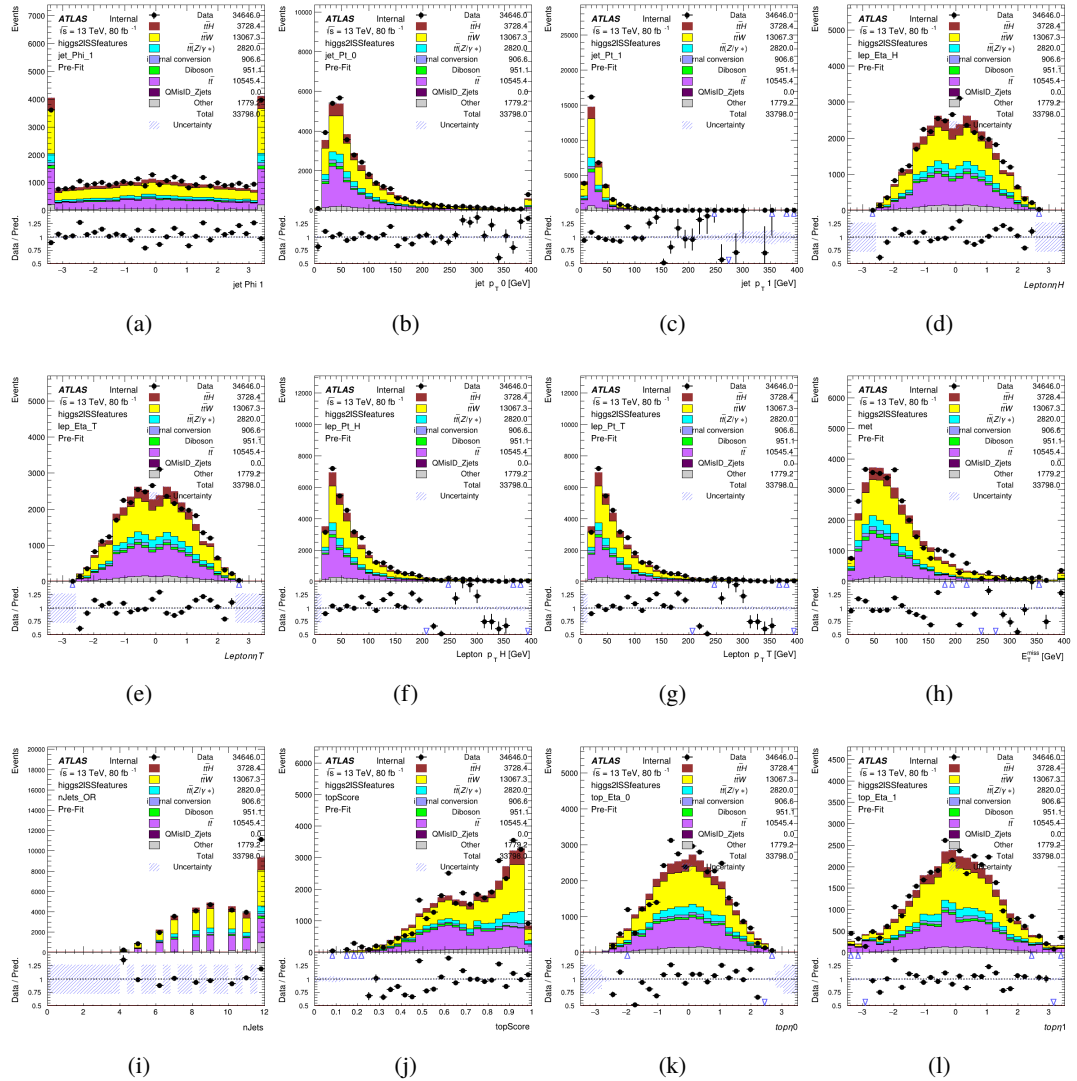


Figure A.10: Input features for higgs2IS

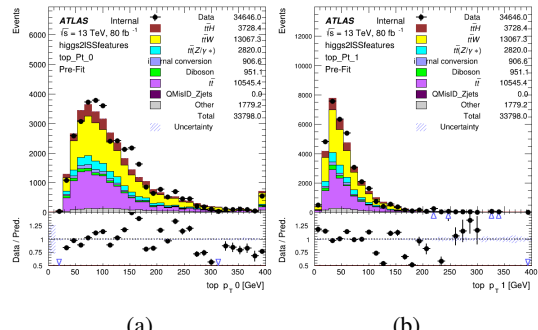


Figure A.11: Input features for higgs2lSS

1864 **A.1.4 Higgs Reconstruction Features - 3lS**

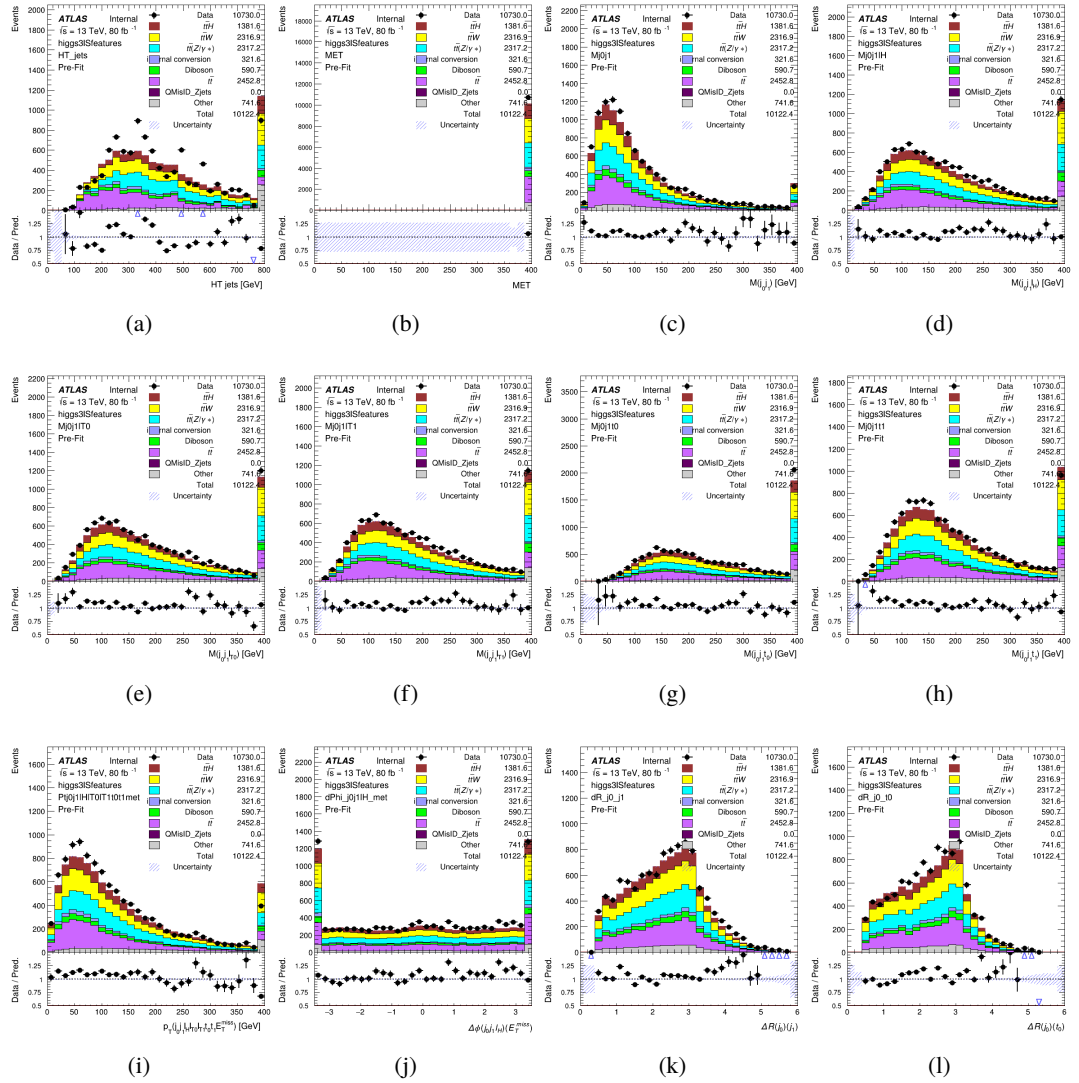


Figure A.12: Input features for higgs3IS

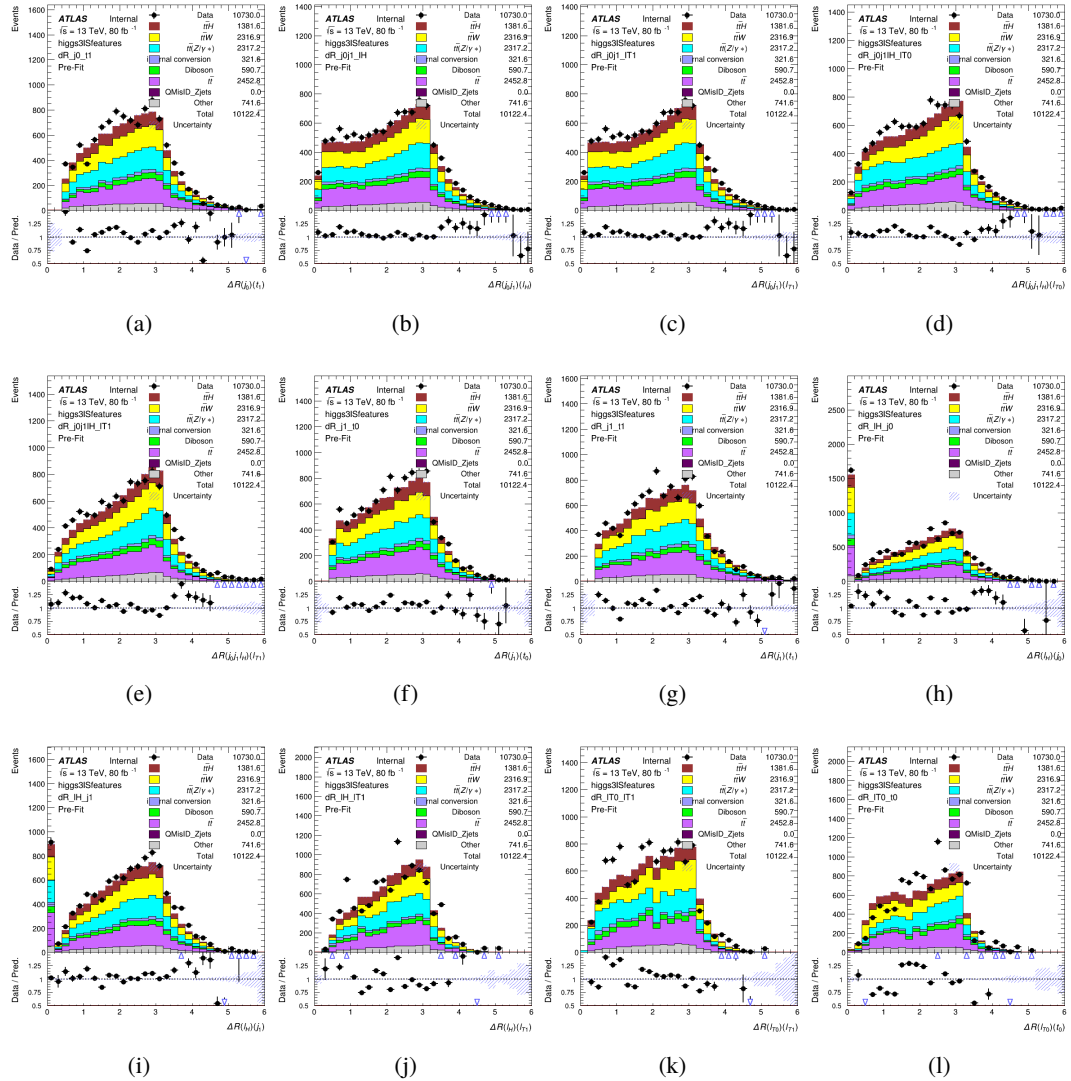


Figure A.13: Input features for higgs3SIS

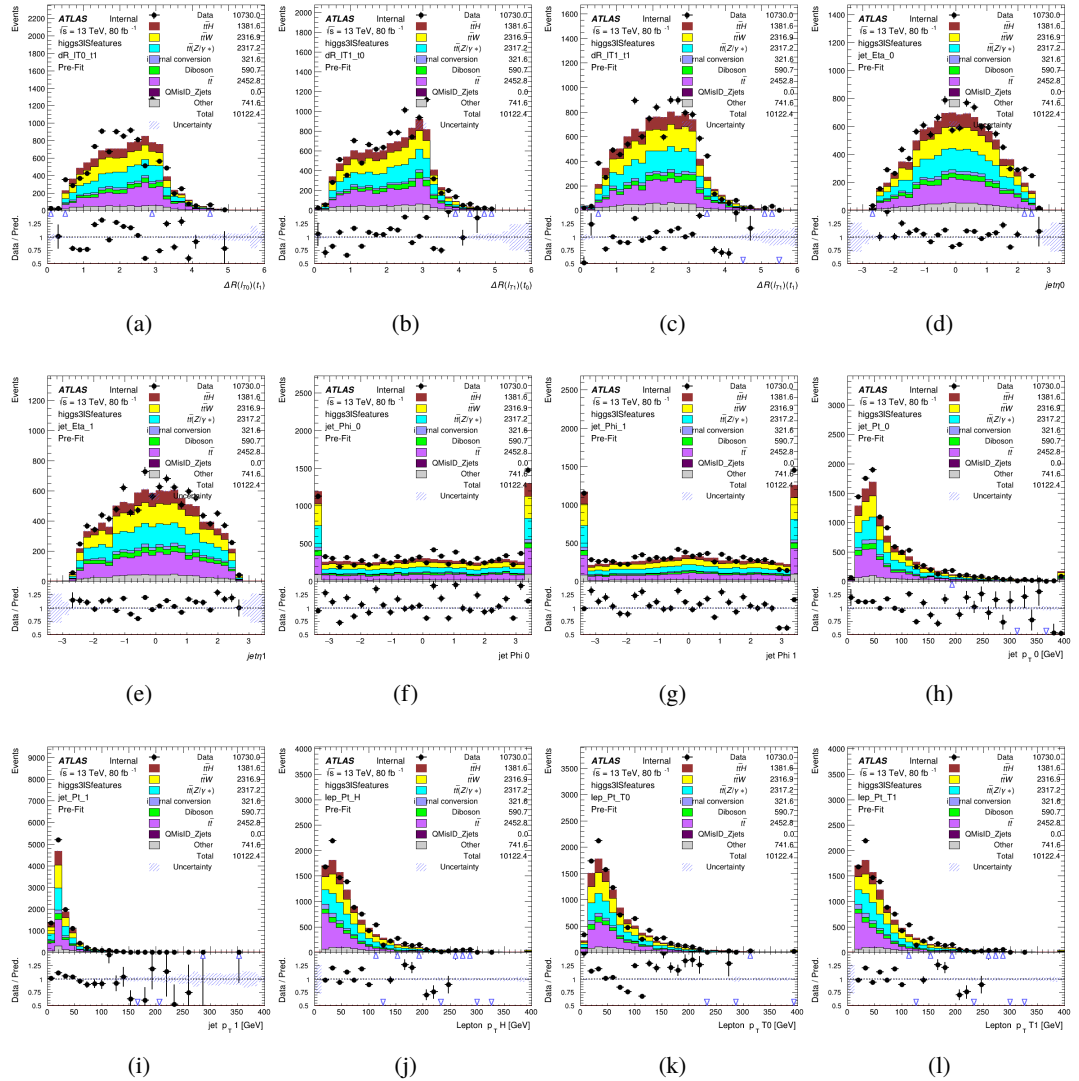


Figure A.14: Input features for higgs31S

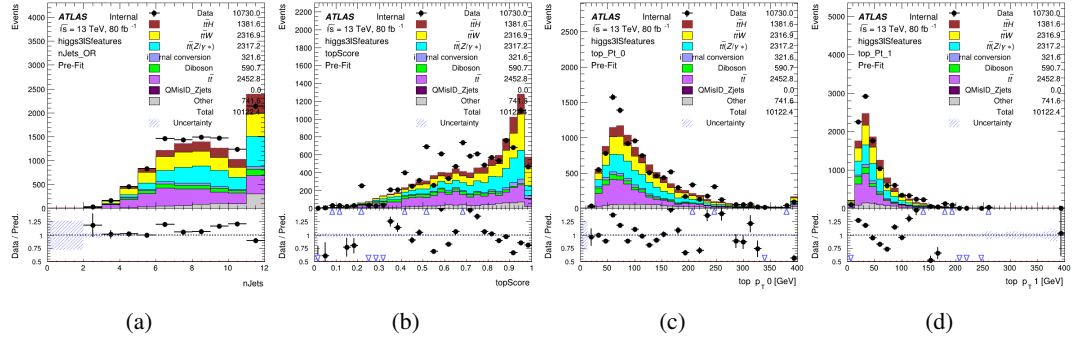


Figure A.15: Input features for higgs3IS

1865 **A.1.5 Higgs Reconstruction Features - 3lF**

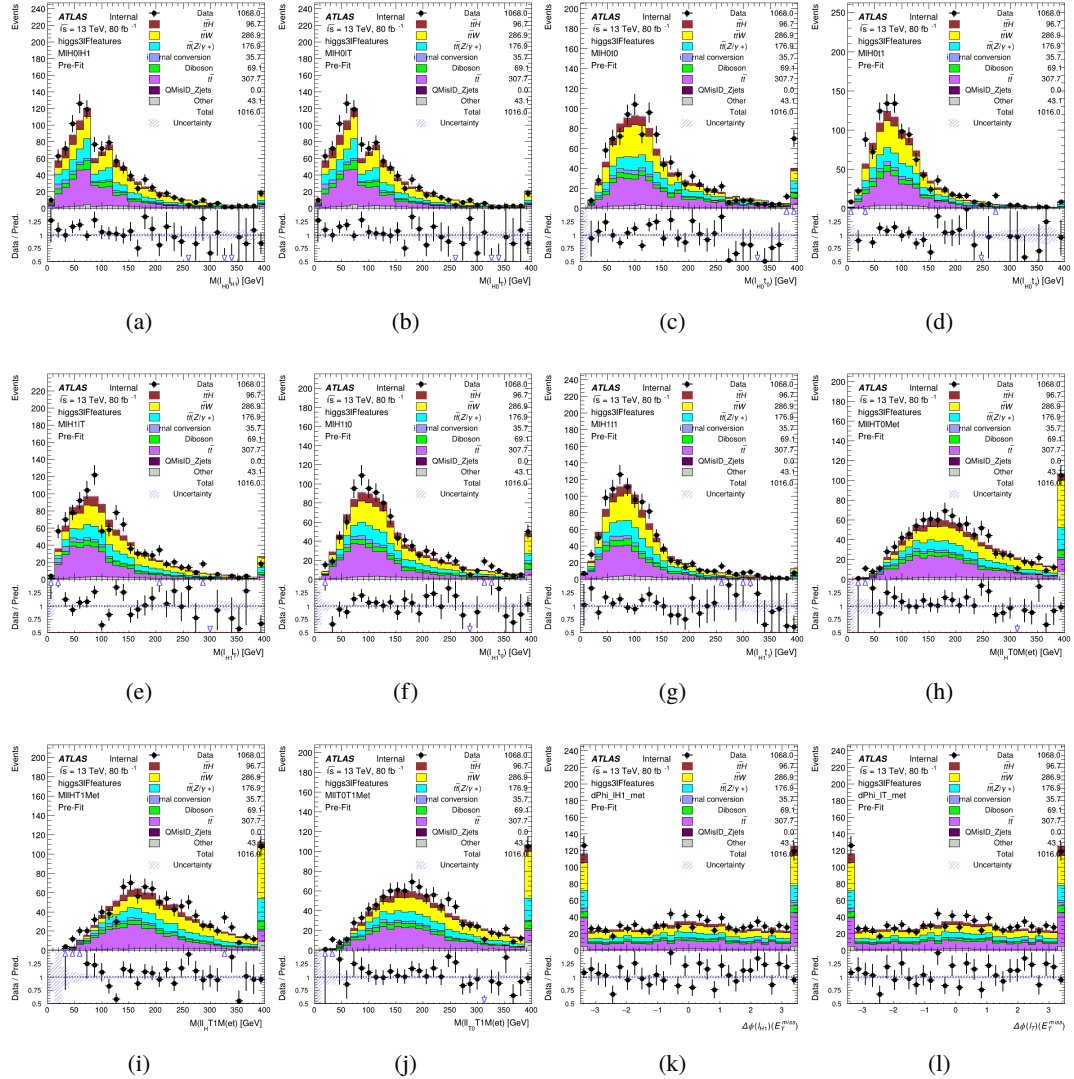


Figure A.16: Input features for higgs3IF

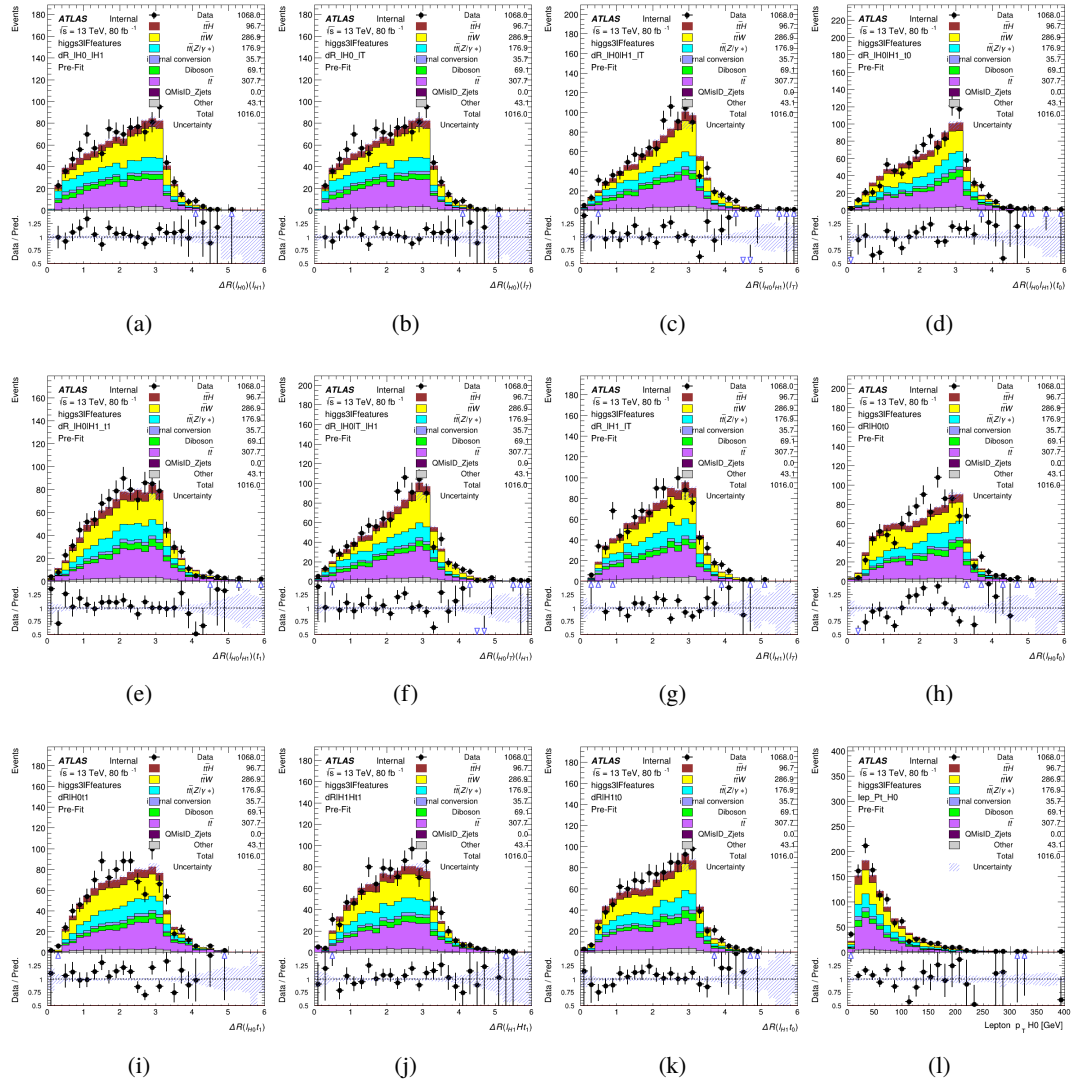


Figure A.17: Input features for higgs3lF

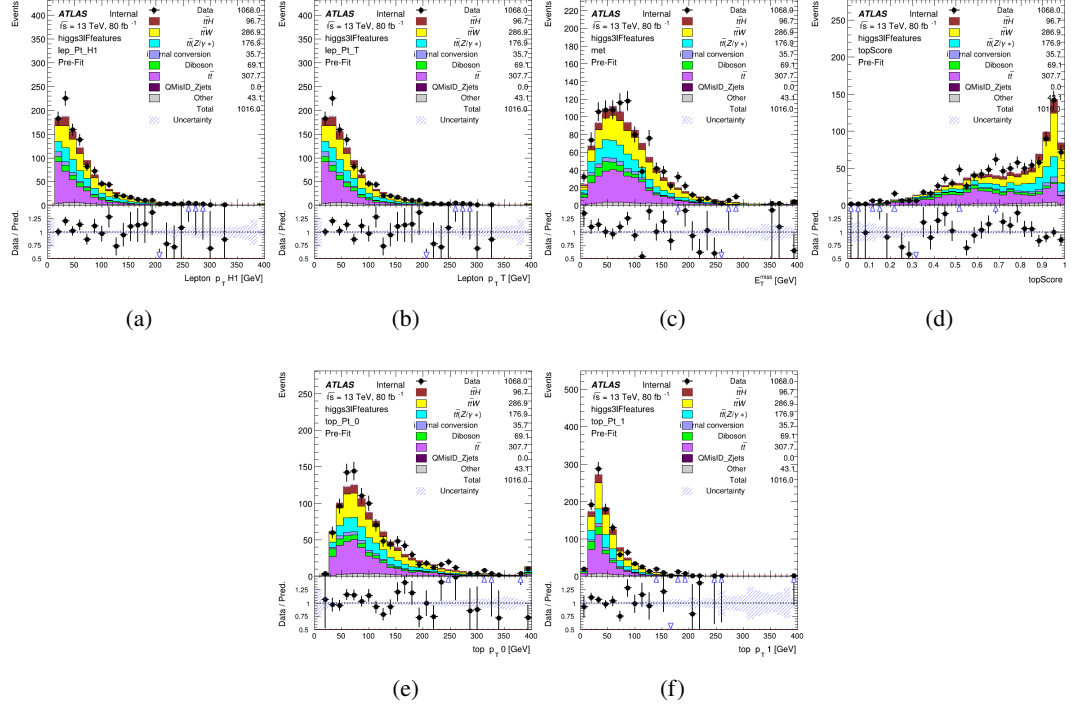
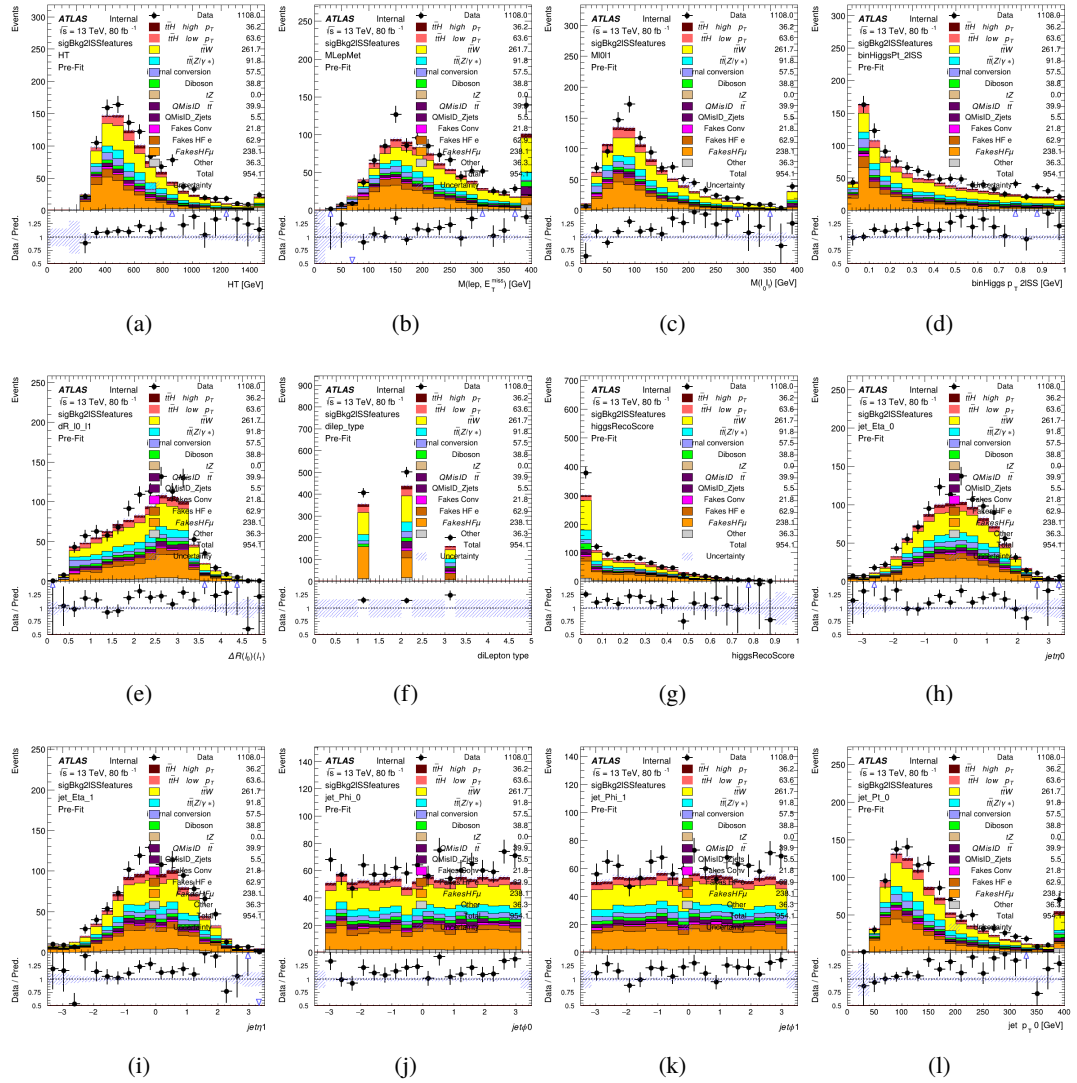


Figure A.18: Input features for higgs3lF

¹⁸⁶⁶ **A.2 Background Rejection MVAs**

¹⁸⁶⁷ **A.2.1 Background Rejection MVA Features - 2lSS**

Figure A.19: Input features for `sigBkg2lSS`

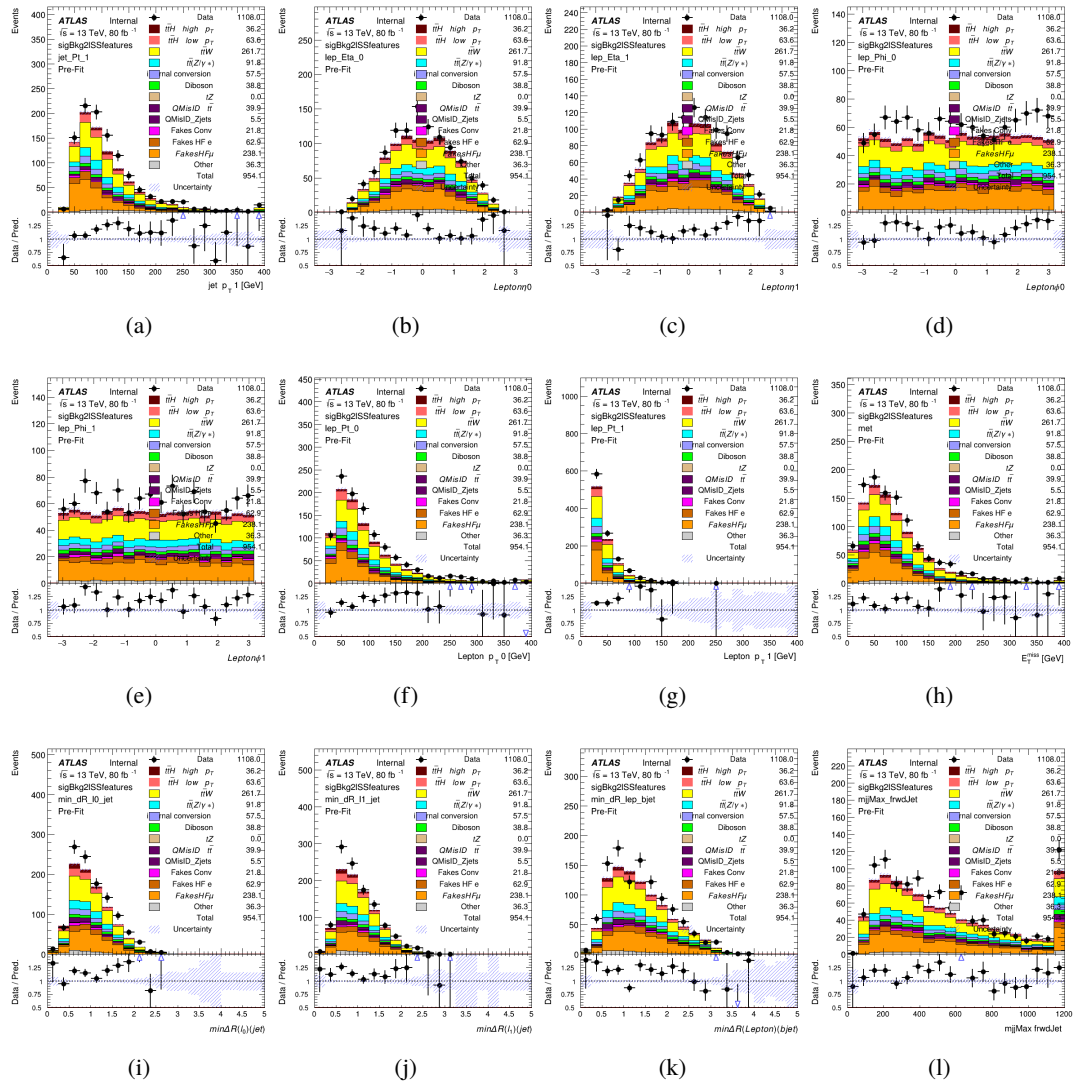


Figure A.20: Input features for sigBkg2lSS

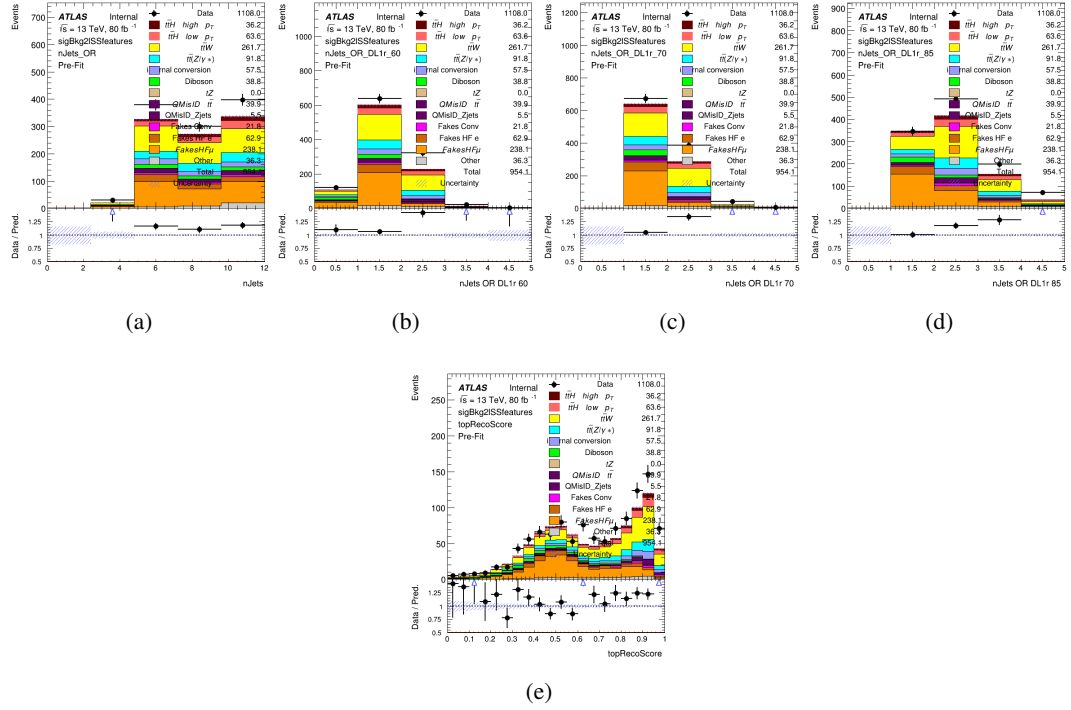


Figure A.21: Input features for sigBkg2lSS

1868 **A.2.2 Background Rejection MVA Features - 3l**

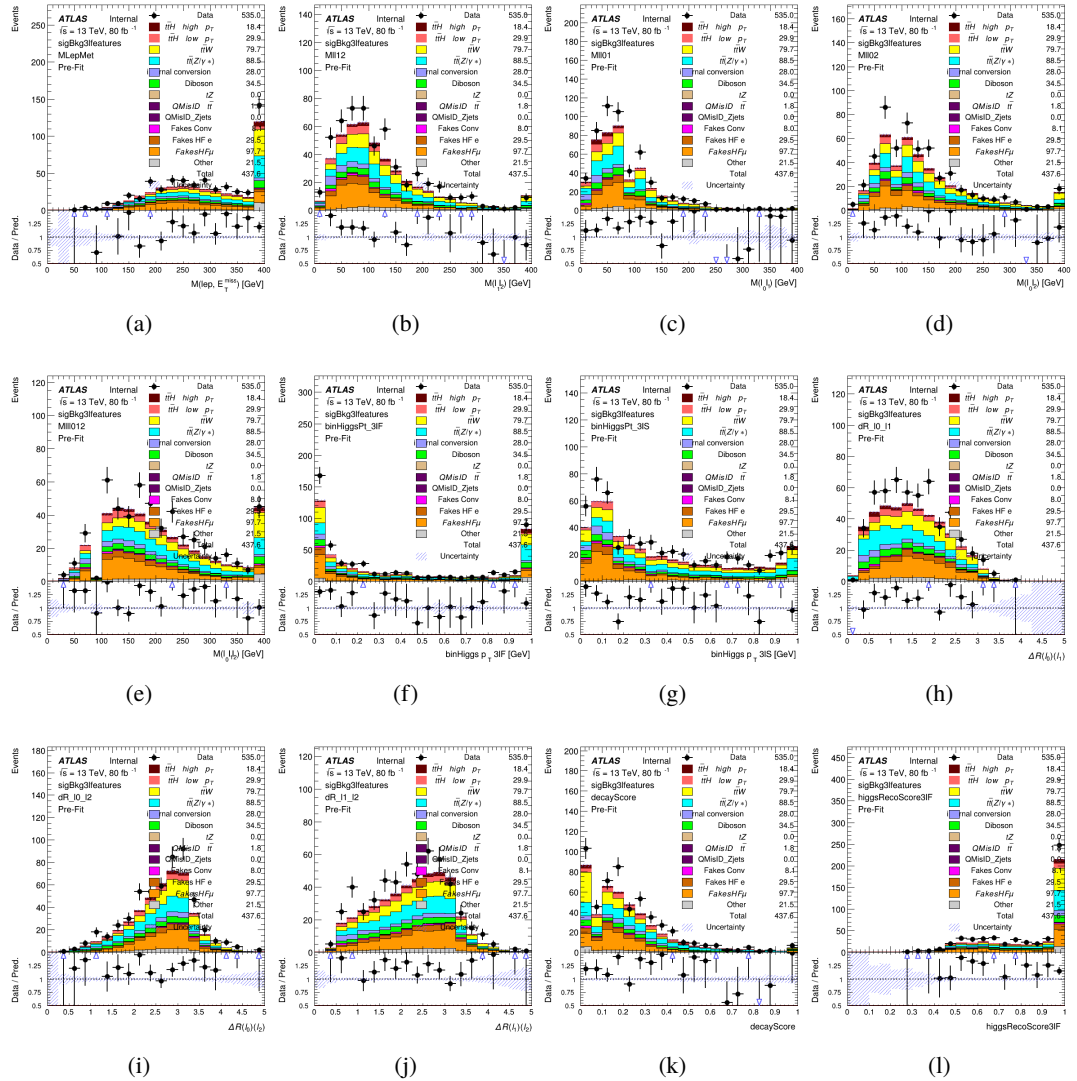


Figure A.22: Input features for sigBkg31

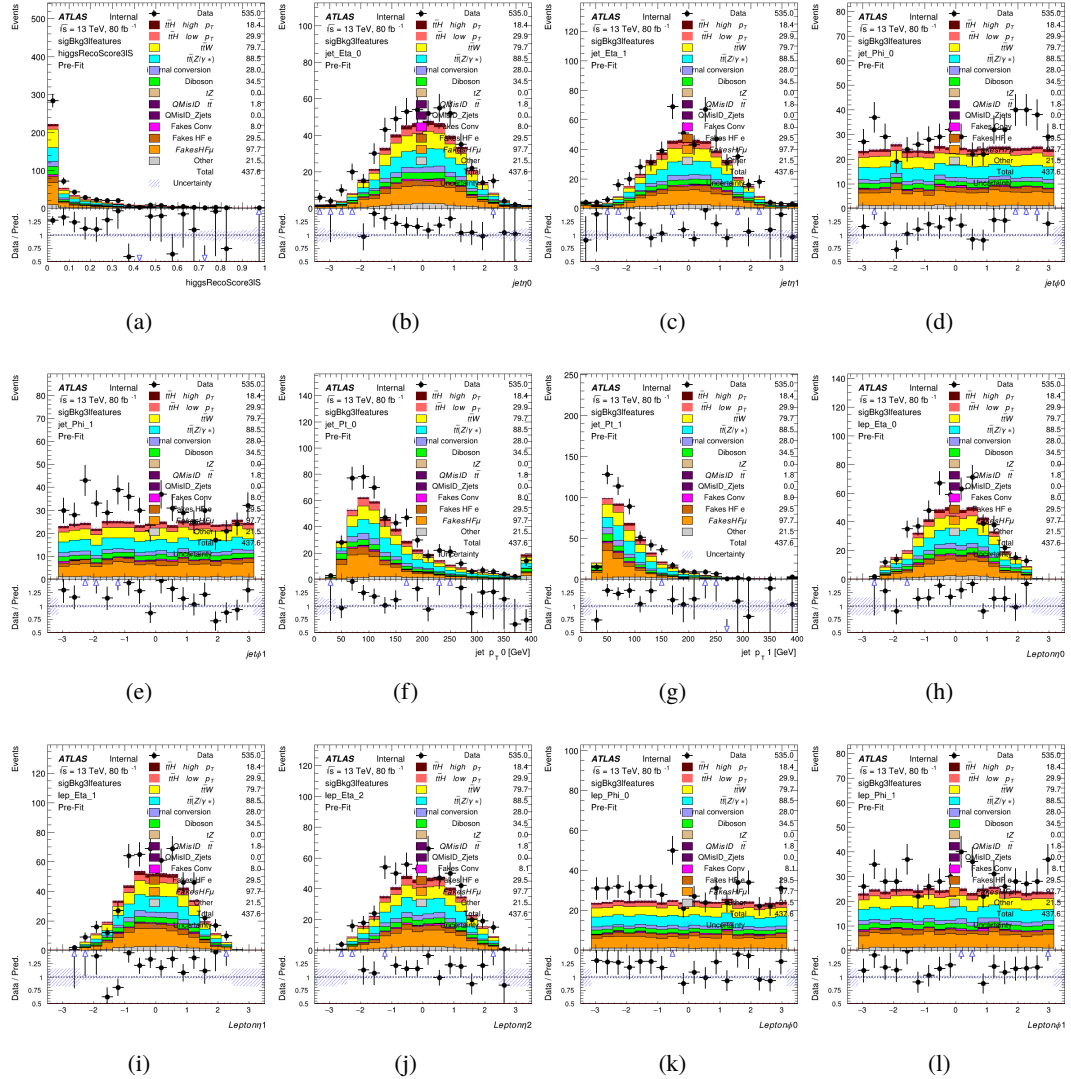


Figure A.23: Input features for sigBkg3l

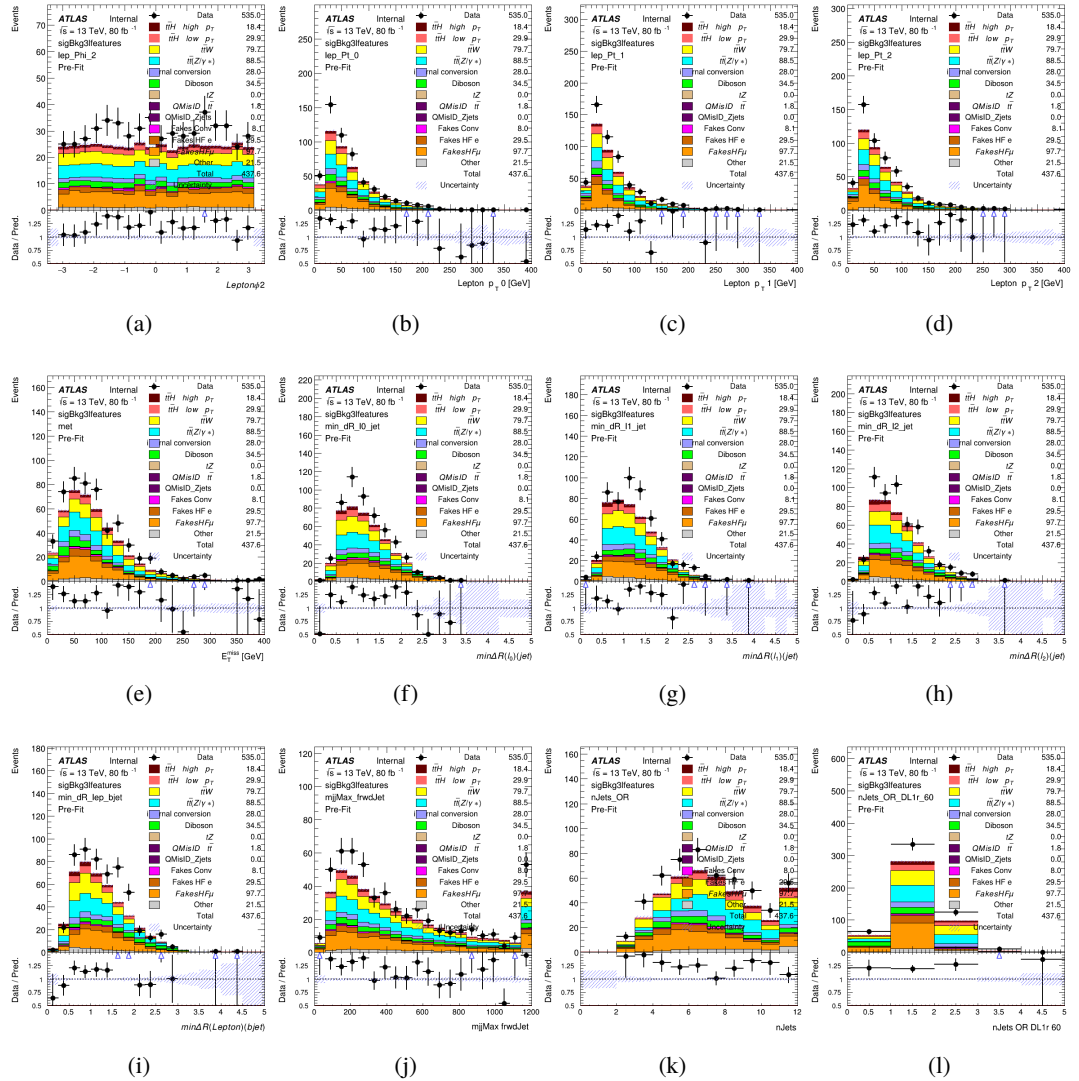


Figure A.24: Input features for sigBkg3l

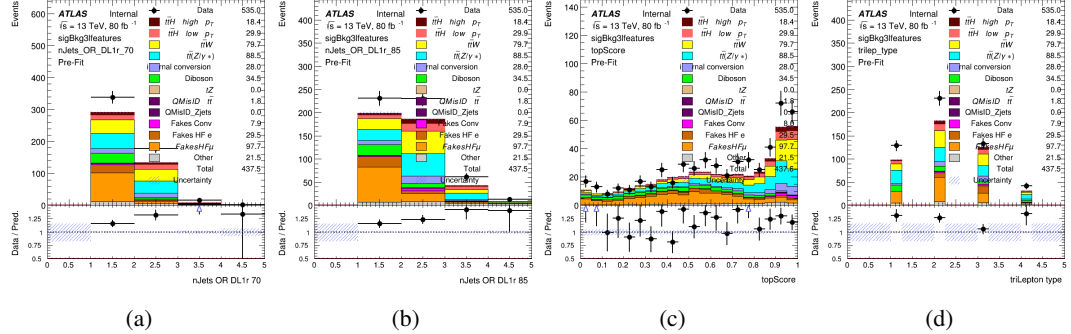


Figure A.25: Input features for sigBkg3l

1869 A.3 Alternate b-jet Identification Algorithm

1870 The nominal analysis reconstructs the b-jets by considering different combinations of jets, and
 1871 asking a neural network to determine whether each combination consists of b-jets from top quark
 1872 decays. An alternate approach would be to give the neural network about all of the jets in an event
 1873 at once, and train it to select which two are most likely to be the b-jets from top decay. It was
 1874 hypothesized that this could perform better than considering each combination independently, as
 1875 the neural network could consider the event as a whole. While this is not found to be the case,
 1876 these studies are documented here as a point of interest and comparison.

1877 For these studies, the kinematics of the 10 highest p_T jets in each event are used for
 1878 training. This includes the vast majority of truth b-jets. Specifically the p_T , η , ϕ , E , and DL1r
 1879 score of each jet are used. For events with fewer than 10 jets, these values are substituted with 0.
 1880 The p_T , η , ϕ , and E of the leptons and E_T^{miss} are included as well. Categorical cross entropy is
 1881 used as the loss function.

Table 61: Accuracy of the NN in identifying b-jets from tops in 2lSS events for the alternate categorical method compared to the nominal method.

| Channel | Categorical | Nominal |
|---------|-------------|---------|
| 2lSS | 70.6% | 73.9% |
| 3l | 76.1% | 79.8% |

1882 **A.4 Binary Classification of the Higgs p_T**

1883 A two bin fit of the Higgs momentum is used because statistics are insufficient for any finer
 1884 resolution. This means separating high and low p_T events is sufficient for this analysis. As
 1885 such, rather than attempting the reconstruct the full Higgs p_T spectrum, a binary classification
 1886 approach is explored.

1887 A model is built to determine whether $t\bar{t}H$ events include a high p_T (>150 GeV) or low
 1888 p_T (<150 GeV) Higgs Boson. While this is now a classification model, it uses the same input
 1889 features described in section 18.4. Binary crossentropy is used as the loss function.

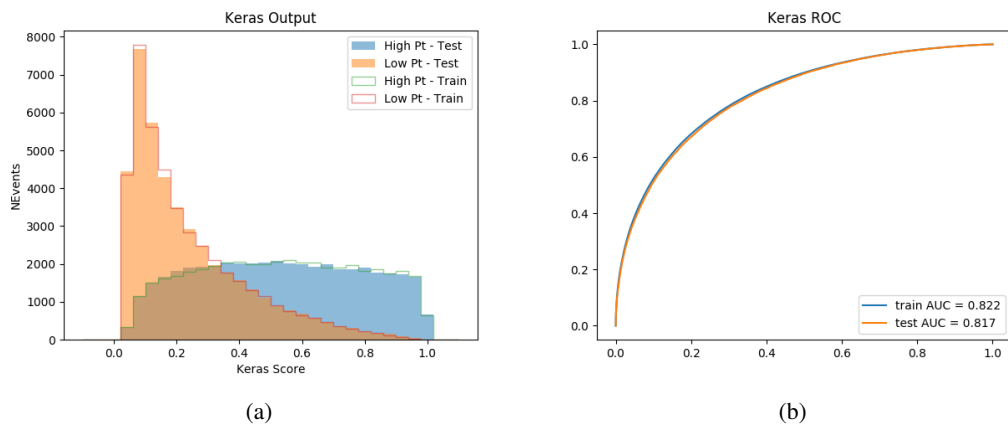


Figure A.26:

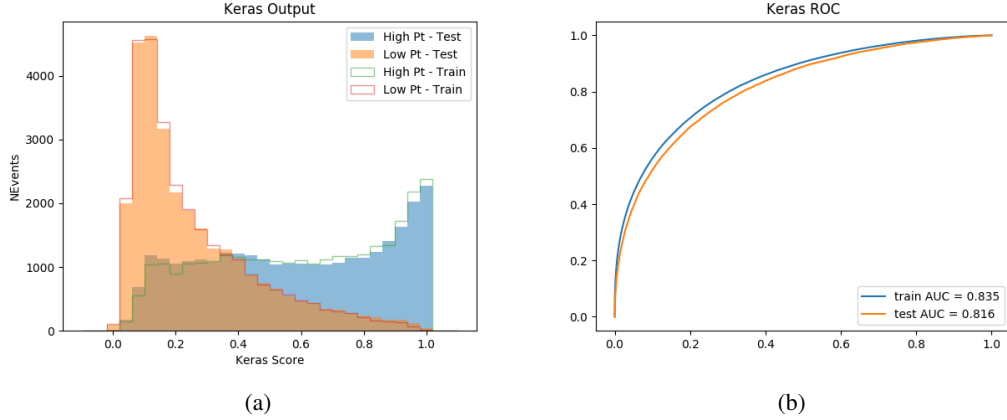


Figure A.27:

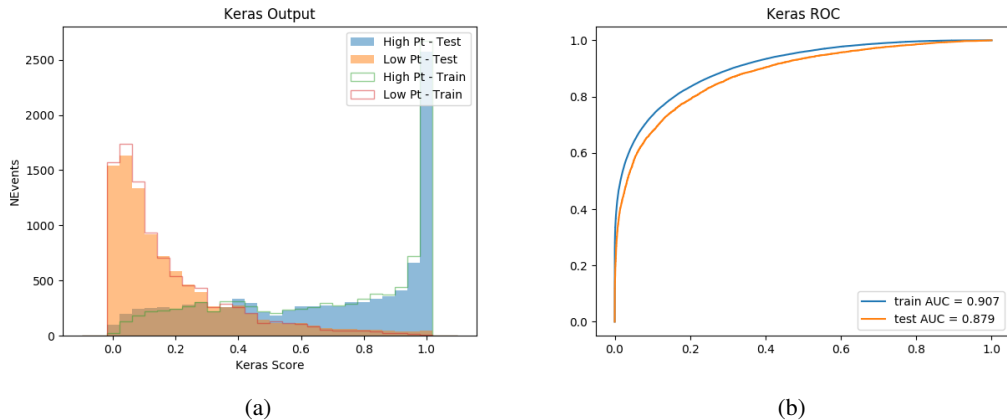


Figure A.28:

1890 A.5 Impact of Alternative Jet Selection

1891 A relatively low p_T threshold of 15 GeV is used to determine jet candidates, as the jets originating
 1892 from the Higgs decay are found to fall between 15 and 25 GeV a large fraction of the time. The
 1893 impact of different jet p_T cuts on our ability to reconstruct the Higgs p_T is explored here. The

1894 performance of the Higgs p_T prediction models is evaluated for jet p_T cuts of 10, 15, 20, and 25

1895 GeV.

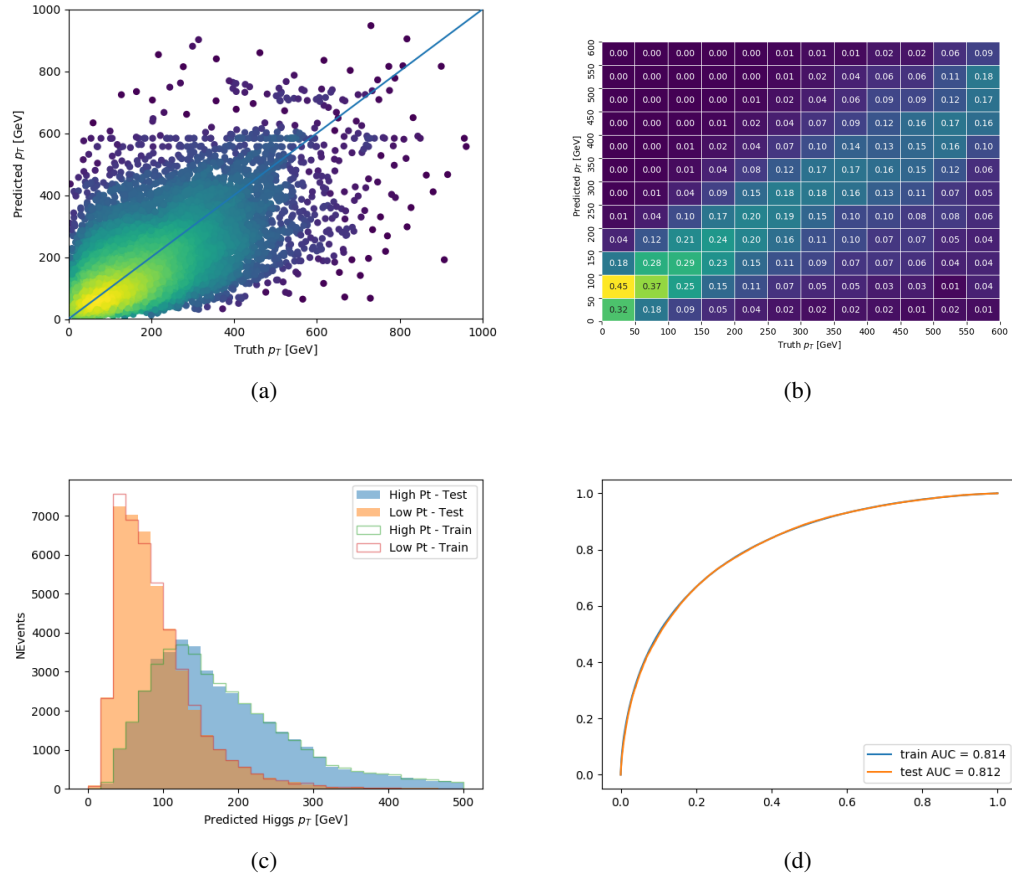


Figure A.29:

1896 **B**